

## FOREWORD

This book of proceedings collects the extended abstracts of the oral lectures and posters presented at the 34th Danubia Adria Symposium on Advances in Experimental Mechanics, 19 - 22 September 2017, Trieste, Italy, organized by prof. Francesca Cosmi, Department of Engineering and Architecture at University of Trieste and M2Test srl, under the patronage of Danubia-Adria Society on Experimental Methods (DAS) and its Italian Member Organization, Società Scientifica Italiana di Progettazione Meccanica e Costruzione di Macchine (AIAS).

This book collects 90 extended abstracts coming from European and non-European countries: Argentina , Austria, Croatia, Czech Republic, Germany, Hungary, Italy, Japan, Poland, Romania, Serbia, Slovakia, Slovenia. It features 16 oral lectures and 74 posters. Each extended abstract published in the proceedings has been evaluated by members of the Scientific Committee of Danubia-Adria Society on Experimental Methods, <http://das.tuwien.ac.at> .

Several areas of experimental mechanics are covered in these proceedings. The range of subjects addressed testifies the relevance of experimental validation, reliability assessment and characterization of new materials as we move further into a digital and connected world of automation and data exchange in manufacturing technologies.

*Francesca Cosmi*

## EXTENDED ABSTRACTS

- 1. ORAL presentations**
- 2. POSTER presentations: Biomechanics**
- 3. POSTER presentations: Integration of mathematical/numerical methods with experimental mechanics**
- 4. POSTER presentations: Instrumentation**
- 5. POSTER presentations: Material characterization and testing**
- 6. POSTER presentations: Practical applications and case studies**
- 7. POSTER presentations: Recent developments in international Standardization and technical regulations**
- 8. POSTER presentations: Structural analysis**



# MEASUREMENT OF OPENING DISPLACEMENT AND STRESS INTENSITY FACTOR OF TWO BRANCHES OF BIFURCATED NOTCH BY MOIRÉ INTERFEROMETRY

Shinichi Suzuki<sup>1</sup>, Mohd Azrin Bin Yusof<sup>2</sup>, Tomotaka Miyashita<sup>3</sup>

<sup>1</sup> Toyohashi University of Technology, Department of Mechanical Engineering, Tempaku-cho, Toyohashi, Aichi, 441-8580, Japan. E-mail: [shinichi@me.tut.ac.jp](mailto:shinichi@me.tut.ac.jp) or [suzukiss1124@gmail.com](mailto:suzukiss1124@gmail.com)

<sup>2</sup> Toyohashi University of Technology, Department of Mechanical Engineering, Tempaku-cho, Toyohashi, Aichi, 441-8580, Japan. E-mail: [azrinyusof5811@gmail.com](mailto:azrinyusof5811@gmail.com)

<sup>3</sup> Yamaha Motor Engineering Co. Ltd., Iwata, Shizuoka, 438-0026, Japan. E-mail:

## 1. Introduction

When a brittle material breaks under external force, fast propagating cracks often appear and propagate at a speed more than two hundred m/s. When crack speed is high enough, a crack bifurcates into two cracks suddenly. Since the crack bifurcation is a characteristic feature of fast propagating cracks, many researchers have been studied it,<sup>[1],[2]</sup> however, the mechanism of the rapid crack bifurcation is not yet fully understood.

Experimental studies on crack bifurcation are classified into two groups. One is dynamic experiments that measure the rapidly bifurcating cracks directly.<sup>[1],[2]</sup> The dynamic experiments are indispensable to figure out rapid crack bifurcation, however, measurement methods are limited.

The other is static experiments that use bifurcated notches under static or quasi-static loading.<sup>[3]-[5]</sup> In the static experiments, one can make bifurcated notches of various shapes and can easily apply many measurement methods. Such static experiments often provide knowledge that cannot be given by the dynamic experiments. The present study is one of the static experiments.

The present study applies Moiré interferometry to measure the opening displacement of two branch notches as well as the mother notch. From the measurement results, stress intensity factors of the two branch notches are obtained. Such study has close relation to the problem of continuity of energy release rate at dynamic crack bifurcation.<sup>[2]</sup>

## 2. Experimental method

Figure 1 shows the PMMA plate specimen used in the present study. There is a bifurcated notch

that has the two branches of 12 mm. The bifurcation angle that is the half of the angle between the two branches is 13.5 degrees. Diffraction grating is passed for Moiré interferometry. Tensile force  $P$  is applied to the specimen, and the opening displacement parallel to  $P$  is measured by Moiré interferometry.<sup>[5]</sup>

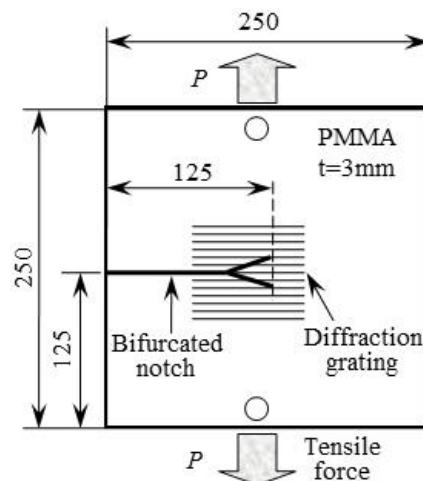


Fig. 1. PMMA plate specimen with bifurcated notch.

## 3. Results

Figure 2 shows Moiré interference fringes around the bifurcated notch. One can measure the opening displacement of the notch by counting the number of the fringes. The displacement between a fringe and the next is 1.02  $\mu\text{m}$ .

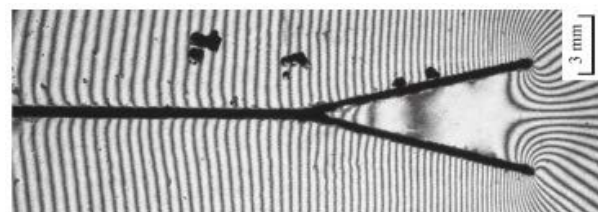


Fig. 2. Interference fringes around a bifurcated notch.

Figure 3 shows the opening displacements of the bifurcated notch measured on the photograph in Fig. 2. The opening displacement of the mother notch,  $COD_M$ , is denoted by black circles, and is proportional to the square root of the distance  $r$  from the virtual notch tip in Fig. 1.

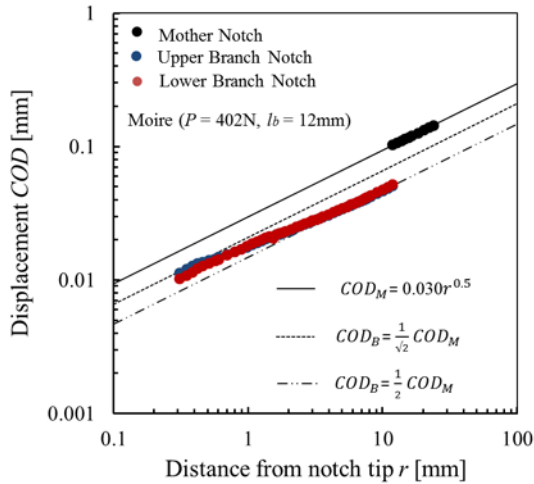


Fig. 3. Opening displacement versus  $r$ .

The opening displacements of the two branch notches,  $COD_B$ , denoted by red and blue circles are a half of  $COD_M$  at the bifurcation point. As approaching to the tip of each branch notch,  $COD_B$  deviates from the line of the half of  $COD_M$ , and approaches to the line of  $COD_M/\sqrt{2}$ .

Figure 4 shows the stress intensity factors that were obtained from  $CODs$  in Fig.3 through the formula of  $COD$  in the singular stress field.

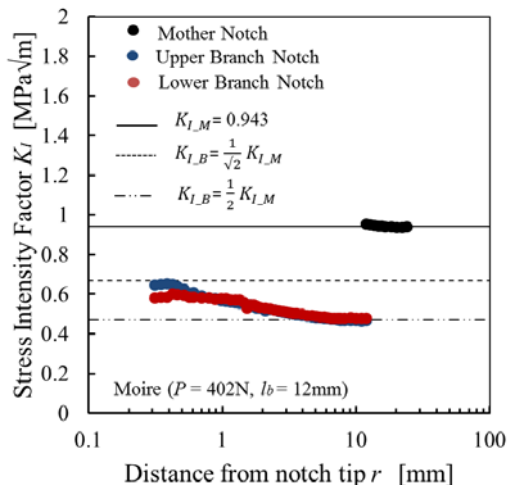


Fig. 4. Stress intensity factor versus  $r$ .

Stress intensity factor  $K_{IM}$  of the mother crack is constant, which says the  $K_{IM}$  indicates the true  $K$  value of the whole bifurcated notch.<sup>[5]</sup> Stress intensity factors  $K_{IB}$  of each branch notch are the

half of stress intensity factor  $K_{IM}$  of the mother notch at the bifurcation point of  $r=12$  mm. The  $K_{IB}$  increases with getting close to the tip of the branch notch, and seems to approach the line indicating  $K_{IM}/\sqrt{2}$ . This is in agreement with the theoretical prediction based on energy release rate of bifurcated cracks.

#### 4. Remarks

- The behavior of stress intensity factor  $K_{IB}$  obtained from opening displacement  $COD_B$  is in agreement with the theoretical prediction based on the energy release rate of bifurcated cracks.
- Similar result is expected to appear in dynamic crack bifurcation. .

#### Acknowledgements

The present study was supported by Grant-in-Aid for Scientific Research (15K05675) by Japan Society for the Promotion of Science.

#### References

- [1] Ravi-Chandar, K., Knauss, W. G., An Experimental Investigation into Dynamic Fracture: III. On Steady-state Crack Propagation and Crack Branching, Int. J. Fracture, 26, 1984, pp.141-154.
- [2] Suzuki, S., Sakaue, K., Iwanaga, K., Measurement of Energy Release Rate and Energy Flux of Rapidly Bifurcating Crack in Homalite 100 and Araldite B by High-speed Holographic Microscopy, J. Mech. Phys. Solids, 55, 2007, pp.1487-1512.
- [3] Kalthoff, J. F., On the Propagation Direction of Bifurcated Cracks. In Dynamic Crack Propagation: editor G. C. Sih, Nordhoff, 1972, pp.449-458.
- [4] Suzuki, S., Iwasaki, Y., Shimizu, Y., Yusof, M. A. B., Static Experiment on Rapid Crack Bifurcation with Y-shaped and Parallel Notches, Mech. Eng. J., 3, 2016, pp.1-12, [DOI: 10.1299/mej.16-00541].
- [5] Suzuki, S., Miyashita, T., Measurement of Opening Displacement and Stress Intensity Factor of Bifurcated Notch by Moiré Interferometry, J. Solid Mech. Mater. Eng., 2, 2008, pp.25-37.

# INTEGRATION OF GENDER IN THE DESIGN PROCESS OF MECHATRONIC PRODUCTS: AN INTERDISCIPLINARY APPROACH

Helmut J. Holl<sup>1</sup>, Eugenia C. Cojocaru<sup>2</sup>, Peter Hehenberger<sup>3</sup>, Waltraud Ernst<sup>4</sup>, Ilona Horwath

- <sup>1</sup> Johannes Kepler University of Linz, Institute of Technical Mechanics, Altenbergerstr. 69, A-4040 Linz, Austria. E-mail: helmut.holl@jku.at
- <sup>2</sup> Plasser & Theurer GmbH, Pummererstraße 5, A-4020 Linz, Austria.
- <sup>3</sup> University of Applied Sciences Upper Austria, School of Engineering, Stelzhamerstraße 23, A-4600 Wels, Austria.
- <sup>4</sup> Johannes Kepler University of Linz, Department of Women's Studies and Gender Research, Altenbergerstr. 69, A-4040 Linz, Austria.

## 1. Introduction

During the design process a lot of information and requirements have to be considered and evaluated. In order to develop the best product or machine for the market a complex engineering process has to be performed. Numerous design criteria and requirements ranging from purchase, manufacturing up to sales should be considered and fulfilled but they can be in conflict. This evaluation is a laborious process and the trade off should result in an efficient performance of the machine depending on its functionality and the acceptance of the operator. So it is important to consider gender and operator requirements in the design process, which is not usually done in the industrial application of mechatronic products.

A systematic research process has been performed and established in order to evaluate the impact of user requirements onto the functionality and design of industrial devices with the main focus on the gender dimension and its social aspects in all steps of the design process. The results of this research lead to developing guidelines for finding and including the most important requirements in the design process. The proper evaluation of these requirements determines the success of the product, e.g. including them in a specific human-machine-interface. Innovation and new ideas have to be evaluated with respect to the requirements profile derived by these guidelines.

## 2. Product Development Process

Different strategies and methods are applied when designing a new or an improved product. Many components of machines have to be

designed to fulfill specific functions and their operation and availability is critical for the performance of the machines. Particularly finite element method analysis of the deformation of the components of the machines and numerical simulation and experimental measurements of the vibrations of machine components and the acoustic emission depending on the operation conditions should be performed. Simulation of the air flow during the production process of defined materials is performed to predict the quality of products. The knowledge of the machine operator requirements is important in finding the best machine parameters.

### 2.1 Conventional mechanical engineering approach

During the development and design process all relevant requirements are evaluated with respect to their impact to functionality. In this I-methodology procedure the design engineer considers all the known parameters and influence factors, like function, productivity, reduced faults, availability, emission, ergonomics, etc., see [1], according to the own experience and preferences. Involuntary important requirements can be unconsidered which can be challenged by taking gender and operational experiences systematically into account.

### 2.2 Multicriterial approach

In the process of integrated product development various additional factors are considered so that the product is suitable designed for processing, mounting, maintenance, ergonomic, wear, corrosion, risks, etc, see [2]. In evaluating and weighting various influence factors a pareto-optimal product can be derived based on a checklist and possible general requirement profiles and a flow chart of the design process are used. In

the participative design process more persons are involved and bring in their knowledge as experts.

### 2.3 Integrated gender approach

More factors are considered when the gender dimension is included, see Fig. 1. Frequently in the design process the focus is on objective and rational factors but there is an extension if the machine operators are included as experts into the design process of the new machine generation. A procedure was developed in this research project, which allows the integration of gender aspects in requirements at every level and in all fields of the design process. The results are modifications of e.g. the acoustic emission, the size of the operator panel, the outer shape of the machine and the positioning of the human-machine interface.

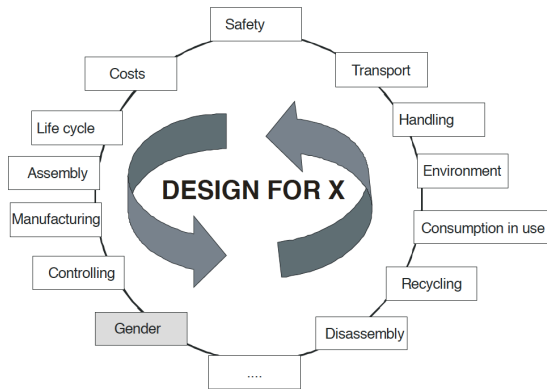


Fig. 1. Scheme of Design for X.

### 3. Methods of Analysis

For the analysis of gender-relevant requirements qualitative and quantitative methods have been applied. The procedure was developed in a general setting and is demonstrated for the application to laser engraving and cutting machines, see [3]. As *quantitative methods* in a first step structured interviews with experts and operators were conducted to explore their different requirements. Based on this information in a second step a written questionnaire has been developed and sent to the machine operators from different companies. In a third step the workflow-analysis was monitored on a group of operators to get additional information. As *qualitative methods* an exchange of opinions about daily experience by the work with the machines was organized within a framework of designed focus groups with operators. To gain further insight the existing and necessary functions have been discussed. The results of these two methods were included in a

extensive participatory design process. The result of these settings is a list of gender relevant requirements, which has to be matched with all other requirements in the design process of a new product or machine as shown in Fig. 2.

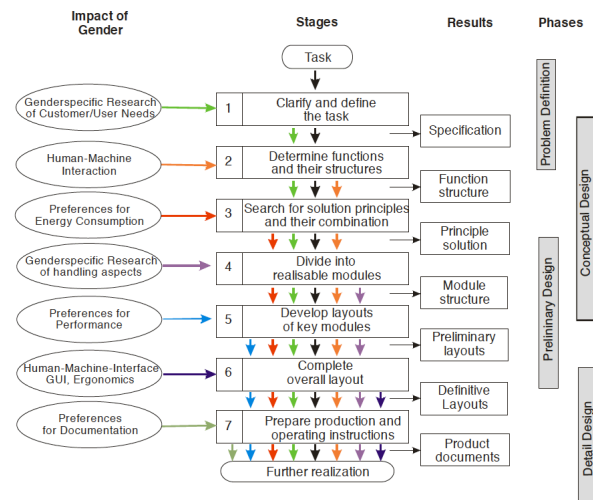


Fig. 2. Influence of Gender in the Design Process.

### 4. Results

A new design procedure for industrial machines was developed taking the complexity of users experience and gender into account. Product requirements lists including the user requirements have been derived in a stepwise procedure. The application to the new design of a laser engraving and cutting machine resulted in an improved machine with many new features.

### Acknowledgements

The support of this work within the Austrian research project Ge:MMaS funded by the FFG – the Austrian Research Promotion Agency and BMVIT – Federal Ministry for Transport, Innovation and Technology is gratefully acknowledged.

### References

- [1] Pahl, G., Beitz, W., Feldhusen, J., Grote, K.-H., Konstruktionslehre. 7<sup>th</sup> ed, Springer, 2007.
- [2] Ehrenspiel, K., Integrierte Produktentwicklung. Carl Hanser Verlag, 2007.
- [3] Cojocaru, E.C., Ernst, W., Hehenberger, P., Holl, H.J., Horwath, I., Design for Gender: Bedienungsgerechte Maschinenentwicklung durch Expertise von MaschinenbedienerInnen. In: Agenda Gute Arbeit: geschlechtergerecht!, eds: Weg, M., Strolz-Willig, B., VSA Verlag, pp.158-168, 2014.

## FABRICATION OF NANOCOMPOSITES WITH SILICA NANOPARTICLES

Dan M. Constantinescu<sup>1</sup>, Dragos A. Apostol<sup>1</sup>, Catalin R. Picu<sup>2</sup>, Krzysztof Krawczyk<sup>3</sup>,  
Manfred Sieberer<sup>4</sup>, Anton Hadar<sup>1</sup>, Michael Feuchter<sup>3</sup>

- <sup>1</sup> University POLITEHNICA of Bucharest, 060042 Bucharest, Romania. E-mails: [dan.constantinescu@upb.ro](mailto:dan.constantinescu@upb.ro), [dragos.apostol@upb.ro](mailto:dragos.apostol@upb.ro), [anton.hadar@upb.ro](mailto:anton.hadar@upb.ro)
- <sup>2</sup> Rensselaer Polytechnic Institute, Troy, 12180 NY, USA. E-mail: [picuc@rpi.edu](mailto:picuc@rpi.edu)
- <sup>3</sup> University of Leoben, A-8700 Leoben, Austria. E-mails: [k.k.krawczyk@unileoben.ac.at](mailto:k.k.krawczyk@unileoben.ac.at), [michael.feuchter@unileoben.ac.at](mailto:michael.feuchter@unileoben.ac.at)
- <sup>4</sup> BTO-Epoxy, A-3300 Amstetten, Austria. E-mail: [manfred.sieberer@bto-epoxy.com](mailto:manfred.sieberer@bto-epoxy.com)

### 1. Introduction

Nanocomposites exhibit a combination of exceptional properties which usually cannot be achieved in standard composites. Some of the most studied systems are nanocomposite thermosets, which are filled with various forms of nano-carbon (carbon nanotubes, graphene), silica and alumina nanopowders, and other nanofillers. The influence of the technological methods used to produce nanocomposites was extensively discussed, only as an example [1]; more than 100 recipes can be found in the literature. Essentially, the main problem is to disperse uniformly the nanofillers, as mentioned [2] and [3]. Some considerations on the fabrication technology of nanocomposites filled with multi-wall carbon nanotubes (MWNT), alumina ( $Al_2O_3$ ) and silica ( $SiO_2$ ) nanoparticles were presented elsewhere, [4, 5]. Improvements of the manufacturing process were established in order to produce uniformly distributed fillers in the epoxy matrix. On the other hand it is important to use functionalized nanoparticles that are more compatible with the matrix and easier to mix.

### 2. Technologies of fabrication

For dispersing the fillers in the epoxy resin special equipment is needed. A shear mixer Thinky ARE-250 (Japan) with maximum rotation speed of 2000 rpm was used for mechanical mixing. A high energy sonicator, Sonics VCX-750 (US), having a generator with 750 W output, a 20 kHz convertor and a temperature controller, was used to fragment the conglomerated nanoparticles. A programmable vacuum oven Memmert VO 400 (UK) was used for curing. The final mixture of resin, nanofillers and hardener was poured in a silicon mould. For each batch 14 specimens were produced.

Several manufacturing procedures were explored such to improve the dispersion and avoid the formation of air bubbles in the resin. The sample preparation steps that led to the best results are as follows: mixing the resin with the nanoparticles with the shear mixer for 10 minutes at a speed of 1500 rpm; the resulting solution R+NP (R = resin, NP = nanoparticles) is sonicated for 2 hours. In Method M1, R+NP was put under a vacuum of 30 mbar for 2 hours at room temperature for degassing. In Method M2 this step was omitted. The hardener H (H = hardener) was added to R+NP after this step. The R+NP+H solution was mixed by hand for about 2 minutes, and poured in the silicon mold.

### 3. Materials used for fabrication

Various types of resin were used. These include Neukadur EP 986 produced by Altropol Kunststoff GmbH, Germany, which was used together with the hardener Neukadur HN 242 (with a pot time of 25 minutes). Another system considered was the same epoxy with Neukadur HN 246 as hardener (with a pot time of 240 minutes); the second curing agent gives more time for mixing with the resin.

Furthermore, two epoxy systems produced by BTO Epoxy and named System 2 (S2) and System 5 (S5) were considered. S2 uses a resin notated IR 77.31 and a slow hardener IH 77.15 (with a pot life of 110 minutes at 25 °C). S5 is under development and has a low viscosity of 100-300 mPas at 25 °C and a pot life of 80 minutes at 25 °C.

Both unfunctionalized and functionalized silica nanopowders were used. The unfunctionalized silica was produced by Sigma Aldrich and was supposed to have particles of 5-15 nm diameter and purity 99.5 wt% with some traces of metal.

The functionalized nanopowder was obtained by coupling of azidophenylsilanes to nanosilica with a specific surface area of 175-225 m<sup>2</sup> (determined using the Brunauer–Emmett–Teller (BET) theory). This is a fumed silica, with a fractal structure, consisting of particles of approximately 20-80 nm which are agglomerated and intergrown to form bigger aggregates.

Fig. 1 TEM images of the unfunctionalized (but clustered) nanoparticles (a) and the functionalized fumed silica nanopowder (b) are presented.

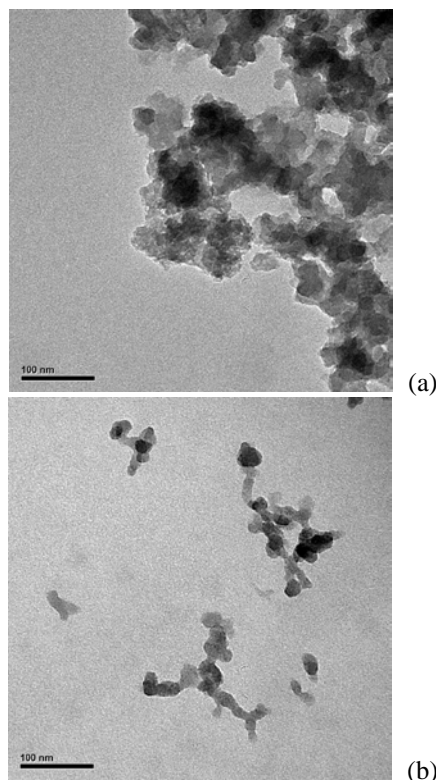


**Fig. 1.** Sigma Aldrich nanopowder: (a) clustered unfunctionalized silica of nominal particle size 5-15 nm; (b) functionalized fumed silica of 20-80 nm.

#### 4. Mechanical testing of nanocomposites

Uniaxial traction testing of the specimens was performed using a Zwick/Roell testing machine, model Z010, with a maximum force of 10 kN. For each batch specimens were tested to determine the modulus of elasticity, the ultimate tensile strength, and the elongation at failure. Tests were carried on nanocomposites with unfunctionalized and functionalized silica nanopowder. The testing speed was 1.5 mm/min which corresponds to an initial strain rate of approximately 10<sup>-3</sup> s<sup>-1</sup>.

Weight percentage wt% of silica powder was 0.1, 0.3, 0.5, 1.0, and 3.0 in different batches. The

mechanical properties for samples prepared using method M1, for which the R+NP mixture was kept under a vacuum of 30 mbar for 2 hours at room temperature for degassing, and for samples prepared using method M2 (degassing was omitted as it was found that in some cases it generates additional gas bubbles in the specimens) were obtained.

#### Acknowledgements

All partners of this project acknowledge the M.ERA-NET transnational call 2013 which led to common researches started at the end of 2015. The Romanian partner acknowledges that this work was supported by a grant of the Romanian National Authority for Scientific Research and Innovation, project number 11/2015. The Austrian partners acknowledge that this work was supported by the Austrian Ministry for Transport, Innovation and Technology within the funding programme Production of the Future.

#### References

- [1] Zhou, Y., Pervin, F., Lewis, L., Jeelani, S., Fabrication and characterization of carbon/epoxy composites mixed with multi-walled carbon nanotubes, *Mater. Sci. Eng. A*, 475, 2008, pp. 157-165.
- [2] Gkikas, G., Barkoula, N.-M., Paipetis, A.S., Effect of dispersion conditions on the thermo-mechanical and toughness properties of multi walled carbon nanotubes-reinforced epoxy, *Compos. Part B-Eng.*, 43, 2012, pp. 2697-2705.
- [3] Montazeri, A., Chitsazzadeh, M., Effect of sonication parameters on the mechanical properties of multi-walled carbon nanotube/epoxy composites, *Mater. Design*, 56, 2014, pp. 500-508.
- [4] Cosmoiu, I., Apostol, D.A., Picu, C.R., Constantinescu, D.M., Sandu, M., Manufacturing and testing of nanocomposites with carbon nanotubes and nanoparticles, *UPB Sci. Bull.*, 77, 2015a, pp. 107-119.
- [5] Cosmoiu, I., Apostol, D.A. Constantinescu, D.M., Picu, C.R., Sandu, M., 2015b. Advances on the Manufacturing Process of Nanocomposites with MWNT and Nanopowders, *Appl. Mech. Mater.*, 760, 2015b, pp. 281-286.

# EVALUATION OF OUT-OF-PLANE DEFORMATION OF MASONRY INFILL WALLS DUE TO IN-PLANE LOADING BY DIGITAL IMAGE CORRELATION

Goran Gazić<sup>1</sup>, Tihomir Dokšanović<sup>2</sup>, Hrvoje Draganić<sup>3</sup>

- <sup>1</sup> Faculty of Civil Engineering Osijek, University of Osijek, Department of Technical Mechanics, Drinska 16a, HR - 31000, Osijek, Croatia. E-mail: [ggazic@gfos.hr](mailto:ggazic@gfos.hr)
- <sup>2</sup> Faculty of Civil Engineering Osijek, University of Osijek, Department for Materials and Structures, Drinska 16a, HR - 31000, Osijek, Croatia. E-mail: [tdoksanovic@gfos.hr](mailto:tdoksanovic@gfos.hr)
- <sup>3</sup> Faculty of Civil Engineering Osijek, University of Osijek, Department for Materials and Structures, Drinska 16a, HR - 31000, Osijek, Croatia. E-mail: [draganic@gfos.hr](mailto:draganic@gfos.hr)

## 1. Introduction

Effects of in-plane and out-of-plane loading are generally observed separately [1, 2] but recent investigations [3] are trying to combine the influence of in-plane damage on out-of-plane strength. In this paper, out-of-plane effects caused by in-plane loading are observed through digital image correlation.

## 2. Experimental investigation

Test setup, model description, and behaviour of tested models under in-plane loading can be found [1].

This paper presents an extension of previously published results, providing unique insight into out-of-plane behaviour of tested models caused by in-plane loading.

### 2.1 In-plane behaviour

Response of tested models was evaluated according to limit states. Three limit states were considered based on a certain damage mode and overall global behavior (Fig. 1) [5].

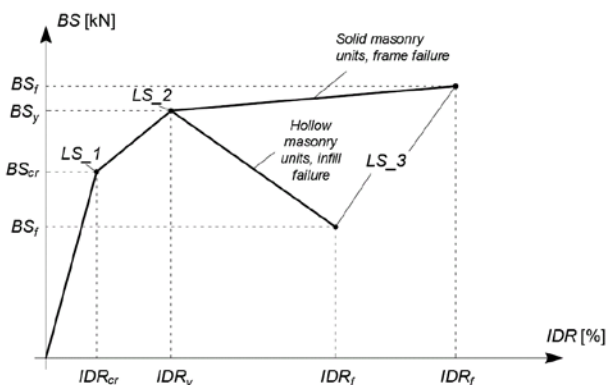


Fig. 1. Backbone curves and limits states of tested models.

### 2.2 Out-of-plane deformations

Out-of-plane deformations were observed in terms of displacement mode and only qualitative representation is given. It was observed that displacement mode was highly influenced by masonry unit robustness. Shift from plate like to rigid body behaviour of infill walls was related to masonry unit robustness. In the range of small in-plane deformations, out-of-plane effects were related to imperfections. When a certain in-plane limit state was reached, out-of-plane deformation mode changes accordingly (Fig. 2 and Fig. 3). Only masonry infill type was considered while frame properties were constant.

## 3. Conclusions and recommendations

Out-of-plane deformation mode of masonry infill caused by in-plane loading was investigated based on conducted experimental research on models with varied masonry unit robustness and frame properties. Conclusions were drawn as follows:

- masonry unit robustness played a major role in terms of both in-plane and out-of-plane behaviour,
- masonry infills constructed of solid clay units exhibited plate like behaviour, characterized by inflection points,
- masonry infills made of hollow clay units behaved in a rigid body fashion,
- frame properties influenced out-of-plane behavior only in case of infills made of hollow clay units,
- out-of-plane deformations caused by in-plane loading are to be taken in account

when coupled actions (in and out-of-plane loading condition) are considered.

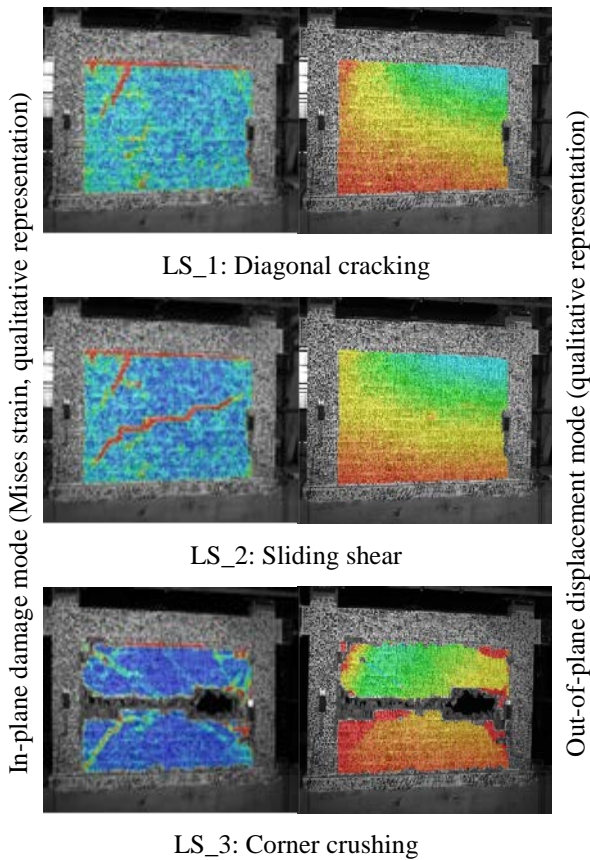


**Fig. 2.** In-plane damage and out-of-plane displacement mode for sample *O4\_bpm*.

### Acknowledgements

Research presented in this paper is a part of the research project "Frame-masonry for modelling and standardization" No. IP-11-2013-3013, funded by the Croatian Science Foundation and its support is gratefully acknowledged.

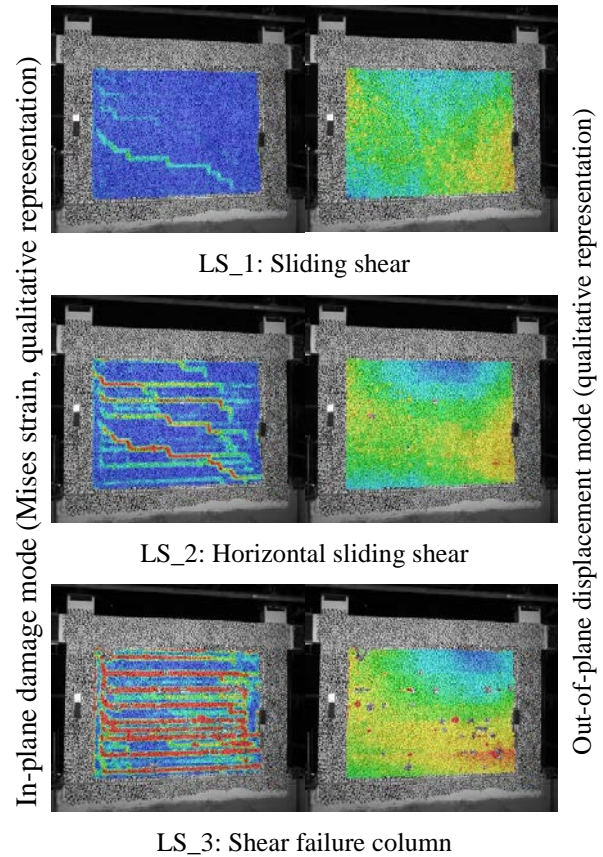


**Fig. 3.** In-plane damage and out-of-plane displacement mode for sample *O4\_cpm*.

### References

- [1] Gazić, G., Sigmund, V., Cyclic testing of single-span weak frames with masonry infill, *Gradevinar*, 8, 617-633, 2016.
- [2] Abrams, D. P., Angel, R., Uzarski, J., Out-of-Plane Strength of Unreinforced Masonry infill Panels, *Earthquake Spectra*, 12, 825-844, 1996.
- [3] Furtado, A., Rodrigues, H., Arede, A., Varum, H., Experimental evaluation of out-of-plane capacity of masonry infill walls, *Engineering Structures*, 111, 48-63, 2016.

# FEASIBILITY STUDY OF STRAIN PROFILE MEASUREMENT BY A DISTRIBUTED FIBER OPTIC SENSING SYSTEM UNDER MODE I INTERLAMINAR FRACTURE TOUGHNESS OF FIBER-REINFORCED POLYMER MATRIX COMPOSITES

Andrea Bernasconi<sup>1</sup>, Andrea Gianneo<sup>1</sup>

<sup>1</sup> Politecnico di Milano, Department of Mechanical Engineering, Via La Masa 1, 20156, Milano, Italy.  
E-mail: [andrea.bernasconi@polimi.it](mailto:andrea.bernasconi@polimi.it)

## 1. Introduction

The measurement of the mode I interlaminar fracture toughness of composite materials is usually conducted according to the ASTM D5528-13 or the ISO 15024 standards [1,2], using a Double Cantilever Beam (DCB) specimen (Fig. 1). The propagation of this crack is obtained by imposing a relative displacement to the pins inserted into the load blocks. In order to evaluate the values of the critical energy release rate  $G_{IC}$ , the length of the crack must be measured. This is usually performed in two ways: a) by observing the position of the tip of the crack, using an optical microscope; b) by data reduction schemes, that relate the opening of the crack to the displacement of the loading pins and the applied load. In the second case, knowledge of the elastic properties of the material and a calibration that takes into account the compliance of the testing equipment is required.

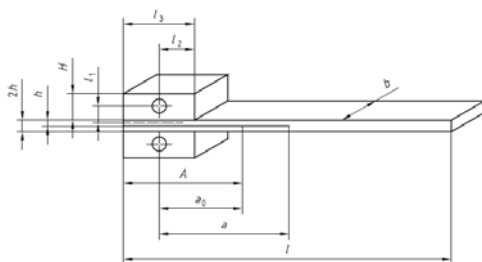


Fig. 1. The DCB specimen [2]

In this work we present a method for the determination of the crack length based on the measurement of the longitudinal strain field on the surface of the DCB specimen, using distributed sensing by Optical Backscatter Reflectometry (OBR). This techniques was successfully applied

to the fatigue crack monitoring in adhesive joints [3].

## 2. Methods

An OBR ODiSI-B interrogator by Luna Innovations was used to measure the evolution of the strain profile. Strain measurement can be performed along the entire fibre with thousands of sensing locations interrogated simultaneously (gauge length was 1.3 mm, with a gauge separation of 0.65 mm), transforming an ordinary optical fibre into a high spatial-resolution strain sensor. One single low bending optical fibre, (type “Strain sensor 2m”, by Luna Innovations Inc.) was bonded on the top surface of a DCB specimen, as shown schematically in Fig. 2.

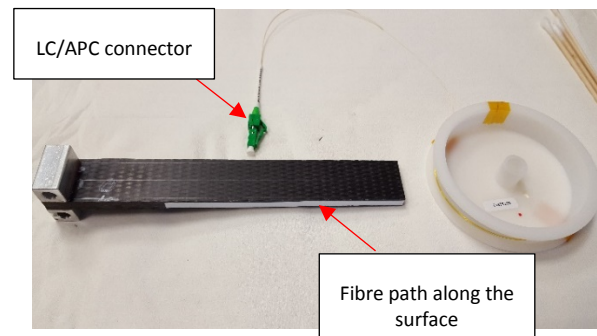


Fig. 2. OBR fibre surface bonded on a DCB specimen.

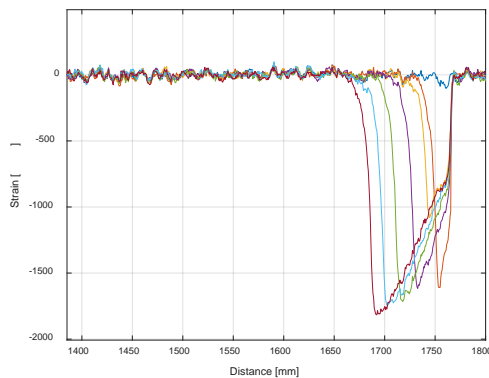


Fig. 3. Experimental setup.

Then, test was performed according to ASTM D5528-13 using an electro-mechanical tensile machine, whose maximum loads capacity is 1kN; as shown schematically in Fig. 3.

### 3. Results

Strain profile were recorded during the test with a sampling frequency of 23.8Hz. Fig. 4 shows the evolution of the surface strain profile: as the delamination front is advancing, the position of the minimum peak also moves in the same direction, suggesting a method to infer the position of the crack by recording and analyzing the surface strain profile. Fig. 5 shows the absolute value of the minimum peak strain, due to the presence of the delamination, during the test.



**Fig. 4.** Surface strain profile recorded on a DCB specimen under test.

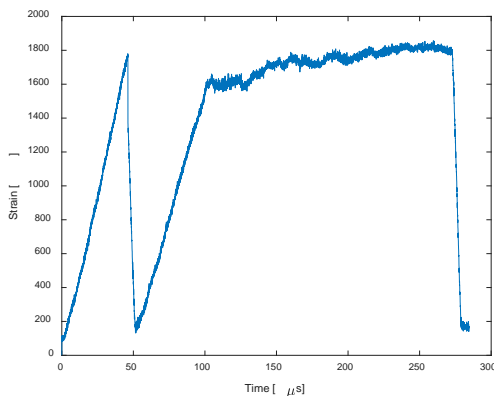


**Fig. 5.** Peak strain profile of a DCB specimen under Mode I interlaminar fracture toughness test.

Once the initial position of delamination (PTFE insert) is known, its growth can be determined by subtracting the actual position of the minimum peak determined by OBR to its original position.

Fig. 6 shows the estimated delamination growth of a DCB specimen as a function of the test time.

### 4. Concluding remarks

- the distributed sensing capabilities of OBR technology allows for measuring the strain profile in DCB specimens, which is characterized by a minimum peak due to the delamination;
- by following the evolution of the minimum strain peak it is possible to monitor the position of delamination
- results are based on one single test and more tests are planned to validate the method.

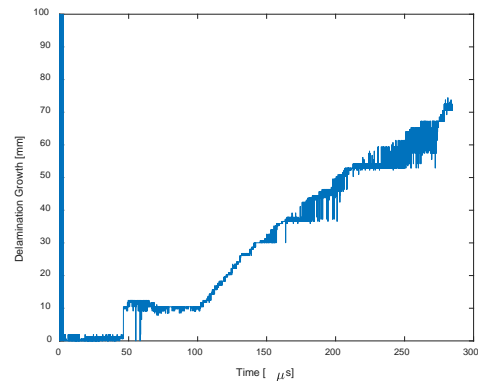


**Fig. 6.** Delamination growth of a DCB specimen under Mode I interlaminar fracture toughness test.

### Acknowledgements

The authors acknowledge the use of experimental facilities available at “LAFOS” Laboratory on Fiber Optic Sensors of Politecnico di Milano

### References

- [1] ASTM D5528-13 Standard Test Method for Mode I Interlaminar Fracture Toughness of Unidirectional Fiber-Reinforced Polymer Matrix Composites
- [2] ISO 15024:2001 - Fibre-reinforced plastic composites -- Determination of mode I interlaminar fracture toughness, GIC, for unidirectionally reinforced materials
- [3] A. Bernasconi, M. Carboni, L. Comolli, R. Galeazzi, A. Gianneo, and M. Kharshiduzzaman, “Fatigue Crack Growth Monitoring in Composite Bonded Lap Joints by a Distributed Fibre Optic Sensing System and Comparison with Ultrasonic Testing,” J.



34th Danubia-Adria Symposium on Advances in Experimental Mechanics  
University of Trieste, Italy, 2017



Adhes., vol. 92, no. 7–9, pp. 739–757, Dec.  
2016.

# EXPERIMENTAL INVESTIGATION OF THE SHEAR ANGLE VARIATION DURING ORTHOGONAL CUTTING

**Szabolcs Berezvai, Tamas G. Molnar, Daniel Bachrathy, Gabor Stepan**

Budapest University of Technology and Economics, Department of Applied Mechanics, Muegyetem rkp. 5., Budapest, 1111 Hungary. E-mail: [berezvai@mm.bme.hu](mailto:berezvai@mm.bme.hu)

## 1. Introduction

In this contribution, we investigate the variation of the shear angle during orthogonal cutting processes illustrated in Fig. 1. In orthogonal cutting, the material in front of the cutting edge is sheared over a primary shear zone that is approximated by the shear plane located at shear angle  $\Phi$ . The shear angle determines the magnitude of the cutting force acting on the tool and the coefficients of theoretical cutting force models. An important application of the cutting force models is the investigation of machine tool vibrations [1-3], where the cutting force coefficients have significant effect on the dynamics of metal cutting. Consequently, modelling and measuring the shear angle is important in terms of developing accurate cutting force expressions to investigate the dynamics of cutting processes.

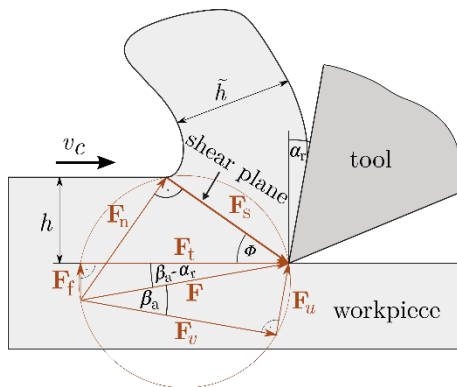


**Fig. 1.** The Merchant's model of cutting forces

## 2. Shear angle models

The most well-known approach of modelling cutting forces is Merchant's circle [4] illustrated in Fig. 1. In this model, the cutting force component  $F_s$  aligned with the shear plane is calculated as the product of the yield shear stress and the shear plane area, from which other components of the cutting force  $F$  can also be determined based on the rake angle  $\alpha_r$  and the average friction angle  $\beta_a$ . Since the shear plane area depends on the shear

angle, the coefficients of theoretical cutting expressions are in fact functions of the shear angle. The most well-known shear angle models are the maximum shear stress principle, which states that the angle of the cutting force vector and the shear plane is 45 degrees; and the minimum energy principle, which assumes that the power of the cutting force is minimal and determines the shear angle accordingly [4]. These models are typically used to describe stationary cutting processes where the uncut chip thickness  $h$  is constant. However, during cutting the chip thickness may vary in time, especially in the case of machine tool vibrations.

## 3. Experimental layout

The goal of this contribution is to determine the shear angle experimentally during non-stationary orthogonal cutting of a single aluminum rib with thickness of  $w = 2$  mm, and to investigate the relationship between the chip thickness, the cutting force and the shear angle using high-speed camera recordings [5].

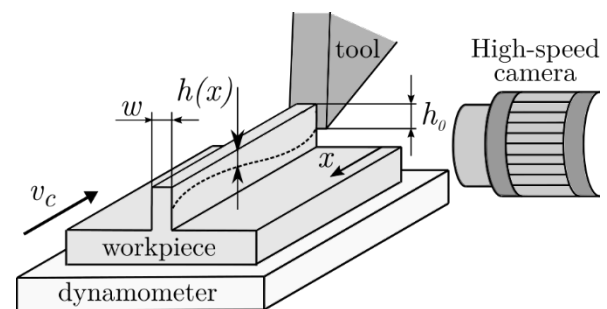


**Fig. 2.** The schematics of the experimental layout

As the measurement layout shows (see Fig. 2), the workpiece was placed on a KISTLER 9129 AA multicomponent dynamometer, while the chip formation process was recorded by Photron SA5 high-speed camera with 10,000 fps. The chip thickness was prescribed according to the sinusoidal function  $h(x) = h_0 + h_A \sin(2\pi x/\lambda)$ , where  $h_0$  is the average chip thickness,  $h_A$  the amplitude and  $\lambda$  the wavelength.

The geometry of the tool can be characterized by rake angle of  $\alpha_r = 15^\circ$  and flank angle of  $\alpha_f = 10^\circ$ . The cutting speed  $v_c$  was set between 5,000 and 10,000 mm/min. Based on the high-speed camera recordings the shear-layer could be detected using displacement-based image processing techniques.

#### 4. Results

The results of the experimental investigation can be summarized on Figs. 3-4., which show the detected shear layer, and the variation of the cutting forces during time-varying orthogonal cutting, respectively. It can be concluded, that the image processing method is able to detect adequately the shear plane and angle. Moreover, the comparison of the variation of the shear angle with the cutting forces helps to understand the dynamics of non-stationary cutting processes with time-varying chip thickness.

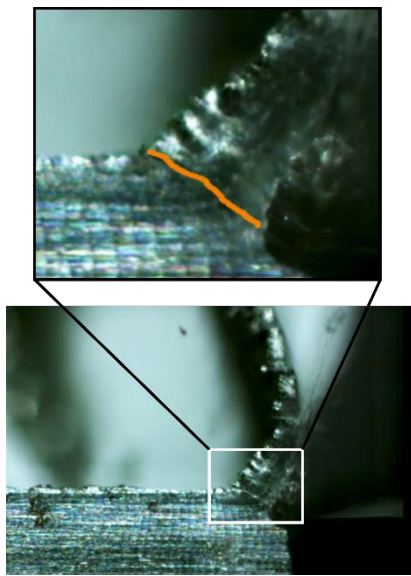


**Fig. 3.** The detected shear layer in case of sinusoidal cutting process with  $h_0 = 0.25$  mm,  $h_A = 0.1$  mm,  $\lambda = 10$  mm and  $v_c = 5000$  mm/min

#### Acknowledgements

This research has been supported by the ÚNKP-16-3-I. New National Excellence Program of the Ministry of Human Capacities, Hungary. The research leading to these results has received funding from the European Research Council under the European Union's Seventh Framework Programme (FP/2007-2013) / ERC Advanced Grant Agreement n. 340889.

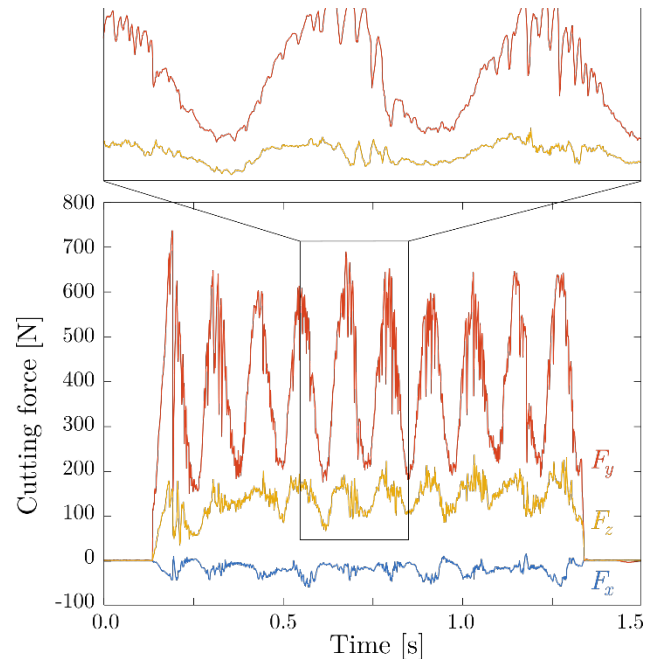


**Fig. 4.** The variation of the cutting force during sinusoidal cutting process with  $h_0 = 0.2$  mm,  $h_A = 0.1$  mm,  $\lambda = 10$  mm and  $v_c = 5000$  mm/min

#### References

- [1] S. A. Tobias and W. Fishwick, Theory of regenerative machine tool chatter, *The Engineer*, **205**(7), 1958, pp.199-203, 238-239.
- [2] J. Tlustý and M. Poláček, The stability of the machine tool against self-excited vibration in machining, *ASME Production Engineering Research Conference*, Pittsburgh, 1963, pp. 454-465.
- [3] E. Budak and Y. Altintas, Analytical Prediction of Chatter Stability in Milling - Part I: General Formulation, *ASME Journal of Dynamic Systems, Measurement, and Control* **120**, 1998, pp. 22-30.
- [4] Y. Altintas, *Manufacturing Automation - Metal Cutting Mechanics, Machine Tool Vibrations and CNC Design*, Second Edition, Cambridge University Press, Cambridge, 2012.
- [5] Y. Guo, W.D. Compton and S. Chandrasekar, In situ analysis of flow dynamics and deformation fields in cutting and sliding of metals, *Proceedings of the Royal Society A*, **471**, 2015.

# ENHANCING THE LABORATORY ASSESSMENT OF THE THERMAL CRACKING RESISTANCE OF ASPHALT MIXTURES

Daniel Steiner<sup>1</sup> and Bernhard Hofko<sup>1</sup>

<sup>1</sup> Vienna University of Technology, Institute of Transportation, Gusshausstrasse 28/E230-3, 1040 Vienna, Austria, E-Mail of corresponding author: Bernhard.hofko@tuwien.ac.at

## 1. Introduction

Asphalt mixtures as the main construction material for road pavements are a composite of bitumen as the binder and mineral aggregates with a predefined mix design. Bitumen as a viscoelastic material exhibits highly temperature dependent characteristics. The stress relaxation capability of the binder decreases upon cooling and once the tensile strength is reached, the pavement fails by thermal cracking [1]. A common method is the thermal stress restrained specimen test (TSRST) or cooling test. This method has been introduced and improved from the 1960s on [2-4]. In the TSRST, an asphalt mix specimen is mounted within a test device in a thermal chamber. The length of the specimen is kept constant while the thermal chamber cools the specimen down at a constant rate until the specimen fails.

## 2. Problem Statement and Objectives

Two different devices for TSRST are run in the authors' lab, manufactured in 2003 and 2013. Both devices comply with all requirements given by TSRST standard EN 12697-46. However, a comparative test program discovered that there is a systematic deviation in results obtained from both devices. While the resulting failure stresses are within the repeatability, the failure temperature deviates by more than 3°C. The trend that the 2013 device produces higher failure temperatures was observed for more 10 different asphalt mixtures.

An analysis of the recorded data from the LVDTs (Linear Variable Differential Transformers) that are used for deformation control showed that both devices are controlled with high precision. A significant impact of the deformation control can be omitted. The evolution of cryogenic stresses in TSRST is also affected by the air and specimen temperature. Thus, the present hypothesis is that there is a difference in the air temperature control in the two devices. Preliminary tests revealed that the air cooling rate is within expected range for both devices. However, it was observed that in the 2013 device,

the specimen core cools down with the same rate as the air temperature, whereas in the 2003 device, the specimen core cools down significantly slower. This difference between air and specimen temperature can explain why the 2003 device produces better results since the specimen cools down more slowly and therefore, cryogenic stresses are built up at a slower pace. This prolongs the period of stress relaxation in the 2003 device and leads to a later failure. However, since the air temperature rates are comparable in both devices, the larger deviation between air and specimen core temperature in the 2003 device cannot be explained by a significant difference in air cooling temperature. Finding the reason for this temperature deviation is subject of this paper.

## 3. Materials and Methods

3 dense graded (low air void content) asphalt concrete (AC) samples with different cross sections (5x5 cm and 6x6 cm) were analysed, as well as a binder rich (no air voids) mastic asphalt (MA) and an open graded (high air void content) stone mastic asphalt (SMA).

To record the core temperature, a dummy specimen is prepared for each mixture. The dummy specimen is cut in half and a hole is drilled in the centre of one end plane. The hole is covered with an adhesive aluminium insulation foil and filled with glycerine. A temperature probe is inserted into the hole to record the core temperature. For the presented study, the dummy specimen was placed into the thermal chamber at the position, where the actual test specimen would be mounted in the TSRST. The thermal program that is used for TSRST was run as follows: start at +10°C kept for 60 min, subsequent cooling at a rate of 10°C/h until -40°C air temperature is reached. Air and specimen core temperature are recorded every 4 seconds.

## 4. Results and Outlook

Main results are shown in Fig. 1. The left diagram shows the temperature lag between air and specimen core temperature for each mix and both

devices vs. the TSRST temperature. The right diagram shows the maximum temperature lag. SMA shows the smallest temperature lag (3.6°C max 2003, 8.4°C max 2013). This can be explained with the higher content of larger aggregates and therefore a better temperature conductivity of the material. MA 8 and AC 16 (5x5 cm) both show similar temperature lags. A difference can be found between 5x5 cm and 6x6 cm cross section: the maximum lag increases by 0.8°C to 0.9°C. On average, the 2003 device shows a 4.7°C higher max temperature lag. The essential evidence for explaining this effect was a measurement of air flow velocity. The vane anemometer (vane diameter 2.5 cm) can measure the air velocity continuously. The data show different air velocities on specimen height in vertical direction: The 2003 device exhibits a lower air velocity (0.5 m/s) than the 2013 device (1.4 m/s).

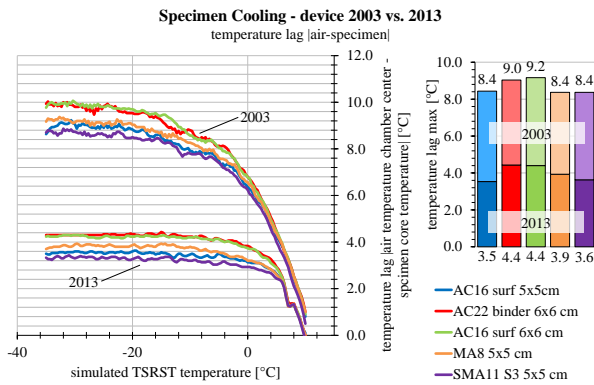


Fig. 1. Temperature lag between specimen core and air temperature for both devices.

To validate the impact of air flow velocity on lag between air and specimen core temperature, an efficient, quick adaption of the 2003 device was set up: Two standard CPU cooling fans were placed on the bottom of the thermal chamber close to the air outlet. The fans' direction was adjusted so that the dummy specimen was in the centre of the air flow. 3 different settings to study the impact of fan power were used: a 12, 20 and 29 Voltage standard PC fan (air flow velocity 12V: 2.9 m/s, 20 V: 5.2 m/s, and 29 V: 7.0 m/s). The thermal program was carried out with one dummy specimen in the 2003 device again, including the supporting fans.

The results of the improved 2003 device are presented in Fig. 2. The left diagram shows the evolution of the temperature lag between air and core temperature vs. TSRST temperature, the right diagram shows the maximum temperature lag. While the initial setup of the 2003 device leads to a temperature lag of 10.0°C, even a low powered fan brings down the temperature lag by 4°C. With the strongest fans, the temperature lag could be

brought down to same level as for the 2013 device. These results show that the difference in temperature lag between the two devices is strongly related to the air flow velocity within the temperature chamber and that a higher air flow velocity can be easily and economically realized.

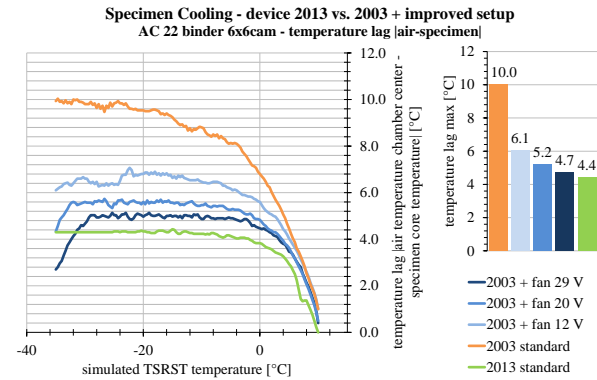


Fig. 2. First improved setup to increase air flow velocity in the 2003 device.

Next steps will be to run TSRST in the enhanced 2003 device and compare results to the 2013 device. It is expected that the improved air flow velocity will lead to more reproducible results. In addition, a larger round robin study should analyse the presented effects in other devices around the world, overcome differences and produce data for reproducibility of standard TSRST according to EN 12697-46.

## References

- Steiner, D., et al., *Impact of Loading Rate and Temperature on Tensile Strength of Asphalt Mixtures at Low Temperatures*, in *8th RILEM International Conference on Mechanisms of Cracking and Debonding in Pavements*, A. Chabot, et al., Editors. 2016, Springer Netherlands: Dordrecht. p. 69-74.
- Monismith, C.L., G.A. Secor, and K.E. Secor, *Temperature induced stresses and deformations in asphalt concrete*. Journal of the Association of Asphalt Paving Technologists, AAPT, 1965. **34**: p. 248-285.
- Fabb, T.R.J., *The influence of mix composition, binder properties and cooling rate on asphalt cracking at low-temperature*. Journal of the Association of the Asphalt Paving Technologists, AAPT, 1974. **43**: p. 285-331.
- Arand, W., *Influence of bitumen hardness on the fatigue behavior of asphalt pavements of different thickness due to bearing capacity of subbase, traffic loading, and temperature*. Proc., 6th Int. Conf. on Structural Behavior of Asphalt Pavements, 1987: p. 65-71.

# 25 YEARS BASIC RESEARCH IN THE FIELD OF STRAIN GAGE TECHNOLOGY ON CHEMNITZ UNIVERSITY OF TECHNOLOGY - INSTITUTE OF MECHANICS

Martin Stockmann<sup>1</sup>, Jochen Naumann<sup>2</sup>, Jörn Ihlemann<sup>1</sup>

<sup>1</sup> Chemnitz University of Technology, Professorship of Solid Mechanics, Reichenhainer Str. 70, 09126 Chemnitz, Germany. E-mail: [martin.stockmann@mb.tu-chemnitz.de](mailto:martin.stockmann@mb.tu-chemnitz.de)

<sup>2</sup> Head of the Professorship Experimental Mechanics, Chemnitz University of Technology (until 2008)

## 0. Introduction

The technique of strain measurement by electrical strain gages is one of the most essential methods in experimental analysis of mechanical loads and in the field of transducer techniques. Investigated where many fundamental strain gage problems in the last 25 years. The paper gives an overview about the most important problems and any research results in this time.

### 1. Strain transmission and nonlinear resistance strain relations

The precise determination of strain in the high deformation range requires the consideration of the strain transmission and the non-linear strain resistance relation, [1]. It is possible to measure the displacement field of loaded original strain gage installations, using the high sensitive moiré Interferometry, Fig. 1. Furthermore, the nonlinear resistance strain relations are presented, [1].

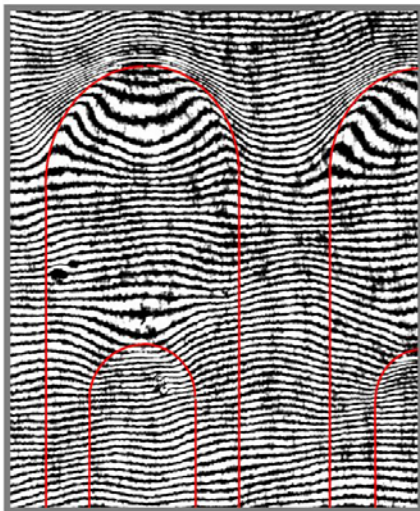


Fig. 1. Fringe pattern, moiré-interferometry, displacement field of strain gage end-loops.

### 2. Transverse sensitivity, determination and compensation

Strain gages have a small percentage of strain sensitivity in direction transverse to the axis of the gage. A special device to determine this transverse sensitivity was developed, [2]. Furthermore, a special strain gage construction with transverse sensitivity compensation was theoretically calculated, practically implemented and investigated, Fig. 2.

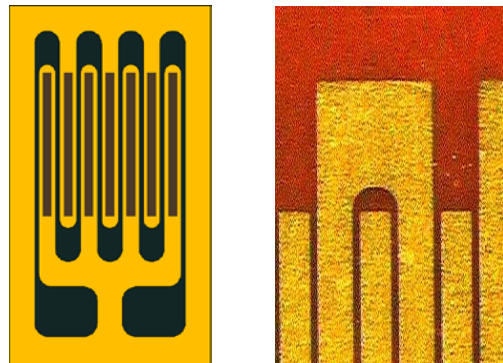
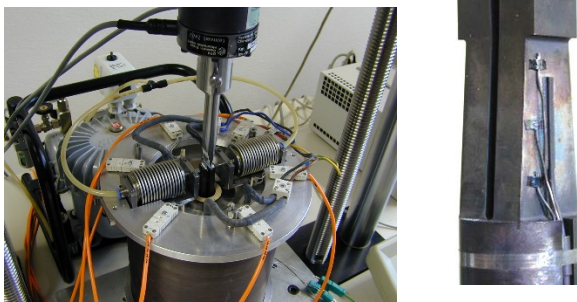


Fig. 2. Gage with transverse sensitivity compensation, schematic layout and industrial design.

### 3. Calibration of high temperature strain gages

The strain analysis in the range of high temperatures (120–1000 °C) using electrical strain gages is more difficult and it is for various reasons more imprecise in comparison with the measurement at room temperature, [3]. That requires particular kinds of gages, special installation techniques and knowledges in relation to the behavior of the gages during change of temperature. Fig. 3 shows the developed calibration device for the determination of the

apparent strain and the gage factor change with temperature.



**Fig. 3.** Calibration device for the experimental determination of the apparent strain and the gage factor change with temperature.

#### 4. Differential strain gage, a new strain sensor for micro application

Differential strain gages consist of a thin square resistance layer with four symmetrically arranged electrical contacts, [4]. Two opposite contacts are connected with a voltage source. The other two contacts must be used to measure the output voltage, Fig. 4.

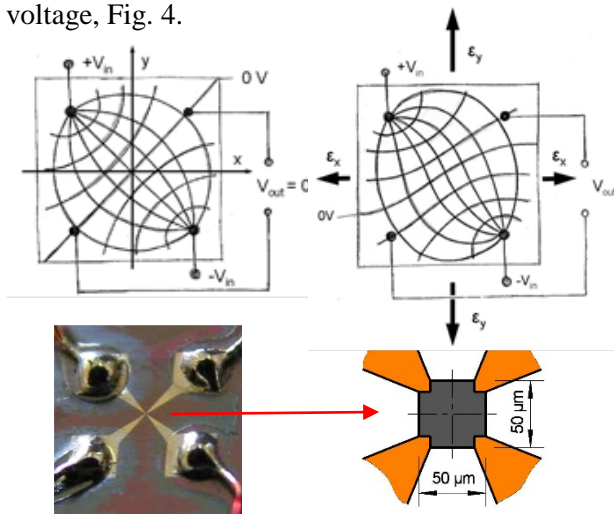


**Fig. 4.** Differential strain gages, potential lines, subminiature design.

The developed differential strain gage is new and completely differs in function and geometry from the traditional resistance strain gage. The changed basic operating principle and the simple geometric design induce a lot of special properties and some science-based advantages, especially the application in microsystems.

#### 5. Long-term stability in hostile environment

Outdoor applications of strain gages are exposed to environmental influences such

as temperature and humidity cycles which lead to irreversible changes in the matrix foils, the adhesives and also in the metallic foils. Therefore it is necessary to protect strain gage installations carefully with special layers against these environmental influences. A test regime with accelerated temperature cycles and test results for gages with different protection coats and different gage constructions is described in the paper, [5]. The climatic chamber with strain gage installations is shown in Fig. 5. This regime consists of continuing temperature changes (10–60 °C) with a period of 6 hours and a superimposed humidity change (30–80 % rel. H.) with a period of 144 hours. The complete testing time lasts 1500 hours.

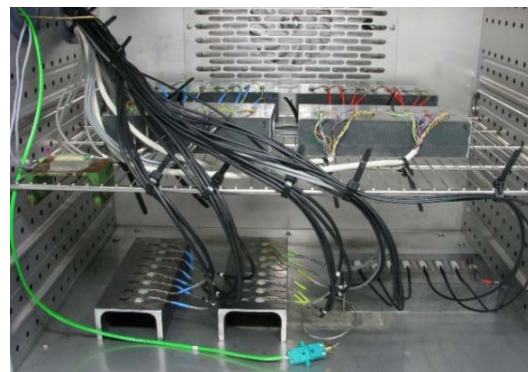


**Fig. 5.** Long-term stability test of strain gage installations in a climatic chamber.

#### References

- [1] Stockmann, M (2000). Mikromechanische Analyse der Wirkungsmechanismen elektrischer Dehnungsmessstreifen, *Habilitationsschrift*, <http://archiv.tu-chemnitz.de/pub/2000/0049>.
- [2] Stockmann, M., Naumann, J. (2004). Transverse Sensitivity of Strain Gages – Determination and Compensation, *Transactions of Famena XXVII-1*, 43-50.
- [3] Stockmann, M., Naumann, J., Cermáková, I. (2002). High Temperature Strain Gauges - Design and Properties. *19th Danubia-Adria Symposium on Experimental Methods in Solid Mechanics*.
- [4] Stockmann, M., Naumann, J., Schumann, J., Mönch, I. (2011). Differential Strain Gage - A Sensor Device for Macro- and Microsystems, *Strain*, 47, 104-112.
- [5] Herrmann, R., Stockmann, M., Marx, S. (2015). Untersuchungsstrategie zur



34th Danubia-Adria Symposium on Advances in Experimental Mechanics  
University of Trieste, Italy, 2017



Bewertung der Langzeitstabilität von  
elektrischen Dehnungsmessstreifen.  
*Bautechnik* (92) 451-460.

# METALLURGICAL AND SURFACE DAMAGE ANALYSIS IN A COPPER MOLD AFTER SERVICE

J. Srnec Novak<sup>1</sup>, A. Lanzutti<sup>1</sup>, D. Benasciutti<sup>2</sup>, S. Carretti<sup>3</sup>, F. De Bona<sup>1</sup>, A. De Luca<sup>3</sup>, L. Moro<sup>1</sup>

<sup>1</sup> University of Udine, Politechnic Department of Engineering and Architecture (DPIA), Via delle Scienze 208, 33100, Udine, Italy. E-mails: [jelena.srnec@uniud.it](mailto:jelena.srnec@uniud.it), [alex.lanzutti@uniud.it](mailto:alex.lanzutti@uniud.it), [francesco.debona@uniud.it](mailto:francesco.debona@uniud.it), [luciano.moro@uniud.it](mailto:luciano.moro@uniud.it)

<sup>2</sup> University of Ferrara, Department of Engineering, Via Saragat 1, 44122, Ferrara, Italy. E-mail: [bnsdns@unife.it](mailto:bnsdns@unife.it)

<sup>3</sup> Danieli Research Center, Via Nazionale 41, 33042, Buttrio (UD), Italy. E-mails: [s.carretti@danieli.it](mailto:s.carretti@danieli.it), [a.deluca@danieli.it](mailto:a.deluca@danieli.it)

## 1. Introduction

Copper mold is the main component of the continuous casting process. The mold is a tube, where a huge thermal flux is transferred from the molten steel, close to the inner surface, to the water cooled outer side. Thus a high thermal gradient takes place across mold walls, generating thermal fatigue cracks in the meniscus area, which is the most thermally stressed region.

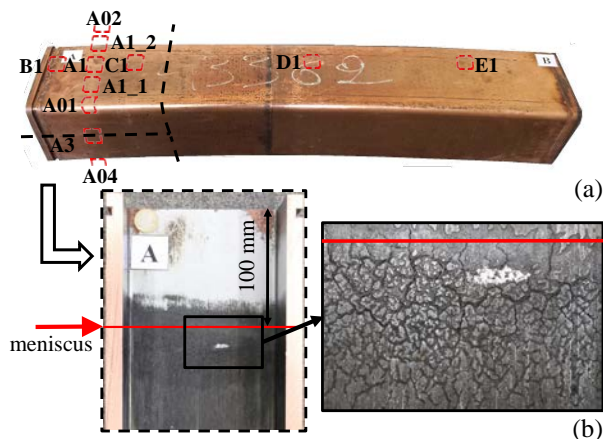


**Fig. 1.** Mold under investigation with positions of specimens (a), damaged inner surface area (b).

This paper presents a failure analysis of a square copper mold after service; see Fig. 1a. Metallurgical investigations (light microscope and SEM) have been performed on samples extracted from different areas of interest to characterize the mold microstructure and to determine the mechanism of cracking.

## 2. Experimental procedure

The copper mold, removed from service at the end of its service life, has been visual inspected to determine the most damaged areas, as done in [1, 2]. The inner surface of the mold after service is presented in Fig. 1b. A slice of the copper mold has then been extracted in the meniscus area, (region labeled with A in Fig. 1a). In this area 10 metallographic samples have been extracted. Four samples have also been taken from “undamaged” areas (labels B, C, D, E). Each sample underwent to metallographic preparation (grinding and polishing) to obtain a mirror-like surface. The samples have been etched, using a solution of  $H_2O:NH_3:H_2O_2=1:1:1$ , and then analyzed by light microscope to determine the crack morphology, grain size (intercept method) and the microstructure. Some samples underwent to SEM+EDXS analysis to investigate the origin of deposits inside the cracks.

## 3. Results

The visual inspection has evidenced that the mold is heavily damaged in the meniscus area, as indicated in Fig. 1b. Close examination of the mold inner surface shows that a web of cracks is formed approximately 130 mm from the mold top, i.e. in the level where the surface of the mold reaches the maximum temperature.

The microstructural examination of the samples, extracted in the area of meniscus, has evidenced the presence of many cracks, mainly in the samples A1, A1\_1, A1\_2, A3, and A4. These samples are situated in the most stressed region of the mold. Fig. 2a and 2b (samples A3 and A1\_2

respectively) show that cracks initiate at the surface and then propagate through the mold walls. The cracks seem to be transgranular and are contoured of some blue deposits, which will be further investigated by means of SEM+EDXS. It is observed that the crack nucleation region lacks the original chromium protective coating that probably has been detached by the degradation process.

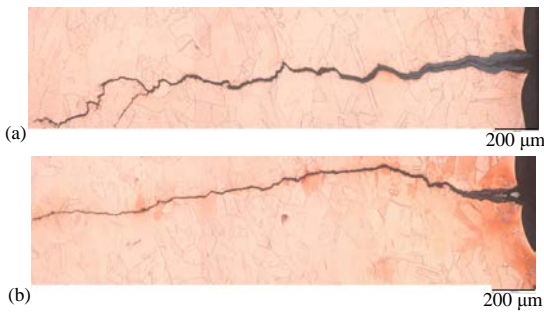


**Fig. 2.** Cracks on specimen A3 (a), and A1\_2 (b).

The microstructure of the material is composed by austenitic equiaxed grains typical of pure Cu. The grain size of the Cu is coarse and in the range of  $\sim 70 \pm 30 \mu\text{m}$ . These dimensions are in the range of the microstructural requirements for this kind of application. At surface the material seems to be recrystallized because of the presence of finer grains compared to the bulk of material. The recrystallization process could be produced by the presence of both a strain hardened layer, caused by the machining process of the internal wall of the mold, and of high temperatures, at which the material has been exposed.

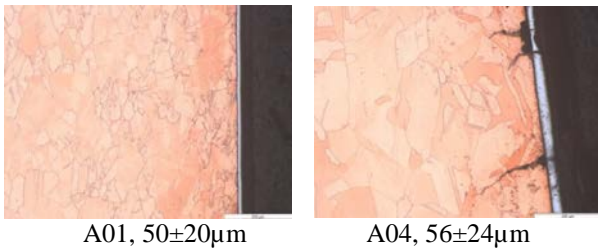


**Fig. 3.** Microstructure of samples taken at corners.

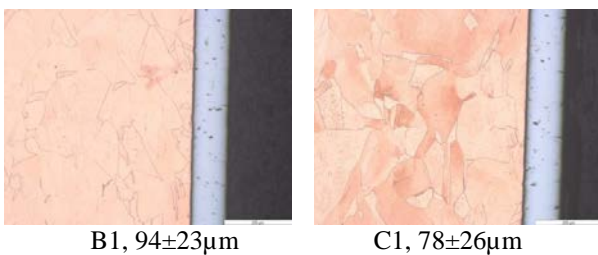


**Fig. 4.** Microstructure of B1 and C1 samples.

Considering samples from corners, only few small cracks are found on one side (e.g. A04), while no

visible cracks are observed on the opposite side (e.g. A01), see Fig. 3. Some samples present a detachment of the coating, caused by the wear of the mold. The samples B1 and C1 do not have both visible cracks and the chromium coating layer, which presents a thickness of approximately 100  $\mu\text{m}$  (Fig. 4). Indeed, these samples have been extracted outside the meniscus area, where probably the thermal stresses are lower. The SEM analyses performed on specimen A1, have evidenced the presence of Pb, Zn and S, see Fig. 5. These elements probably are present in the molten steel as residuals and they have been infiltrated because of the high chemical affinity with Cu. It is possible that these elements, reacting with the Cu, have produced a brittle phase, which has promoted the crack nucleation and propagation.

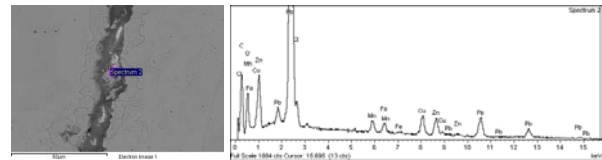


**Fig. 5.** X-ray spectrum of the damaged zone.

Metallurgical analysis proved the transgranular characteristics of the cracks, thus suggesting that thermal fatigue is the main cause of failure, as suggested in [2].

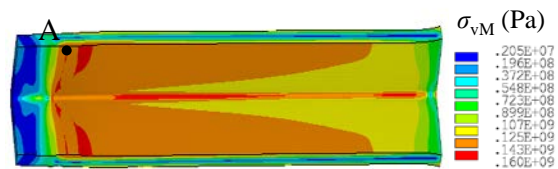


**Fig. 6.** Von Mises stress distribution.

This hypothesis was also confirmed by results of finite element analyses (see Fig. 6), simulating the cyclic behavior of the mold, which showed critical values of stress and strain in the area where cracks appear [3].

## References

- [1] Barella, S. et al., Investigation of failure and damage on a continuous casting copper mould, *Eng. Fail. Anal.*, 36, 2014. pp. 432-438.
- [2] Park, J.K. et al., Thermal and mechanical behavior of copper molds during thin-slab casting (ii): mold crack formation, *Metall. Mater. Trans.*, 33B, 2002. pp. 437-449.
- [3] Novak Srnc, J. et al., Thermo-mechanical finite element simulation and fatigue life



34th Danubia-Adria Symposium on Advances in Experimental Mechanics  
University of Trieste, Italy, 2017



assessment of a copper mould for continuous casting of steel, *Procedia Engineering*, 133, 2015. pp. 688-697.

# IMPACT RECONSTRUCTION AND LOCALIZATION ON LAMINATED STRUCTURE

Robert Zemčík<sup>1</sup>, Jan Bartošek<sup>2</sup>, Tomáš Kroupa<sup>3</sup>

- <sup>1</sup> University of West Bohemia, Faculty of Applied Sciences, Univerzitní 8, 301 00 Pilsen, Czech Republic. E-mail: [zemcik@kme.zcu.cz](mailto:zemcik@kme.zcu.cz)
- <sup>2</sup> University of West Bohemia, Faculty of Applied Sciences, Univerzitní 8, 301 00 Pilsen, Czech Republic. E-mail: [bartose4@kme.zcu.cz](mailto:bartose4@kme.zcu.cz)
- <sup>3</sup> University of West Bohemia, Faculty of Applied Sciences, Univerzitní 8, 301 00 Pilsen, Czech Republic. E-mail: [kroupa@kme.zcu.cz](mailto:kroupa@kme.zcu.cz)

## 1. Introduction

Finite element model of an airfoil segment made of laminated glass fiber composite is created. The model is calibrated using data from experimental tests, namely the modal characteristics and oscillations measured with laser sensors in selected locations. Passive monitoring method is applied for the reconstruction of impact in unknown location [1]. The location and time variation of impact force is obtained using transfer-based functions approach. The dedicated overdetermined and ill-posed inverse problem is solved using Tikhonov regularization [2, 3]. The interpolation of transfer-based functions is used to increase the accuracy of the reconstruction.

## 2. Inverse problem

The methodology used in this work is based on the transfer (or transfer-based) function approach [4]. For a linear system, its response  $h$  to an input  $f$  can be expressed by convolution  $h = f * g$  where  $g$  is so-called transfer function and it represents the characteristics of the system [2, 5]. In order to find the location of impact and to reconstruct the time dependence of the impact force, it is necessary to perform two consecutive steps; a) a calibration procedure, i.e., to perform experimental measurements while recording the corresponding input and response, and to calculate the transfer functions for all combinations of impact (calibration) locations and sensors, and b) a reconstruction procedure, i.e. to reconstruct the force in each possible location for measured response for unknown impact and to seek the impact location, for example by minimizing the error of response reconstruction [6].

## 3. Experiment

A propeller blade segment made of laminated glass-fiber textile composite was used throughout the testing (Fig. 1). It consisted of two parts, a beam (or spar) and an airfoil segment (skin), glued together. The airfoil segment was excited using the impact hammer B&K 8204 in several locations (one at a time). The force was measured using the embedded force sensor. The response was measured with a set of 4 piezoelectric foil transducers (patches) DuraAct P-876.SP1 with shunt resistors ( $R = 1 \text{ M}\Omega$ ) and a set of 4 laser sensors Micro-Epsilon optoNCDT 2200. All signals were recorded using NI CompactDAQ device with various I/O modules with sampling frequency of approximately 10 kHz.

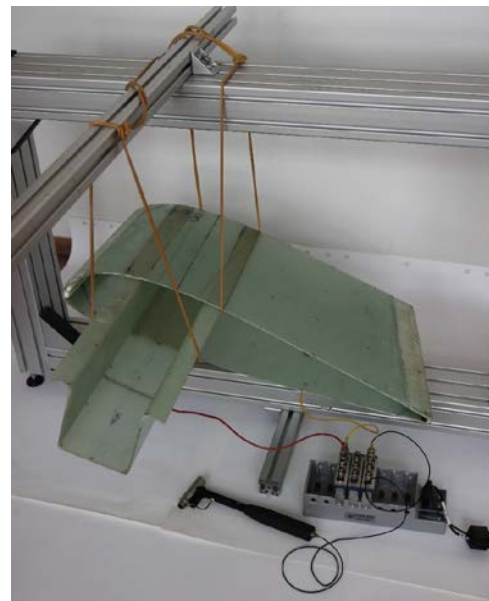


**Fig. 1.** Experimental setup for free oscillations measurement.

First, the blade was hanged on rubber strings and the free oscillations due to the impacts were measured (Fig. 1). This scenario was used for calibration of the numerical model (mainly the elastic properties). Afterwards, the blade was fixed using a turn-table at the beam's end for precise positioning of numerous impacts and the laser beam measurement spots (Fig. 2).



**Fig. 2.** Experimental setup with turn-table for precise positioning of impacts and sensors.

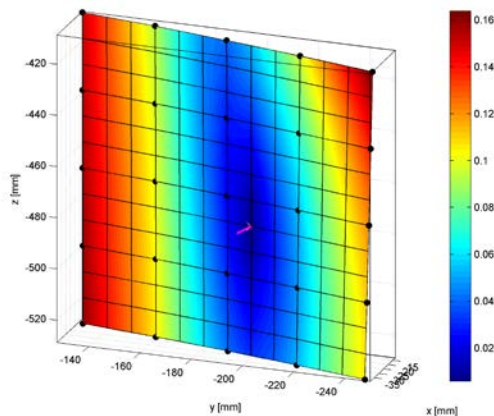


**Fig. 3.** Localization error contours on 4×4 grid.

#### 4. Numerical model and reconstruction

A numerical model was created for finite element analysis performed in Abaqus solver. The process used 3D laser scanning probe, CAD tools and, finally, a quadrilateral mesh was created respecting the margins of various regions with different laminated layups (plain- and twill-weave layers were used).

The response of the blade was calculated for 169 locations arranged in a 12×12 grid (covering an area of 120 mm × 120 mm) of almost square

regions in the central part of the airfoil. The effect of interpolation of transfer functions was then analysed on 5 different simplifications of this grid by reducing the number of hypothetically known impact locations by a factor of 2, 3, 4, 6 and 12, thus obtaining grids with 12×12, 6×6, 4×4, 3×3, 2×2 and 1×1 regions. An example of impact localization is shown in Fig. 3.

#### 5. Conclusions

A methodology for passive structural health monitoring was introduced and applied to laminated structures. The proposed methods for impact location identification and force reconstruction proved to provide results with sufficient accuracy on curved composite structures for selected configurations of calibration data.

#### Acknowledgements

This publication was supported by the project LO1506 of the Czech Ministry of Education, Youth and Sports.

#### References

- [1] Seydel R, Chang FK. (2001) Impact identification of stiffened composite panels: I. System development, II. Implementation studies, *Smart Materials and Structures*, 10, 354–369 and 370–379.
- [2] Gunawan FE, Homma H, Kanto Y. (2006) Two-step B-splines regularization method for solving an ill-posed problem of impact-force reconstruction, *Journal of Sound and Vibration*, 297, 200–214.
- [3] Hu N, Fukunaga H, Matsumoto S, Yan B, Peng XH. (2007) An efficient approach for identifying impact force using embedded piezoelectric sensors, *International Journal of Impact Engineering*, 34, 1287–1271.
- [4] Park J, Chang FK. (2005) System identification method for monitoring impact events, *Proc. SPIE*, 5758, 189–200.
- [5] Jacquelin E, Bennani A, Hamelin P. (2003) Force reconstruction: analysis and regularization of a deconvolution problem, *Journal of Sound and Vibration*, 265, 81–107.
- [6] Atobe S, Kuno S, Hu N, Fukunaga H. (2009) Identification of Impact Force on Stiffened Composite Panels, *Transactions of Space Technology Japan*, 7, 1–5.

# THE INFLUENCE OF IN718 ALLOY ANNEALING ON FATIGUE LIFETIME CHANGES

Juraj Belan<sup>1</sup>, Miloš Matvija<sup>2</sup>, Lenka Kuchariková<sup>1</sup>, Eva Tillová<sup>1</sup>

- <sup>1</sup> University of Žilina, Department of Materials Engineering, Faculty of Mechanical Engineering, Univerzitná 8215/1, 01026 Žilina, Slovakia. E-mails: [juraj.belan@fstroj.uniza.sk](mailto:juraj.belan@fstroj.uniza.sk), [lenka.kucharikova@fstroj.uniza.sk](mailto:lenka.kucharikova@fstroj.uniza.sk), [eva.tilova@fstroj.uniza.sk](mailto:eva.tilova@fstroj.uniza.sk)
- <sup>2</sup> Technical University of Košice, Faculty of Metallurgy, Institute of Materials, Letná 9, 04200 Košice, Slovakia. E-mail: [Milos.Matvija@tuke.sk](mailto:Milos.Matvija@tuke.sk)

## 1. Introduction

Alloy IN718 is widely used Ni – Cr – Fe hardenable material used mostly up to 700°C working temperature. Its microstructure is well described in works of authors [1-3]. Generally, as hardened conditions consist of solid solution gamma (FCC  $\gamma$  – phase, NiCr(Fe)), semi-coherent precipitate gamma prime ( $L1_2$   $\gamma'$  – phase Ni<sub>3</sub>Al(Ti)), main strengthening also semi-coherent phase gamma double prime (BCT DO<sub>22</sub>  $\gamma''$  – phase Ni<sub>3</sub>Nb), and incoherent delta (orthorhombic  $\delta$  – phase Ni<sub>3</sub>Nb). All mentioned phases above are responsible for alloy's unique properties. However, not all phases are considered as helpful for mechanical properties. The influence of  $\delta$ -phase is questionable, in small amounts situated at grain boundaries improves mechanical properties – especially ultimate tensile strength (UTS). At higher content may act as crack initiation site when cyclic loading is applied. There are two possible ways how to artificially increase the  $\delta$ -phase amount. The first one is to vary the chemical composition, mainly the Nb content.  $\delta$ -phase at temperature range 1010°C-870°C needs at least 6 to 8% of niobium to crystallize.

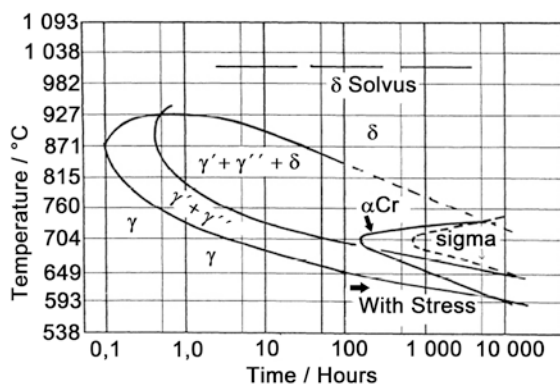


Fig. 1. T-T-T diagram according to work of and Armida Oradei-Basile and J. F. Radavich [4]

The second, easier way is to apply annealing at approximately 800°C for time over 50 hrs., Fig. 1 [4].

The aim of article is to provide a TEM (Transmission Electron Microscopy) and SEM (Scanning Electron Microscopy) analysis of applied annealing to increase  $\delta$ -phase volume. The simple blocky samples were loaded with three-point flexure cyclic loading after annealing to evaluate positive or negative influence of increased volume of  $\delta$ -phase onto fatigue lifetime.

## 2. Experimental

The experimental material, alloy IN718, with chemical composition, see Tab. 1, were annealed at 800°C/72 hrs.

C	Ni + Co	Mn	Ti	Al	B	Co
0.026	53.46	0.07	0.96	0.57	0.004	0.14
Ta	Nb + Ta	Cr	Cu	Mo	Nb	Ni
<0.01	5.31	19.31	0.03	2.99	5.30	53.32

Tab. 1. Chemical composition of IN 718 (wt. %)

Specimens for SEM observation were prepared via regular metallography steps and etched with 10g CrO<sub>3</sub> + 100ml H<sub>2</sub>O electrolyte reagent. Specimens for TEM observation were cutted as thin cuts and next electrolytic thin foils at 18V and reagent 10% HClO<sub>4</sub> + 90% CH<sub>3</sub>OH were prepared.

The ZWICK/ROELL Amsler 150 HFP 5100 were used as experimental machine for three-point flexure loading. Parameters for high cycle fatigue low frequency loading were set as follows:

- the static force  $F_{static} = -15$  kN;
- the dynamic force  $F_{dynamic} = 6.31$  to  $12.8$  kN;

- the cycle limit  $N_c = 2.10^7$ ;
- frequency  $f = 150$  Hz.

### 3. Results

The tested alloy microstructure at the starting stage is presented in Fig. 2a, and Fig. 2b shows it after applied annealing at  $800^\circ\text{C}/72$  hrs. Generally, the microstructure consists of very fine grain sizes according to ASTM = 12 (length of grains is around  $10\ \mu\text{m}$ ), and various forms of segregated  $\delta$ -phase (light gray particles). The  $\delta$ -phase is presented mainly at grain boundary in a needle-like shape and in form of fine blocks inside the grains.

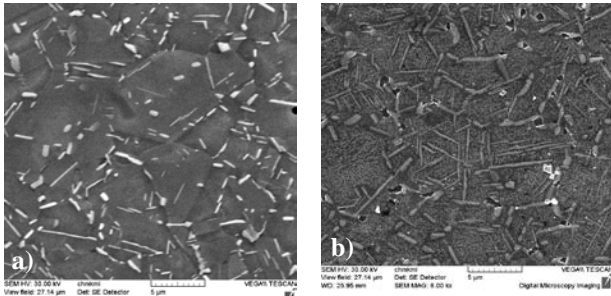


**Fig. 2.** SEM micrographs of wrought IN718 alloy,  $10\% \text{CrO}_3 + 100\text{ml H}_2\text{O}$  etch.

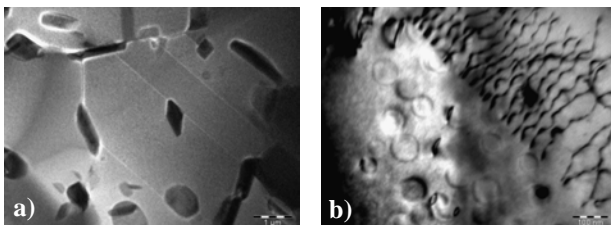


**Fig. 3.** TEM micrographs of wrought IN718 alloy,  $10\% \text{HClO}_4 + 90\% \text{CH}_3\text{OH}$  etch.

After application of annealing at  $800^\circ\text{C}/72$  hrs. the main strengthening phase  $\gamma''$  became more obvious because of temperature and  $\delta$ - phase grew as well, Fig. 2b. According to reference [3], mechanical properties should deteriorate due to the  $\delta$ -phase presence at grain boundaries and its growth. Moreover, with TEM analysis employed is clear to see the  $\delta$ -phase of various shapes and formatted at grain boundary or inside grains, Fig. 3a. The microstructure is polyedric with deformation twins. Also note the higher volume of dislocation, which are cutting through the  $\gamma'$ -phase after applied annealing, Fig. 3b. Increasing the dislocation volume due to annealing increased mechanical properties as well, especially UTS

and fatigue properties, even if more  $\delta$ -phase presented in alloy structure. These results confirm the S-N curve obtained after fatigue tests, Fig. 4.

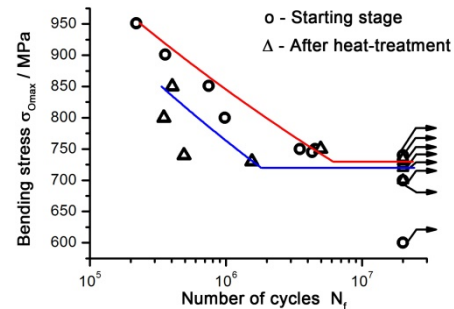


**Fig. 4.** The S-N curve plotted after three-point flexure fatigue tests.

### 4. Conclusions

Well known Ni – Cr – Fe alloy, IN718, was used for experimental procedure. Brief conclusions can be drawn. Applied annealing has influence on increasing the volume of  $\delta$ -phase. The fact, that it causes decreasing mechanical properties (UTS or fatigue lifetime) was not confirmed. The most probably reason is higher volume of dislocation anchored to  $\gamma'$ -phase. This theory confirms the results after three-point flexure fatigue tests.

### Acknowledgements

The project is supported by Scientific Grant Agency of Ministry of Education of The Slovak Republic and the Slovak Academy of Sciences, No. 1/0533/15 and No. 049ŽU-4/2017.

### References

- [1] Radavich, J.F., The physical metallurgy of cast and wrought alloy 718: Superalloy 718 – Metallurgy and Applications, editor E.A. Loria, TMMMS, 1989. pp. 229-240.
- [2] Belan, J., High frequency fatigue test of IN 718 alloy – Microstructure and fractography evaluation, Metalurgija, 54, 2015, pp. 59-62.
- [3] Leo Prakash, D.G.L., Walsh, M.J., Maclachlan, D., Korsunsky, A.M., Crack growth micro-mechanisms in the IN718 alloy under the combined influence of fatigue, creep and oxidation, International Journal of Fatigue 31(11-12), 2009, pp. 1966-1977.
- [4] Oradei-Basile, A., Radavich, J.F., A current T-T diagram for wrought alloy 718: Superalloys 718, 625 and Various Derivatives,



34th Danubia-Adria Symposium on Advances in Experimental Mechanics  
University of Trieste, Italy, 2017



editor E.A. Loria, TMMMS, 1991, pp. 325-335.

# FAILURE MECHANISM IN FEATHERED KEY SHAFT HUB CONNECTIONS UNDER TORSIONAL LOAD

F. Kresinsky<sup>1</sup>, E. Leidich<sup>1</sup>

<sup>1</sup> Chemnitz University of Technology, Faculty of Mechanical Engineering, Department of Engineering Design, Reichenhainer Str. 70, 09126 Chemnitz, Germany. E-mail: [felix.kresinsky@mb.tu-chemnitz.de](mailto:felix.kresinsky@mb.tu-chemnitz.de)

## 1. Introduction

Because of the miscellaneous purposes there are manifold variants for the transmission of rotational torque from shaft to hub. On the account of its cost-effective manufacturing and the possibility of assembling and disassembling the feathered key shaft hub connection is still a very popular way to transmit torque. Although the feathered key shaft hub connection seems to be well known and simple in design. But the experience shows that different locations and different mechanisms of failure complicate the evaluation of fatigue strength and cause major uncertainties in engineering design.

## 2. Methods

The design of feathered shaft hub connections are used to be done due to two criterions. On the one hand there is the fatigue strength of the shaft or hub [1] and on the other hand there is the maximum permissible contact pressure at the keyway walls [2]. The investigated feathered key shaft hub connection with the boundary conditions is shown in Fig. 1.

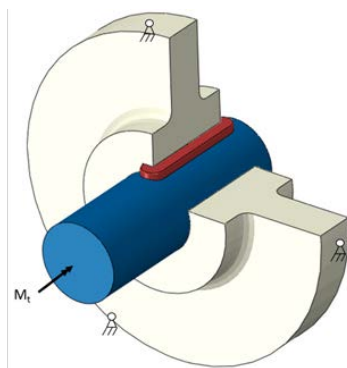


Fig. 1. Boundary conditions at feathered key shaft hub connections

Nevertheless, different investigations [3; 4, 5; 6] reveal that the reasons for real life failures seems to be more complex. Plastic deformation of the keyway may cause loss of function and system errors. This failure criterion can be observed by

shafts with low yield stresses [7] or thin-walled aluminum hubs.

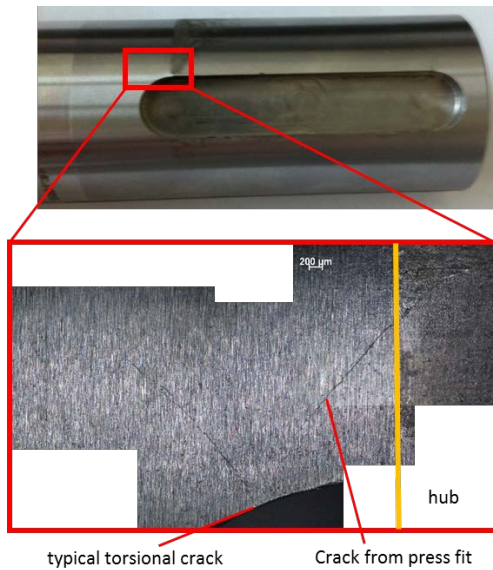
The experimental results were carried out on a servo hydraulic torque test station which is shown in Fig. 2. The determination of the test frequency was 20 Hz. The torque set the feathered key shaft hub connection under load and was transmitted via a metal bellow coupling. This prevented the connection from lateral forces.



Fig. 2. Servo hydraulic torque test station

## 3. Results

The study was based in extensive experimental and numerical investigations. The results are exemplary represented on a typical Q & T steel (C45, 1.0503, tensile strength 650 MPa). The fracture of the shaft or the hub was the observed system failure. The fracture of the hub occurred only at cast iron hubs and will not be object of research in this paper. This paper focuses on cracks in shafts. The torsion fracture of a shaft is well known. The torque and the different torsional stiffnesses of the components (shaft, hub and key) leads to a maximum stress in the rounding of the keyway at the load-bearing side. Due to the maximum principal stress the crack is initiated. The tensile opening (mode I) occurs and the fracture is propagated in a 45° angle to the shaft axis. Other cracks e.g. from the contact between shaft and hub occurred but they will never reach a critical state or may cause failure of the system (see Fig. 3).



**Fig. 3.** Cracks in feathered key shaft hub connections with crack initiation at keyway top (critical) and press fit

The next experiments were done at a lesser load level that does never occur a fracture which was initiated at the top of the keyway. A fracture occurred and led to system failures. An investigation reveals that the crack was initiated in the keyway ground fillet (Fig. 4).

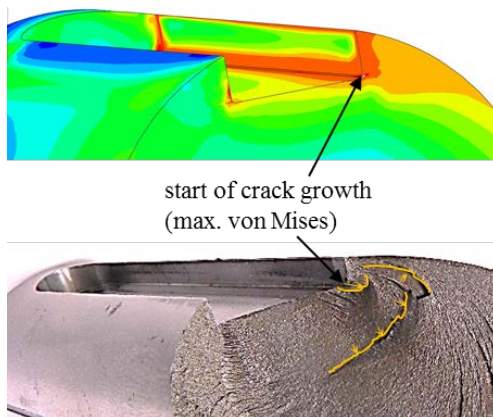


**Fig. 4.** Cracks in feathered key shaft hub connections with crack initiation at keyway ground (termed rest lines yellow)

The keyway ground fillet is an area of no contact, which leads to a non-fretting fatigue problem. In feathered key shaft hub connections system errors can be vary from different loads and cycle numbers (<10 mill.). The experimental results will be prepared and compared with numerical results. The investigation will be extend on materials with higher strength and it will be shown that the notch effect is more increasing with the tensile strength of the shafts than known in standards [1]. It means

in effect that the benefit of high-strength steels will not benefit the level of fatigue strength feathered shaft hub connections.

#### 4. Remarks

- The fatigue strength of feathered key shaft hub connections is low is in comparison to the material strength.
- The crack initiation point vary with load and cycle number and not all initiated cracks will became critical.
- Increasing tensile strength does not increase the fatigue life of feathered key shaft hub connections

#### Acknowledgements

The authors would like to thank the German Federation of Industrial Cooperative Research Associations (AiF) and the German Research Association for Power Transmission Engineering (FVA) for the financial support.

#### References

- [1] DIN 743, Tragfähigkeitsberechnungen von Wellen und Achsen, Beuth-Verlag, Berlin 2012.
- [2] DIN 6892, Passfedern – Berechnung und Gestaltung, Beuth-Verlag, Berlin, 2012.
- [3] Oldendorf, U., Nordmann, R., Lebensdauerberechnungen von Passfederverbindungen. FVA-Abschlussbericht, Heft 961, 1999
- [4] Leidich, E.; Brůžek, B., Ermittlung von Grenzlastkriterien für Passfederverbindungen unter Torsionsbeanspruchung. FVA-Abschlussbericht, Heft 1047, 2013
- [5] Kresinsky, F., Leidich, E., Ermittlung der Grenzbelastung von torsionsbeanspruchten Passfederverbindungen. FVA-Abschlussbericht 600II, published soon
- [6] Forbrig, F., Untersuchungen zur Gestaltfestigkeit von Passfederverbindungen. doctoral thesis, Chemnitz University of Technology, 2007.
- [7] Kresinsky, F. ; Leidich, E., 7. VDI-Fachagung "Welle-Nabe-Verbindungen" 2016 Auslegung-Analyse-Optimierung, 09.-10. November, 2016, Karlsruhe

# DEVELOPMENT OF MULTIFUNCTIONAL SELF-REINFORCED COMPOSITES

D. Brendstrup<sup>1,2</sup>, J. Mariné<sup>1,2</sup>, J. Walker<sup>1,2</sup>, C. Londoño<sup>1,2</sup>, M. Mollo<sup>3</sup>, C. Bernal<sup>1,2</sup>

<sup>1</sup> Universidad de Buenos Aires, Facultad de Ingeniería, Buenos Aires, Argentina. E-mail: cbernal@fi.uba.ar

<sup>2</sup> CONICET-Universidad de Buenos Aires, Instituto de Tecnología en Polímeros y Nanotecnología (ITPN), Buenos Aires, Argentina

<sup>3</sup> Centre of Research and Development for the Plastics Industry (INTI-Plastics), Av. Gral. Paz 5445, B1650KNA, San Martín, Argentina. E-mail: mariana@inti.gob.ar

## 1. Introduction

Fibre reinforced polymers are specially designed materials to obtain light high performance structures. In order to apply these materials in the design of structural components, they have to retain their high mechanical performance during a long service life. Their failure is mainly due to delamination, matrix cracking and/or fibre fracture and, its detection is an important issue of scientific and technological current interest. The development of new techniques for damage detection in composite structures represents a key factor to increase their service reliability.

In addition, the growing interest in multifunctional materials is driven by the need of developing new materials and structures, which simultaneously have different structural functions or combined structural and non-structural functions. Therefore, the possibility to develop multifunctional materials able to monitor damage seems to be very attractive.

On the other hand, the environmental impact of the growing use of plastics and composites derived from non-renewable sources makes necessary the development of new combinations of materials with better properties but also with lower environmental impact. As a result, the development of completely recyclable composites is a main topic of research. Currently, there is a great interest in self-reinforced composites based on thermoplastic polymers due to their easy of recycling and the possibility to obtain light structures and components. In these materials, the reinforcement is made of high strength highly oriented fibres or tapes while the matrix is a polymer of the same chemical nature but with a

lower melting temperature. Self-reinforced composites compete with traditional composites in different applications depending on their performance/cost ratio. A great number of papers have been published in the literature regarding different aspects of many types of self-reinforced composites [1-4].

In this work, multifunctional nanocomposites based on different thermoplastic polymers (Polypropylene (PP) and Polyethylene Terephthalate (PET)) and carbon nanotubes are developed. These nanocomposites are subsequently used as the matrix and/or the reinforcement in self-reinforced composites. Morphological, thermal and mechanical characterisation is performed on the different matrices, reinforcements and self-reinforced composites. The ability of the obtained materials to monitor damage is also investigated from changes in their electrical behaviour induced by mechanical deformation.

## 2. Experimental

Films containing 2 wt.% multiwall carbon nanotubes (MWCNT) are obtained by two different methods. Films based on amorphous PET (PETg) are prepared by mechanical stirring of different- viscosity solutions and solvent casting whereas films based on a random PP copolymer (rPP) are obtained by twin extrusion at two different screw speeds (50 and 300 rpm) followed by compression moulding. Mechanical characterisation of the different films is performed through uniaxial tensile tests and their morphology is studied by scanning electron microscopy (SEM).

In addition, nanocomposite fibres based on the different polymers are manufactured by solid state stretching of filaments previously obtained in a twin-screw extruder. Morphological, thermal,

structural and mechanical characterisation of the fibres is performed.

Self-reinforced composites are manufactured based on the obtained nanocomposite matrix films and fibres by film stacking followed by compression moulding. Composites mechanical behaviour is studied through uniaxial tensile tests and fracture mechanics experiments under different loading conditions (quasi-static and impact loading conditions).

The potential capability of the obtained nanocomposite films and fibres and self-reinforced composites to monitor damage is also investigated by measuring changes in their electrical behaviour induced by mechanical deformation.

### 3. Results and discussion

Significantly improved films morphology is obtained from mixing rPP and MWCNTs at high processing speed (300 rpm) or mechanical stirring a high viscosity solution of PETg and MWCNTs. This result is also confirmed from the mechanical behaviour observed in uniaxial tensile tests. While films obtained at high mixing speed or high solution viscosity present stress-strain curves similar to those of neat polymers exhibiting high ductility, films obtained at low processing speed or low viscosity display a much more brittle behaviour derived from the presence of filler aggregates that induce premature failure.

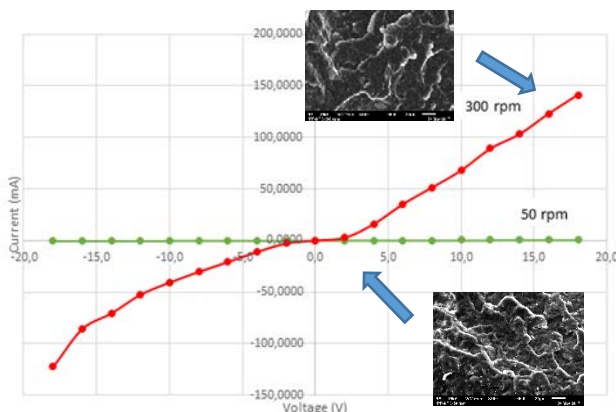


**Fig. 1.** Current-voltage curves and morphology of rPP nanocomposites obtained at different processing speed.

On the other hand, the electrical resistivity of the different nanocomposite films is significantly lower than that of the polymeric matrices (rPP or PETg), as expected. In addition, a pronounced effect of the extrusion speed on the rPP based films

electrical behaviour is observed (Figure 1), confirming the improvement of films morphology promoted by the high shear stresses developed at high speed of mixing. This result is also in agreement with the results of tensile behaviour mentioned before.

Currently, uniaxial tensile tests are being developed on the films up to different subcritical strain levels (before fracture) to determine a correlation between deformation and electrical resistivity and therefore, to analyse the capability of the obtained materials to monitor damage.

Conducting nanocomposite fibres based on PET and PP modified with carbon nanotubes are also being prepared. Based on the nanocomposite films and fibres, self-reinforced composites are being obtained and morphological, thermal and mechanical characterised. Their ability of damage monitoring is also being investigated.

### 4. Remarks

- An important effect of the processing conditions on the films morphology, tensile behaviour and electrical response is observed for rPP based nanocomposites.
- Currently, self-reinforced composites potential candidates for health-monitoring are being developed based on conductive nanocomposites films and fibres.

### Acknowledgements

The authors want to thank the University of Buenos Aires, the National Research Council of Argentina, the Argentinian Nanotechnology Foundation and the ANPCyT (PICT 2014-1955).

### References

- [1] Matabola K. P., De Vries A. R., Moolman F. S., Luyt A. S., Single polymer composites: a review, *Journal of Material Science* 44, 2009, pp. 6213–6222.
- [2] Karger-Kocsis J., Bárány T., Feature article single-polymer composites (SPCs): Status and future trends, *Composites Science and Technology*, 92, 2014, pp. 77–94.
- [3] Gao C., Yua L., Liu H., Chen L., Development of self-reinforced polymer composites, *Progress in Polymer Science*, 37, 2012, pp. 767–780.



- [4] Kmetty A., Barany T., Karger-Kocsis J., Self-reinforced polymeric materials: A review, Progress in Polymer Science, 35, 2010, 1288–1310.

# EFFECT OF ACID CONCENTRATION ON MECHANICAL PROPERTIES OF PA6 FOILS PREPARED BY METHOD OF CHANGING PHASE STATES

Alexandra Aulova<sup>1</sup>, Anže Cvenkel<sup>2</sup>, Igor Emri<sup>1</sup>

<sup>1</sup> University of Ljubljana, Faculty of Mechanical Engineering, Center for Experimental Mechanics, Aškerčeva ulica 6, Ljubljana 1000, Slovenia. E-mails: [alexandra.aulova@fs.uni-lj.si](mailto:alexandra.aulova@fs.uni-lj.si), [igor.emri@fs.uni-lj.si](mailto:igor.emri@fs.uni-lj.si)

<sup>2</sup> LOTRIČ Certificiranje d.o.o., Savska loka 4, SI-4000 Kranj, Slovenia. E-mail: [anze.cvenkel@lotric.si](mailto:anze.cvenkel@lotric.si)

## 1. Introduction

Polyamide 6 (PA6), also known as Nylon 6 is widely used in variety of applications including automotive, textile, medicine and engineering solutions. Great mechanical properties, resistivity to abrasion and chemicals are the main properties of PA6 [1]. It also possesses properties important for drug delivery system material: biocompatibility, osseointegrativity and biodegradability.

In our previous works [2] we investigated the absorptive properties of bulk PA6 as a drug delivery container, while within this research the foils made of PA6 for controlled drug release are considered.

Particularly, paper presents the effect of concentration of formic acid in the composition of PA6 solution used to prepare the foil by method of changing phases on the tensile mechanical properties of the foils. Mechanical properties of foils are important for handling and have to be characterized before further application.

## 2. Materials

Ultramid B3S (BASF, Germany) polyamide 6 (PA6) material was used as a polymer, formic acid (FA) 99% Calro Erba and deionized water as a solvent. The compositions of solutions are presented in the table 1.

Notation of solution	PA6 [wt.%]	FA [wt.%]	Water [wt.%]	FA concentration in solution* [wt.%]
PA620/FA100	20	80	0	100
PA620/FA81	20	65	15	81.25
PA620/FA73	20	58	22	72.5
PA625/FA100	25	75	0	100
PA625/FA84	25	63	12	84
PA625/FA71	25	53	22	70.67

Tab. 1. Composition of solutions.

Two different concentrations of PA6 in solutions were considered, while concentration of formic acid in solvent was changed from 100% to approximately 70% wt.

## 3. Methods

Within this section the method of foil preparation is presented and characterization of foils is shown.

### 3.1 Foil preparation

All the procedure of foil preparation was accomplished at the room conditions ( $23 \pm 2^\circ\text{C}$ ).

Granules of PA6 were preliminary dried in the vacuum chamber at  $T=75^\circ\text{C}$ ,  $t=24\text{h}$  and  $P_{\text{abs}}=5000\text{ Pa}$ .

Every component of the solution (FA, PA6 and DW) was precisely measured using lab scale and pipette. Components were mixed together and left in the closed laboratory glass jars for 48 hours till the polymer is fully dissolved.

Method of immersion precipitation [3] was chosen for preparation of the membranes for drug delivery application and it is presented in Figure 1. The polymer solution is spread as a layer on glass support and together with it is submerged into non-solvent bath. Due to differences in concentration of the solvent (FA in this case) the diffusion process starts and water washes of the acid from the solution leaving only polymer.

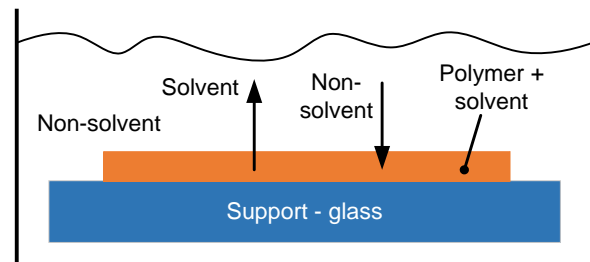


Fig. 1. Scheme of immersion precipitation process.

For preparation of the membrane the polymer solution should be evenly applied to the flat surface of a support, glass in our case. It was applied with the manual applicator ZUA 2000 (Zehntner, Switzerland) and manufactured according to ASTM D823. The speed of applicator was adjusted in a way to obtain the membranes with the thickness close to the 100-120 microns.

Precipitation bath contained only deionized water. During precipitation process deionized water covered the glass for 10 mm. The glass was submerged for 10 minutes.

### 3.2 Foil testing

Membranes were tested for tensile strength and elastic modulus. Tests were done according to ISO 527-1: 2012 [32] and ISO 527-3: 1995, conducted at Lotrič Certificiranje, d.o.o.

## 4. Results

Tensile strength and elastic modulus in dependence of the concentration of formic acid in solvent are presented in figures 2 and 3 respectively.

As expected, we found that membranes with higher amount of polymer show superior mechanical properties compared to foils with lower amount of polymer.

More important finding was that at some optimal FA concentration, which is for both mechanical properties at about 80%, we obtain foils with best mechanical properties. As seen from both figures, beyond this FA concentration mechanical properties start to decrease. Defining the ultimate FA concentration requires further investigation.

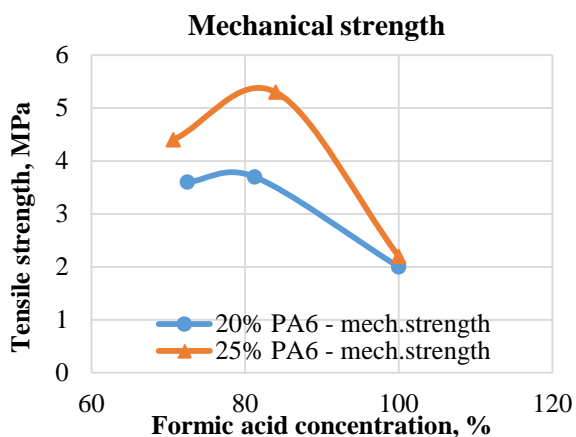


Fig. 2. Mechanical strength of foils in dependence of formic acid in solvent concentration.

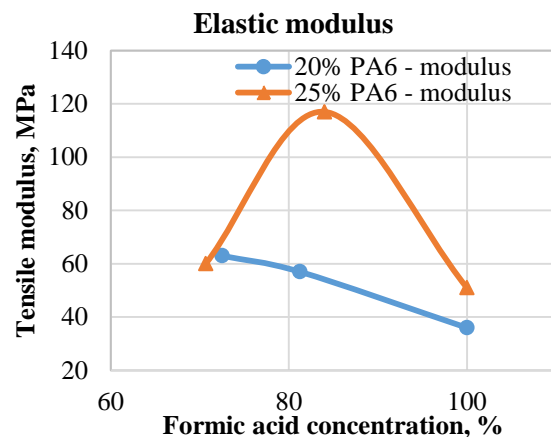


Fig. 3. Elastic modulus of foils in dependence of formic acid in solvent concentration.

## 5. Conclusions

- The results show that the amount of polyamide 6 in the solution determines the mechanical properties of the foils.
- The optimum of mechanical properties is observed at concentrations of formic acid of approximately 75-85%, therefore this region requires further investigation.
- Certain mechanical properties of the foil are required for handling and further processing, however for the drug delivery application superior mechanical properties should be optimized together with the permeability properties of the membrane which is a matter of further research.

## Acknowledgements

Authors would like to thank the Slovenian Research Agency for financing in a frame of project L2-7550 and research program P2-0264 as well as LOTRIČ Certificiranje d.o.o.

## References

- [1] Brandrup, J., Immergut E.H., Grulke E.A., Polymer Handbook: fourth edition, John Wiley&Sonc inc, New York, 1999.
- [2] Aulova, A., Gallegos, C., Emri, I. Absorptive Properties of PA6 as Drug Delivery Container, DAS 2015, Slovakia.
- [3] Bulte, A., Nylon 4,6 as membrane material, Polymer crystallization during immersion precipitation: doctoral thesis, Netherlands 1994.

## INTER-FACILITY CORRELATIONS OF TRANSONIC TEST RESULTS OF THE AGARD-C STANDARD WIND-TUNNEL MODEL

Dijana Damljanović<sup>1</sup>, Jovan Isaković<sup>2</sup>, Marko Miloš<sup>3</sup>

- <sup>1</sup> Military Technical Institute (VTI), Experimental Aerodynamics Department, Ratka Resanovića 1, 11030 Belgrade, Serbia. E-mail: [didamlj@gmail.com](mailto:didamlj@gmail.com)
- <sup>2</sup> Tehnikum Taurunum, College of Applied Engineering Studies, Nade Dimić 4, 11000 Zemun Belgrade, Serbia. E-mail: [jisakovic@tehnikum.edu.rs](mailto:jisakovic@tehnikum.edu.rs)
- <sup>3</sup> University of Belgrade, Faculty of Mechanical Engineering, Department of General Machine Design, Kraljice Marije 16, 11120 Belgrade, Serbia. E-mail: [mmilos@mas.bg.ac.rs](mailto:mmilos@mas.bg.ac.rs)

### 1. Introduction

Periodical wind-tunnel testing of standard models is an important item in a health monitoring of the wind-tunnel structure, instrumentation and flow quality. A series of tests of an AGARD-C standard model was performed in the 1.5 m T-38 trisonic wind-tunnel of the Military Technical Institute (VTI) in Belgrade. The tests comprised measurements of forces and moments in the transonic Mach number range with the purpose of correlating the model's obtained aerodynamic characteristics with those from other wind-tunnel laboratories. Inter-facility correlations are part of an adopted procedure for standard models testing in VTI experimental facilities, [1]. VTI finds it important to obtain these standard wind-tunnel data which serve to ascertain the stability of the measurement process and are helpful in future tests of similar configurations (especially with the T-tail). Also, an intention of the authors is to expand the database of published test results of this model, which is somewhat smaller than the one for the well-known AGARD-B model, [1].

### 2. Methods

#### 2.1 Wind-tunnel facility

The T-38, the most powerful test facility in the VTI, Belgrade, Serbia is a trisonic blowdown-type pressurized wind-tunnel with a 1.5 m square test section, Fig.1.

Mach number in the range 0.2 to 4 can be achieved in the test section, with Reynolds numbers up to  $110 \times 10^6$  per metre. In the subsonic configuration, Mach number is set by sidewall flaps in the tunnel diffuser. In the supersonic configuration, Mach number is set by the flexible

nozzle contour, while in transonic configuration, Mach number is both set by sidewall flaps and the flexible nozzle, and actively regulated by blow-off system. Mach number can be set and regulated to within 0.5% of the nominal value.

Stagnation pressure in the test section can be maintained between 1.1 bar and 15 bar, depending on Mach number, and regulated to 0.3% of nominal value. Run times are up to 60 s, which depend on Mach number and stagnation pressure.



Fig. 1. T-38 wind-tunnel facility in VTI, Belgrade.

Model is usually supported in the test section by a tail sting mounted on a pitch-and-roll mechanism. The facility supports both step-by-step and continuous model movement during measurements.

#### 2.2 Standard AGARD-C model

Standard AGARD-C model, a derivative of the well-known standard AGARD-B model [2], is an ogive-cylinder with a delta wing and a horizontal and a vertical stabilizer in the T-tail configuration, Fig.2.

The AGARD-C standard model, used in T-38, was supplied by *Boeing* and model size of 115.8 mm dia. was chosen with respect to the tunnel's

test section size. Model had been used in previous T-38 wind-tunnel calibrations and tests in other wind-tunnels. A large database is available in the VTI for inter-facility correlations.

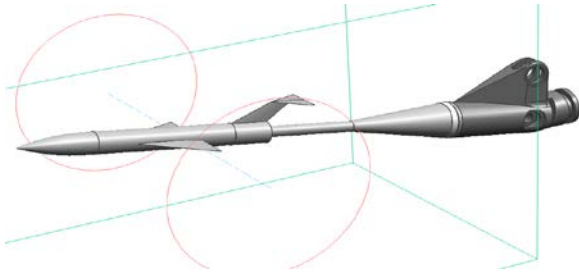


Fig. 2. CAD rend. of the AGARD-C model used in VTI.

### 3. Results

The new T-38 tests have been performed at the transonic Mach numbers 0.7 to 1.15 at moderate angles of attack traversed by the continuous pitching movement of the AGARD-C during the run.

Inter-facility correlations were based on test results of **physically the same model** (the 115.8 mm dia.) in the 1.5 m (5 ft) trisonic wind-tunnel of the National Research Council (then operated as National Aeronautical Establishment) of Canada, in the 1.2 m trisonic wind-tunnel of the Romanian National Institute for Scientific and Technical Creation (INCAS, later INCREST) and in the T-38 wind-tunnel during the commissioning period. Correlated test results are presented in the wind axes system in Fig. 3 and Fig. 4, showing forebody drag-force and pitching-moment coefficients as function of the angle of attack. Test results are given for the model aerodynamic center. Model reference length is the mean aerodynamic chord.

It should be noted that, because of the smaller size of the INCREST test section the blockage of the AGARD-C model in tests was higher than in VTI and NAE tests. Also, according to INCREST, there was insufficient ventilation of the plenum chamber causing the boundary layer to be too thick in the high transonic regime, which has affected the measurement of the pitching-moment. The AGARD-C model is known for the high sensitivity of the pitching-moment to local conditions.

### 4. Remarks

A good agreement of the correlated test results has been found, which confirms a high flow quality in the T-38 test section, good condition of the wind-tunnel structure and instrumentation and the correctness of the data reduction algorithm.

Making visible the standard test results provides a general benefit to the experimental aerodynamics community.

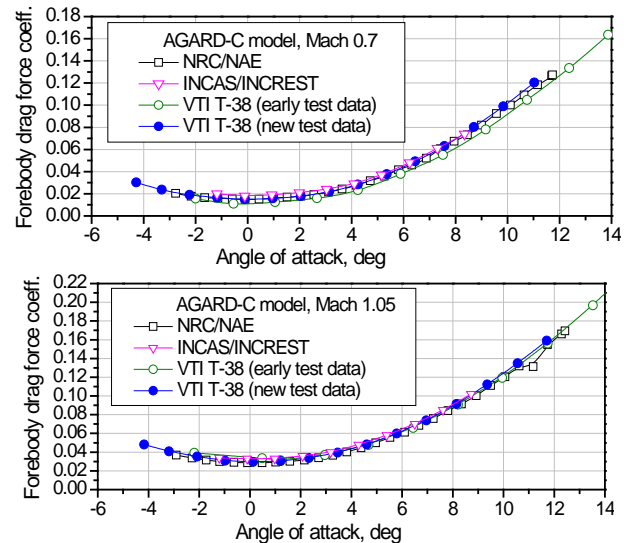


Fig. 3. Inter-facility correlations in the drag-force measurements, Mach 0.7 and 1.05.

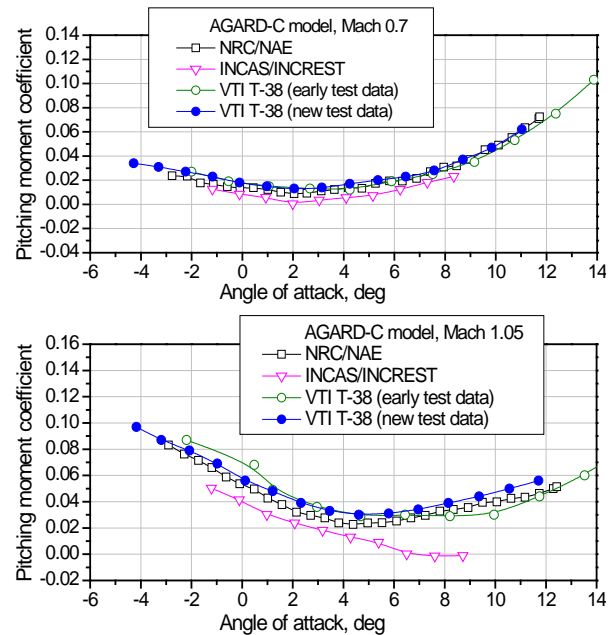


Fig. 4. Inter-facility correlations in the pitching-moment measurements, Mach 0.7 and 1.05.

### References

- [1] Damljancovic, D., Isakovic, J., Rašuo, B., T-38 Wind-Tunnel Data Quality Assurance Based on Testing of a Standard Model, *Journal of Aircraft*, 50 (4), 2013. pp. 1141-1149.
- [2] Hills, R., *A Review of Measurements on AGARD Calibration Models*, AGARDograph 64, Aircraft Research Association, Bedford, England, 1961.

# THE BAUSCHINGER EFFECT IN THIN SHEET MAGNESIUM ALLOY USING ANTI-BUCKLING FIXTURE

Tomasz Libura<sup>1</sup>, Zbigniew L. Kowalewski<sup>1</sup>, Katarzyna Kowalczyk-Gajewska<sup>1</sup>,

<sup>1</sup> Institute of Fundamental Technological Research Polish Academy of Sciences,  
ul. Pawinskiego 5B, 02-106, Warsaw, Poland. E-mail: [tlibura@ippt.pan.pl](mailto:tlibura@ippt.pan.pl)

## 1. Introduction

Ultralight magnesium alloys with additions of other metals are already used in a variety of aerospace and automotive semi-products, and also in many other industrial applications requiring good properties and high values of the strength to weight ratio. Magnesium alloys have a special feature that is particularly visible during the forming of industrial parts. The basic tool to quantify the formability of metallic sheet which is Forming Limit Diagram (FLD) built with the in-plane principal strains in which a Forming Limit Curve (FLC) can distinguish between safe and necked points. However, during the forming of industrial parts made of magnesium alloy, instead of linear deformation path very complex strain paths are usually observed and can affect the formability of the sheet. Example of strain path change is shown in Fig.1 [1].

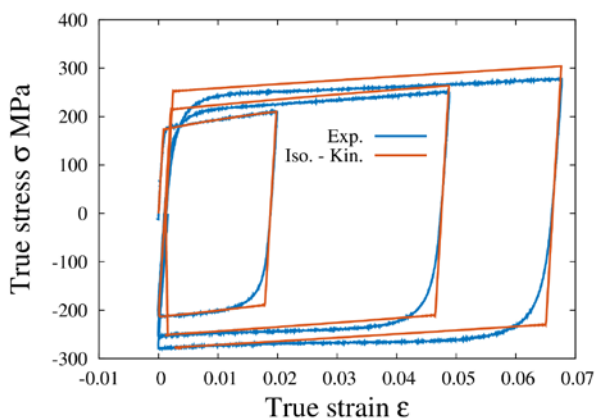


**Fig. 1.** Deformation process with strain path change; blue line - experimental results, red line - numerical results.

Among many important effects necessary to be taken into account one can indicate Bauschinger effect observed after change of the loading direction. It should be noted that material testing of flat specimens under compression within a large

deformation range procures many difficulties, and the buckling phenomenon seems to be the most important. To avoid buckling problem a special device is necessary. In the last decade many new solutions were created [2]. Among them one can indicate the anti-buckling fixture proposed by IPPT PAN in 2012, which is illustrated in Fig.2.

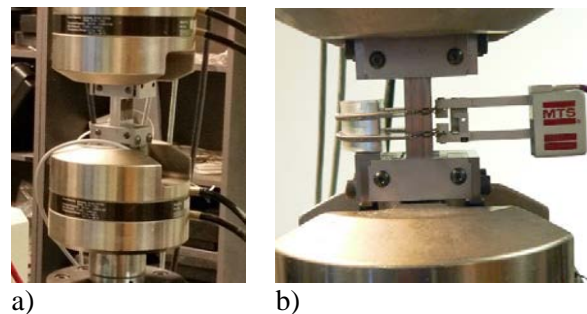


**Fig. 2.** Fixture mounted in loading frame (a) with attached extensometer (b).

The device is designed to carry out the compression or tension-compression tests in the standard testing machine. The most important feature of the device is its automatic alteration and adaptation of its length during tests, depending on loading type, which leads to specimen elongation under tension or shrinkage under compression. The next crucial feature of the device is the fact that it makes possible to measure the friction force which is generated due to movement of its parts. Therefore, fixture is equipped with four strain gauges cemented to surfaces of two measuring bars. These elements assembled into a full bridge system create the sensor of friction force measurement. This solution enables on-line measurement of the friction force and reduction of additional calculation errors.

The aim of this paper is to investigate the strain-hardening effect in thin sheet of ultralight magnesium alloys by application of the anti-buckling fixture.

## 2. Experimental procedure and results

All tension-compression tests were carried out on thin sheet specimens with nominal thickness equal to 1 mm. Cyclic loading was performed under displacement control with the rate of 0.025 mm/s. Boundary conditions were set into the loading controller to limit strain range during cycling. A special set up for the friction force measurements was applied. It consisted of two coupling bars with strain gauges calibrated in the range of  $\pm 2$  kN.

In the first type of cyclic test, 15 cycles within a strain range  $\pm 0.04$  were planned with the start in tension direction. In the second one, a similar program was arranged, however, with the start in compression direction. All tests were carried out using extensometer with a range of  $\pm 0.2$ . The loading cell was calibrated in the range of  $\pm 25$  kN.

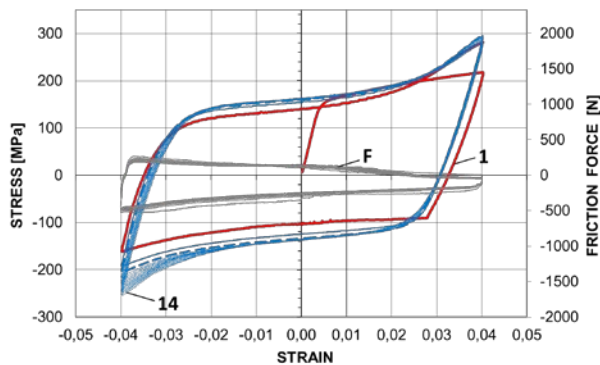


**Fig. 3.** Hysteresis loops of the AZ31B alloy and friction force variation - start in tensile direction.

The results of first type of test carried out on the AZ31B magnesium alloy under cyclic loading are presented in Fig. 3. The first cycle is illustrated by solid red line denoted as (1). In the next cycle represented by blue solid line, the magnesium alloy exhibited the highest level of tensile stress and for the rest of planned cycles it remained almost unchanged. A different behaviour may be observed for the compressive stress levels. In this case, a continuous hardening effect was obtained expressed by the gradual increase of the maximum compressive stress in the subsequent cycles denoted by blue dotted lines. Figure 3 also presents an evolution of the friction force (grey lines, denoted as (F)).

The results of second type of test are presented in Fig. 4. Here, the strain-hardening stagnation effect took place for the material in question. It is most remarkable for the first three cycles. During subsequent cycles the tensile stress value in the

specimen tested remained at the same level, while for the opposite direction the alloy showed a continuous cyclic hardening.

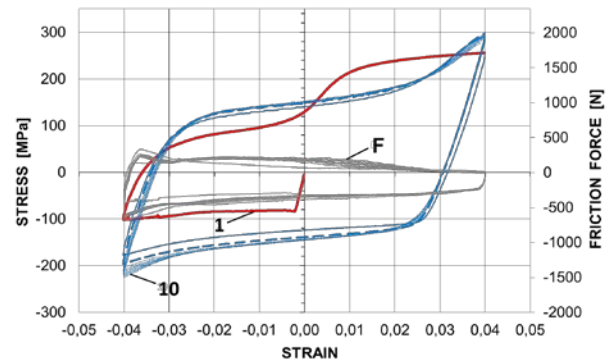


**Fig. 4.** Hysteresis loops of the AZ31B alloy - start in compressive direction.

## 3. Summary

The results shown in Figs. 3 and 4 exhibited the visible effect of strain-hardening stagnation observed after change of the loading direction, especially in the first cycle (1). Three dominant deformation mechanisms are presumably responsible for deformation behaviour of the AZ31B alloy: dislocation slip dominated deformation - Slip Mode, twinning-dominated deformation - Twinning Mode and detwinning-dominated deformation - Detwinning Mode [4]. The strain hardening stagnation may be attributed to the alternation between twinning and detwinning mechanisms.

## Acknowledgements

The work has been accomplished under the research project No. 2013/09/B/ST8/03320 financed by the Scientific Research Committee.

## References

- [1] Lumelskyy D, Rojek J., et al., Numerical simulation of formability tests of pre-deformed steel blanks, Archives of civil and mechanical engineering, 2, 2012. pp. 133-141.
- [2] Libura T., Kowalewski Z.L., Dietrich L., Socha G., Anti-buckling system for flat specimens investigations under cyclic tension-compression, Materials Today: Proceedings, 3, 2016, pp. 1045-1050.
- [3] [4] Wu L., et al., The effects of texture and extension twinning on the low-cycle fatigue behaviour of a rolled magnesium alloy,



34th Danubia-Adria Symposium on Advances in Experimental Mechanics  
University of Trieste, Italy, 2017



AZ31B Materials Science and Engr. A, 527,  
2010, pp. 7057-7067.

## SHORT TERM EVALUATION OF CHANGES IN ELASTIC PROPERTIES OF BOVINE TRABECULAR BONE DUE TO THE STORAGE METHOD

Adam Mazurkiewicz<sup>1</sup>

<sup>1</sup> University of Science and Technology, Mechanical Engineering Faculty, Kaliskiego 7 Street, 85-796 Bydgoszcz, Poland. E-mails: [adam.mazurkiewicz@utp.edu.pl](mailto:adam.mazurkiewicz@utp.edu.pl)

### 1. Introduction

A trabecular bone is a one of main bone component determining the strength of the entire bone [1, 2]. It is present in the epiphysis of long bones and fills the interior of short, flat and irregular bones. Even a small reduction in mass and quantity of trabeculae in the bone leads to a significant reduction of the bone strength. The studies of the trabecular bone are undertaken by many researchers analyzing the bone strength.

One of the most important aspects regarding the trabecular bone studies is a method of storing the bone samples [3-5]. Since the bone is a composite material including an organic and mineral phase, as well as a solid and liquid phase, the storage method may affect the mechanical properties of the trabecular bone in time.

The study aimed to evaluate the effects of the trabecular bone storage method on its elastic properties. The bovine trabecular bone samples stored in air at room temperature (G1 group), in formalin at room temperature (G2 group) and frozen stored (G3 group) for 21 days were subject to tests.

### 2. Material and Method

The samples were taken from the spongy part of the head of bovine femoral bone. All animals were at similar age and came from the same species and herd.

Slices were cut from the epiphysis of the head of the femoral bone and 90 cylindrical samples with a diameter and height of 10 mm were taken. Depending on its size, 2-3 samples were taken from each bone.

The whole bones were stored in a cold room. The first measurement made immediately after sampling ( $T_1$  time) was used as a reference

measurement. The samples were stored in the following conditions: room temperature 21°C and humidity 35% in 10% formalin solution and frozen at -20°C.

The samples were subject to compression tests on Instron E3000 testing machine to determine the elastic modulus. The test procedure was as follows:

The sample was subject to initial compression force 3 N for 10 seconds, and five compression cycles in the elastic range were carried out until 0.65% strain was recorded. Each loading-unloading cycle lasted 60 seconds with 10 second intervals between the cycles. For loop obtained from fifth cycle tangential modulus was calculated. After every cycle strain channel was reset to zero.

The control measurements for samples in each group were carried out after 7 ( $T_2$ ), 14 ( $T_3$ ) and 21 ( $T_4$ ) days from the sampling date.

A Szapiro-Wilk test at  $p=0.05$  value was used to determine the distribution type for sample moduli recorded for each group.

A statistical Kolmogorov-Smirnov test at  $p=0.05$  value was used to evaluate changes in average modulus value in time for each group using "R" software.

### 3. Results

Table 1 shows average, minimum and maximum values and standard deviations for the compression test for each group.

	G1 group	G2 group	G3 group
Modulus T <sub>1</sub> [MPa]	1759 (SD ±1626)	1985 (SD ±0.1267)	1756 (SD ±1157)
Modulus T <sub>2</sub> [MPa]	1937 (SD ±1384)	1837 (SD ±117)	1745 (SD ±1378)
Modulus T <sub>3</sub> [MPa]	2500 (SD ±1218)	1714 (SD ±915)	1770(SD ±1147)
Modulus T <sub>4</sub> [MPa]	3015 (SD ±1174)	1785 (SD ±1173)	1872 (SD ±1289)

**Tab. 1.** List of average value of moduli recorded for each group.

For a group of frozen samples, the values were characterized by a normal distribution for all measurements. All measurements for a group of samples stored in formalin and dry samples were characterized by a log-normal distribution. Divergent results can be observed in some cases and up to three results divergent from the normal distribution were recorded for each group.

For a group of frozen samples and samples stored in formalin, changes in average modulus value were statistically insignificant.

For a group of dry samples (G1), an increase in average module value in time was recorded. The changes average modulus in this group were statistically significant.

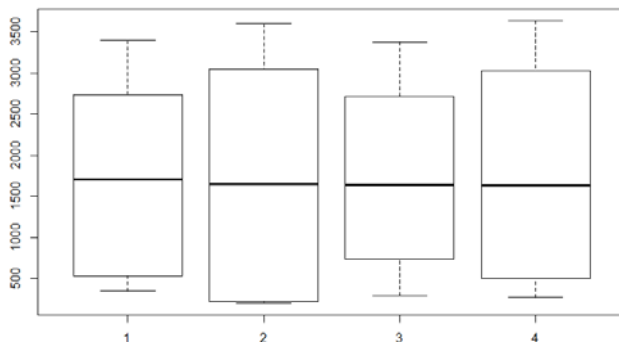


**Fig. 1.** Changes in time average modulus value for a group of frozen samples.

Fig. 1 show the statistical test results using box plots for frozen group. For frozen samples and samples stored in formalin, average values for subsequent measurements were similar. For dry samples, average values increased during subsequent measurements.

## 4. Discussion

Based on the results, freezing the samples and storing the samples in 10% formalin solution did not significantly affect changes of elastic modulus within a period of 21 days. Thus, the methods can be used to store bovine trabecular bone samples.

Storing the samples at room temperature resulted in an increase in elastic modulus, most probably due to the loss of moisture. Based on the data available in the literature, dry bones show better strength properties, i.e. higher elastic modulus and relative strength compared to the wet bone. Thus, the method should not be used to store trabecular bone samples.

A significant scatter of the recorded values compared to the average value was observed between the groups. It is due to the fact that some samples were taken from the same bone which may affect the recorded values, since the strength may vary depending on the area of the femoral bone head the sample was taken from.

## References

- [1] Goulet, R. W., Goldstein, S. A., Ciarelli, M. J., Kuhn, J. L., The relationship between the structural nad orthogonal compressive properties of trabecular bone, *Journal of Biomechanics*, 27, 1994. pp.375-389.
- [2] Yuehuei, H., Draughn, R., *Mechanical testing of bone and the bone-implant interface*, CRC Press, New York 1999.
- [3] Fölsch, C. Mittelmeier, W., Bilderbeek, U. et al., Effect of Storage Temperature on Allograft Bone, *Transfus Med Hemother*, 39, 2012. pp 36-40.
- [4] Vastel, L., Meunier, A., Siney, H., Sedel, L., Courpied, J.P., Effect of different sterilization processing methods on the mechanical properties of human cancellous bone allografts, *Biomaterials*, 11, 2004. pp. 2105-10.
- [5] Borchers, R.E, Gibson, L.J, Burchardt H, Hayes WC. Effects of selected thermal variables on the mechanical properties of trabecular bone, *Biomaterials*, 16, 1995. pp. 545-51.

# INFLUENCE OF THE TRABECULAR BONE STRUCTURE INDICATORS ON ITS STATIC AND FATIGUE STRENGTHS

Adam Mazurkiewicz<sup>1</sup>

<sup>1</sup> University of Science and Technology, Mechanical Engineering Faculty, Kaliskiego 7 Street, 85-796 Bydgoszcz, Poland. E-mail: [adam.mazurkiewicz@utp.edu.pl](mailto:adam.mazurkiewicz@utp.edu.pl)

## 1. Introduction

Trabecular bone fills in the ends of long bones, the inside of small bones and irregular-shaped bones. It is porous, and its structure is dependent on gender, age, bone diseases history and other factors [1, 2].

In particular cases, differences in the number of trabeculae, their shape and thickness occur, which is strictly related with the bones strength [1, 3-5].

In this paper it was evaluated how the individual trabecular bone structure indicators influence its static and fatigue strength.

## 2. Material and Method

The tests were performed on samples collected from femoral heads. The bones were collected as a result of implanting femoral joint of persons suffering from arthrosis.

The samples were collected in the following mode. Firstly, a plaster of depth 10 mm was cut out from the head, perpendicular to the neck axis. Then, samples of 10 mm diameter were cut out from the plaster. Then, the face surfaces were ground until 8,5 mm sample height was achieved. Finally, the samples were 10 mm in diameter and 8,5 mm in height. They were stored in a 10% formalin solution, at room temperature.

The samples structure was examined using SkyScan 1172 microtomograph. The scanning resolution was 25  $\mu\text{m}$ . Based on the examination results, parameters of the structure, including trabeculae number, trabeculae thickness, ratio of tissue volume in the sample to the sample volume were calculated.

Based on this, the samples suitability for the test was also evaluated. In advanced cases of arthrosis, pathological changes at the joint surface of

the head, and near the trabecular bone occur. The microtomographic examination allowed to evaluate the occurrence of this type of changes in the sample. Those samples in which such changes were identified were eliminated from further tests. 30 samples were used in the tests, divided at random into two groups. One of them was used for testing static strength (GS group), and the other for fatigue tests (GF group).

The samples were subjected to tests on a Instron E3000 strength testing machine.

Was subjected to initial load of force 3N. Then, 5 cycles of load up to value 0,65% of the sample height were performed. Cycle time 30 s, with a 5 s pause between the cycles. Then, the test was conducted at fixed deformation speed until obtaining the maximum force value. Static strength was evaluated as quotient of maximum force and sample surface area.

Fatigue test was performed at gradually increasing amplitude. The initial load was 5N. Maximum load started from 20N and incremented by 10N at each subsequent level. The volume of each level was 500 cycles. At each level, the minimum and maximum load was constant. Fatigue life was evaluated as follows: determined the median values of deformation increment of sample. Assumed that fatigue life is defined as: number of the first loop for which value the deformation gain exceeded the value of the median by 10%.

## 3. Results

Shapiro- Wilk test ( $p=0.05$  value) was used for evaluating the distribution of the obtained values of structure and values of static and fatigue strengths

The test results show that the all the values are normal or log-normal distribution.

Table 1 presents the results of measurement of the structure indicators. Table 2 presents the value of static and fatigue strength, calculated for both of the tested groups. The values of correlation coefficients obtained between the structure indicators and the strength were presented in table 3.

	<b>Tb.N, 1/mm</b>	<b>Tb.Th, mm</b>	<b>BV/TV, -</b>
GS group	1.47 (SD ±0.24)	0.167 (SD ±0.032)	0.252 (SD ±0.063)
GF group	1.39 (SD ±0.22)	0.148 (SD ±0.038)	0.233(SD ±0.052)

**Tab. 1..** Values of trabecular bone structure indicators.

<b>US, MPa</b>	<b>NS, cycles</b>
12.12 (SD ±5.71)	26 163 (SD±12 182)

**Tab. 2.** Values of static strength and fatigue life.

	<b>Tb.N</b>	<b>Tb.Th</b>	<b>BV/TV</b>
US, MPa	0.59	0.64	0.69
Ns, cycles	0.51	0.61	0.62

**Tab. 3.** Values of the coefficients of correlation between the structure indicators and strength.

#### 4. Discussion

The correlation between the structure indicators values and static strength  $R=0.59\div0.69$ .

The correlations with fatigue strength are in range  $R=0.51\div0.62$ .

Based on the above it may be concluded that the structure indicators are useful for evaluating static and fatigue strength of trabecular bone.

A certain limitation to the usability of the test results is that the bones were collected from persons suffering from arthrosis, and that several samples might have originated from the same bone. This introduces certain difficulties in evaluating the results. For instance, the impact of the sickness and treatment on changes to the chemical content of the trabecular bone tissue is unknown. These factors could have effected in varying strength between the trabecular bones collected from persons with arthrosis and from healthy persons, at comparable trabecular bone structure in the sample.

Another limitation was the sample size used in the tests. In order to obtain a more credible static evaluation of the results, a larger number of

samples would be required. The use of several samples collected from the same bone could influence the test results due to the individual features of persons from which the heads were collected.

Also, the samples were not divided according to age or gender. A comparable number of persons of the same gender and age were qualified to both groups. In the view of the sample size, a different approach to splitting the groups seemed unjustified.

#### Acknowledgements

The author of the paper had the consent of the local ethics committee for performing the tests described in text.

#### References

- [1] Yuehuei, H., Draughn, R., Mechanical testing of bone and the bone-implant interface, CRC Press, New York 1999.
- [2] Mosekilde, L., Danielsen, C., Biomechanical competence of vertebral trabecular bone in relation to ash density and age in normal individuals, Bone, 8,1987. pp 79-85.
- [3] Rapillard, L., Charlebois, M., Zysset, P.K., Compressive fatigue behavior of human vertebral trabecular bone, Journal of Biomechanics, 39, 2006. pp. 2133-2139.
- [4] Goulet, R.W., Goldstein, S.A., Ciarelli, M.J. et al., The relationship between the structural nad orthogonal compressive properties of trabecular bone, Journal of Biomechanics, 27, 1994. pp. 375-389.
- [5] Rice, C., Cowin, S., Bowman, J., On the dependce the elasticity and strength of cancellous bone on apparent density, Journal of Biomechanics, 21, 1988. pp. 155-168.

## OSSEOINTEGRATION SPECIFIED GRIT BLASTING PARAMETERS

Alexandra Kemény<sup>1</sup>, István Hajdu<sup>1</sup>, Dóra Károly<sup>1</sup>, Dávid Pammer<sup>1</sup>

<sup>1</sup> Budapest University of Technology and Economics, Faculty of Mechanical Engineering, Department of Materials Science and Engineering, H-1111 Budapest, XI. Bertalan Lajos u. 7. Building MT, Hungary. E-mails: [alexandra.kemeny@edu.bme.hu](mailto:alexandra.kemeny@edu.bme.hu), [hajdu999@gmail.com](mailto:hajdu999@gmail.com), [kdora@eik.bme.hu](mailto:kdora@eik.bme.hu), [pammer@eik.bme.hu](mailto:pammer@eik.bme.hu)

### 1. Introduction

Nowadays, it is very common to have spinal diseases such as scoliosis. When the curve of the spine reaches a certain deformation, it can only be healed by surgery. These implants are staying in the patient forever.

The osseointegration is a complex process. First, the implant needs to have a direct interaction with the bone. If the implantation is successful, and the surface of the implant is suitable for osteoblasts, these cells start forming new bone. This creates a strong bond between the bone and the implant [1].

There are plenty of dental implants and hip prosthesis femoral stems on the market with grit blasted surfaces and great results in patients. Grit blasting creates a micrometer roughness which stimulates osteoblasts [2]. However spinal implants' surfaces are not yet treated this way.

Some researches already shown that grit blasted spinal implants needed twice the torque to remove from sheep vertebrae in vivo, twelve weeks after implantation that the smooth screws [3]. Other research has shown, that the success of an implant is highly dependent of the surface characteristics, and also the macro design of the implant. Surface microroughness has been well established to achieve better osseointegration [1].

Implant materials can be very diverse. In implantology the most widespread material nowadays is the titanium and its alloys, because of its great biocompatibility and mechanical properties [4]. Grit blasting is a surface modification treatment. The morphology of the surface changes significantly as the small particles hit the implant with high speed [5].

The purpose of our research is to optimize the blasting parameters on disks and then do the surface treatment on the spine implants.

### 2. Materials and methods

In the research, we examined implants and disks made of Ti 6Al 4V ELI, also known as Grade23 Titanium. For the chemical composition see Tab. 1. This alloy is a bioinert material, so it has a stable oxide film on its surface which provides corrosion resistance and biocompatibility [4].

C %	Al %	N %	O %	Ti
≤ 0.08	5.5 to 6.5	≤ 0.03	≤ 0.13	Balance
Fe %	V %	H %	Other %	
≤ 0.25	3.5 to 4.5	≤ 0.013	≤ 0.40	

Tab. 1. Ti 6Al 4V chemical composition

As blasting material alumina powder was used. The following five technological parameters of the sandblasting were investigated: size of blasting material, distance between the tip of the blasting pen and the samples, time, pressure and angle of the blasting pen and the axis of samples. Each parameter was tested in three different levels.

In total 135 disks and 6 implants were used in the experiment. The disks were 1.5 mm in thickness and 5.5 mm in diameter.

For the blasting process a clamping device was needed which helped to fix the disks during blasting. With this the angle and the distance was adjustable during the blasting process. To calculate the effect of parameters to the surface roughness, Minitab 17 statistical software was used.

After blasting the surface roughness (Ra) was investigated. For this measurement, a Mahr Pocket Surf IV profilometer was used. Olympus SZX16 stereomicroscope and Philips XL30 scanning electron microscope was used for taking images.

### 3. Results

The ideal surface roughness to osseointegration is between 1-2 μm [6]. Based on the experiments 1.5 μm roughness can be created on Grade23 Ti disks

(Fig.1.) with the following parameters: particle size of 354-500  $\mu\text{m}$ , time of 30 s, pressure of 4 bar, distance of 20 mm and angle of  $75^\circ$ .

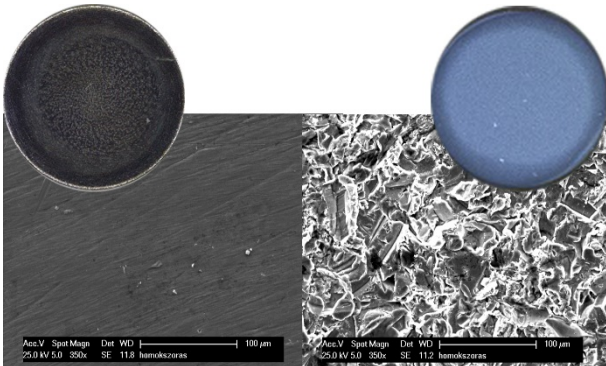


**Fig. 1.** Stereomicroscopic and SEM image of a disk before (left) and after (right) blasting

Using the mentioned blasting parameters, a consistent rough surface was reached with a treatment specific morphology on the implants, see Fig. 2.

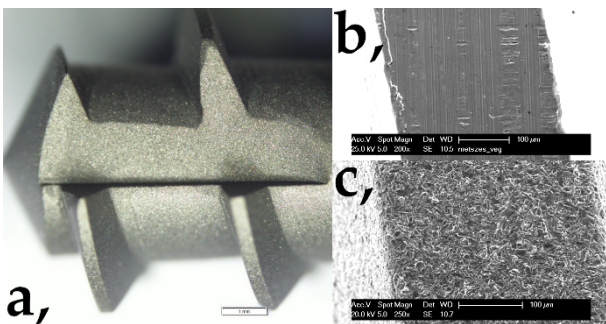


**Fig. 2.** Stereomicroscopic image of the blasted implant (a) and SEM images before (b) and after (c) blasting

The results show that of the five investigated parameters the size of blasting material has the biggest influence on the surface roughness. This follows the pressure the other three parameters are negligible, see Fig. 3.

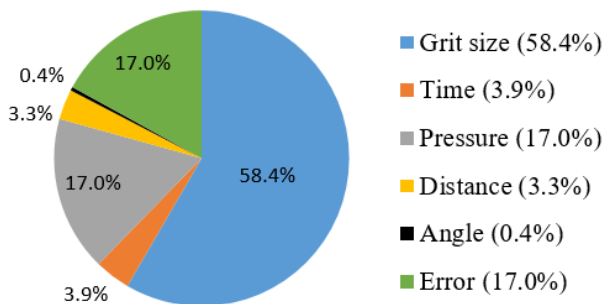


**Fig. 3.** Effects of the five technological parameters to the surface roughness

#### 4. Remarks

- With 354-500 $\mu\text{m}$  particle size, 30 s blasting time,  $75^\circ$  blasting angle, 4 bar pressure and 20 mm blasting distance, the 1.5  $\mu\text{m}$  surface roughness can be created on machined Grande23 Ti disks and implants.
- This experiment processes an important matter in material science, because the osseointegration of the mentioned surface roughness is far better.

#### Acknowledgements

The publication of the work reported herein has been supported by ETDB at BME.

#### References

- [1] Rolando A. Gittens et al., Implant osseointegration and the role of microroughness and nanostructures: Lessons for spine implants, *Acta Biomaterialia* 10, 2014. pp. 3363-3371.
- [2] Rene Olivares-Navarrete, DDS, PhD et al., Rough titanium alloys regulate osteoblast production of angiogenic factors, *The Spine Journal* 13, 2013. pp. 1563-1570.
- [3] Zvi Schwartz et al., Effect of Micrometer-Scale Roughness of the Surface of Ti6Al4V Pedicle Screws in Vitro and in Vivo, *The Journal of Bone and Joint Surgery Vol. 90A* No.11, 2008. pp. 2485-2498.
- [4] D.M. Brunette et al., *Titanium in medicine: Material Science, Surface Science, Engineering, Biological Responses and Medical Applications*, Springer Science & Business Media, 2001. ISBN 978-3-642-56486-4.
- [5] Xuanyong Liu et al., Surface modification of titanium, titanium alloys, and related materials for biomedical applications, *Materials Science and Engineering R47*, 2004. pp. 49-121.
- [6] T. Albrektsson, A. Wennerberg, Effects of titanium surface topography on bone integration: a systematic review, *Clinical Oral Implants Research*, vol. 20 (4), 2009, pp. 172-184.

# CORROSION BEHAVIOUR OF OVERLAPPING CORONARY ARTERY STENTS

Dóra Károly<sup>1</sup>, Lilla Asztalos<sup>1</sup>, Éva Fazakas<sup>2</sup>

- <sup>1</sup> Budapest University of Technology and Economics, Faculty of Mechanical Engineering, Department of Materials Science and Engineering, H-1111 Budapest, Bertalan Lajos u. 7. Hungary. E-mails: kdora@eik.bme.hu, lilla@eik.bme.hu
- <sup>2</sup> Bay Zoltán Nonprofit Ltd. for Applied Research, H-1116 Budapest, Kondorfa u. 1. Hungary. E-mail: eva.fazakas@bayzoltan.hu

## 1. Introduction

We only have one heart. If a larger part dies, the rest cannot take over the work of the fell out part, so that the performance of the organ weakens and cannot supply the body with adequate amount of oxygen. Cardiovascular diseases are leading both morbidity and mortality statistics worldwide. The negative economic and social impacts of these diseases are increasing continually. The high mortality numbers clearly indicate the importance of the development in the field of cardiology research, diagnostic and therapeutic procedures [1].

Coronary artery stents are widely used for the treatment of ischemic heart disease. After implantation the stent remains in the body. Stents are gradually incorporated into the vascular connective tissue – depending on the health and genetics of the patient – until they eventually become a part of the vessel wall. Due to the differences in coronary flow, shear stress and turbulences bifurcation lesions (stenosis at the division of an artery into two branches) are common anatomy features of the human coronary tree. In the case of bifurcation lesions or severe stenosis, several stents are implanted in the same vessel segment, dilating them into each other, overlapping. The blood flow in the vessel provides ideal environment for corrosion damage processes [2].

During bifurcation stenting physicians can dilate two stents into each other made of a different material (with distinct normal potentials). In this case galvanic or crevice corrosion can occur, so special attention was paid to this field. Only some studies carried out according to stent corrosion and none of them pay attention to the case of overlapping stents with different materials [3,4]. In

this study corrosion behaviour of overlapping coronary stents are described.

## 2. Materials and methods

The investigated stents are made of Co-Cr and Fe-Pt-Cr alloys. According to ISO 5832-5 [5] the material composition of the CoCr alloy can be seen in Tab. 1.

Chemical composition (%)							
Cr	Ni	W	Fe	Mn	Si	P	C
19-21	9-11	14-16	3	1-2	0,4	0,4	0,05-0,15

Tab. 1. L605 CoCr material chemical composition

The Pt-Cr alloyed steel cannot be found in any ISO standard because it is protected by the manufacturer [6], the composition can be seen in Tab. 2.

Chemical composition (%)						
Pt	Cr	Ni	Mo	C	Si	Others
32,5-33,5	17,5-18,5	8,5-9,5	2,43-2,83	0,003-0,023	≤0,1	≤0,05

Tab. 2. PtCr material chemical composition

The standard electrode potential of the components: Pt: +1,20 V, Co: -0,28, so galvanic corrosion can be predictable.

The test were carried out at 37°C in 0.9 w/w% saline to establish the actual circumstances in the more approximate environment. One test lasted one hour, during it potentiodynamic test was performed, after that images were taken of the stents and the saline solution was exchanged. The tests were performed with a Zahner IM6e complex electrochemical measuring equipment, CTV 101 PID electrode system, Agilent 347960A data collector. With the measurement results the corrosion rate of the stents for the test environment can be calculated.

Several recordings were made of the stents from different angles with an Olympus SZX16 stereomicroscope and a FEI Inspect S50 scanning electron microscope. JEOL EX-54175JMU energy-dispersive X-ray spectroscopy (EDS) was used to determine the material composition of the samples.

### 3. Results

The CoCr stent were dilated into the PtCr stent with nominal pressure (Fig. 1.). Two circles (1+1 hour) of corrosion test was performed on the sample.



**Fig. 1.** Stereomicroscopic image of the overlapping stents, CoCr stent is surrounded by the PtCr stent

The mass of the stents were measured before and after each corrosion test session. After 2 hours of measurement 11,63% of the sample disappeared. Most of the mass lost from the CoCr stent.

- Original mass: 0,0430 g
- After 1 hour measurement: 0,039 g
- After another 1 hour measurement: 0,038 g

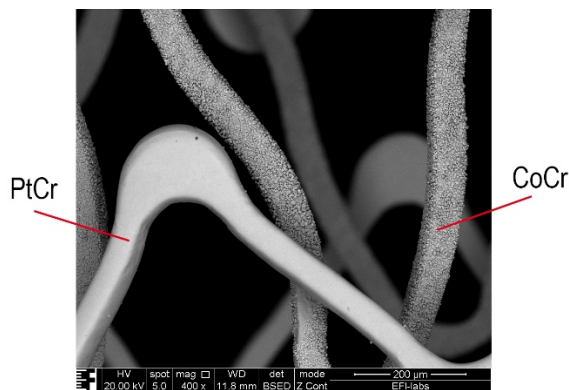


**Fig. 2.** SEM image of the stents after 1+1 hour of corrosion test

Even after a 2 hours measurement an average corrosion can be observed on the CoCr stent (Fig.2.), and pitting corrosion can be seen on the PtCr stent (Fig.3.) The average size of the hole shaped pit on the PtCr stent is 1-2  $\mu\text{m}$ .

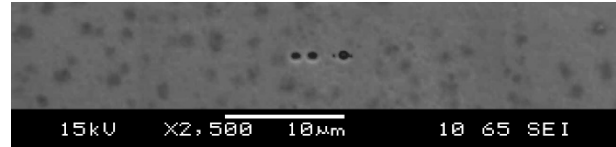


**Fig. 3.** Pitting corrosion on the PtCr stent

The results of the EDS measurements show that after the 2 hour test less Ni can be found in the CoCr material which means that during the corrosion process Ni can be released to the body.

### 4. Remarks

- The dilation of overlapping coronary artery stents with different material and standard potential clearly induces galvanic corrosion processes.

### Acknowledgements

This research was supported by the National Talent Programme of the Hungarian Ministry of National Resources (NTP-NFTÖ-17-B-0359).

### References

- [1] A.N. NOWBAR, et al. Global geographic analysis of mortality from ischaemic heart disease by country, age and income. *Int. J. of Cardiol.* 174:2 (2014) pp.293-298.
- [2] M.R. Mohaved, et al. Coronary artery bifurcation lesions: a review and update on classification and interventional techniques. *Card. Rev. Medicine* 9 (2008) pp.263-268.
- [3] H. YANG, et al. Pitting corrosion resistance of La added 316L stainless steel in simulated body fluids. *Materials Letters* 61. (2007) pp.1154-1157.
- [4] C.L. LIU, et al. Anti-corrosion characteristics of nitride-coated AISI 316L stainless steel coronary stents. *Surface & Coatings Technology* 201. (2006) pp.2802-2806.
- [5] ISO 5832-5:2007 Implants for surgery – Metallic materials – Part 5: Wrought cobalt-chromium-tungsten-nickel alloy.



- [6] B O'BRIEN, et al. A platinum–chromium steel for cardiovascular stents. *Biomaterials* 31. (2010) pp.3755–3761.

# IMPLEMENTATION OF CORRECTNESS CRITERIA FOR THE BONE STRUCTURE ANALYSIS BY MEANS OF A HAND-HELD X-RAY SYSTEM

Francesca Cosmi<sup>1</sup>, Alessandra Nicolosi<sup>2</sup>

<sup>1</sup> University of Trieste, Department of Engineering and Architecture, Via A. Valerio 10, 34127, Trieste, Italy. E-mail: [first.author@units.it](mailto:first.author@units.it)

<sup>2</sup> M2TEST srl, Area Science Park, Padriciano 99, 34149 Trieste, Italy. E-mail: [info@bestest.it](mailto:info@bestest.it)

## 1. Introduction

The social costs of osteoporosis are huge and keep growing because of increased life expectancy. Densitometry represents the current gold standard for osteoporosis diagnosis and a low bone mineral density is considered to be associated with a higher risk of fracture. However, densitometry alone has been shown to be inadequate to predict fractures in 40-50% of cases, since these occur in people who do not have a significant reduction in bone density.

In fact, trabecular bone tissue is extremely complex (Fig.1) and its shape and function are influenced by the constant physiological or pathological modifications that occur during lifetime. In particular, its mechanical properties – and consequently its resistance – are strongly influenced not only by the composition (mineralization and density but also, to a large extent, by the trabecular microarchitecture, that is by the spatial arrangement of the internal structure of bones.



**Fig. 1.** Trabecular bone and micro-CT 3D reconstruction of its architecture.

Although trabecular bone accounts for only 20% of our skeleton, the quality of bone structure is an additional key factor responsible for its resistance. Measuring bone density alone, therefore, is insufficient to assess the bone's load-bearing capacity, and the spatial arrangement of the trabecular structure should be assessed, too.

Hence the need to develop innovative and low-cost diagnostic methods that can be used together with the consolidated systems.

## 2. The BESTEST<sup>®</sup>

The BESTEST<sup>®</sup>, Bone Elastic Structure Test, applies a patented technique [1] to virtually simulate the application of compressive loads on the trabecular architecture's reconstructions obtained from digital radiographs of the patient. Thus, the bone structure alterations due to osteoporosis can be detected and quantified, providing a low cost complement to the tools currently in use and assuring a better management of the patient [2].

Specifically, the BESTEST<sup>®</sup> processes the radiographic images of first proximal epiphyses of the non-dominant hand. The radiograms are acquired by a hand-held portable x-ray system equipped with a digital sensor like, for example, the NOMAD2PRO<sup>®</sup>, a lightweight (2.5 kg) device originally developed for intraoral radiography and the Gendex GXS-700 (Fig.2).



**Fig. 2.** Hand-held system (A) and digital sensor (B).

## 3. Hand-held radiology implications.

The recent introduction of handheld portable X-ray devices has brought new concerns in order to avoid any additional risk to the operator, patient or third party, compared with conventional radiography [3, 4]. While in certain cases these systems have been proved to present risks that are no greater than with

standard systems [5], and despite the use of a digital sensor ensuring that the required dose is minimized according to the ALARA (As Low As Reasonably Achievable) principle, the following issues must still be addressed in order to ensure a complete safety and repeatability of the exam:

1. the position of the handheld X-ray device relative to the operator has a significant effect on the overall radiation exposure received by the operator and it is crucial that the operator is positioned within the conical protective area, shown in Fig.3, created by the antiscatter shield with the beam in horizontal position [5];
2. with hand-held devices there is always a risk of misalignment and of displacing the X-ray units during exposure, that must be avoided;
3. patient protection requires the use of the smallest possible field size, besides the already mentioned choice of the sensor.
4. last but not least, the acquired image quality depends on the interaction among the X-ray device, exposure time, exposure geometry and image receptor. Given the fixed exposure time prescribed by the BESTEST® protocol, caution must be used to ensure a correct positioning of the sensor, which may affect the results of the subsequent image elaborations.

#### 4. Results

A special stand and a customized sensor holder have been designed in order to solve the aforementioned issues, as shown in Fig.3.



**Fig. 3.** Configuration of stand and sensor holder during the radiographic procedure.

The BESTEST® protocol requires the use of a rectangular collimator to further limit radiation exposure and to ensure the correct positioning of the beam with respect to the proximal epiphysis, that must appear at the center of the radiogram.

In Fig.4, two radiographic images of the same proximal epiphysis acquired respectively before (a) and after (b) implementation of the correctness criteria are depicted.

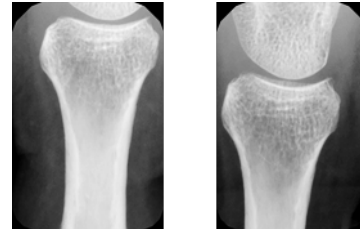


**Fig. 4.** Radiographic images before (a) and after (b) implementation of the correctness criteria.

#### 5. Remarks

- The stand correctly positions the operator with respect to the beam and behind the conical protective area, while allowing an easy operation of the equipment.
- By completely supporting the weight of the equipment, the stand also ensure stability of the equipment during acquisition.
- The customized holder minimizes patient's discomfort, while ensuring a correct positioning of the finger with respect to the sensor, and at the same time minimizing patient's discomfort.
- Safety for patient and operator and repeatability of the exam have been improved.

#### References

- [1] Cosmi F. USA Patent 7,386,154B2, 2008.
- [2] Cosmi F., Numerical Evaluation of Trabecular Bone Alterations: A Cell Method Application, MCB,12 (2), 2015, pp.87-105.
- [3] Berkhout W.E.R. et al. Justification and good practice in using handheld portable dental X-ray equipment: a position paper prepared by the European Academy of DentoMaxilloFacial Radiology, Dentomaxillofac Radiol, 44, 2015.
- [4] Makedissi J. et al. The effects of device position on the operator's radiation dose when using a handheld portable X-ray device, Dentomaxillofac Radiol, 45, 2016.
- [5] Goren A.D. et al., Radiation exposure with the NOMAD portable X-ray system,



34th Danubia-Adria Symposium on Advances in Experimental Mechanics  
University of Trieste, Italy, 2017



Dentomaxillofac Radiol, 37(2), 2008, pp.109-  
112

# CONCEPT OF THE NEW SYSTEM FOR THE MANDIBLE BASE FRACTURE FIXATION

Dominik Pachnicz<sup>1</sup>, Agnieszka Szust<sup>1</sup>

<sup>1</sup>Wroclaw University of Technology, Faculty of Mechanical Engineering, Wybrzeże Wyspiańskiego St. 27, 50-370 Wrocław, Poland. E-mail: [agnieszka.szust@pwr.edu.pl](mailto:agnieszka.szust@pwr.edu.pl)

## 1. Introduction

Mandible fractures are one of the most frequently occurring craniofacial trauma. Despite the fact that fixation techniques available nowadays give satisfying results, there is still need to search for new solutions. Complications and technical considerations related to those methods are still encountered. The aim of this article is to present concept of a fixation system for the mandible base fractures. Design of the system is modular, it consists of layered, 0,5 mm thick titanium mesh. Compared with commonly used miniplates, smaller thickness of components allows for greater adaptation to mandible bone geometry. The system can be adapted to all-embracing applications in cases of simple and comminuted fractures.

## 2. Methods

### 2.1 Models production and analysis details

The numerical mandible model was created on the base of polyurethane Synbone 8596 model of the mandible. Two volumes corresponding to materials of cortical and cancellous bone were generated. The cortical bone volume was obtained from laser scanning, cancellous was based on computer tomography results. Isotropic elastic properties - Young's Modulus and Poisson's Ratio were assigned to components. Finite element method (FEM) in Ansys 15.0 was utilized to solve number of boundary problems. Contact between mesh layers, bone- implant and between bone fragments were considered to be frictional. Strain intensity in the bone material, as well as von Mises stress values in designed elements are the index of the system effectiveness [1, 2]. Proposed fixation was also compared with recommended by AO Foundation techniques: double miniplate for simple and reconstruction plate for comminuted fracture case [3]. Additionally analysis of full, intact mandible was performed.

### 2.2 Simulation of mastication

The values of muscle forces were estimated to generate reaction force on the incisors circa 60 N, which is an average value of occlusal force 6 weeks after the operation. [4]. In the numerical calculation boundary conditions considered muscle forces and their directions. On the place of condylar process head zero displacement in all directions was assumed. Upward translation of incisors was fixed. Muscles were modeled as forces applied in the insertion places. Three elevator muscles of the mandible: masseter, temporalis and medial pterygoid were taken into consideration in the calculation. The scheme showing boundary condition and mandible loading is presented on Fig. 1.

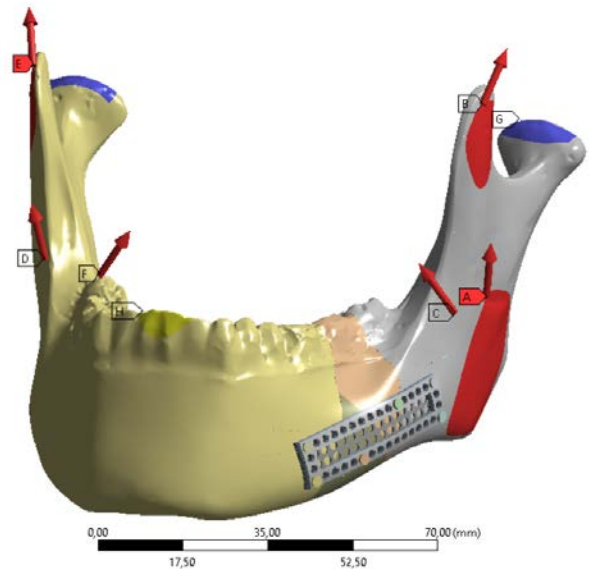
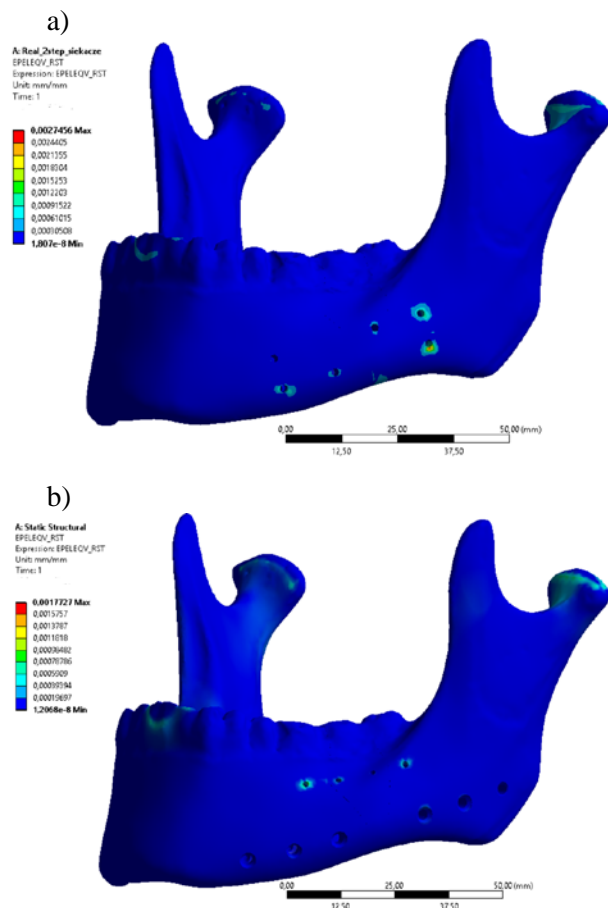


Fig. 1. Boundary conditions applied in mastication simulation: G-fixed support, A,D- masseter, C,F-medial pterygoid, B,E- temporalis, H- upward fixed

### 3. Results

The results show that the new construction is able to fulfill strength and stability requirements for carrying average occlusal forces occurring in mastication process during first few weeks after surgical procedure. The conditions in bone exhibit noticeable resemblance to standard implants and new system application. Exemplary comparison of simulation for comminuted case with use of new system and standard reconstruction plate is presented on the Fig. 2. The results of numerical analysis are presented in the Tab. 1. In all cases strain intensity in cortical bone did not exceeded threshold value above which microfractures and bone resorption is remarkable. Appearing in implant loads are under materials yield point.



**Fig. 2.** Comparison of strain intensity in cortical bone: a) conceptional system, b) standard method with reconstruction plate

Type of fixation and fracture type	Equivalent Elastic Strain [mm/mm]	Equivalent (von-Mises) Stress [MPa]
Standard simple	0,0011	85,15
Conceptional simple	0,0011	122,82
Standard comminuted	0,0018	187,52
Conceptional comminuted	0,0027	192,17

**Tab. 1.** Results of numerical analysis

### 4. Remarks

- This preliminary research constitutes the foundation for the further extended laboratory and numerical tests
- Obtained results suggest that proposed conceptional solution fulfills strength and deformation requirements for the element as well as stability condition for the bone

### References

- [1] Knoll W.D., Gaida A., Maurer P. Analysis of mechanical stress in reconstruction plates for bridging mandibular angle defects, *J. Craniomaxillofac. Surg.*, 2006, Vol. 34(4), 201–209.
- [2] Chladek W., Źmudzki J., Lipski T. Finite element analysis of mandible equilibrium depending on the way of its loading and supporting, *Acta of Bioengineering and Biomechanics*, 200, Vol. 2(1), 63–69.
- [3] <https://www2.aofoundation.org> (18.05.2017)
- [4] Tate G, Ellis E III, Throckmorton GS (1994) Bite forces in patients treated for mandibular angle fractures. *J Oral Maxillofac Surg* 52:734–736

## A NEW PROCEDURE FOR AUTOMATIC PATH PLANNING IN BRONCHOSCOPY

C. Ciobirca<sup>1</sup>, T. Lango<sup>2</sup>, G. Gruionu<sup>3</sup>, H.O. Leira<sup>4</sup>, L.G. Gruionu<sup>5</sup>, S.D. Pastrama<sup>1</sup>

- <sup>1</sup> University Politehnica, Department of Strength of Materials, Splaiul Independentei 313, Sector 6, 060042, Bucharest, Romania; e-mail: catalin.ciobirca@yahoo.com, stefan.pastrama@upb.ro
- <sup>2</sup> SINTEF Technology and Society, Department of Medical Technology, Olav Kyrres gate 9, Trondheim, Norway; e-mail: Thomas.Lango@sintef.no
- <sup>3</sup> Edwin L. Steele Laboratory for Tumor Biology, Harvard University, 55 Fruit Street Boston, MA 02114, USA; e-mail: ggruionu@steele.mgh.harvard.edu
- <sup>4</sup> St. Olavs Hospital, Department of Thoracic Medicine, Prinsesse Kristinas gate 3, Trondheim, Norway; e-mail hakon.o.leira@ntnu.no
- <sup>5</sup> University of Craiova, Department of Mechanics, Calea Bucuresti nr. 107, 200512, Craiova, Dolj County, Romania; e-mail: lgruionu@yahoo.com.

### 1. Introduction

Lung cancer can be diagnosed using a bronchoscopy procedure together with a biopsy from the affected area, performed using a forceps introduced through the working channel of the bronchoscope in order to obtain a tissue specimen from the prospective tumor location. Virtual bronchoscopy is a very useful tool that can be used for a proper planning of the real bronchoscopy or even to replace it if considered too invasive, for example in case of children [1]. Software applications for virtual bronchoscopy are based on the segmentation of the tracheobronchial tree from the medical image scan which is a difficult operation, both conceptually and from the computer implementation and running time point of view.

In this paper, a method for bronchoscopy procedure planning that does not require such a segmentation is presented.

### 2. Description of the method

The method is based on the discretization of the 3D reconstructed CT scan in voxels. A Hounsfield unit value corresponding to the gray scale from CT is assessed to each voxel. Airways tubes will be the voxels having the Hounsfield unit values of the air, taken in this research between  $-1100$  and  $-850$ . Based on the 3D image volume discretization, two geometric methods are implemented: i. A “line” tool that enumerates the voxels intersected by a certain line segment between two points and ii. A

“wave” tool that creates iteratively a certain wave surface centered on a fixed voxel and that enumerates the voxels of a specific wave generation.

In the set of 2D projections of the CT data, the user selects the starting point and the target point which will appear in the 3D image of the medical data. If, according to the Hounsfield value of the voxel containing the target point, this point is not inside the airways, it is projected using the wave tool iterator inside the “nearest” air tube. Then, a path is automatically generated through voxels containing Hounsfield values for air between the starting point and the projected target point using a modified version of the A\* algorithm [2]. The user validates the generated path by manual navigation through the lung airways, using the mouse.

### 3. Skin removal

The view of the lungs in the 3D reconstructed volume may be blocked by other body tissues that have similar Hounsfield value as the lungs. These layers can be removed from each slice considering the cylindrical organization of the chest volume on layers: skin (outside layer) – fat tissue (middle layer) – lungs tissue (inside layer). A view of the slices after skin removal is shown in Fig. 1.

### 4. Virtual navigation and collision detection

In this method, virtual navigation through the lungs and airways can be undertaken using a computer mouse with three buttons. The 3D visualization camera is rotated around its own axes

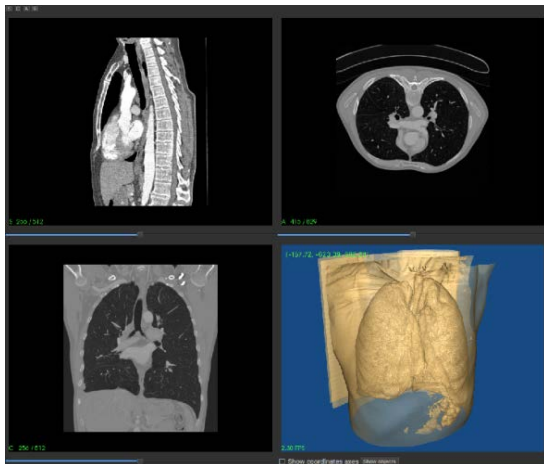


**Fig. 1.** Axial, sagittal, coronal slices and Lungs 3D view after "skin removal" algorithm is applied

with mouse drag operations, through quaternion computations that implement a method known as "arc ball" rotation. Once a mouse click and drag operation is started, the camera is rotated in such manner that the point in 3D space perceived under the mouse position when the operation is started will remain in the same position during dragging. Translations are done along the 3D axes perpendicular to the screen, and rotations can be performed around the same axes to better simulate the bronchoscope rotations. The camera view angle and other view parameters can be modified from the software application interface.

In order to constrain the visualization camera to remain always inside the airways, an algorithm for collisions detection and resolution is used. The algorithm is adapted from the one presented in [3], with the main improvement that, in the new one, there is no segmentation of the airways. Only the Hounsfield values for the voxels and the "line" tool iterator are used to detect the collision and to find the position where the camera trajectory intersected the lungs tissue. For the collision resolution, the gradient in the collision place is used to move camera back "inside" the airways tube.

### 5. A\* algorithm and automatic path

The A\* algorithm tries to find the shortest path from a starting voxel to a destination voxel iterating from one neighbor voxel to another until the destination is reached.

For virtual bronchoscopy, it is important to find the airways tubes that form the path from the trachea to the area of interest. An automatic path and the manual validation are shown in Fig. 2.



**Fig. 2.** Automatic generated path, yellow, and manually validation with virtual bronchoscopy, red

### 6. Conclusions

In this paper, a method for path planning in bronchoscopy interventions is described. The method has the advantage that it does not need segmentation of the tracheobronchial tree from the medical image scan. The procedure is very easy to use and navigation through airways can be performed using only the computer mouse.

Together with a system for tracking the bronchoscope during the real procedure, this method can improve the diagnostic success rate and decrease the discomfort perceived by the patient.

### Acknowledgements

This research has received funding from EEA Financial Mechanism 2009 - 2014 under the project EEA-JRP-RO-NO-2013-1-0123 - Navigation System For Confocal Laser Endomicroscopy To Improve Optical Biopsy Of Peripheral Lesions In The Lungs (NaviCAD), contract no. 3SEE/30.06.2014.

### References

- [1] De Wever, W., Bogaert, J., Verschakelen, J.A., Virtual Bronchoscopy: Accuracy and Usefulness - An Overview, *Semin Ultrasound CT MR*, 26, 2005, pp. 364–373.
- [2] A\* search algorithm. (2017, April 27). Retrieved April 30, 2017, from [https://en.wikipedia.org/wiki/A\\*\\_search\\_algorithm](https://en.wikipedia.org/wiki/A*_search_algorithm)
- [3] Ciobirca, C., Popa, T., Gruionu, G., Lango, T., Leira, H.O., Pastrama, S.D., Gruionu, L.G., Virtual bronchoscopy method based on marching cubes and an efficient collision detection and resolution algorithm, *Ciência & Tecnologia dos Materiais*, 28, 2016, pp. 162-166.

# EFFECTS OF PERTURBATION DIRECTION ON SINGLE-LEG STANCE BALANCE RECOVERY PERFORMANCE

Balint Petro<sup>1</sup>, Rita M. Kiss<sup>1</sup>

<sup>1</sup> Budapest University of Technology and Economics, Department of Mechatronics, Optics and Mechanical Engineering Informatics. Bertalan L. Street 4-6, Budapest, Hungary H-1111. E-mails: [petro@mogi.bme.hu](mailto:petro@mogi.bme.hu); [rikiss@mail.bme.hu](mailto:rikiss@mail.bme.hu)

## 1. Introduction

The assessment of balancing abilities is an integral part of orthopaedic and physiotherapeutic evaluation. There is a need to test abilities associated with complex coordination as stabilizing posture and recovery of balance after a sudden perturbation. A widely used therapeutic and diagnostic method is to apply a sudden unidirectional perturbation on a free oscillating platform. Following the perturbation, the participant instinctively attempts to regain postural balance. This balancing acts as a damping agent to decrease and eventually stop the oscillation. Previous works suggested that different balance recovery strategies can be observed based on stance, personal abilities and sports background [1]. The goal of our current study is to evaluate the effect of the medio-lateral (ML) perturbation direction on balancing performance in a single-leg stance. We hypothesize that one of these directions is more difficult to recover from and the successful completion of both directions can be associated with superior balancing abilities.

## 2. Methods

### 2.1 Participants

Thirty-two young collegiate men (age:  $22.8 \pm 1.3$  yrs, height:  $182.3 \pm 7.1$  cm, body weight:  $76.9 \pm 10.4$  kg) participated in sudden perturbation balance measurements. Exclusion criteria included any pathological condition of the central nervous system or the musculoskeletal system. The tests were authorized by the Science and Research Ethics Committee of Semmelweis University (174/2005) and written consent was obtained from participants.

### 2.2 Procedure

The free oscillating platform PosturoMed® (Haider Bioswing, Weiden, Germany) was used to deliver sudden unidirectional perturbations as previously described in [2]. Direction of

perturbation depends on the direction of the stance with respect to the fastening apparatus. Please note that the perturbation direction is the opposite of the initial platform motion.

Balance regain tasks were carried out in bipedal and single-leg stances standing on the preferred (dominant) leg. The balancing task was repeated with the participant facing in all four directions to change the direction of perturbation. For this study, only ML perturbation during single-leg stance was considered: the lateral (L, towards the outer edge of the body) or contralateral (CL, towards the raised leg) nature of the test was noted. Participants were allowed up to three trials to complete each balance regain successfully with the goal of two successful attempts facing every direction and in both (bipedal and single-leg) stances. Participants unable to perform the single-leg task in none of L or CL directions were excluded from this study.

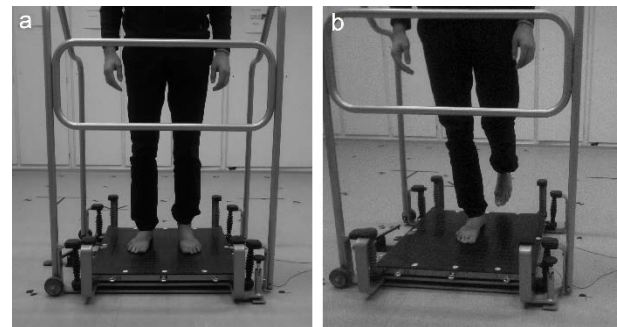


**Fig. 1.** Measurement setup: a) bipedal stance; b) single-leg stance

### 2.3 Data collection and analysis

Motion of the platform was captured with sub-millimetre precision using an OPTITRACK (NaturalPoint Inc., Oregon, USA) infra-red 18 camera motion capture system with passive reflecting markers at a frame rate of 120Hz. The calculated parameters were damping time ( $T_{end}$ ), path length in AP and ML directions ( $S_x$ ,  $S_y$ ), total path length ( $S_{xy}$ ), directional ratio ( $R$ ) defined by the AP-ML path length ratio, and Lehr's damping factor ( $D$ ). Boxplots were created and independent

samples t-tests were carried out using MatLab (The MathWorks Inc., Natick, Massachusetts, USA).

### 3. Results

The number of targeted successful balance recoveries were 128 for the whole group, of which 98 attempts were successful: 61 out of 68 (90%) in L direction and 37 out of 68 (54%) in CL direction. The results of independent samples t-tests (**Tab. 1**) shows that the end time and damping of balance recovery are statistically similar for L and CL directions but the travelled path and the trajectory of balancing are significantly different ( $p=0.001$ ). This means that different balancing strategies with similar effectiveness are used depending on the direction of perturbation.

single-leg: L vs. CL	equal variances	df	Sig. (2- tailed)
$T_{end}$	assumed	96	0.112
$D$	assumed	96	0.690
$S_{xy}$	not assumed	91.7	<b>0.001</b>
$R$	not assumed	45.5	<b>0.001</b>

**Tab. 1.** Results of independent samples t-tests: L vs. CL directional perturbation

The rate of successful attempts suggest that the CL perturbation is more difficult to recover from when single-leg stance must be maintained. However, the end time and the path length (**Fig. 2**) have smaller variations with CL perturbation, showing consistently more effective balancing. This suggests that participants who can recover from CL perturbations have superior balancing abilities than those who can recover only from L perturbations.

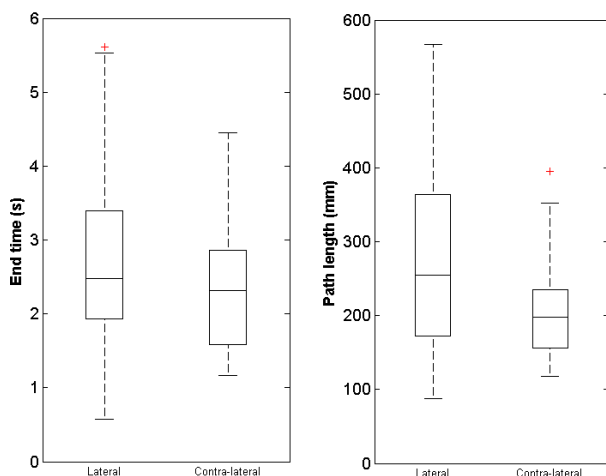


**Fig. 2.** Box-plots of end time and path length for lateral and contra-lateral perturbations

To test for possibly superior balancing abilities, the participants were sorted into two groups: 'group A' for those who could recover in both directions ( $n=17$ ) and 'group B' who could not ( $n=15$ ). Single-leg L perturbation recoveries were compared with t-tests (**Tab. 2**). End time and path of recovery were significantly lower ( $p=0.012$  and  $p=0.014$ , resp.) for 'group A'. This can be quantitative proof that participants able to recover from CL perturbations have indeed superior balancing abilities.

single-leg, L, group A vs. B	equal variances	df	Sig. (2- tailed)
$T_{end}$	assumed	59	<b>0.012</b>
$D$	assumed	59	0.108
$S_{xy}$	not assumed	48.6	<b>0.014</b>
$R$	assumed	59	0.193

**Tab. 2.** Results of independent samples t-tests: L directional perturbation for group A vs. group B

### 4. Remarks

- It was shown that recovering from a contra-lateral perturbation is more difficult than recovering from a lateral perturbation and this may require a different recovery strategy.
- Participants who were able to recover from contra-lateral perturbations showed significantly better balancing abilities in the lateral direction as well.
- A future study can aim at identifying different recovery strategies used following lateral and contra-lateral perturbation directions.

### Acknowledgements

The authors would like to thank Alexandra Papachatzopoulou for her help with conducting the measurements. This project was supported by the Hungarian Scientific Fund (K083650).

### References

- [1] Petró B, Nagymáté G, Kiss RM. A new method in dynamic balancing capability evaluation. In: 22nd Congress of the European Society of Biomechanics, Lyon, France. 2016.07.10-13. Paper 79-1734-1. 1 p.
- [2] Kiss RM. A new parameter for characterizing balancing ability on an unstable oscillatory platform. Medical Engineering & Physics. 2011. doi:10.1016/j.medengphy.2011.04.017

# DETERMINATION OF DIFFERENCE BETWEEN SIMILAR POLYMER MODELS SIMULATING THE BEHAVIOUR OF BIOLOGICAL TISSUES

Barbara Kmiecik<sup>1</sup>, Jerzy Detyna<sup>1</sup>

<sup>1</sup> Wroclaw University of Science and Technology, Department of Mechanics, Materials Science and Engineering, Smoluchowskiego str, 25, 50370, Wroclaw, Poland.  
e-mail: [barbara.kmiecik@pwr.edu.pl](mailto:barbara.kmiecik@pwr.edu.pl), [jerzy.detyna@pwr.edu.pl](mailto:jerzy.detyna@pwr.edu.pl)

## 1. Introduction

Biological tissue can be characterized by time – dependent behaviour [1]. During the stress analysed material deforms and after removing load factor it return to initial state [2]. Generated curve is called hysteresis and is characteristic for viscoelastic nature of biological tissues [3]. This behaviour can be observe by cameras and analysed by image processing algorithms like digital image correlation or optical flow [4].

## 2. Materials and methods

Studied were made in a special design system. The stand consists of two high-speed cameras and their setup, a stationary part (camera stand), a robotic arm, and a microcontroller with sensors. All parameters included in the equipment were selected according to the literature and to the expected measurement possibilities. In Fig. 1 was presented camera configuration.

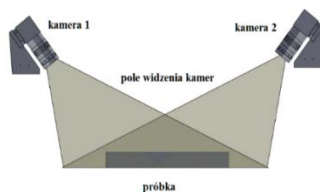


Fig. 1. Camera configuration in designed system.

The measuring system was designed to deflect the sample at central region and analyse the changes occurring on its surface during mechanical stress (Fig. 2).

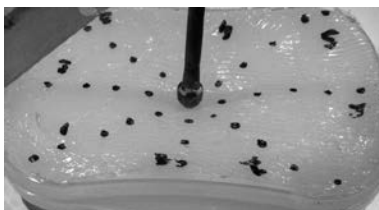


Fig. 2. Analysed sample during the measurement

Then, on the basis of the tracked points, the surface of the analysed sample was reconstructed (3D). It allows to determine the real displacement (in all dimensions) and create the displacement-force curve. The area of the resulting hysteresis is a measure of the energy absorbed by the material during mechanical stress, and its decomposition may suggest potential local rigidities.

Comparison of silicone layer (thickness 15 mm) (SL) and silicone layer (thickness 15 mm) with 1 mm NBR rubber elements (SL+NBR) (Fig. 3) was investigate in this study.

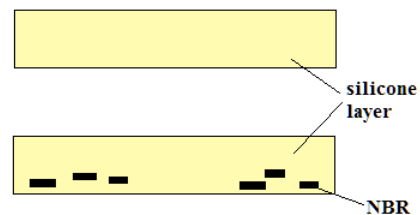


Fig. 3. Visualization of studied samples.

## 3. Results

After measurements the changes of points position on the surface were analysed by optical flow algorithm. This data let to determinate X, Y and Z coordinates of marks and generate displacement-force curve (Fig. 4.).

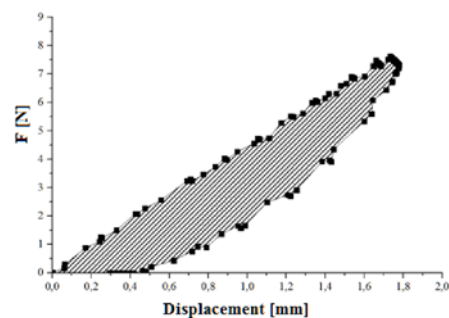


Fig. 4. Visualization of studied samples

Presented relationship let to determine the energy absorbed by the material during mechanical stress as the hysteresis area. Obtained results are presented in Tab. 1.

**Tab. 1.** Example of average results for a several points for analysed sample

	r [mm]	A [N*mm]	SD [N*mm]	CV [%]
SL	10	2,76	0,54	19,65
	17	1,46	0,18	12,44
	24	0,87	0,26	29,49
	31	0,71	0,1	13,37
	38	0,7	0,06	9,03
SL+NBR	10	3,07	0,28	9,2
	17	1,09	0,17	15,52
	24	0,76	0,08	9,93
	31	0,76	0,04	5,38
	38	0,54	0,07	11,05

Legend: A – hysteresis area, r – distance from centre of the sample, SD – standard deviation CV - coefficient of variation

Average hysteresis area allow to determine distribution map of energy absorbed by analyse sample. Example of obtained maps are presented in Fig. 5. and Fig. 6..

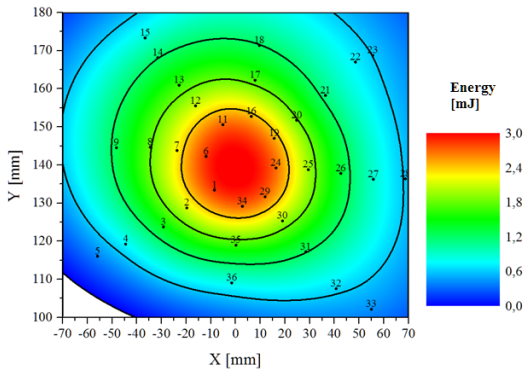


**Fig. 5.** Distribution map of absorbed energy by SL

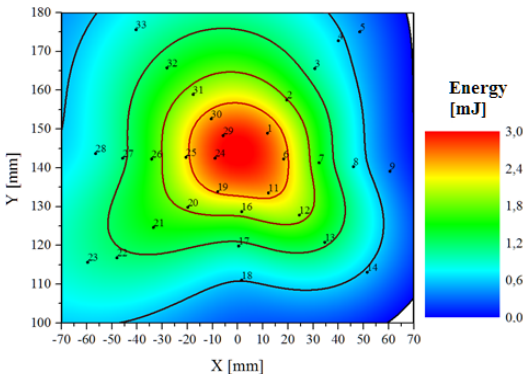


**Fig. 6.** Distribution map of absorbed energy by SL+NBR

Analysis of Fig. 6 let to successful determine region with NBR components.

#### 4. Conclusion and summary

Presented measurements system and experimental method show that it is possible to analyse the continuity of the structure on the basis of the surface observation under the influence of mechanical force.

The presented method is cheaper ,faster and the results obtained are easily interpretable.

Further studies are needed to fully understand proposed method.

#### References

- [1] M. Meyers, P. Chen, A. Lin, and Y. Seki, “Biological materials: structure and mechanical properties,” Prog. Mater. Sci., 2008.
- [2] A. Natali, P. Pavan, E. Carniel, P. Dario, and I. Izzo, “Characterization of soft tissue mechanics with aging,” IEEE Eng. Med. Biol. Mag., 27, 2008, pp. 15–22..
- [3] Y.-C. Fung, Biomechanics : Mechanical Properties of Living Tissues. Springer New York, 1993.
- [4] J. N. Reddy, An introduction to continuum mechanics : with applications. Cambridge University Press, 2008.

# EXAMINATION OF SAILORS' BALANCING ABILITY CONSIDERING THE ROLE OF THE HEAD MOVEMENT

Bernadett Kiss<sup>1</sup>, Gergely Nagymáté<sup>1</sup>, Rita M Kiss<sup>1</sup>

<sup>1</sup> Budapest University of Technology and Economics, Dept of Mechatronics, Optics and Mechanical Engineering Informatics, Műegyetem rakpart 3, Budapest 1111, Hungary. E-mails: bettgo95@gmail.com, nagymate@mogi.bme.hu, rikiss@mail.bme.hu

## 1. Introduction

Human is an unstable system unless a control system is continuously acting [1]. This control system is characterized by the balancing ability. The present study examines the dynamic balancing ability using ultrasound-based provocation tests.

Three major sensory systems are involved in balance: vision, the vestibular system, and the somatosensory system. When upright human stance is perturbed, the vestibular system in the inner ear transmits the related signals to the brain. In the study, the movement of the head was considered as a crucial determinant of the balancing capability. The head is a natural frame of reference for action since it contains the two most important perceptual systems for detection of self-motion relative to space, the visual and vestibular systems [2].

During sailing the sportsmen have to face a continuously changing environment. This could be responsible for establishing a common sailor balancing ability. The present study aims to determine differences in the dynamic balancing method of professional sailors compared to the method of a non-sailor control group.

## 2. Methods

### 2.1 Subjects

Subjects involved in the study were professional sailors, who have been competing in sailing in at least the last 3 years, and a non-sailor control group, who haven't competed in any sports. Exclusion criteria were locomotor disorders for both groups.

The sailor group included 3 women and 8 men ( $n = 11$ ; average age:  $17.73 \pm 3.32$  years; average height:  $171.95 \pm 10.63$  cm; average body mass:  $66.85 \pm 12.23$  kg). The control group consisted of 3 women and 8 men ( $n = 11$ ; average age:  $20.91 \pm 1.45$  years; average height:  $176.32 \pm 10.81$  cm; average body mass:  $76.47 \pm 22.37$  kg). Each subject provided informed written consent to participation in the tests and information about their sailing/sporting practice (duration,

regularity, best results on sailing competitions (only for the sailor group), injuries of the locomotor system)

### 2.2 Experimental protocol

Balancing capacity after sudden perturbation was modelled using a PosturoMed<sup>®</sup> (Haider-Bioswing, Weiden, Germany) device (Fig. 1). The rigid platform (60 cm  $\times$  60 cm) is connected to a rigid frame by 8 steel springs with identical strength. The number of working springs (4, 6, or 8 springs) can regulate the displacement characteristics of the platform. The four-spring system was selected for use with both groups. The movement of the platform was recorded with Zebris<sup>®</sup> (ZEBRIS GmbH, Isny, Germany) CMS 10 system using active single ultrasound-based markers attached to the side of the platform. The measuring frequency was 50 Hz. The recorded coordinates of the platform were documented on computer using the original WinPosture (Zebris MedizinTechnik, Germany) software. The details of measuring method could be found in [3]. The movement of the subject's head was recorded by the Optitrack Motion Capture camera system (NaturalPoint, Inc. DBA OptiTrack), consisting of 18 calibrated cameras (Flex 13). The subject wore a well-fixed safety helmet, to which markers were attached (Fig. 1). The cameras recorded the 3D-coordinates of the markers at a frequency of 120 Hz, which were documented by the original Motive<sup>®</sup> (NaturalPoint, Inc. DBA OptiTrack) software and exported by the Fukuda gait test measuring software (developed in our motion lab). The two software were synchronized.

Prior the measurement the platform was moved 20 mm in medio-lateral direction and locked by a fastening/provocation unit. By releasing the unit, the plate swings back into its resting position (Fig 1). The participant should counterbalance this sudden disturbance, so that the oscillated device with a participant on it is a damped system [3]. The measurements involved the standardized double-limb position with eyes closed on the plate with 4 working springs.

### 2.3 Data processing and statistical analysis

Raw measurement data was exported from the WinPosture and Fukuda software and processed by a Wolfram Mathematica (Wolfram®, v11.0) algorithm (developed in our lab). From the processed data, the parameters were calculated with the use of Wolfram Mathematica (Wolfram®, v11.0) and Matlab (MathWorks®, R2014a) algorithms (developed in our lab). The considered parameters were:

- *HeadYMinmax* and *HeadXMinmax*: The difference between the maximum and minimum values of the head coordinates in *Y* (antero-posterior: *AP*) and *X* (medio-lateral: *ML*) directions.
- *PlatYMinmax* and *PlatXMinmax*: The difference between the maximum and minimum values of the platform coordinates in *Y* and *X* directions.
- *AbsDiffMax\_Y* and *AbsDiffMax\_X*: The difference of the head and platform coordinates (both *X* and *Y*) were calculated for the whole measurement. The absolute maximum of these differences were considered as parameters.

For each parameter, the mean and standard deviation were calculated. To separately test the between subject effect of each parameter univariate test results were also considered in the evaluation. Level of significance was set to  $p=0.05$ . The statistical analysis was carried out using IBM SPSS Statistics 22® software.

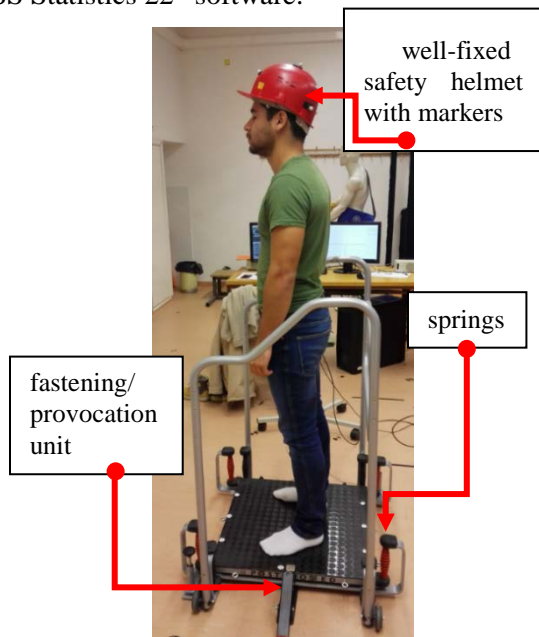


Fig. 1. Double-limb standing with eyes closed on the PosturoMed® device

### 3. Results

Some measurements had to be excluded from the study, because of the errors of the ultrasound based measuring system. The measurements could be evaluated for 7 sailors and 11 control people.

Considering the *HeadYMinmax* parameter, significant difference ( $p=0,039$ ) shows between the sailor and the control group (Tab. 1.). The magnitude of the head movement in *AP* direction was significantly larger in the sailor group.

Parameter	Sailor group - Mean (SD)	Control group - Mean (SD)	Between subject effect - $p$	Observed Power
<i>HeadXMinmax</i>	18,93 (3,27)	23,32 (2,96)	,334	,156
<i>HeadYMinmax</i>	25,19 (3,44)	14,88 (3,11)	<b>,039</b>	,557
<i>PlatXMinmax</i>	34,04 (0,52)	32,67 (0,47)	,068	,451
<i>PlatYMinmax</i>	5,54 (0,96)	5,52 (0,87)	,984	,050
<i>AbsDiffMax_X</i>	22,48 (2,90)	24,19 (2,63)	,666	,070
<i>AbsDiffMax_Y</i>	23,10 (3,61)	13,85 (3,26)	,073	,436

Tab. 1. Results of statistical analysis (**Bold**: significant difference, where  $p < 0.05$ )

### 4. Remarks

The increasing magnitude of the head movement means, that the sailor group actively interfered with the *ML* oscillation by moving their heads in *AP* direction. This could show a more advanced balancing ability in the case of the sailor group. The balancing method of the sailor group and the control group is significantly different.

### Acknowledgements

This work was supported by the Hungarian Scientific Research Fund OTKA [grant number K115894]

### References

- [1] D. A. Winter, Human balance and posture control during standing and walking, *Gait&Posture*, 3, 1995. pp. 193-214.
- [2] Pozzo, T., Berthoz, A., & Lefort, L., Head Stabilization during Various Locomotor Tasks in Humans. 1. Normal Subjects. *Experimental Brain Research*, 82(1), 1990. pp. 97-106.
- [3] R. M. Kiss, A new parameter for characterizing balancing ability on an unstable oscillatory platform, *Medical Engineering & Physics*, 33, 2011. pp. 1160-1166.

# LYPHHEDEMA TREATMENT'S EFFECT OF GAIT PARAMETERS

**Zsofia Palya<sup>1</sup>, Katalin Hampel,<sup>2</sup> Rita Kiss M<sup>1</sup>.**

<sup>1</sup> Budapest University of Technology and Economics, Department of Mechatronics, Optics and Mechanical Engineering Informatics, Muegyetem rkp. 3., Budapest, 1111 Hungary.  
E-mails: [palyazsofia@gmail.com](mailto:palyazsofia@gmail.com) ; [rita.kiss@mogi.bme.hu](mailto:rita.kiss@mogi.bme.hu)

<sup>2</sup> National Institute of Medical Rehabilitation, Szanatorium u. 1., Budapest, 1121 Hungary.  
E-mail: [katalin.hampel@gmail.com](mailto:katalin.hampel@gmail.com)

## 1. Introduction

Lymphedema is the swelling caused by the accumulations of lymph, which may occur if the lymphatic system is damaged. As a result of the damaged functioning some protein rich fluid escape the body's tissue (Fig. 1.). It can affect any part of the body, but usually develops in the limbs and the fingers. The disease affects the locomotion system, therefore it can be assumed that it decreases the effectiveness of the gait parameters and causes malfunction. [1]



**Fig. 1.** A lymphedemic foot in Stage 3.

Unfortunately, there is no any conventional practice to observe the effectiveness of the lymphoedema management. Therefore, the aim of this research is to construct a well defined process offering an opportunity to have this ability.

## 2. Methods

The purpose of this paper is to analyze how the specialized treatment, which was developed in the National Institute of Medical Rehabilitation, changes the overall picture of gait. The 23 examined patients were in different phases of the condition (stage 1., 2. and 3.). Before and after the therapy a pilot study was executed in order to observe the gait parameters. The measurement was performed on an instrumented treadmill with

optional velocity. Applying the data of the treadmill equipped with pressure-measuring sensors, we were able to calculate the force awaking in the forefoot, the midfoot and the heel on both legs, furthermore, the butterfly parameters and gait parameters such as stance phase, swing phase, load response ect., which are illustrated in Fig. 2. During the experimentation the simplified kinematical parameters (e.g. geometry and timing parameters) were defined by the Zebris processing program. The geometry parameters are presented in Fig. 3.

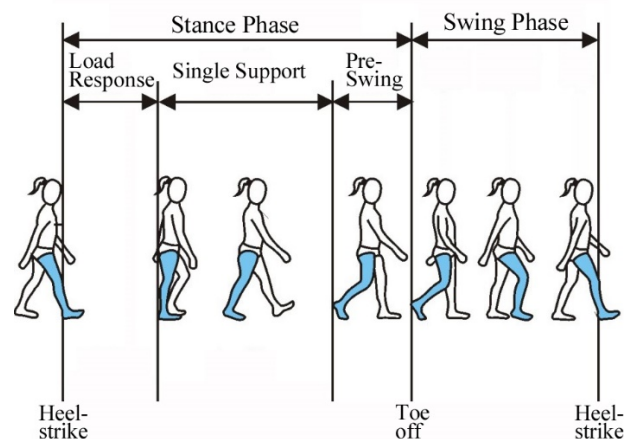


**Fig. 2.** Basic gait parameters during one stride. [2]

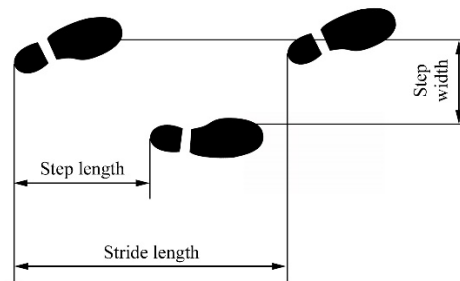


**Fig. 3.** Geometry parameters during one stride.

One-sample t-tests were performed to define the treatment's effectiveness. Moreover, independent two-sample t-tests were applied to compare the different phases of the condition.

There were some patients with one side injured leg, in this case the differences between the healthy and the damaged side were examined using one-sample t-tests. The determining factor was 0.05 in both cases.

### 3. Results

The results could be detached in two ways. Firstly, the average gave information about the overall picture of gait. On the other hand, using the coefficient of variation (CV) calculated by the average and deviation data the regularity of the gait could be estimated.

Observing the both side injured patients apart from the phases of conditions the therapy primarily influenced the kinematical parameters (Tab. 1.). Taking into consideration the seriousness of the disease, the results showed that the various treatments did not affect in the same way. In Stage 1. the regularity of the gait was mending while in case of patients with more serious (Stage 2. and 3.) lymphedema the kinetical parameters were changed significantly especially the average values. Some of these changes are summarized in Tab. 2.

	step length	stride length	cadence	length of gait line
average	0.0373	-	-	0.0209
CV [%]	-	0.0291	0.0365	0.0226

**Tab. 1.** Significant differences when the treatment's effectiveness were observed.

#### Significant differences in Stage 1.

	foot rotation	swing phase
average	-	-
CV [%]	0.0352	0.0455

#### Significant differences in Stage 2. and 3.

	force backfoot (left leg)	force backfoot (right leg)	length of gait line
average	0.0157	0.0027	0.0241
CV [%]	-	-	-

**Tab. 2.** Significant differences when the treatment's effectiveness were observed in variant stages.

Compared to the healthy and damaged side in case of one side injured patients it could be assumed that both the regularity and the overall picture of gait were mending on the intact side. Probably, the corrective-gymnastic part of the

therapy was enough to develop the healthy leg, but not enough to improve the diseased.

Finally, comparing the different phase of the condition the progress of the lymphedema could be traceable. Several differences are showed in Tab. 3. In sum, the seriousness of the disease affected the butterfly parameters as a result in stance phase the weight transmission changed significantly. This accomplishment is in accordance with the result of the obese patients' gait analysis. [3]

#### Before the therapy:

	step length	single support line	length of gait line
average	-	0.0190	-
CV [%]	0.0435	-	0.0343

#### After the therapy:

	load response	ant/pos position	length of gait line
average	0.0335	-	-
CV [%]	-	0.0096	0.0393

**Tab. 3.** Significant differences comparing the phase of condition.

### 4. Conclusions

In this paper we declare that the seriousness of the lymphedema significantly influences the kinematical and kinetical gait parameters. As a result of the treatment some improvement were observed. In conclusion, our results provide that the disease modifies the gait parameters, and the effectiveness of lymphedema management is exceedingly traceable with a pilot study.

### Acknowledgements

This research is contribution to the Hungarian Scientific Research Found project Nr. 115894.

### References

- [1] C.J. Moffatt, P.J. Franks, D.C. Doherty, A.F. Williams, C. Badger, E. Jeffs, N. Bosanquet, P.S. Mortimer.: Lymphoedema: an underestimated health problem, QJM, 2003. 96 (10): 731-738.
- [2] Rita Kiss M.: Biomechanikai módszerek a csípőízületi kopás hatásának vizsgálatára (Biomechanical methods for observing the effects of hip coxarthrosis). DSc thesis, 2012
- [3] C. Lai, P. P., Leung, A. K., Li, A. N., Zhang, M.: Three-dimensional gait analysis of obese adults. Clinical Biomechanics, 2008.



34th Danubia-Adria Symposium on Advances in Experimental Mechanics  
University of Trieste, Italy, 2017



# NON-INVASIVE METHOD FOR PARAMETER IDENTIFICATION IN A LUMPED MODEL OF PULMONARY CIRCULATION

Fabijan Lulić<sup>1</sup>, Zdravko Virag<sup>2</sup>, Ivan Korade<sup>2</sup>, Marko Jakopović<sup>1</sup>

<sup>1</sup> University of Zagreb, Pulmonary Disease Clinic, Jordanovac 104, 10000 Zagreb, Croatia. E-mails: [fabijan.lulic@kbc-zagreb.hr](mailto:fabijan.lulic@kbc-zagreb.hr), [marko.jakopovic@kbc-zagreb.hr](mailto:marko.jakopovic@kbc-zagreb.hr)

<sup>2</sup> University of Zagreb, Faculty of Mechanical Engineering and Naval Architecture, Ivana Lučića 5, 10000 Zagreb, Croatia. E-mails: [zdravko.virag@fsb.hr](mailto:zdravko.virag@fsb.hr), [ivan.korade@fsb.hr](mailto:ivan.korade@fsb.hr)

## 1. Introduction

Understanding of function of the right heart and pulmonary circulation becomes more and more important in treatment of cardiac and pulmonary diseases [1]. Hemodynamic data for examination of pulmonary circulation are usually obtained invasively which is unacceptable in healthy subjects. That is why we need a non-invasive clinical method for estimation of pulmonary circulation function, which would be suitable for all subjects (with normal function and with cardiorespiratory diseases).

The aim of this work is to define a lumped model of pulmonary circulation and to define a method for parameter identification of this model, based on non-invasive (Echocardiography) measurements of velocity profiles through heart valves.

## 2. Methods

### 2.1 Mathematical model

Fig. 1 schematically shows the right heart, pulmonary artery, lungs, pulmonary veins and left atrium, as well as the electrical analogue scheme of the proposed lumped model of the pulmonary circulation. Resistor  $R$  models the total pulmonary vascular resistance, capacitors  $C$  and  $C_1$  model compliances of proximal and distal chambers,  $L$  represents the inertial effects between chambers,  $\eta$  is the wall resistance of the proximal chamber (the Voigt model) and  $Z$  models the impedance of the rest of the system. For given model parameters and input pulmonary valve flow ( $Q_{pv}=v_{pv}A_{pv}$ ), it is possible to calculate pulmonary root pressure ( $p_{PA}$ ). When  $p_{PA}$  is measured it is possible to find optimal values of model parameters which

minimize the RMS error between measured  $p_{PA}$  and  $p_{PA}$  from the model.

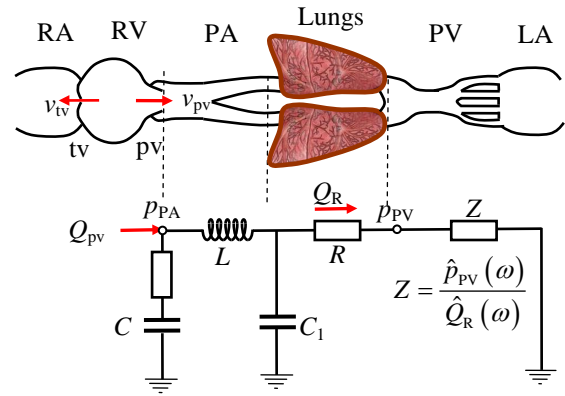


**Fig. 1.** Schematic representation of the pulmonary circulation and electrical analogue scheme of its lumped mathematical model. RA/RV = right atrium/ventricle, PA/PV = pulmonary arteries/veins, LA = left atrium, tv/pv = tricuspid/pulmonary valve,  $Z$  = impedance,  $\omega$  = circular frequency.

### 2.2 Measurements

By using Echocardiography it is possible to measure pulmonary valve ( $v_{pv}$ ) and tricuspid regurgitant blood velocity ( $v_{tv}$ ). In each case several measurements were recorded and the average profiles are calculated. The “measured”  $p_{PA}$  is obtained from unsteady Bernoulli equation

$$p_{PA}^B = p_{RA} + \frac{1}{2} \rho v_{tv}^2 - \frac{1}{2} K \rho v_{pv}^2 - \rho l \frac{dv_{pv}}{dt}, \quad (1)$$

where  $K$  and  $l$  are the minor loss coefficient and inertial length through the pulmonary valve,  $p_{RA}$  is the average right atrium pressure, which is estimated from the width of vena cava inferior. Similarly, the average pressure in pulmonary veins ( $p_{PV}$ ) is estimated from the mitral inflow pattern. The stroke volume calculated from the pulmonary and aortic valve velocity should be the same

$$V_{\text{stroke}} = \int_0^{T_{ej}} v_{pv} A_{pv} dt = \int_0^{T_{ej}} v_{av} A_{av} dt \quad (2)$$

where  $T_{ej}$  is the ejection time. Since the aortic valve area can be measured more precisely, we calculate  $A_{pv}$  indirectly from Eq. (2).

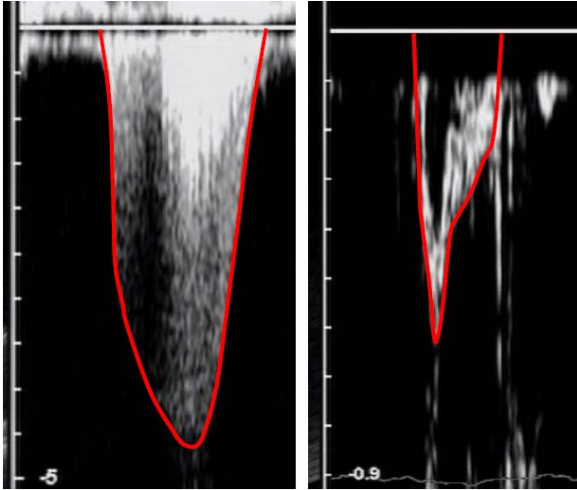


Fig. 2. Example of Doppler regurgitant tricuspid (left) and pulmonary velocity (right). Red lines are plotted for a digitization purpose.

### 2.3 Parameter identification

First, the pulmonary artery input impedance  $Z_{in} = \hat{p}_{PA} / \hat{Q}_{pv}$  (the ratio of the pressure and flow phasors defined by the Fourier series) is calculated, and then, based on measured  $Q_{pv}$  the  $p_{PA}^{WK5}$  is obtained. This pressure is compared with the  $p_{PA}$  defined by Eq. (1), and the error defined as

$$RMSE = \sqrt{\frac{1}{N} \sum_{i=1}^N (p_{PA}^{WK5} - p_{PA})^2}, \quad (3)$$

where  $N$  is the number of points within the ejection time ( $T_{ej}$ ) is minimized.

### 3. Results

The method was applied to an elderly patient with pulmonary arterial hypertension with following data: Cardiac Output: 5 l/min, Heart Rate 78 beat/min, pulmonary valve diameter  $D_{pv} = 2.73$  cm, isovolumic contraction of RA  $t_{ivc} = 34.4$  ms,  $p_{RA} = 5$  mmHg,  $p_{RA} = 10$  mmHg,  $l = 1.53D_{pv}$ ,  $K = 1$ . Fig. 3 shows measured pulmonary flow, and comparison of measured and calculated pressure during  $T_{ej}$ . The  $p_{PA}^{WK5}$  from the model describes “measured” pressure very well, and shows incisure immediately after pulmonary valve closing. Fig. 4.

shows the pulmonary input impedance, and the values of model parameters that minimize RMSE. The absolute value of  $Z_{in}$  shows minimum, and zero crossing frequency of the phase angle is 5.4 Hz, what is in good agreement with observations for elderly subjects.

### 4. Remarks

The proposed method is capable to accurately identify PA model parameters and input impedance of pulmonary circulation by using the pressure data from the ejection time window only.

The method is limited to the subject with nicely obtainable tricuspid regurgitant velocity and pulmonary valve flow.

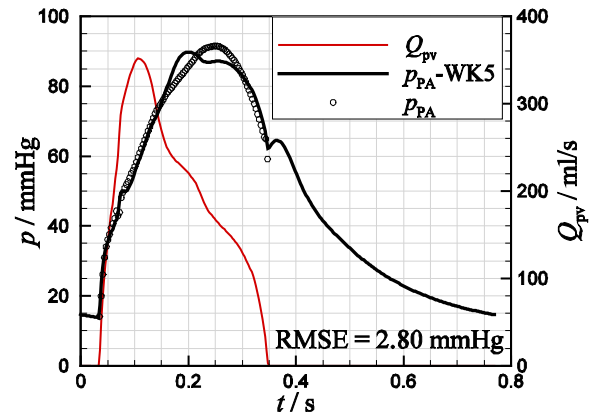


Fig. 3. Velocity through the pulmonary valve (thin red line), “measured” pulmonary root pressure from Eq. (1) (circles), and pulmonary root pressure from the five element lumped model (thick black line).

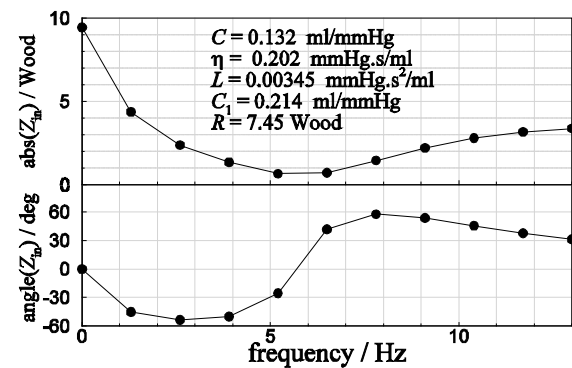


Fig. 4. Upper diagram shows the absolute value of pulmonary input impedance, and the lower one shows its phase angle.

### References

- [1] Peacock, A.J., Naeije, R., Rubin, L.J., Pulmonary circulation: Diseases and their Treatment. Hodder Arnold, 3<sup>rd</sup> ed., 2011.

# EVALUATION OF ANATOMICAL LANDMARK CALIBRATION ACCURACY OF A MOTION CAPTURE BASED GAIT ANALYSIS SYSTEM

Kristóf Rácz<sup>1</sup>, Zsófia Palya<sup>1</sup>, Mária Takács<sup>2</sup>, Rita M. Kiss<sup>1</sup>

<sup>1</sup> Budapest University of Technology and Economics, Dept. of Mechatronics, Optics and Mechanical Engineering Informatics, Műegyetem rakpart 3, Budapest 1111, Hungary. E-mails: [racz.kristof26@gmail.com](mailto:racz.kristof26@gmail.com), [palyazsofia@gmail.com](mailto:palyazsofia@gmail.com), [rikiss@mail.bme.hu](mailto:rikiss@mail.bme.hu)

<sup>2</sup> MÁV Hospital and Clinic, Orthopedia, Versegly F. út 6-8, Szolnok 5000, Hungary. E-mail: [drtakacsmaria@gmail.com](mailto:drtakacsmaria@gmail.com)

## 1. Introduction

The accuracy, with which anatomical landmarks can be located on the human body, while not being the largest source of inaccuracy in a gait analysis, is still not dismissible [1]. This study repeated a previous experiment [2], with a larger number of subjects and with both a professional and an untrained examiner.

The gait analysis method tested is based on a motion capture system (OptiTrack motion capture system, NaturalPoint, Inc. USA), and uses the Calibrated Anatomical Systems Technique (CAST) to record the 3D movements of selected anatomical landmarks [3]. Hypotheses for this study are: a) a trained person can locate anatomical landmarks more accurately, and b) average accuracy for locating these points are smaller than 10 mm.

The goal for this study is to examine, whether the gait analysis method described is sufficiently accurate to not bottleneck the accuracy of the measurements.

## 2. Methods

### 2.1 Subjects

Measurements were conducted on a total of 8 subjects, by 2 examiners. Demographic data for the subjects can be seen in Tab. 1. All subjects have given their written consent to take part in the experiment, after they were informed about all aspects of it. The study was approved by the National Science and Research Ethics Committee (21/2015).

### 2.2 Examiners

The professional examiner was a trained orthopedic surgeon. The untrained examiner was a

master's student studying biomechanics. Note, that untrained in this case means not having conducted medical/anatomical studies. The examiner had one year of experience in gait analysis measurements with the described method. The professional examiner used this particular system for the first time, but had experience with an ultrasound based system, which followed the same principle of calibration.

Age	Sex	Height [cm]	Wight [kg]
83	m	174	84
75	m	170	87
74	f	156	66
21	f	170	62
22	m	177	77
21	m	189	85
22	f	173	65
8	m	136	28.3

Tab. 1. Demographic data of subjects.

### 2.3 Measurement procedure

On every subject, 10 calibrations for all 24 points of the used biomechanical model were created by both examiners. A calibration contains a 3D position vector of the anatomical landmark in the local coordinate system of their respective body segment for all 24 points.

The procedure of calibrating a landmark consists of pointing a calibration wand's designated calibration point at the landmark, which was first palpated by hand (Fig. 1.). The local coordinates are calculated by a measurement software, based on the data collected by the motion capture system.



**Fig. 1.** Anatomical landmark calibration. Calibrated on the picture is a lateral femoral epicondyle.

### 2.4 Evaluation

The accuracy  $a_n$  of the  $n$ th anatomical landmark is defined by Eq. (1), where  $\mathbf{r}_{i,n}$  is the calibrated position of the  $n$ th landmark, in calibration  $i$ , and  $k$  is the number of calibrations. The overall calibration accuracy for a subject is the mean of the  $a_n$  accuracies of the 24 landmarks.

$$a_n = \frac{\|\sum_{i=1}^k (\mathbf{r}_{i,n} - \bar{\mathbf{r}}_n)\|}{k} \#(1)$$

### 3. Results

Overall calibration accuracy for each subject can be seen on Fig. 2. Results are processed for all calibrations, which were not filtered for measurement errors, meaning that filtered values are likely to be smaller. In every case, where accuracy is over 10mm, there were calibrations found with significantly discrepant values, indicating human error.

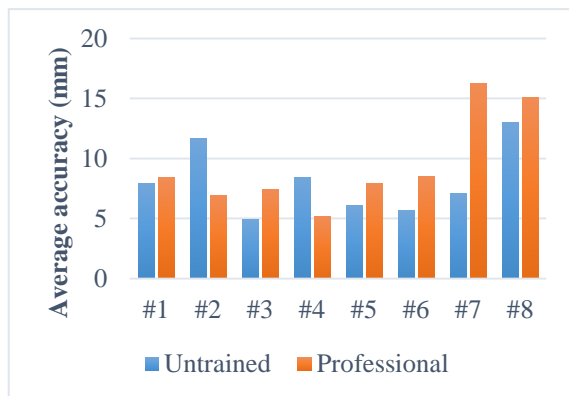


**Fig. 2.** Average accuracy per subject.

Contrary to the expected, the untrained examiner had a better accuracy in most cases. This suggests, that experience with the specific measurement system might be more important, than the amount of training in the field of anatomy,

at least from the point of consistency. Age, and therefore body structure seemed to also have less significant effect on accuracy than previously considered.

Lowest (meaning best) accuracy scores were in the 2.5-3.5 mm range. Considering that many anatomical landmarks have sizes comparable, - or greater - this is a good result. The measurement method can be said to be satisfyingly accurate. Furthermore, it's likely, that the system can be more accurate in calibrations than 2.5 mm, and the results are limited by human accuracy.

### 4. Remarks

- The results show, that the measurement system and technique allows for high consistency in calibration.
- Experience with the specific measurement system might be more important, than medical training, when it comes to the consistency of calibrating anatomical landmarks.
- Body shape have less effect on calibration consistency than previously thought.

### Acknowledgements

This work was supported by the Hungarian Scientific Research Fund OTKA [grant number K115894].

### References

- [1] U. Della Croce, A. Leardini, L. Chiari, A. Cappozzo, Human movement analysis using stereophotogrammetry Part 4: Assessment of anatomical landmark misplacement and its effects on joint kinematics, *Gait and Posture*, 21, 2005. pp. 226-237.
- [2] K. Rácz, G. Nagymáté, R. M. Kiss, Effect of Anatomical Landmark Placement Variation on the Angular Parameters of the Lower Extremities: *Biomedical Engineering*, 2017. pp. 158-163.
- [3] A. Cappozzo, F. Catani, U. Della Croce, A. Leardini, Position and orientation in space of bones during movement: anatomical frame definition and determination, *Clinical Biomechanics*, 10, 1995, pp. 171-178.

# 3D-PRINTABLE FOOT PROSTHESIS DESIGN FOR TRANSTIBIAL AMPUTEES

Bence Rochlitz<sup>1,a</sup>, David Pammer<sup>2,b,\*</sup>, Dr. Rita Kiss<sup>3</sup>

- <sup>1</sup> Budapest University of Technology and Economics, Faculty of Mechanical Engineering, Department of Materials Science and Engineering, Bertalan Lajos str. 7, MT building, H-1111 Budapest, Hungary. <sup>a</sup>E-mail: rbence94b@gmail.com, <sup>b,\*</sup> corresponding author e-mail: pammer@eik.bme.hu
- <sup>2</sup> Budapest University of Technology and Economics, Faculty of Mechanical Engineering, Department of Mechatronics, Optics and Informatics, Bertalan Lajos str. 4-6, D building, H-1111 Budapest, Hungary. E-mail: rita.kiss@mogi.bme.hu

## 1. Introduction

Most commercially available dynamic foot prostheses are made of either carbon or glass fiber reinforced composites which are able to store and return a sufficient amount of energy to provide propulsion [1, 2]. These prostheses are expensive, and the more affordable SACH (Solid Ankle Cushioned Heel) designed for patients with low activity level fails to return enough energy [3].

The rapid development of additive manufacturing (AM) techniques [4] makes it possible to design 3D-printable foot prostheses that have the properties of ESAR (Energy Storage and Return) feet. In this study, an ESAR foot was designed and prototyped using ABS plastic. Such products are not yet available on the market because they are still under development.

## 2. Methods

### a. Design and geometric model

The biomimetic design was mainly based on the human foot. A number of CAD models were designed, all adjustments of the model were followed by FEA, thus optimizing its strength. The split forefoot and the heel provide a 3-point support, e.g. Fig. 1.



Fig. 1. CAD conceptions

The prototype was made for a 245 mm long foot (EU size 39). It corresponds to a woman's old child's foot.

### b. Quasi - static finite element analysis

The FEA was conducted in each of the three support phases of the walking cycle. It was decided that FDM filament ABSplus-P430 from Stratasys would be used for the prototyping and its material properties were applied in the FEA.

### c. Prototype and testing

The prototype was manufactured with a Stratasys Dimension 1200es printer using a 30% rectangular infill pattern and a 1.5 mm wall thickness to reduce mass and printing time. After the production, the prototype was tested twice using Instron 5965 (Instron, Norwood, MA, USA) tensile test machine. Quasi-static and cyclic loads were applied.

## 3. Results

### a. FEA results

The critical phase turned out to be heel strike. The maximum stress was calculated at 17 MPa considering the auxiliary torque and the maximum lateral force besides the vertical load, e.g. Fig. 2.

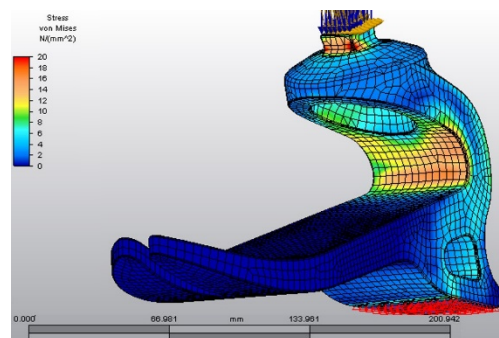


Fig. 2. FEA simulation under critical load

b. Test results

First, a maximum vertical load of 600 N was applied using different loading speeds. The curves were quasi-linear meaning that the weight is within the elastic deformation range, e.g. Fig. 3. The ankle geometry of the prosthesis generates a torque that wants to rotate it forward and will provide propulsion for the user. Because of that, the prosthesis kept slipping frequently, which resulted in non-continuous curves.

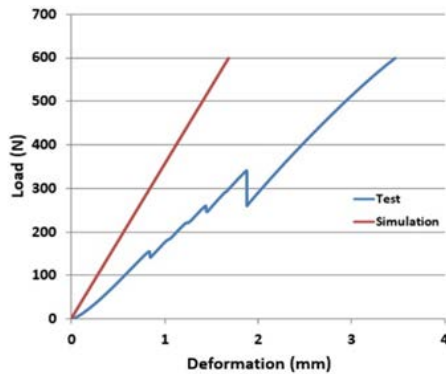


Fig. 3. 600 N vertical load (FEA and testing)

During the second test, 200 N, 400 N, 600 N, 800 N and 1000 N maximum loads were applied. The deformation axes of the graphs are adjusted by 0, 1, 2, 3 and 4 mm respectively so that all of them are visible, e.g. Fig. 5. The prototype failed at 850 N and the yield point is at approximately 750 N.

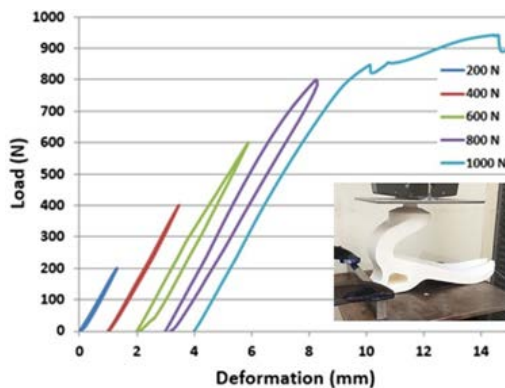


Fig. 2. Incremental cyclic loads

The area of each hysteresis loop corresponding to the dissipated energy was calculated by numerical integration. The returned energy for each load is shown in Tab. 1. The average was 88 % with a corrected standard deviation of 5 %.

Load (N)	200	400	600	800
Energy returned (%)	88,4	95,0	85,7	83,1

Tab. 1. Returned energy in each case

4. Remarks

In conclusion, the 3D-printable prosthetic foot design presented in this paper shows that such products built of ABS filament have a potential to be a low-cost solution for moderate activity level amputees. Based on the data collected during quasi-static testing, the energy return of the prosthesis is sufficient.

Considering that human feet weigh a few times more than the prototype [5], it is desirable to increase its mass in order to improve its strength and provide a more natural feeling for the user. The way to do so is adjusting printing settings such as wall thickness and structural infill percentage, as well as the geometry of the model, which is not the optimal yet.

Future work, based on this study will focus on testing the prosthesis with patients and improving its strength and lifetime.

5. Acknowledgements

I would like to thank my supervisor, Dávid Pammer, who also manufactured the prototype, and I also thank Dr. Rita Kiss for her contribution to the design process. The present work was funded by the National Research, Development and Innovation Fund, connecting to the NVKP\_16-1-2016-0022 project.

6. References

- [1] Versluys, R., et al., Prosthetic feet: State-of-the-art review and the importance of mimicking human ankle-foot biomechanics, *Disability, and Rehabilitation: Assistive Technology*, 4 (2), 2009. pp. 65-75.
- [2] Takahashi, KZ., Stanhope, SJ., Mechanical energy profiles of the combined ankle-foot system in normal gait: Insights for prosthetic designs, *Gait & Posture*, 38, 2013. pp. 818-823.
- [3] Yap, J., Renda, G., Low-cost 3D-printable Prosthetic Foot, In *Design4Health*, editor Kirsty Christer, 3rd European Conference, 2015.
- [4] Campbell, T, et al., Could 3D Printing Change the World?, In *Strategic Foresight Report*, Atlantic Council, Oct. 2011.
- [5] Ma, Y., et al., Segment inertial parameters of Korean adults estimated from three-dimensional body laser scan data, *International Journal of Industrial Ergonomics*, 41, 2011. pp. 19-29.

# VERIFICATION OF 3D DIC SOFTWARE FOR CURVILINEAR SURFACES USING FE METHOD AND RAY-TRACING

Karol Suprynowicz<sup>1</sup>, Michal Kowalik<sup>1</sup>, Pawel Pyrzanowski<sup>1</sup>

<sup>1</sup> Warsaw University of Technology, Institute of Aeronautics and Applied Mechanics, Faculty of Power and Aeronautical Engineering,; Nowowiejska 24, 00-665 Warsaw, Poland, E-mails: ksupyrynowicz@meil.pw.edu.pl, mkowalik@meil.pw.edu.pl, pyrzan@meil.pw.edu.pl

## 1. Introduction

Digital Image Correlation (DIC) is currently one of the most popular methods of shape and strain field acquisition during structural and material testing. For planar strain cases single camera 2D DIC usually gives accurate results, but it cannot be used for measuring out-of-plane deformations. 3D DIC (stereo or multi-view stereo) systems allow acquisition of specimen's shape and deformation without aforementioned limitations. Because of this, they are popular in disciplines like biomechanics and structural testing. This paper presents method for verification of 3D DIC system for large strain, out of plane biomechanics cases, using FE model and physically based ray-tracing software for generating test images.

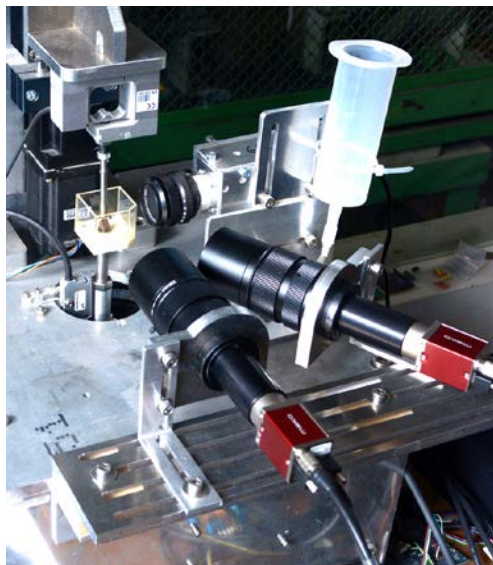


**Fig. 1.** 3D DIC setup for testing mechanical properties of ring-shaped rat aorta specimens.

## 2. Methods

Presented 3D DIC system was developed for biomechanical material testing with large out-of-plane deformation and non-planar specimens.

Planned use cases include circumferential loading of ring-shaped rodent aorta samples and inflation test of aorta samples. Experimental setup for ring-shaped aorta samples is presented on Fig. 1. Setup consists of testing machine with electrodynamic actuator and three-camera setup for DIC and image analysis. During the initial phase of test specimen deforms from initial ring shape (Fig. 2), resulting in large out-of-plane displacement. The sample is coated with printer toner particles for providing contrast necessary for DIC method. The load is applied vertically, by moving one of the fixtures. Second fixture is attached to a load cell. During testing the sample is submerged in saline solution inside transparent vessel attached to lower fixture.

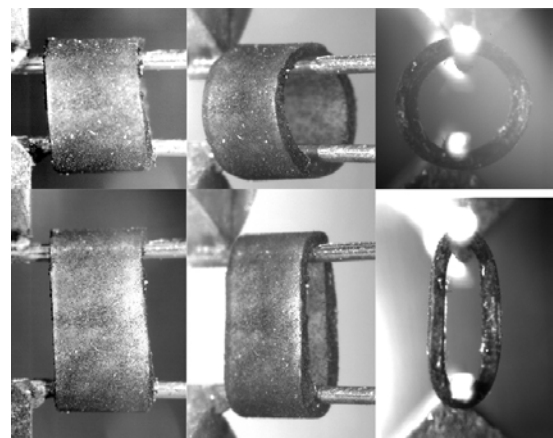


**Fig. 2.** Ring shaped specimen, unloaded and under load. Specimen is made from natural rubber and has inside diameter of 2 mm.

Verification method is based on aforementioned use case. Test case consists of Finite Element (FE) model (Fig. 3) representing ring shaped aorta and fixture through which load is

introduced. The FE model behavior was compared to real rat aorta samples in [1], and gave satisfactory results.

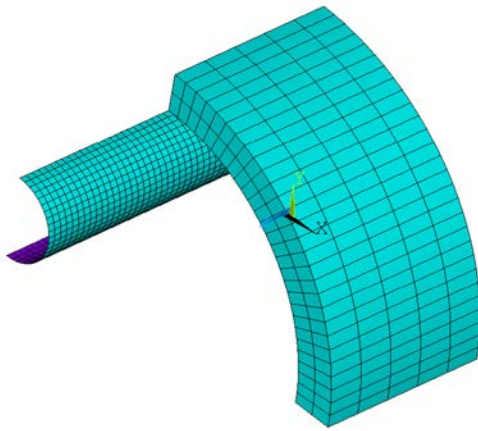


**Fig. 3.** Finite Element mesh representing specimen and loading conditions.

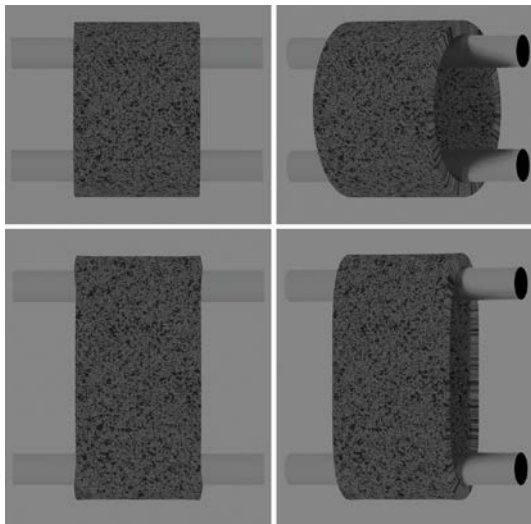


**Fig. 4.** Test images generated from FE model

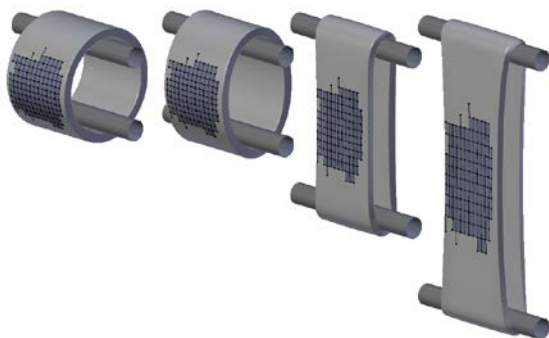


**Fig. 5.** Mesh generated by DIC algorithm overlaid on FE model.

Results from FE model were imported to Blender mesh editing software [2] to apply optical material properties, camera and lighting parameters.. Texture resembling toner particles

was applied to specimen's surface. The model was then exported to physically based ray-tracing software LuxRender [3] (based on academic PBRT project[4]). Images for each camera and each loading step (Fig. 4) were computed using ray-tracing software. Images of calibration board used by DIC software for calibrating camera parameters were computed in similar way.

Generated images were used by 3D DIC software, first to determine camera parameters and then to acquire specimen's shape and deformation for each loading step.

### 3. Results

Shape, displacement and strain fields computed by 3D DIC algorithm are compared to results from FE model (Fig. 5). For specimen with 2mm diameter, shape and displacement measurements had typical measurement error of less than 0.01mm. Results were used to determine optimal angle between cameras for real-life experimental setup.

### 4. Conclusions

Initial results have proven usability of tested DIC algorithm. In later phase optical model will be extended to check DIC algorithm's response to lens distortion, light refraction and subsurface light scattering inside specimen. Investigation of optimal light sources' positions will also be conducted.

### References

- [1] Kowalik M, Pyrzanowska J., Piechal A. [et al.] : Determination of mechanical properties of rat aorta using ring-shaped specimen, in: Solid State Phenomena, Trans Tech Publications, vol. 240, 2016, pp. 255-260
- [2] <https://www.blender.org> , Retrieved 2017-05-05
- [3] <http://www.luxrender.net> , Retrieved 2017-05-05
- [3] Pharr, M., Jakob, W. , Humphreys, G., Physically Based Rendering, 3rd Edition. Morgan Kaufmann, 2016

# BONE STRUCTURE AND FRAGILITY FRACTURE RISK FACTORS: A POPULATION ANALYSIS

F. Cosmi<sup>1,2</sup>, A. Nicolosi<sup>2</sup>, and G. Zatta<sup>3</sup>

<sup>1</sup> *Department of Engineering and Architecture, University of Trieste, Italy; email: cosmi@units.it*

<sup>2</sup> *M2TEST srl, Area Science Park, Trieste, Italy; email: alessandra@bestest.it*

<sup>3</sup> *Centro Radiologico Giuliano, Trieste, Italy*

## 1. Introduction

Osteoporosis (OP) is a silent disease, characterized by a decreasing bone strength, which leads to a progressive increase in fracture risk. As mean average human lifespan is growing, a parallel rise in the rate of osteoporosis is observed.

Mechanical properties of bone depend on both its composition and its trabecular component micro-architectural arrangement [1]. OP diagnosis is made on the basis of bone mineral density (BMD), possibly combined with algorithms based on the clinical risk factors, e.g. FRAX<sup>®</sup>, but about half of those at risk of OP still go undetected, since their OP risk is linked to alterations of the trabecular architecture [2].

The mechanical response of bone structure to the applied loads can be evaluated from 3D reconstructions of the examined tissue, e.g. obtained by micro-CT scans. However, these costly techniques are usually limited to research applications, for example to evaluate the effects on bone structure under microgravity conditions [3] - [5]. The BESTEST<sup>®</sup> is a test based on the simulated application of loads on a virtual biopsy of the patient. Briefly, the test uses planar X-rays projections to assess the mechanical properties of the patient's trabecular bone tissue, Fig.1. A specific hand-held radiological device acquires the radiographic image (AP projection) of the proximal epiphysis in the finger of the non-dominant hand with a specific protocol [6], [7].

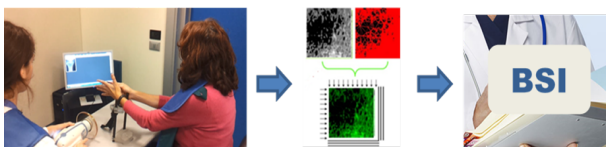


**Fig. 1.** Clinical application: scheme of BSI bone quality analysis

The images are then converted into a Cell Method numerical model [8] and application of compressive loads is simulated [9] - [10]. The results are combined in the Bone Structure Index (BSI) that quantifies the pathological alterations of bone micro-architecture [11] - [12].

## 2. Methods

### 2.1 Experimental design

The study was structured in 3 phases.

1. During the Trieste NEXT2015 event, contact details of over 400 caucasian female volunteers  $\geq 20$  yrs were collected.

2. Volunteers compiled an anonymous anamnestic questionnaire and X-rays for BSI evaluation were acquired. Age, weight, height and, when available, DXA T-score at the femoral neck (BMD\_T-score) are considered.

3. The BSI of each volunteer was calculated.

4. Radiographs with insufficiently included trabecular bone, fractures in measurement regions, foreign material or unacceptable positioning were manually excluded.

The reports were delivered anonymously and free of charge to the volunteers. The Ethics Committee of the University of Trieste gave a favorable opinion (No 66 of 11.11.2015).

## 3. Results

Population eligible for the study resulted in  $N_p=336$  females, age 20 - 95 yrs. BMD T-score was available for a population subgroup of  $N_s=65$ , age 40-85yrs. The age breakdown for population and subgroup is given in Fig.2. The age (mean  $\pm$  st. dev.) of the subjects is  $61 \pm 12$  yrs in the population and  $65 \pm 10$  yrs in the subgroup.

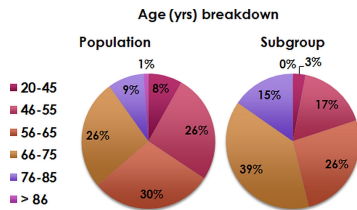


Fig. 2. Age in population (left) and subgroup (right).

An hypocaloric diet therapy, while improving cardiovascular risk indexes, decreases total BMD in the arms and legs, both in pre- and post-menopausal women [13], [14]. The majority of our subjects reports a Body Mass Index (BMI) associated to a moderate risk of fractures and less than 30% falls into the low risk category, Fig.3.

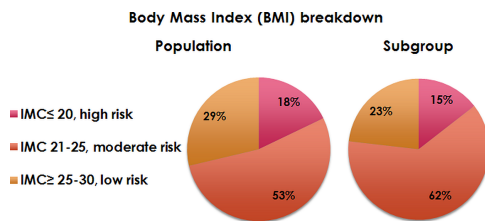


Fig. 3. BMI in population (left) and subgroup (right).

The distribution of femoral neck DXA diagnostic categories in the subgroup is shown in Fig.4.

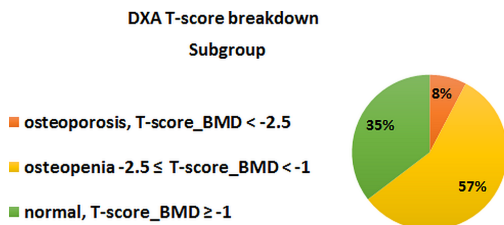


Fig. 4. Distribution of femoral neck DXA T-score.

The bone structure quality as measured by the BESTEST<sup>®</sup> can be again interpreted by T-score concept, Fig.5.

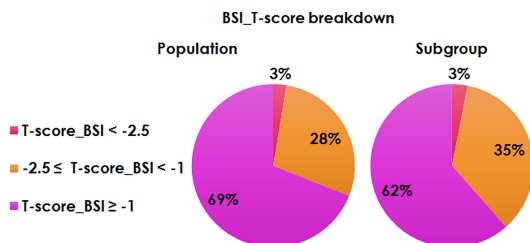


Fig. 5. Distribution of BSI T-score.

#### 4. Brief discussion

The usefulness of BSI as an add-on to BMD assessment is clearly shown in Fig.6. The BSI and DXA values are independent ( $R^2 = 0.0631$ ). This type of diagram can be very useful in clinical practice since it can drive both the prognosis and

the choice of the appropriate treatment, improving diagnostic accuracy. The very low X-ray doses used for BSI assessment imply that the treating physician can monitor the bone changes in response to any therapeutic strategy and quickly introduce any adjustment (treatment tailoring) every few months if necessary, providing patients with a strong motivation to strictly adhere to their therapy and avoid discontinuation. The rapidity and convenience of the test are highly appreciated by both patients and physicians.

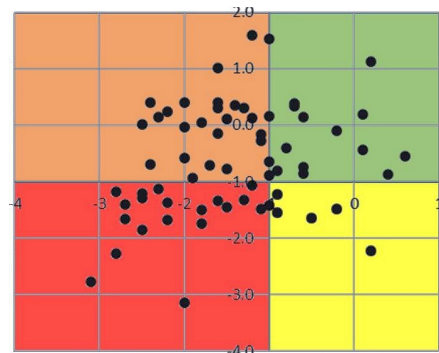


Fig. 6. BSI\_T-score vs. femoral neck DXA T-score (subgroup).

#### 5. References

- [1] World Health Organization Scientific Group.. *Technical Report*. (2008)
- [2] Pasco J.A. et al. *Osteoporos. Int.* 17(9), 2006 1404-1409
- [3] Cosmi F. and Dreossi D. *Meccanica*. 42(1) , 2007, 85-93.
- [4] Cosmi, F. et al. *JMBBM*, 44, 2015, 61-70
- [5] Cosmi, F. et al. *JMBBM* 2(2) , 2009, 164-172
- [6] Cosmi, F., Tomanik M. *Materials Today: Proceedings*. 3, 2016, 947 – 952.
- [7] Cosmi, F. (2008) *US Patent* 10509512,B2
- [8] Tonti E. *CMES*. 2(2), 2001, 237-258
- [9] Cosmi, F. *CMES*, 2(3), 2001, 365-372
- [10] Cosmi, F. *MCB*: 12(2). , 2015. 87-105
- [11] Cosmi F., Dreossi D. *Acta Bioeng. Biomech..* 9(2), 2007, 35-39
- [12] Cosmi F., Mazzoleni, G. *JMBBM* 29, 2014, 517-528
- [13] Jensen LB et al. *J Bone Miner Res* 9, 1994, 459-463.
- [14] Salamone LM, et al.. *Am J Clin Nutr* Vol 70, N 1, 1999, 97-103

# MOTOR SPEED TRANSFER FUNCTION FOR WIND VECTOR ESTIMATION ON MULTIROTOR AIRCRAFT

Dino Hüllmann, Niels Paul, Patrick P. Neumann

<sup>1</sup> Bundesanstalt für Materialforschung und -prüfung (BAM), Unter den Eichen 87, 12205 Berlin, Germany. E-mail: [dino.huellmann@bam.de](mailto:dino.huellmann@bam.de)

## 1. Introduction

Ambient wind plays an important role in aviation because it can affect the flight characteristics significantly. Especially small unmanned aircraft (UA) are very sensitive to wind due to their low inertia. Hence, it can be crucial for several applications to measure the wind vector, i.e. both speed and direction, in real-time. Since the wind field varies locally, the measurements have to be performed on board the UA. In case of fixed-wing aircraft, typically pitot tubes are used for this purpose, as shown, for instance, in [1]. However, this method cannot be easily adopted to rotary-wing aircraft like multicopters because their rotor wash causes strong perturbations of the aerodynamic field surrounding the aircraft. Instead, the state variables of the aircraft can be used to estimate the wind field. Neumann et al. inferred the 2D wind vector from simple pose measurements of an UA [2]. In this paper, this approach is extended to the 3D case, which requires knowledge of the rotor speeds. Therefore, the motor speed transfer function is analysed exemplary for a DJI S1000 octocopter.

## 2. Methods

The relation between ground speed  $\mathbf{v}_{\text{gnd}}$ , wind speed  $\mathbf{v}_{\text{wind}}$  and airspeed  $\mathbf{v}_{\text{air}}$  is given by the wind triangle [2]:

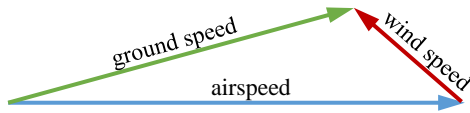


Fig. 1. Wind triangle.

This yields the following equation:

$$\mathbf{v}_{\text{gnd}} = \mathbf{v}_{\text{air}} + \mathbf{v}_{\text{wind}} \quad (1)$$

According to the Newton-Euler equations the translational dynamics of a rigid body can be described by

$$m {}_B \dot{\mathbf{v}}_{\text{air}} + {}_B \boldsymbol{\omega}_{IB} \times m {}_B \mathbf{v}_{\text{air}} = {}_B \mathbf{f}^e \quad (2)$$

where  $m$  denotes the mass,  ${}_B \mathbf{v}_{\text{air}}$  is the velocity expressed in the body coordinate frame  $B$ ,  ${}_B \boldsymbol{\omega}_{IB}$  is the angular velocity of  $B$  with respect to the inertial coordinate frame  $I$  expressed in  $B$  and  ${}_B \mathbf{f}^e$  are the external forces acting on the body.

Mainly, the thrust and drag (or friction) force contribute to  $\mathbf{f}^e$ . Let  $f_i$  denote the thrust force generated by rotor  $i$ , the total thrust becomes [3]

$$T = \sum f_i = C_T \rho A_R \sum (r_R \omega_i)^2 \quad (3)$$

where  $C_T$  is an aircraft specific thrust constant,  $\rho$  is the air density,  $A_R$  the area swept out by the rotor,  $r_R$  the radius of the rotors and  $\omega_i$  the angular velocity of rotor  $i$ . In the body coordinate frame  $B$  the thrust force is defined as

$${}_B \mathbf{f}_T = [0 \quad 0 \quad T]^T. \quad (4)$$

With  $\odot$  denoting the Hadamard (or Schur) product, the drag force can be written as

$${}_I \mathbf{f}_D = \frac{1}{2} \rho (\mathbf{c}_D \odot \mathbf{a}_{\text{proj}} \odot \mathbf{v}_{\text{air}} \odot |\mathbf{v}_{\text{air}}|) \quad (5)$$

where  $\mathbf{c}_D$  is the vector of drag coefficients and  $\mathbf{a}_{\text{proj}}$  is the vector of projected surface areas (cf. [2]). Finally, the gravitational force is given by:

$${}_I \mathbf{f}_g = [0 \quad 0 \quad -g]^T. \quad (6)$$

The total external force becomes

$${}_B \mathbf{f}^e = {}_B \mathbf{f}_T + \mathbf{R}_{BI} ({}_I \mathbf{f}_g + {}_I \mathbf{f}_D). \quad (7)$$

where  $\mathbf{R}_{BI}$  is the rotation matrix from  $I$  to  $B$ . By inserting (7) into (2) a solution for  $\mathbf{v}_{\text{air}}$  can be computed, which gives  $\mathbf{v}_{\text{wind}}$  by using (1).

An UA equipped with typical sensors like an inertial measurement unit (IMU), global positioning system (GPS) and compass can compute or measure  $\mathbf{v}_{\text{gnd}}$ ,  ${}_B \boldsymbol{\omega}_{IB}$  and  $\mathbf{R}_{BI}$ . The values for  $m, \rho, C_T, A_R, r_R, \mathbf{c}_D, \mathbf{a}_{\text{proj}}(\mathbf{R}_{BI})$  and  $g$  are given or can be determined experimentally. In contrast, the rotor speeds  $\omega_i$  have to be measured online.

In case of an open flight controller, it is straight-forward to get the set points of the motor controllers (electronics speed control, ESC), which can be used as an approximation for  $\omega_i$ . However, this does not apply to most commercial products like the DJI S1000. Since the motor controller and the motor itself form a fixed unit, the rotor speed cannot be measured, for example, by tapping the counter-electromotive force from the brushless motors. Instead, the signal from the flight controller to the ESCs is analysed and related to the actual rotor speed. The latter is measured using a digital, non-contact tachometer (UNI-T UT372), which offers a sampling frequency of approximately 6.25 Hz.



Fig. 2. Measuring the angular velocity of the motors.

### 3. Results

A simple signal analysis showed that DJI uses a PWM signal with 400 Hz carrier frequency to control the ESCs. After turning the copter on, the duty cycle is set to 37.6% to signal the presence of the flight controller. In this state the rotors are not turning. If the rotors are set to idle speed the duty cycle is increased to 48%. The flight controller never sets the duty cycle above 74%, which defines the value for top speed.

To obtain the transfer function describing the relation between PWM duty cycle and motor speed a test signal was generated using a microcontroller. The duty cycle was increased steadily from 47% to 74% within 80 seconds, which is shown in figure 3. Basically, the function looks exponentially damped, i.e. similar to

$$f_1(x) = a + b(1 - e^{-c \cdot x}). \quad (8)$$

This function was fitted to the curve showing the revolutions per minute (rpm), but there was an oscillating portion with decreasing frequency and damped amplitude left resulting in a standard deviation of ca. 70 rpm. Therefore, the approach was extended by

$$f_2(x) = d \cdot e^{-e \cdot x} \sin(1 - e^{-g \cdot x}) + e^{h \cdot x}. \quad (9)$$

The remaining difference between the model,  $f(x) = f_1(x) + f_2(x)$ , and the measurement is shown in figure 4. Its standard deviation is 14 rpm, which is in the range of the measurement accuracy of the used tachometer.

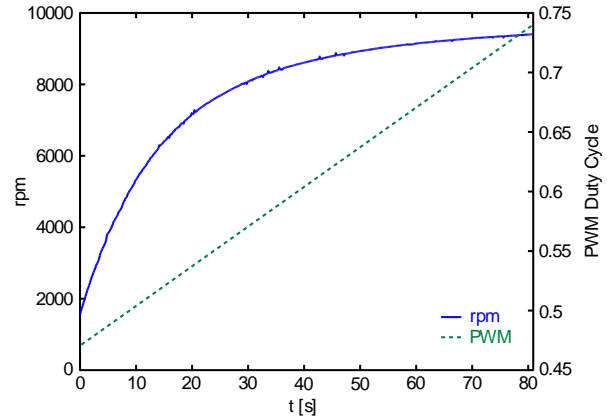


Fig. 3. PWM duty cycle sent to the ESC and the resulting angular velocity of the motor.

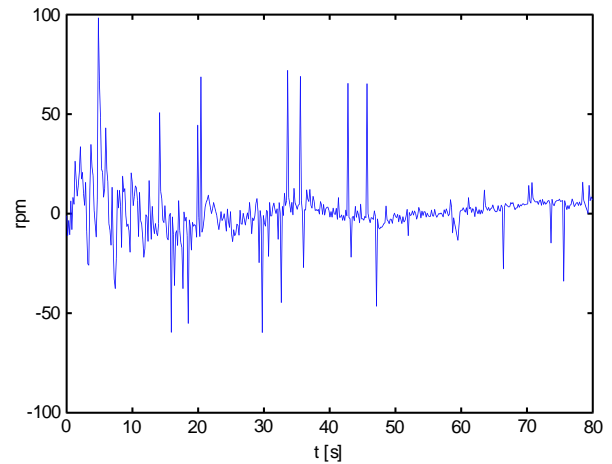


Fig. 4. Difference between model and measurement.

### References

- [1] Kroonenberg, A.v.d., Martin, T., Buschmann, M., Bange, J., Vörsman, P., Measuring the Wind Vector Using the Autonomous Mini Aerial Vehicle M2AV, *Journal of Atmospheric and Oceanic Techn.*, 25, 2008. pp. 1969-1982.
- [2] Neumann, P.P., Asadi, S., Lilienthal, A.J., Bartholmai, M., Schiller, J.H., Microdrone for Wind Vector Estimation and Gas Distribution Mapping, *IEEE Robotics and Automation Magazine*, 19, 2012. pp. 50-61.
- [3] Xiang, X., Wang, Z., Mo, Z., Chen, G., Pham, K., Blasch, E., Wind Field Estimation



34th Danubia-Adria Symposium on Advances in Experimental Mechanics  
University of Trieste, Italy, 2017



Through Autonomous Quadcopter Avionics,  
IEEE/AIAA 35th Digital Avionics Systems  
Conference, 2016.

## DEVELOPMENT OF A MINING MACHINE SEAT MODEL

Paulina Działak<sup>1</sup>, Jacek Karliński<sup>1</sup>, Eugeniusz Rusiński<sup>1</sup>

<sup>1</sup> Wrocław University of Science and Technology, Department of Mechanical Engineering, Łukasiewicza 7/9, 50-371, Wrocław, Poland. E-mail: [paulina.dzialak@pwr.edu.pl](mailto:paulina.dzialak@pwr.edu.pl), [jacek.karliński@pwr.edu.pl](mailto:jacek.karliński@pwr.edu.pl), [eugeniusz.rusinski@pwr.edu.pl](mailto:eugeniusz.rusinski@pwr.edu.pl)

### 1. Introduction

The authors have endeavoured to present the process of the mining machine seat modeling. The relevant data necessary to obtain the proper model were received from two experimental tests. Photogrammetrical survey was used to accomplish the geometry of the seat. To obtain the characteristic of the mounting and the material data for the cushion seat foam, the measurements on the universal testing machine were taken. The model was inspired by the Maximo seat of Grammer company (Fig. 1).



**Fig. 1.** Seat of the mining machine operator subjected to the measurements [1].

The main methods that lead to develop a complete computational model for the further simulation testing of the safety of a mining machine operators [2] were presented in the paper.

### 2. Photogrammetric methods

The geometrical model of the mining machine operator seat was created using an optical system TRITOP and the ATOS Compact Scan device. TRITOP is a portable system, measuring 3D coordinates quickly and precisely. It records points and their orientation in space at quasi-static conditions. Then, the measurement is transformed into the coordinate system of the component.

The shape of a cushion of the seat was determined by the TRITOP device (Fig. 2).

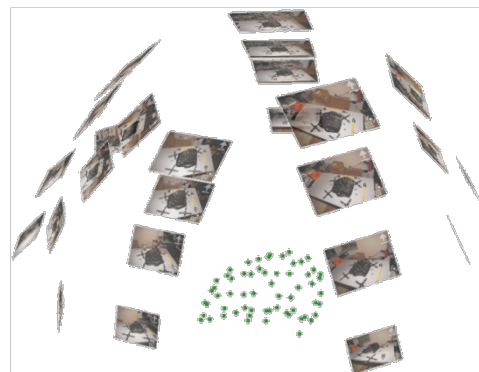
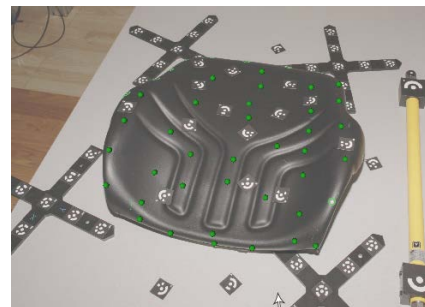


**Fig. 2.** Seat base during the TRITOP measurements (above) and received images with resulting point cloud (below).

The recreation of the geometry was accomplished by the cloud of points received from the system. The geometry of the cushions of a base and the backrest of the operator's seat were obtained by creating surfaces on the spread points.

ATOS on the other hand is an optical 3D scanner based on fringe projection, delivering accurate and traceable 3D coordinates. The technology ensure an adaptability for 3-dimensional measuring of the complex components. Using this method provides a high accuracy and results in complete data even if the shape of the object is complicated and the surface is shiny [3].

The geometry of the seat back obtained by the ATOS scanning device is presented in figure 3.

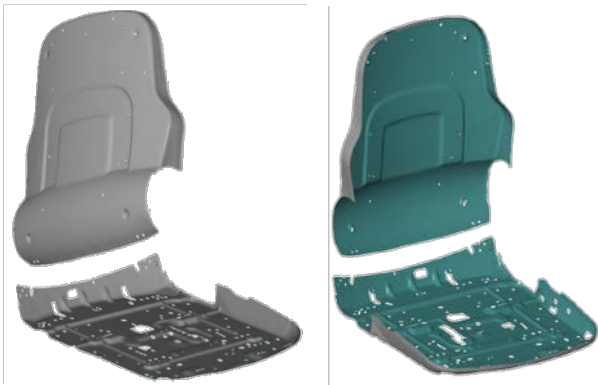


Fig. 3. Geometry of a seat frame (ATOS).



Fig. 5. Final numerical model of the seat.

### 3. Universal testing machine analysis

The stiffness and strength of the seat mounting were examined experimentally on the universal testing machine Zwick Z030 [4]. The measurements enabled the authors to design a simplified model of the mounting (Fig. 4).

The material data for the cushion seat foam were also obtained empirically from the testing machine.



Fig. 4. Measurements of a seat mounting taken on the universal testing device.

### 4. Numerical model

The discrete model was generated, basing on the obtained geometrical shape of the seat and the parameters of the mounting and the material data.

The complete numerical model of the seat of a mining machine operator, achieved by the described process is presented in figure 5.

### 5. Remarks

- The authors attempted to create the numerical equivalent of the seat structure of the mining machine operator.
- To reproduce the geometry two different photogrammetric methods were used.
- To obtain the characteristics of the seat mounting and the material data, the measurements on the universal testing machine were also performed.

### Acknowledgements

Research is co-financed by the National Science Centre Poland within the framework of the project *The assessment of the seismic phenomena effects in the aspect of the operator safety* no. 2015/17/N/ST8/01212.

### References

- [1] <https://www.grammer.com/en/products-markets/seating-systems/construction-machinery/bm-maximo.html>, 09.2016.
- [2] Derlukiewicz, D., Karliński, J., Iluk, A., The operator protective structures testing for mining machines, *Solid State Phenomena*, Vol. 165, 2010. pp. 256-261.
- [3] <http://www.gom.com/metrology-systems/atos/atoscompactscan.html>, 01.2017.
- [4] Xu, J., Lu, L. F., Yang, H. W., Wang, J. N., Zhang, Y., Experimental Research on Relationship of Load and Displacement of Universal Testing Machine, *Advanced Materials Research*, Vols. 250-253, 2011. pp. 1582-1587.

## EXPERIMENTAL AND NUMERICAL INVESTIGATION OF WATER JETS

Freddy Florez<sup>1</sup>, Reinhard Prenner<sup>1</sup> and Norbert Krouzecky<sup>1</sup>

<sup>1</sup> Vienna University of Technology, Institute of Hydraulic Engineering and Water Resources Management, Karlsplatz 13/222 1040 Vienna, Austria. E-mail: [norbert.krouzecky@tuwien.ac.at](mailto:norbert.krouzecky@tuwien.ac.at)

### 1. Introduction

The determination of the breakup length in free falling water jets is difficult, because it is a complex process where the interaction of independent variables as the level of turbulence, the oscillating pressure, nozzle geometry and ambient properties influence the flow characteristics of the jet [1].

In order to improve understanding of air entrainment into water, a so-called free falling water jet ejecting downwards into quiescent air from a circular nozzle has been tested in the laboratory and the results have been validated by means of two-phase Computational Fluid Dynamic (CFD) models.

### 2. Experimental rig

Experimental tests were carried out in the Hydraulics Laboratory of the Institute of Hydraulic Engineering and Water Resources at the Vienna University of Technology. The model rig facility included a 5 m high steel trestle in order to generate free falling water jets into the atmosphere through a nozzle directly attached to the pump line (DN 150 mm) of the laboratory as is schematized in Fig. 1. The model rig is described in detail in [1] and [2].

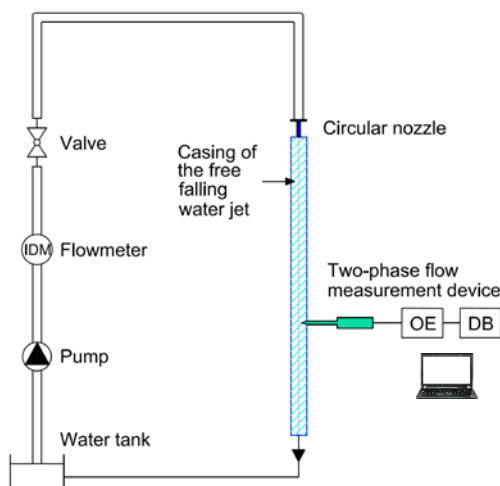


Fig. 1. Experimental rig.

Once the water jet left the nozzle, it fell vertically within a jet casing box to the floor of the tailrace channel to the water tank.

#### 2.1 Nozzle

The nozzle was composed of a circular cylinder built in PMMA and a flange of PVC on one side in order to attach it to the steel flange of the water supply pipe (see Fig. 1). The nozzle had a diameter  $d = 0.02$  m, an exit length  $L_n = 0.35$  m and the sharp edge ( $90^\circ$ ) of the nozzle inlet was smoothed into a circular arc of diameter  $d_n = 4 \times 10^{-3}$  m.

#### 2.2 Instrumentation

The discharge  $Q_w$  was regulated manually by a valve located in the feeding pipe and it was measured by an inductive flowmeter (IDM).

A sapphire fibre-optical double probe manufactured by RBI Instrumentations was used to measure the local air concentration  $C$  (%) at several cross sections from the nozzle exit. The two-phase flow measurement device comprised the following elements (see Fig. 1): a probe with a double sapphire tip, an opto-electronic amplification module (OE), a data acquisition board (DB), a PC and the software ISO-Lite for data processing and analyzing.

### 3. Computational Fluid Dynamics

The open source software OpenFOAM v. 2.3.1 was selected as the tool to carry out three-dimensional (3D) numerical calculations for solving the Navier-Stokes equations for two incompressible fluids, capturing the interface using the Volume of Fluid (VOF) method [3]. Two types of turbulence modelling were implemented: 1) standard  $k-\epsilon$  model, which is a type of Reynolds averaged simulation (RAS) and, 2)  $k$ -equation eddy-viscosity model based on Large Eddy Simulation (LES) models. The computational fluid dynamic domain is shown in Fig. 2, where  $d_2 = 0.06$  m and 0.1 m for RAS and LES models, respectively. The nozzle outlet velocity  $U_0 = 7.96$  m/s generated an atomization mode of

disintegration, confirming the expected behavior according to the Ohnesorge diagram.

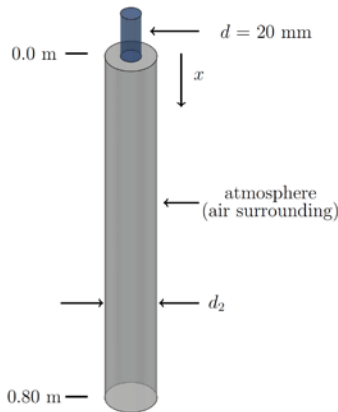


Fig. 2. Computational fluid dynamic geometry.

The minimum computed cell sizes during the construction of the mesh are summarized in Tab. 1.

Model used	$\Delta x$ [m]	$\Delta y$ [m]	$\Delta z$ [m]	Number of cells
RAS $k-\varepsilon$ model	$2 \times 10^{-3}$	$2 \times 10^{-3}$	$2 \times 10^{-3}$	$0.65 \times 10^6$
LES $k$ -Eqn	$0.65 \times 10^{-3}$	$1 \times 10^{-3}$	$1 \times 10^{-3}$	$2.31 \times 10^6$

Tab. 1. Cell size characteristics.

#### 4. Results

In Fig. 3 are shown the jet disintegration results for the experimental test (left), the CFD simulation by using the standard  $k-\varepsilon$  turbulence RAS model after 2.0 s (center), and the CFD simulation by using the k-equation eddy-viscosity turbulence LES model after 2.0 s (right) are shown.

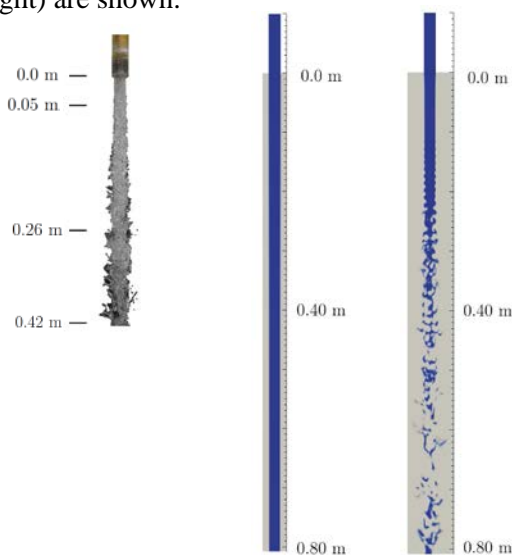


Fig. 3. Experimental test (left), CFD  $k-\varepsilon$  turbulence RAS model after 2.0 s (center) and, CFD k-equation eddy-viscosity turbulence LES model after 2.0 s (right).

In Fig. 4 the air concentration distributions of the experimental test (Exp) and the numerical simulations by using the two turbulence models mentioned at a distance of 0.05 m and 0.683 m from the nozzle exit are presented. The relative position  $y/r$  is defined as the distance  $y$  from the jet axis and  $r$  is the radius of the jet.

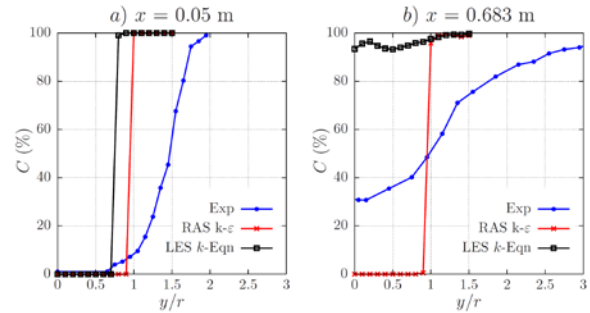


Fig. 4. Air concentration measured and computed at several locations.

#### 5. Remarks

- The standard  $k-\varepsilon$  turbulence RAS model in neither case generated water separation from the surface and no breakup took place. Likewise, the angle of spray was always negative due to the acceleration of gravity.
- The k-equation eddy-viscosity turbulence LES model generated an early breakup and it was able to reproduce the dynamic interaction between the phases air and water. Despite this model requiring a computational time twice that of the RAS model, its use is suggested in hydraulic engineering for studying problems in which the air is of concern.

#### Acknowledgements

To Vienna Scientific Cluster (VSC) Research Center for his support.

#### References

- [1] Florez, F., Air Entrainment in Free Falling Water Jets, PhD Thesis, TU-Wien, 2016.
- [2] Florez, F., Prenner, R., Krouzicky, N., Measurements of Air Concentration and Velocities in a Free Falling Water Jet, Transactions of FAMENA, 40, 2016, pp. 57-68.
- [3] Greenshields, C., OpenFOAM User Guide version 4.0, The OpenFOAM Foundation, 2016.

# CHARACTERIZATION AND MODELING OF THE FATIGUE BEHAVIOR OF TPU

J. Holzweber<sup>1</sup>, J. Müller<sup>2</sup>, U. D. Çakmak<sup>1</sup>, Z. Major<sup>1</sup>

<sup>1</sup> Johannes Kepler University, Institute of Polymer Product Engineering, Altenberger-Strasse 69, 4040, Linz, Austria. E-mails: [juergen.holzweber\\_1@jku.at](mailto:juergen.holzweber_1@jku.at), [umut.cakmak@jku.at](mailto:umut.cakmak@jku.at), [zoltan.major@jku.at](mailto:zoltan.major@jku.at)

<sup>2</sup> DMH Dichtungs- und Maschinenhandel GmbH, Industriepark West 11, 8772, Traboch, Austria. E-mail: [johannes.mueller@dmh.at](mailto:johannes.mueller@dmh.at)

## 1. Introduction

Thermoplastic polyurethanes (TPU) have a wide range of mechanical and chemical properties due to their various available formulations and getting the material of choice for nowadays applications. The comprehensive determination of the material properties as well as the examination of the long-term fatigue behavior of elastomer composites are of particular practical importance for demanding engineering mechatronic applications.

Contrary to many thermoplastic and metallic materials, rubber and rubberlike materials show a highly nonlinear material behavior in the stress-strain behavior. This characteristic is often linked to hyperelasticity with inherent viscoelasticity. In accordance with Qi and Boyce TPUs are very rate-, time- and hysteresis dependent [1]. Especially for materials, exhibiting a strong hyperelastic material response, a throughout characterization of different mechanical loading states are required to gain profound understanding of the mechanical behavior. Based on uniaxial tension, compression, equibiaxial and planar tension tests the complex material behavior can be described and the parameters of more elaborated material models can be reliably determined [2]. Mechatronic applications are usually loaded in non-uniform complex loading states and consequently material parameter determination from a simple tensile test is not adequate. All subsequent analyses, including numerical calculations of components and lifetime estimations, are relying on this.

Therefore, the objectives of this study are:

- The characterization of the complex mechanical material behavior of TPUs under monotonic and cyclic loading.
- The definition of material models and determination of parameters for further FE simulations.

- Application of the local strain based Wöhler curve method for lifetime estimations on a component.

## 2. Methods

One TPU material was selected, characterized and the lifetime of a simplified component was estimated and compared to experimental findings.

### 2.1 Monotonic Deformation Behavior

In the first step the monotonic deformation behavior was characterized. Therefore uniaxial tension and compression, biaxial and planar tests were used. To determine the strong rate and temperature dependence behavior of TPUs, the uniaxial and planar tests were performed with three different rates (0,1 mm/s; 1 mm/s and 200 mm/min) at three different temperature levels (-30°C, RT, and 80°C).

### 2.2 Dynamic Thermomechanical Analysis

A dynamic characterization with focus on the amplitude-, frequency- and temperature dependency of the modulus was studied by DTMA. These data are used to obtain the Prony Series. According to Tschoegl et al. the principle of the use of this approach is only justified if the material shows a thermorheologically simple behavior. If the loss factor follows the storage modulus as a function, the material is defined as thermorheologically simple and in contrast to the general proposition, the method of the superposition and the fitting of the Prony Series can be used [2],[3].

### 2.3 Fatigue Characterization

To determine the longterm behavior of the TPU in terms of cyclic loadings, displacement controlled fatigue tests at room temperature and a frequency of 5 Hz at a constant ratio, the quotient of  $u_{\min}$  to  $u_{\max}$ , of 0,1 were performed. The special methodology for the local strain based Wöhler curve starts with displacement controlled tests at

different amplitudes. The hysteresis are recorded and the number of cycles to failure are determined. To translate the displacements into local strains a Calibration Curve is necessary. Therefore the local strains of the specimen or the component are evaluated. This can be done experimentally with a DIC system, if possible, or numerically with an FE analysis based on a proper material model obtained from the previous generated material data.

Based on the local strain based Wöhler curve, LSWC, a lifetime estimation on a simplified model of an engine mount was done and compared with experimental results. The material models were calibrated with MCalibration 4.3. The component lifetime was estimated with Abaqus 6.14 and nCode 11 from HBM.

### 3. Results

Fig. 1 presents the experimentally determined Wöhler curve of the TPU including the scattering of the data. The more data are available the better is the reliability of the LSWC curve. The hatched area represents the scattering of the specimens lifetime. The fit of all data points (the green line), generated with the JMP software, is based on a Weibull distribution. This data is used for further lifetime calculations.

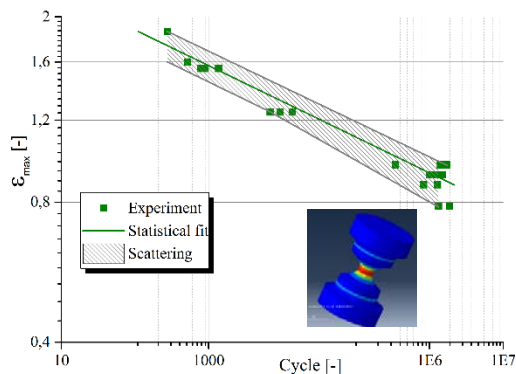


**Fig. 1.** Experimentally determined Wöhler curve

The results and the deviation between the prediction and the experimental data are shown in Fig. 2. The slopes of both curves in the logarithmic plot are quite the same and the curves are following a similar trend. Nevertheless, there is a deviation between the simulated and the experimental determined results. The deviations seem to get larger in the high cycle region. It should be mentioned that the uniaxial limit as well as the endurance limit was not characterized, neither with the specimen or the component. By the fact that only three components were tested, the

scattering of the component tests are not taken into account. However, it should clarify that by fatigue testing and prediction a probability area of failure should always be considered.

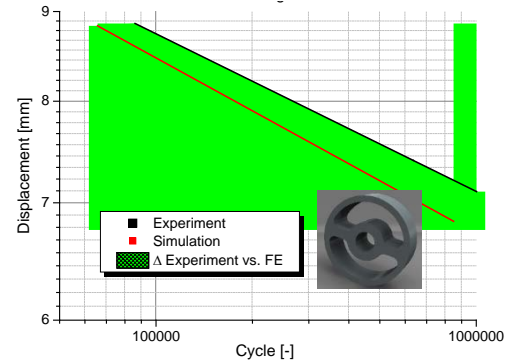


**Fig. 2.** Deviation between predicted lifetime and experimentally determined lifetime of the component.

### 4. Remarks

- The big variety of the mechanical material testing gives a proper understanding of the complex material behavior of TPUs.
- An adequate material model is essential for further component calculations and for the calibration curve.
- Even if there is a big deviation in the simulated and experimental lifetime, the experimentally determined LSWC can be used as a reference on how the fatigue resistance of the material looks like. A lot of data points are required. Even if fatigue testing is a very time- and cost-intensive job, for modern engineering applications it becomes more and more indispensable.

### References

- [1] Qi, H.J., Boyce, M.C., Stress-Strain behavior of thermoplastic polyurethanes, *Mech. Mater.*, vol.37, 2005. pp. 817-839.
- [2] Çakmak, U.D., Major, Z., Experimental Thermomechanical Analysis of Elastomers under Uni- and Biaxial Tensile Stress State, *Exp. Mech.*, vol.54, 2014. pp. 653-663.
- [3] Tschoegl, N.W., Knauss, W.G., Emir, I., The Effect of Temperature and Pressure on the Mechanical Properties of Thermo- and/or Piezorheologically Simple Polymeric Materials in Thermodynamic Equilibrium-A critical review, *Mech. Time-Depend. Mater.*, vol.6, 2002. pp. 53-99.

# NUMERICAL AND EXPERIMENTAL ANALYSIS OF STRESS OF A SEMI-ELLIPTICAL SPRING

Mariusz Stańco<sup>1</sup>, Artur Iluk<sup>1</sup>, Paulina Działak<sup>1</sup>

<sup>1</sup> Wrocław University of Science and Technology, Department of Mechanical Engineering,  
Lukasiewicza 7/9, 50-371 Wrocław, Poland. E-mail: [mariusz.stanco@pwr.edu.pl](mailto:mariusz.stanco@pwr.edu.pl), [artur.iluk@pwr.edu.pl](mailto:artur.iluk@pwr.edu.pl), [paulina.dzialak@pwr.edu.pl](mailto:paulina.dzialak@pwr.edu.pl)

## 1. Introduction

There are two types of the suspension systems offered for the heavy goods vehicles: pneumatic, based on the airbags and the standard ones using the leaf springs. The suspension is selected for each vehicle individually. Decisive influence on the type of the system has a vehicle's purpose. In the military vehicles, suspension systems based on the leaf springs prevail significantly.

## 2. Object specification

A research object, subjected to the numerical and experimental analysis, was the leaf spring. This element is utilized in heavy-duty vehicles, operated in very difficult site conditions. It is used as a spring element in the frontal axis of three and four axle vehicles. A general view of the analysed object is shown in figure 1. It is comprised of the nine leaves with a variable length. The value of a nominal stiffness of the examined spring was defined and it was around 330N/mm.

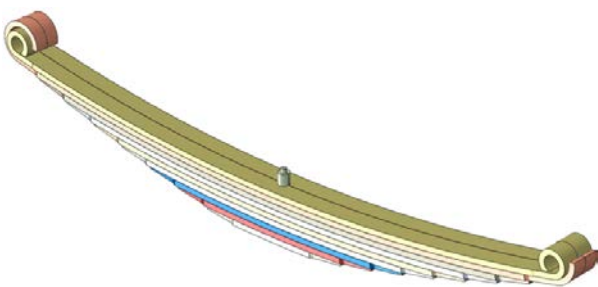


Fig. 1. General view of a leaf spring.

## 3. Experimental testing

In order to determine the number of cycles, which the analysed spring is able to resist, a specific test stand was built. It enabled to conduct a fatigue test of a complete object in a controlled way (fig. 2).



Fig. 2. Testing rig.

The type of a cover of the spring strongly influence the stiffness and the operation of the element. The authors managed to recreate the mounting of the leaf spring on the vehicle. In the middle part of the object the deflection was restricted by the clamp. The endings of the element were placed on the rollers. It enabled unlimited length change during the spring deflection.

The examination was conducted continuously, by the control of the displacement. The aim of the research was to determine the number of cycles with the maximal bend deflection, which the spring can resist.

The experiment was ended after 76 thousands of cycles, when the cracks on the both sides of the mounting between the spring and the frontal axis appeared.



Fig. 3. Cracks on the object examined on a test stand.

#### 4. Numerical model

The experimental study [1-3] enable only spot measurement of the stresses and displacements. Complete overview of the results is possible through the numerical analysis.

A computational model [4] of the examined spring was created (fig. 4). It reflected all the necessary geometric features of the object. Due to the existing symmetry of the geometry and of the loading, the calculation was made for only a half of the model. Boundary conditions, enabling this type of the analysis were used. The loads acting between the leaves of the spring was considered by applying a proper contact connection.

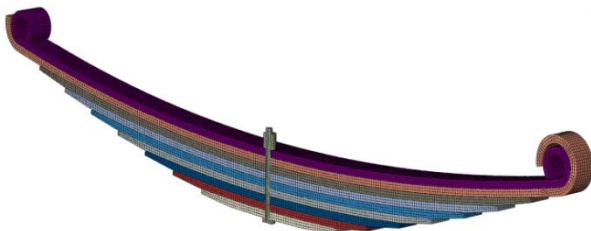


Fig. 4. Discrete model of the analysed leaf spring.

In order to verify a numerical model, comparison of the computational and experimental examination was made. The authors compared received strains, displacements and the reaction forces. There was a broad convergence of the obtained results (fig. 5).

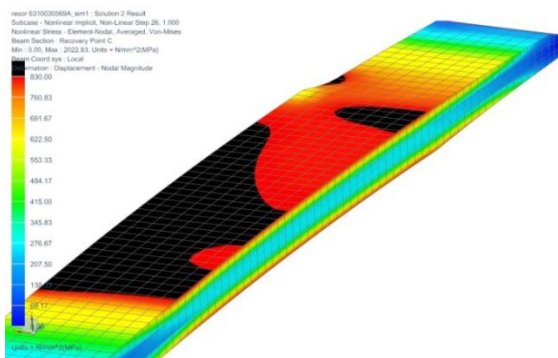


Fig. 5. Distribution of stress contour lines reduced based on H-M-H hypothesis in leaf no. 7.

After adjustment of the numerical model, the influence of the mounted rubber bumpers on the stress values was examined. Figure 6 presents the analysed object in the initial position and in the moment of maximal deflection of the rubber rolls.

An obtained from the numerical simulation stress contour lines confirmed, that the cracks on the object appeared in the spots where the maximal stresses occurred.

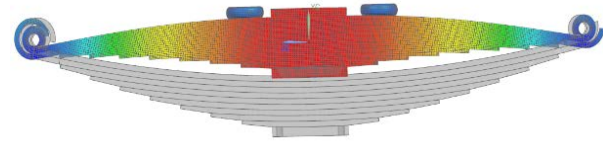


Fig. 6. Displacement contour lines for the maximal deflection of the rubber bumpers.

#### 5. Summary

The experiment and the numerical analysis of the parabolic spring was conducted in order to determine the causes of the crack in the spring structure while operating in the difficult site conditions. On that basis the authors stated that:

- The experimental test established that durability of the analysed spring, while operating on the entire work range, is limited to tens of thousands cycles. It is insufficient number for the vehicle designed for working in the difficult and challenging terrain conditions.
- Numerical simulations confirmed that the cracks appeared in the spots where stress obtained maximal values. It indicates the spring overload, not the material defects.
- The durability of the analysed spring will not allow to exploit the system in the vehicle, which suspension is subjected to the large number of cycles with a high amplitude. Research identified the need of the spring structure modification and/or adjustment of the operating range.

#### References

- [1] Kosobudzki M., Kowalczyk M., Stańco M.: Aktywizacja obciążeń dynamicznych działających na pojazd generowanych przez układ jezdny, *Transport Przemysłowy*, 2007, Vol. 4, pp. 82-85.
- [2] Kosobudzki M, Stańco M. The experimental identification of torsional angle on a load-carrying truck frame during static and dynamic tests. *Maintenance and Reliability* 2016; 18 (2). pp. 285–290.
- [3] Stańco M., Kosobudzki M.: The loads identification acting on the 4x4 truck. *Materials Today* 2016, Vol. 3(4), pp. 167-170.
- [4] Rusiński E.: *Zasady Projektowania Konstrukcji Nośnych Pojazdów samochodowych*. Oficyna Wydawnicza Politechniki Wrocławskiej. Wrocław 2002.

# MEASURING STABILITY OF MILLING PROCESS

Zoltan Dombovari<sup>1</sup>, Dániel Varga<sup>1</sup>, Gabor Stepan<sup>1</sup>

<sup>1</sup> Department of Applied Mechanics, Budapest University of Technology and Economics, Budapest H-1521, Hungary. E-mail: dombovari@mm.bme.hu

## 1. Introduction

This work presents a case study about measuring milling process vibrations. The presented study concentrates on determining linear stability boundaries by keeping in mind the possible involvement of nonlinear effects. The paper includes measurement of the dynamic structure of the machine tool, force measurement of the workpiece material and prediction of stability boundaries. The measurement shown here is a preliminary work of proving so-called unsafe zone [1] exists in milling.

Nowadays, the virtual design of machines pretty much replaced with traditional designing techniques. Engineers can assemble machines in 3D environment routinely. Physical calculations like volume, mass, moment of inertia's and elastic static stress and strain fields are easily calculated in virtual environment. However, vibrations in general, requires specific modelling of part connections and nonlinear effects, which behaves differently in different frequency ranges, and extremely difficult to measure and simulate. Machine tools are subjected to these phenomena, that makes modelling of these important manufacturing processes demanding. Therefore, hybrid semi-analytical models still play important role in predicting machining behavior.

The basic modelling of regenerative vibrations appearing in e.g. turning, milling, boring was first explained in the Pioneering works of Tlustý and Tobias. The mathematical modelling of the governing delayed differential (DDE) was widely discussed in [4]. The stationary cutting is the required vibratory state of a given machining process. In the case of autonomous (time independent) turning process this is only a simple deflection, while in case of non-autonomous milling that is an unavoidable time periodic vibration. The industrial requirement is to have stable stationary cutting solution, which requires of calculating the stability properties of the corresponding DDE model.

There are plenty of methods dealing with the stability of the resulting linearized DDE. In the industry dynamics usually described by frequency response functions (FRF's) that can be easily included in D-subdivision and Hill's representation for autonomous and time periodic DDE's, respectively. This gave the rise of the zeroth order solution (ZOA) [2] and multi-frequency solutions (MF) [2]. Among many time domain based methods, the one, which is easy to use is the semi-discretization (SDM) [3] fully satisfies industrial demands in terms of precision and efficiency.

## 2. Machine Dynamics

The reflected dynamics on the tip of the milling cutter was measured by a micro accelerometer and excited by modal impulse hammer (Fig. 1). We assumed the tiny accelerometer and its cord do not affect the measurement significantly. The measurement showed that using different force levels the reflected FRF's differ in frequency and flexibility (Fig. 2).

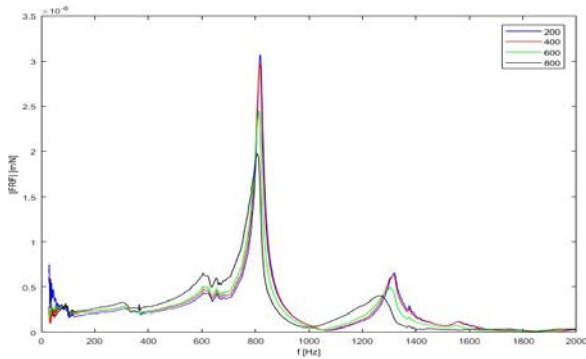


Fig. 1. Measurement arrangement

Regardless of the level of changing, it is important to emphasize that the peak level force for the impulse excitation distributes in the active frequency range. This results in tiny roughly a Newton level of excitation<sup>1</sup>, which is far from the realistic excitation level of the cutting force. That is, even small changes in flexibility and natural frequencies can be a sign of more dramatic change in-operation dynamics.

In calculation-wise, we performed fitting on FRF's using traditional RFP fitting algorithm. Since we have no access for in-operation

measurement, then, we performed stability predictions using all available FRF's assuming linear dynamics for the tool-spindle assembly.



**Fig. 2.** FRF for different force peak levels representing the slightly changing dynamics.

### 3. Force Modell

The empirical force model [1] was determined performing stable  $1/4$  down-milling shoots cutting a workpiece fixed on a dynamometer plate. The empirical force characteristics was calculated from the averaged cutting forces by the method presented in [2] for cylindrical milling cutters.

$$\mathbf{f}(h) = \begin{bmatrix} f_t(h) \\ f_r(h) \\ f_a(h) \end{bmatrix} = \begin{bmatrix} K_{t,c}h + K_{t,e}(1 - e^{-E_t h}) \\ K_{r,c}h + K_{r,e}(1 - e^{-E_r h}) \\ K_{a,c}h + K_{a,e}(1 - e^{-E_a h}) \end{bmatrix}. \quad (1)$$

After performing force measurements for different cutting speeds a set of averaged parameters are determined (see Tab. 1.) for the Al 2024 T351 workpiece material.

$K_{t,c}$ (MPa)	$K_{t,e}$ (kN/m)	$E_t$ ( $10^3/m$ )
1015	30	1/0.009
$K_{r,c}$ (MPa)	$K_{r,e}$ (kN/m)	$E_r$ ( $10^3/m$ )
185	40	1/0.012

**Tab. 1.** The fit parameters of the force model (1).

### 4. Stability of Milling Process

After having fitting on the presented FRF's the linear stability boundaries of the milling process are calculated. Remark that, since the machine is nonlinear neither the fitting nor the linear stability prediction of the stationary solution are mathematically correct. The real motivation here was to show what errors can be made only by fitting wrong data on not carefully measured dynamics of the machine.

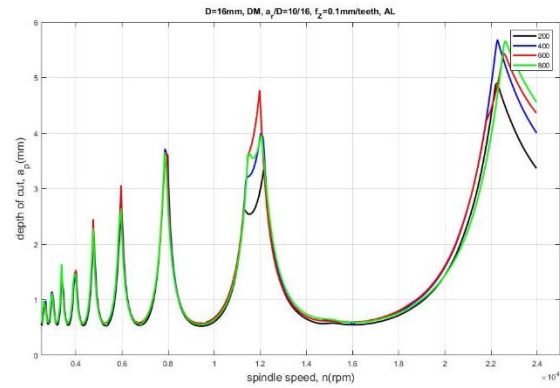


**Fig. 3.** Stability diagram

The stability boundaries were calculated by semi-discretization [3], in which cutting coefficients were calculated using (1) “around” the stationary solution.

### Conclusion

Machines tools (spindle) often show nonlinear stiffening characteristics. Impact test excitation level is not comparable with in-operation excitation level. The stability boundaries are determined by correct linearization, although the dynamics was considered linear for one specific force level due to the lack of correct nonlinear structural model of the machine tool.

### Acknowledgements

The research leading to these results has received funding partially from the ERC uunder the EU's 7<sup>th</sup> (FP/2007-2013)/ERC Advanced grant agreement no. 340889 and Hungarian Scientific Research Foundation OTKA grant no. K108779

### References

- [1] Dombovari, Z., Stepan, G., On the Bistable Zone of Milling Processes, Philosophical Transactions of the Royal Society A Issue, 373(2051), 2015.
- [2] Altintas, Y., Manufacturing Automation: Metal Cutting Mechanics, Machine Tool Vibrations, and CNC Design. Cambridge University Press, Cambridge, 2000.
- [3] Insperger, T., and Stepan, G., Semi-discretization method for delayed systems. International Journal for Numerical Methods in Engineering, 55, 2002, pp. 503–518.
- [4] Hale, J., Theory of functional differential equations. Springer-Verlag, New York, 1977.

## ON THE CRUCIFORM SPECIMENS FOR MATERIALS TESTING

Tadeusz Szymczak<sup>1</sup>, Zbigniew L. Kowalewski<sup>2</sup>

<sup>1</sup> Motor Transport Institute, Centre for Material Testing, ul. Jagiellonska 80, 03-301, Warsaw, Poland. E-mail: [tadeusz.szymczak@its.waw.pl](mailto:tadeusz.szymczak@its.waw.pl)

<sup>2</sup> Institute of Fundamental Technological Research, Department for Strength of Materials, ul. Pawinskiego 5B, 02-106, Warsaw, Poland. E-mail: [zkowalew@ippt.pan.pl](mailto:zkowalew@ippt.pan.pl)

### 1. Introduction

Examination of material behaviour is conducted by the use of various kinds of specimens. Among them one can distinguish: cylindrical, tubular or cruciform. Each specimen type is attributed to selected kind of experiment. For determination of typical mechanical properties such as: Young's modulus, yield point and ultimate tensile strength, which are necessary for analytical or numerical calculations, cylindrical specimens are mostly used. In the case of material examination under complex stress state being combination of axial force and twisting moment the thin-walled tubular specimens are most suitable. The cruciform specimens are usually applied for tests being performed at two axial stress components acting in two mutually perpendicular directions. Such specimens may be applied to investigate plastic flow [1], determination of material resistance on brittle fracture (Fig. 1) [2], and fatigue [3]. Plastic flow is usually tested by means of cruciform specimens having measurement sections in a shape of square, Fig. 3.

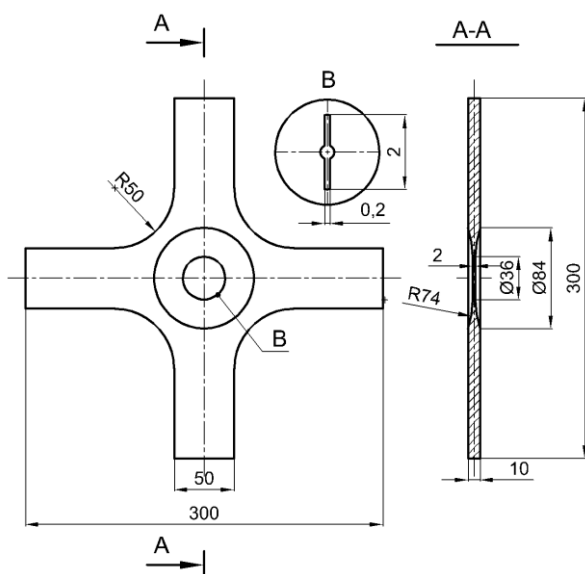


**Fig. 1.** Cruciform specimen for fracture mechanics [2].

Fracture mechanics requires specimens possessing notch located in the centre of measurement zone, while fatigue process can be investigated using specimens of circular section [3]. A condition of high stress distribution uniformity in the measurement part of specimen is not trivial task. Therefore, many research groups use analytical, statistical and numerical (FEA) methods to optimize a geometry of the measurement section and specimen's dimensions [3, 4, 5].

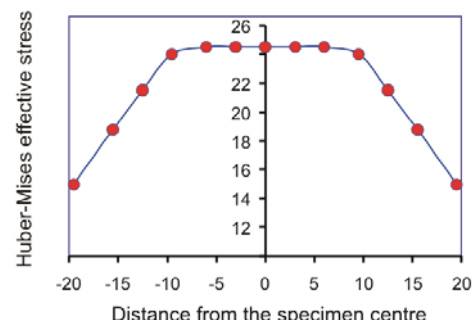


**Fig. 2.** Huber-Mises stress at circular measurement zone of cruciform specimen for fatigue tests [3].

Application of various calculating methods enables to obtain even 80% increase of stress distribution uniformity. Final results can be in a form of stress state components isolines [4] or simple equations [5]. The Huber-Mises effective stress values after optimization are shown in Fig. 2 [3].

Material characterisation on cruciform specimens is usually performed on biaxial testing machines. This type of equipment is typically designed to have four servomotors, which act by means of two digital feedback close loops [3]. With respect to servomotors configuration, two variants of the testing machines are usually produced: the loading frame is a vertical configuration with the actuators mounted at 45° [7] or 90° from the vertical, [6]

In the case of a typical configuration of the cruciform testing machine (90°) an influence of specimen weight on the collected results occurs. If the servomotors arrangement is determined by the angle of 45° from the vertical then the effect disappears. The problems mentioned above indicate that investigations on cruciform specimens are quite difficult and not sufficiently recognized yet. Therefore, further studies are necessary in order to get more thorough knowledge related to cruciform specimens testing. The paper is an attempt in this area. Certain progress can be achieved by means of investigations supported by Finite Element Analysis.

## 2. Numerical procedure

To extend the knowledge of experiments conducting on the cruciform specimens, the Kelly's specimen design was selected [1]. Application of this type specimen for plastic flow and creep analysis was the main motivation of this paper.

The Kelly's specimen was modelled using Patran/Nastran software. 3D Hex 8 elements were applied. Data representing linear stress-strain relationship of material and Young's modulus of 2.1 GPa were implemented to the software. MultiPoint Constrain (MPC) was used to simulate tension in both perpendicular directions.

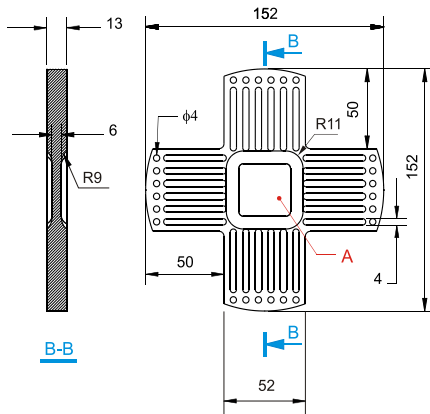


Fig. 4. Kelly's cruciform specimen [1].

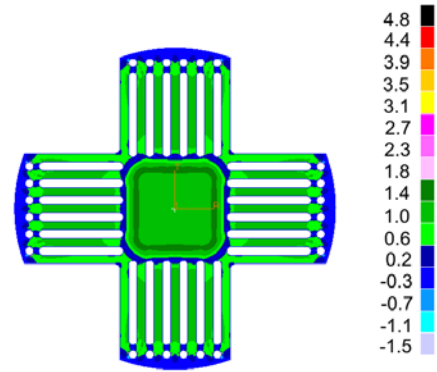


Fig. 5. Radial stress distribution.

FEA results show the uniform distribution of radial stress in almost 90% area of the measurement zone, Fig. 5. For tangential stress even better uniformity was obtained (97%). Stress distribution in 0z direction on 0xy plane was similar to the radial stress distribution map, while in a perpendicular cross section the stress gradient was observed due to the radius between measuring and gripping sections, Fig. 6.

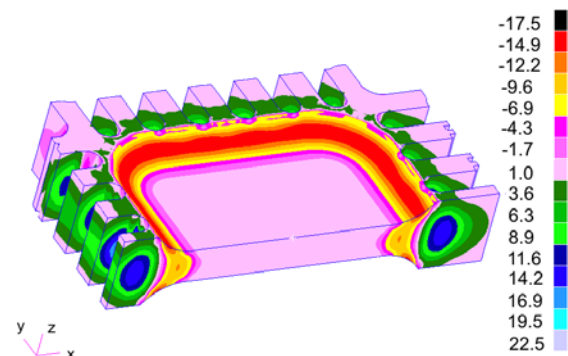


Fig. 6. Distribution of  $\sigma_{zz}$  stress.

## 3. Summary

Determination of stress distribution in 3D coordinate system enables to reach differences in distribution of stress state components important for strain measuring.

## References

- [1] Kelly D.A., Problems in creep testing under biaxial stress systems, J. Strain Analysis, 11, 1976. pp. 1-6.
- [2] Hatanaka K et. al., A study on fatigue crack growth under biaxial loadings using cruciform specimen, 5<sup>th</sup> Int. Conf. Biaxial/Multiaxial Fatigue and Fracture, Poland, 1997, pp. 59-76.
- [3] Ogata T., Takahashi Y., Development of high temperature biaxial fatigue testing machine



using a cruciform specimen, 5<sup>th</sup> Int. Conf. Biaxial/Multiaxial Fatigue and Fracture, Poland, 1997, pp. 5257-272.

- [4] Demmerle S., Boehler J.P., Optimal design of biaxial tensile cruciform specimens, J. Mech. Phys. Solids, 41, 1993, pp. 143-181.
- [5] Makinde A., et al., Development of an apparatus for biaxial testing using cruciform specimens, Exp. Mech., 32, 2, 1992, pp. 138-144.
- [6] [www.mts.com](http://www.mts.com).
- [7] [www.instron.com](http://www.instron.com).

# INVESTIGATION OF THE CHIP FORMATION USING HIGH-SPEED CAMERA AND FINITE ELEMENT METHOD

Attila KOSSA<sup>1</sup>, Gabor STEPAN<sup>2</sup>

- <sup>1</sup> Budapest University of Technology and Economics, Department of Applied Mechanics, Muegyetem rkp. 5., Budapest, 1111 Hungary. E-mail: [kossa@mm.bme.hu](mailto:kossa@mm.bme.hu)
- <sup>2</sup> Budapest University of Technology and Economics, Department of Applied Mechanics, Muegyetem rkp. 5., Budapest, 1111 Hungary. E-mail: [stepan@mm.bme.hu](mailto:stepan@mm.bme.hu)

## 1. Introduction

Cutting can be considered as one of the most important material removal processes. It is well known, that even small enhancement of a machining process can cause significant cost reduction and quality improvement. Better understanding of the relation between machining parameters (cutting speed, feed rate, depth of cut, etc.) and output variables (cutting forces, temperature field, surface roughness, chip morphology, etc.) could be a key to such improvements. This goal requires the accurate description of the chip formation process.

In the last few decades, significant research effort has been invested into the development of computational methods and their implementations regarding to the simulation of various cutting processes. Researchers widely use the finite element method to analyze various cutting processes. However, it should be emphasized, that there is no agreement how to properly model the cutting mechanisms. Consequently, the results delivered by a finite element analysis (FEA) could be inaccurate. Comparison of the experimental and the numerical results is essential to understand the underlying phenomena.

This article investigates, in detail, the results obtained using FEA compared to the experimental observations for planning processes.

## 2. Experiments

### 2.1 High-speed camera recordings

The chip formation processes were recorded using high-speed camera. A Photron Fastcam SA5 775K C3 high-speed camera equipped with a Nikon Nikkor 200mm f/4D AF macro lens was used to capture the chip formation in a planning processes. The setup is illustrated in Fig. 1. Some

sample images are shown in Fig. 2. The machining was carried out on a CNC machining center, NCT EmR-610Ms. The material of the specimen was aluminium A2024-T351.

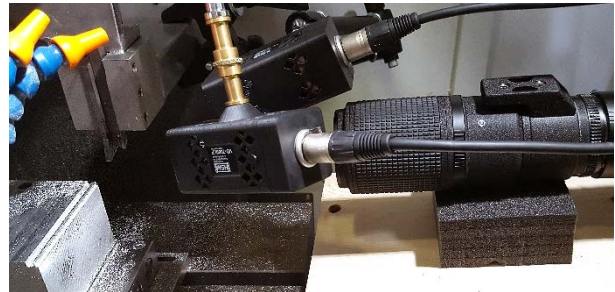


Fig. 1. High-speed camera setup.

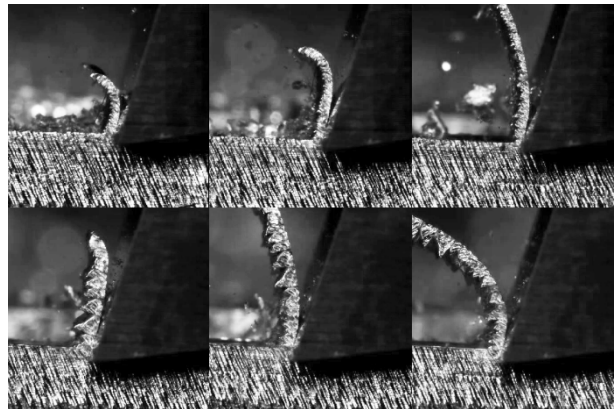


Fig. 2. Chip formation process. Images are extracted from high-speed recordings.

### 2.2 Force measurement

The cutting forces were measured with a multi-component dynamometer (Kistler 9129AA), an adherent multicomponent charge amplifier and a data acquisition device (National Instrument NI cDAQ-9178).

The cutting forces measured in the planning direction (x) and perpendicular (y) to it are plotted in Fig. 3-4. for various rake angle  $\gamma$ . Parameter  $a$  denotes the depth of cut.

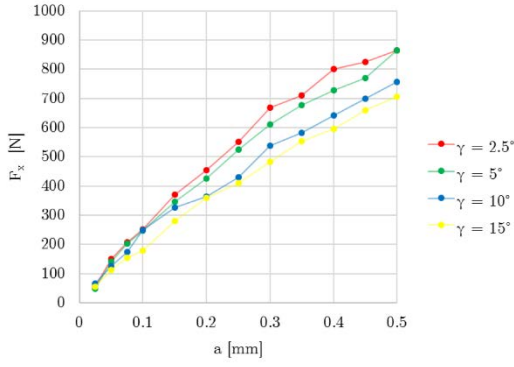


Fig. 3. Average cutting forces in direction x.

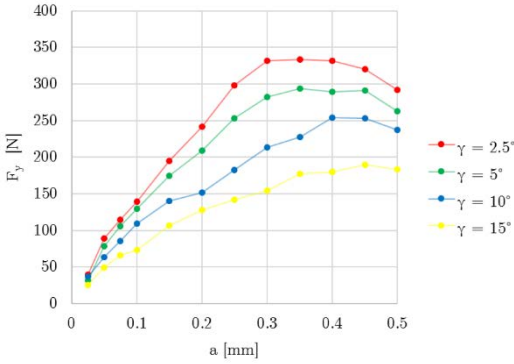


Fig. 4. Average cutting forces in direction y.

### 3. Finite element analysis

The planning process was simulated by two dimensional FE models using the commercial finite element software ABAQUS 2016.

Coupled thermo-mechanical analyses were carried out to include thermal effects. We used sacrificial layers to simulate the cutting mechanisms.

The material behavior was characterized by Johnson-Cook model, where the yield stress at non-zero strain rate is defined as

$$\bar{\sigma} = \left[ A + B(\bar{\epsilon}^{pl})^n \right] \left[ 1 + C \cdot \ln \left( \frac{\dot{\bar{\epsilon}}^{pl}}{\dot{\epsilon}_0} \right) \right] \times \left[ 1 - \hat{T}^m \right] \quad (0.1)$$

$\bar{\epsilon}^{pl}$  denotes the equivalent plastic strain and  $A$ ,  $B$ ,  $n$ ,  $C$ ,  $\dot{\epsilon}_0$  and  $m$  are material parameters measured at or below the transition temperature  $T_t$ . The dimensionless temperature field  $\hat{T}$  is defined as

$$\hat{T} \equiv \begin{cases} 0 & \text{for } T < T_t \\ \frac{T - T_t}{T_m - T_t} & \text{for } T_t \leq T \leq T_m \\ 1 & \text{for } T > T_m \end{cases} \quad (0.2)$$

where  $T_m$  is the melting temperature. The Johnson-Cook dynamic failure model was applied in this analysis to determine the fracture initiation strain. The plastic strain at failure is calculated by

$$\bar{\epsilon}_f^{pl} = \left[ d_1 + d_2 \exp(-d_3 \eta) \right] \left[ 1 + d_4 \ln \left( \frac{\dot{\bar{\epsilon}}^{pl}}{\dot{\epsilon}_0} \right) \right] \times \left[ 1 + d_5 \hat{T} \right], \quad (0.3)$$

where  $\eta = \text{tr}(\boldsymbol{\sigma}) / (3\bar{\sigma})$  is the stress triaxiality and  $d_1 \dots d_5$  are material parameters. Failure is assumed to occur when the damage parameter

$$\omega = \sum \left( \frac{\Delta \bar{\epsilon}^{pl}}{\bar{\epsilon}_f^{pl}} \right) \quad (0.4)$$

exceeds the critical value 1. Different damage evolution rules ( linear, exponential ) were tested in the simulations. The heat generated by the plastic dissipation and the friction was included in the model. The contact behavior of the tool-chip interface was modelled using modified Columb friction law.

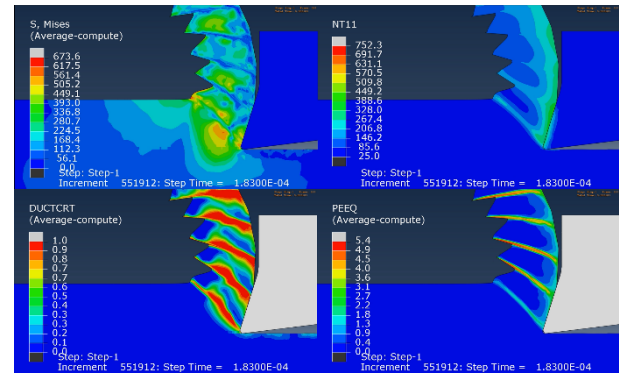


Fig. 5. Finite element simulation of the chip formation process.

### Acknowledgements

The research leading to these results has received funding from the European Research Council under the European Union's Seventh Framework Programme (FP/2007-2013) / ERC Advanced Grant Agreement n. 340889.

# CHARACTERIZATION OF THE TEMPERATURE BEHAVIOR OF A PIEZORESISTIVE ACCELEROMETER

Matthias Bartholmai, Klaus-Dieter Werner, Sergej Johann, Werner Daum

BAM Federal Institute for Materials Research and Testing, Unter den Eichen 87, 12205 Berlin, Germany. E-mail: [matthias.bartholmai@bam.de](mailto:matthias.bartholmai@bam.de)

## 1. Introduction

Piezoresistive accelerometers use a strain-sensing element, generally made of semiconductor material, e.g., silicon to convert the mechanical motion into an electrical signal. This element is usually designed in form of a cantilever beam loaded with a mass. Acceleration causes bending of the beam, which produces a change of electrical resistance proportional to the applied acceleration. Main advantages of piezoresistive accelerometers in comparison to other types, e.g., piezoelectric and capacitive, is their robust and highly dynamic behavior, which qualifies them for application in high impact shock applications. Mechanical damping is typically implemented with silicon oil in a way that the output signal is undistorted over a wide frequency range. These characteristics principally qualify them for the application in drop tests carried out at BAM [1], for which they are calibrated over the frequency range from 1 to 4 kHz. However, using silicon oil for damping, has the drawback of temperature dependent change of its viscosity, leading to temperature dependent deviation of the accelerometer's sensitivity.

This study presents experimental results of the temperature behavior of a piezoresistive accelerometer with a dynamic range up to  $\pm 5000$  g. This type of accelerometer is applied for drop tests which are partially performed at temperatures of  $-40$  or  $+100$  °C.

## 2. Experimental method and setup

BAM uses a Hopkinson Bar to characterize accelerometers for their application in drop tests corresponding to ISO 16063-13:2001 [2]. Its mode of operation is based on the propagation of an elastic shock wave in a long and thin bar. An independent measuring reference is given through a laser vibrometer. By combining a Hopkinson Bar with a temperature chamber [3], a method was implemented to test and characterize

accelerometers at conditions corresponding accurately to drop test scenarios (Fig. 1).



Fig. 1. Hopkinson Bar with its front end integrated in a temperature chamber.

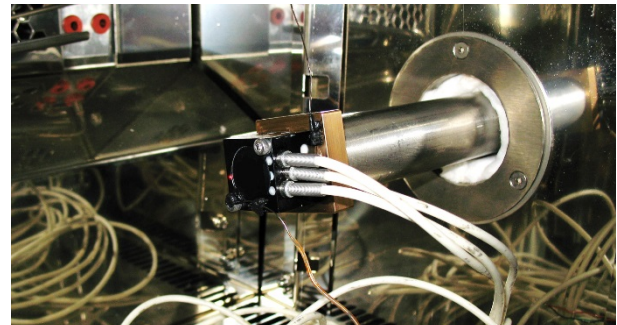
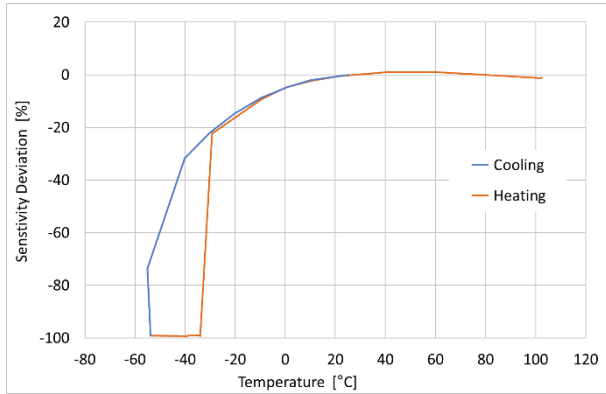


Fig. 2. Front end of the bar with an attached three-axial piezoresistive accelerometer.

Fig. 2 shows the piezoresistive accelerometer attached to the front end of the bar inside the temperature chamber. To characterize its temperature behavior Hopkinson Bar tests were performed between temperatures of  $-55$  and  $102$  °C, starting at room temperature of  $25$  °C, going stepwise down to  $-55$  °C with exposure times of minimum 1 h. Correspondingly to drop tests, the exposure at  $-55$  °C was kept for about 48 h. This time is required to assure the temperature adaption of the whole drop object. Subsequently, temperature increase was applied stepwise up to  $102$  °C, again with exposure times of minimum 1 h. At each temperature step a Hopkinson Bar test was performed with dynamic impact of ca. 1000 g.

### 3. Results

Fig. 3 displays the temperature dependent deviation of sensitivity of the accelerometer, normalized to the sensitivity at 25 °C. The sensitivity is averaged over excited frequencies from 1 to 4 kHz.



**Fig. 3.** Temperature dependent sensitivity deviation from 1 to 4 kHz.

By manufacturer's data the sensor's storage and operating temperature reaches from -40 to 120 °C with temperature compensation from 20 to 80 °C. The test results clearly confirm the temperature compensated range with sensitivity deviations in the range  $\pm 1.5$  %. However, for operation at temperatures below 20 °C a considerably lower sensitivity must be respected, with a deviation of -22 % at -30 °C. While the sensor was basically functioning at -40 °C during the stepwise cooling process, it failed after 48 h exposure at -55 °C, what is the usual cooling procedure for drop test at -40 °C. During stepwise heating and testing, the accelerometer only showed functioning at -30 °C, again. The following sensitivity results were approximately the same as before cooling.

Another interesting aspect is the frequency response of sensitivity at different temperatures. Fig. 4 shows the results during the cooling process, while Fig. 5 displays the results for the subsequent heating process, each normalized to 25 °C and 1000 Hz. For temperatures above 20 °C the typically stable output signal can be found over the frequency range up to 6000 Hz. In contrast, at lower temperatures the sensitivity decreases, particularly with increasing frequency. This behavior clearly illustrates the temperature characteristics caused by using silicon oil for the damping mechanism. The increase of viscosity limits the dynamic of the sensor at low temperatures, resulting in clearly reduced average

sensitivity and dramatically reduced sensitivity at high frequencies.

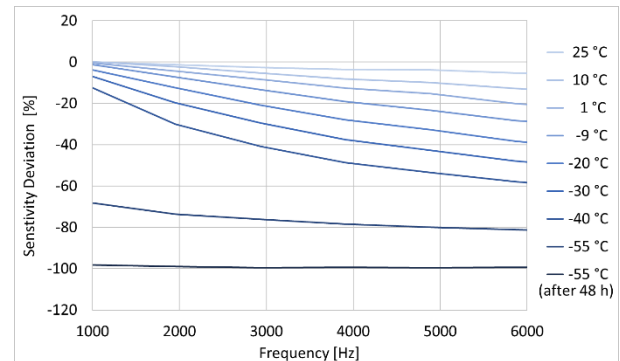


**Fig. 4.** Frequency response of sensitivity at different temperatures during the cooling process.

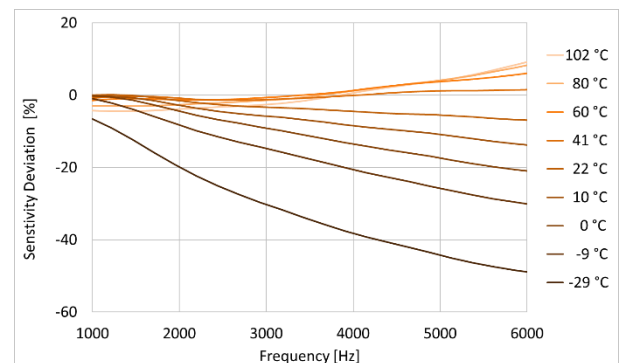


**Fig. 5.** Frequency response of sensitivity at different temperatures during the heating process.

### 4. Remarks

- Conclusively, it is important to consider the reduced sensitivity of piezoresistive accelerometers at temperatures below 20 °C and possible failure at temperatures below -30 °C.
- Additionally, the dynamic of the application has to be respected, since measurements with frequencies above 1000 Hz are mostly affected.
- However, for application at temperatures close to their operation limits, it is reasonable to calibrate any accelerometers in good accordance with application conditions.

### References

- [1] Musolff, A., et al., Impact Analysis of RAM Packages under Kinematic Aspects, Proceedings 18th PATRAM 2016, pp. 1030 ff.
- [2] ISO 16063-13:2001: Methods for the calibration of vibration and shock transducers.



- [3] Bartholmai, M., et al., Hopkinson bar method for temperature dependent testing and calibration of accelerometers, Proceedings 31st Danubia Adria Symposium 2014, pp. 244-245.

# MOTION CAPTURE SYSTEM VALIDATION WITH SURVEYING TECHNIQUES

Gergely Nagymáté<sup>1</sup>, Rita M Kiss<sup>1</sup>

<sup>1</sup> Budapest University of Technology and Economics, Faculty of Mechanical Engineering, Dept of Mechatronics, Optics and Mechanical Engineering Informatics, Hungary. E-mail: nagymate@mogi.bme.hu, rikiss@mail.bme.

## 1. Introduction

Studies with motion capture measurements should always consider system errors when evaluating their results, but it's rarely done. Validation studies evaluate the accuracy of motion capture systems in the form of measuring the detected deviations of coordinate distances of rigidly fixed markers in various places of the measuring volume [1]–[4], or by measuring small relative translations [5]. The present study aims to analyze the absolute volume accuracy of a 18 camera OptiTrack Flex13 motion capture system using a geodetic reference points.

## 2. Methods

### 2.1 Setup

The independent control network used for the quality control of the OptiTrack system has been created as a 0.5m raster grid with the total dimension of 4m x 2.5m. The grid points of the control network was set out using a Leica TS15i 1" Total station. The local coordinate system was aligned approximately with the orientation of the grid. We considered important to check the marked control points with independent measurements. The coordinates of the two independent observations were compared, and the mean three dimensional coordinate residual between the two measurements was 0.758 (0.315) mm with maximum residual of 1.672 mm. The final coordinates of the control points were calculated as the mean value of the two coordinate solutions. Thus it can be stated that the accuracy of the coordinates of the control network is 1mm in the worst case scenario.

### 2.2 Measurement protocol

Retro reflective markers (diameter: 8mm) are used for all motion capture measurements. These markers were placed on the geodetic reference points onto their bore on the bottom with the

possible largest precision to measure the reference positions by the OptiTrack system (Fig. 1). However, this process includes human inaccuracy on the placement of the markers. Therefore to give a statistical basis for the marker placement the whole process was repeated by four people, 10 repetition each. The average coordinate of the 40 repetition of each calibrated reference point will approach the true position of the reference points. Measurements were recorded in the Motive software (NaturalPoint, OR, USA) for 30 seconds, at 120 Hz.



**Fig. 1.** IR marker placed on the geodetic reference point.

### 2.3 Determination of absolute accuracy

The comparison requires the matching of the geodetic and the OptiTrack coordinate system. OptiTrack coordinate system can be assigned with three markers designating the origin, a point on X axis and a point on X-Z plane. Three of the geodetic reference points were used for this purpose to define a simple transformation between the two coordinate systems. Two dimensional deviations between the coordinates of the geodetic reference points and the average coordinates of the repeatedly placed markers measured by the OptiTrack system were analyzed. Mean, standard

deviation and RMS of the 2D deviations and correlation between the observed error and the distance from the origin was calculated to characterize the error of the system.

### 3. Results

Results on the comparison of reference coordinates and measured average coordinates of the markers showed significantly larger deviations than the reliability of the reference coordinates. The errors are characterized by RMS deviation: 1.735 mm, average deviation: 1.576 (SD: 0.733 mm) and maximum deviation of 3.072 mm. Deviations of the marker coordinates from the reference coordinates showed strong correlation to their distance from the reference frame origin (correlation: 0.81). This high positive correlation suggested that there must be a scaling factor behind the observed errors as seemingly the virtual space is a bit larger than the real space.

The observed average error vectors of each measured points are indicated on Fig. 2. Error vectors are displayed in hundredfold magnification for sufficient visibility.

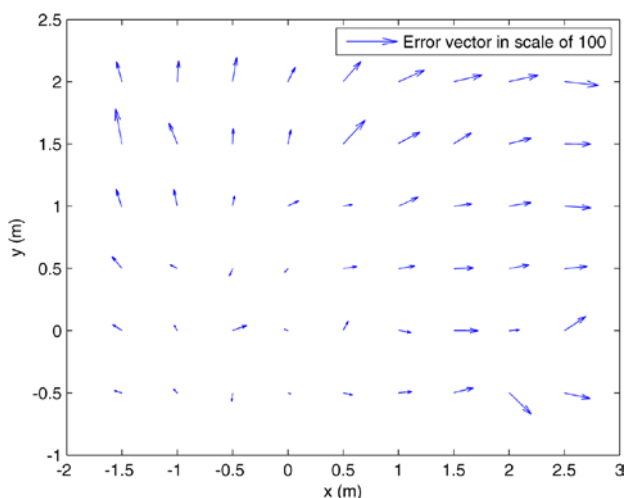


**Fig. 2.** 2D deviation vectors of the detected average marker coordinates and the geodetic references. Vector magnitudes are scaled with 100% for visibility.

### 4. Remarks

- The study analyzed the absolute accuracy of a 18 camera OptiTrack Flex 13 motion capture system using geodetic reference points, which method is capable to detect inaccuracies of the system that are undetectable using conventional camera system validation methods.

- A distance dependent distortion in the measurement volume was detected that is owed to scaling errors that can be compensated after detection.
- Similar validations should be performed on every camera system that is used for precise robotic or human motion analysis.

### Acknowledgement

This work was supported by the Hungarian Scientific Research Fund OTKA [grant number K115894]; and the New National Excellence Program of the Hungarian Ministry of Human Resources [grant number ÚNKP-16-3-I].

### References

- [1] B. Carse, B. Meadows, R. Bowers, and P. Rowe, Affordable clinical gait analysis: An assessment of the marker tracking accuracy of a new low-cost optical 3D motion analysis system, *Physiother. (United Kingdom)*, vol. 99, no. 4, pp. 347–351, 2013.
- [2] Y. Ehara, H. Fujimoto, S. Miyazaki, M. Mochimaru, S. Tanaka, and S. Yamamoto, Comparison of the performance of 3D camera systems II, *Gait Posture*, vol. 5, no. 3, pp. 251–255, 1997.
- [3] Y. Ehara, H. Fujimoto, S. Miyazaki, S. Tanaka, and S. Yamamoto, Comparison of the performance of 3D camera systems, *Gait Posture*, vol. 3, no. 3, pp. 166–169, 1995.
- [4] D. Thewlis, C. Bishop, N. Daniell, and G. Paul, Next-generation low-cost motion capture systems can provide comparable spatial accuracy to high-end systems, *J. Appl. Biomech.*, vol. 29, no. 1, pp. 112–117, 2013.
- [5] M. Windolf, N. Götzen, and M. Morlock, Systematic accuracy and precision analysis of video motion capturing systems-exemplified on the Vicon-460 system, *J. Biomech.*, vol. 41, no. 12, pp. 2776–2780, 2008.

# A NEW METHODOLOGY FOR MEASURING THE FLOWABILITY OF GRANULAR MATERIALS

Ragunanth Venkatesh<sup>1</sup>, Marko Bek<sup>1</sup>, Arkady Voloshin<sup>1,2</sup>, and Igor Emri<sup>1</sup>

<sup>1</sup> University of Ljubljana, Faculty of Mechanical Engineering, Aškerčeva cesta 6, 1000, Ljubljana, Slovenia. E-mail: [ragunanth.venkatesh@fs.uni-lj.si](mailto:ragunanth.venkatesh@fs.uni-lj.si), [marko.bek@fs.uni-lj.si](mailto:marko.bek@fs.uni-lj.si), [igor.emri@fs.uni-lj.si](mailto:igor.emri@fs.uni-lj.si)

<sup>2</sup> Lehigh University, Mechanical Engineering, 19 Memorial Dr. West, Bethlehem, PA 18015, USA. E-mail: [avol4607@gmail.com](mailto:avol4607@gmail.com)

## 1. Introduction

Flow of granular material during processing, handling and transportation strongly influences the quality of the final product and its cost. Flowability (ability to flow) of granular materials depends on the characteristics of the material and on the conditions at which the flow is occurring. For example, the pharmaceuticals industries face complications on tablet filling where the flowability of granular materials plays a significant role. If the granular materials flow freely, it can ensure uniform filling of the feed from hoppers into the tableting equipment so that uniform mass and content of the tablet are maintained [1].

The previous paper [2] has proved the concept and working principle of GFA apparatus, a new methodology which was developed for predicting the flowability of powders and in paper [3], Schulze has found the interrelation between GFA index and Janssen's parameters (K-stress ratio and  $\phi$  internal friction angle between particle and wall). Janssen's parameters are standard method for evaluating the flowability of powders and are used for design of silos.

In this paper, the authors are presenting the upgraded GFA apparatus using optical measurement technique called digital image correlation to overcome the drawbacks related to usage of strain-gauges – Optical Granular Friction Analyzer (O-GFA). As an example, soil material was used to demonstrate the working principle of O-GFA.

## 2. Concept and working of GFA

The goal of the GFA is to obtain the pressure profile along the length of the cylinder filled with granular material and to introduce such profile as a measure of internal friction between particles of granular materials. The concept of the GFA is such

that forces through the granular material and the pressure distribution along the length of the cylinder is a measure of how force is transmitted from the piston to the powder and from the powder to the cylinder. In this context, one expects that depending on the friction properties of the powder, the pressure will be transmitted in diversified ways along the cylinder, thus allowing us to obtain a method for determining internal friction between particles and condition at which the granular material will start to move.

Fig.1 illustrates how one can compare the internal friction properties of two granular materials using the GFA. Taking as a reference the pressure profile of a fluid which is constant along the length of the cylinder, one determines if certain powder has higher or lower internal friction by analyzing how steep is the pressure drop along the length of the cylinder, i.e. a granular material with less pressure drop will have lower internal friction (behavior closer to liquid) than another with very rapid pressure drop. Based on the literature, it is expected that powders with a smaller average particle size will exhibit higher internal friction [4,5]; for this reason, Powder 1 in Fig.1 has a much faster pressure drop than Powder 2.

Loading of the granular materials causes deformation to the cylinder, which is in the existing GFA apparatus measured using strain gauges at discrete locations in the axial and tangential direction as shown in Fig.1. From the measured strains, the axial pressure distribution is calculated. The internal friction of the granular material is represented by axial distribution of pressure within the measuring cylinder. As a measure of the internal friction Bek et al., defined a parameter called "GFA" index, defined as

$$GFA_{INDEX} = \frac{S_{granular}}{S_{fluid}} = \frac{\int_0^L p(z) dz}{p_{NF} \cdot L} = \frac{A}{FL} \int_0^L p(z) dz, \quad (1)$$

where  $A$  is the area of the cylinder,  $F$  is the force applied,  $L$  is the length of the cylinder,  $p(z)$  is the pressure obtained along the length of the cylinder for granular materials. The maximum value of the "GFA index" is 1 and indicates that tested granular material does not exhibit any internal friction, i.e., it behaves as a Newtonian fluid.

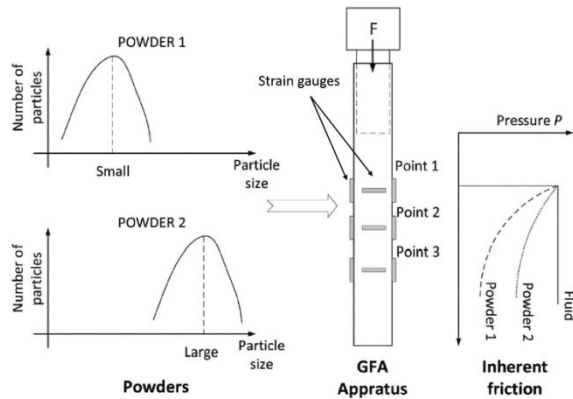


Fig. 1. GFA apparatus (GFA) [2]

### 3. Optical - GFA (O-GFA)

Although the GFA apparatus proved the concepts in powder technology [3-5], it had certain drawbacks. It only had 3 measuring points as shown in Fig.1. By using optical measuring technique, one can increase the number of measurement points and consequently improve the accuracy of GFA index calculation according to Eq.1.

The GFA was upgraded using optical measurement setup commonly called as Digital Image Correlation (DIC). DIC is a non-contact optical experimental setup widely used in the field of experimental mechanics for measuring the surface deformation and characterization of the material. Through the 2D DIC setup one can measure the in-plane deformations (in  $x$  and  $y$  direction).

#### 3.1 Method of experiment

Sand size 0-1mm was used as testing sample. The sand was dried in oven for 5 hours to remove the humidity. Then the dried sand was filled into the entire cylinder length ( $L=295\text{mm}$ ) and experiments were performed at room temperature. The applied load was 6764N (approx. pressure of 26MPa).

#### 3.2 Results

The results show a sharp decrease of pressure profile along the length of the cylinder. The

pressure drop is a strong indication that internal friction was large resulting in self-locking of sand particles.

The results, shown in Fig.2, clearly demonstrate that by using O-GFA one can obtain more number of measurement points, which improves the accuracy of GFA-index calculation.

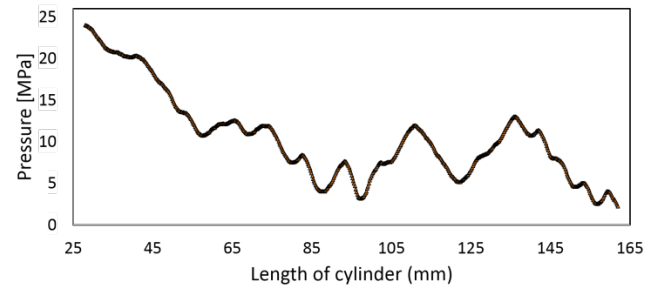


Fig. 2. Normal pressure profile calculated along the axial direction of the cylinder

### 4. Summary and conclusions

- A new upgraded granular friction analyzer (O-GFA) was developed for evaluating the internal friction between granular particles.
- The number of measurement points were increased from 3 (GFA) to more than 100, which substantially improves the accuracy of GFA-index computation.

### Acknowledgements

The authors would like to thank the financial support of the Slovenian Research Funding Agency (research program - P2-0264) and the young researcher grant (39190).

### References

- [1] Kato, Y., Ohkuma, M., Shimada, Y., Sunada, H., Evaluation of flowability of surface-modified preparations by the measurements of the inter-particle adhesive force, *J. Drug dev. Sci. Tech.* (2005) 217–222.
- [2] Bek, M., Gonzalez-Gutierrez, J.A., Moreno Lopez, Bregant, D., Emri, I., Apparatus for measuring friction inside granular materials — Granular friction analyzer, *Powder Technol.* 288 (2016) 255–265.
- [3] Schulze, D., Comment on the paper “Apparatus for measuring friction inside granular materials – granular friction analyzer”, Marko Bek et al., *Powder Technol.* 288 (2016) 255-265.
- [4] Campbell, C.S., Granular material flows - An overview, *Powder Technol.* 162 (2006) 208–229.
- [5] Rao, K.K., Nott, P.R., *An Introduction to Granular Flow*, Cambridge University Press, New York, 2008.

# MOTION DEVIATIONS OF A ROTATIONAL POSITIONING TABLE INDUCED BY THERMAL EFFECTS

Michael Nirtl<sup>1</sup>, Johannes Hauck<sup>1</sup>, Friedrich Bleicher<sup>1</sup>

<sup>1</sup> Technische Universität Wien, IFT – Institute for Production Engineering and Laser Technology, Getreidemarkt 9/311, 1060 Wien, Austria. E-mail: [nirtl@ift.at](mailto:nirtl@ift.at)

## 1. Introduction

When considering the positioning deviations of measurement systems which are equipped with an additional rotational axis, usually only the angle error is compensated during the measurement. Other systematic errors revealed during the machine acceptance test, for instance the wobbling of the axis, can be minimized by respective correction factors in the control. Besides these mechanically induced deviations, environmental effects, such as thermal influences are typically neglected. In order to guarantee high-precision measurements, the exact positioning of the probe is a basic prerequisite and hence requires the consideration and quantification of environmental effects. Especially when looking at optical measurement systems, positioning deviation affects stitching and will strike down as artefacts in merged images. Furthermore a precise and repeatable probe positioning is indispensable for the optimal focussing of the optical unit, in order to produce images with highest possible precision [1]. The accuracy of a measurement particularly depends on the temperature change over time [2]. Previous research revealed that the step motor (Fig.1-a) of a typical rotational unit is the most influential, non-constant heat source in close proximity of the probe if the measurement device is used in a temperature controlled room. Therefore this paper discusses the temperature influence of the step motor on the positioning accuracy.

## 2. Experimental Setup

In order to evaluate the spatial positioning accuracy of the rotational unit, a particularly designed ball measurement standard (BMS, see Fig.1-b) is fixed in the rotational unit. The BMS consists of two ceramic ( $Al_2O_3$ ) balls, which are connected by two carbon fibre rods with a thermal expansion coefficient  $\alpha=0.3 \times 10^{-6} K^{-1}$ , as well as titanium elements  $\alpha=8.6 \times 10^{-6} K^{-1}$ . The implemented balls have a guaranteed form deviation of less than 40 nm. The position of the

BMS is then tactilely evaluated upon reproducibility using a coordinate measuring machine Zeiss Prismo Navigator (MPE  $0.7+L/350 \mu m$  according to ISO 10360-2:2009). The experiments are carried out in a measuring laboratory with quality class 3 (VDI/VDE 2627-Blatt 1) and cleanroom class ISO 6 (DIN EN ISO 14644-1). However, as shown in Fig. 1-c, two temperature sensors, of which one is attached directly upon the rotational unit and the second is in close proximity of the BMS without a material contact, monitor the temperature profile over time.

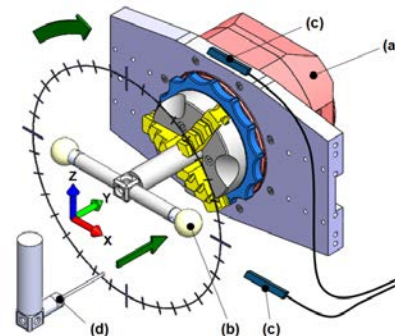


Fig. 1. Experimental setup: (a) step motor; (b) BMS; (c) temperature sensors; (d) +Y-probe

## 3. Experimental investigation

In order to determine the position of the centre point of the BMS the measuring adaptor will be scanned over several positions on a particular trajectory with over 2000 measuring points in each position. The positions are defined to replicate the nominal diameter of the spherical surface. To ensure the measurement of exactly the same pose in each angular position of the rotational unit, an axially aligned (Y-axis) measuring probe is applied (see Fig.1-d). The experimental testing procedure is divided into four phases. In the first and second experimental phase the centre points of the BMS are determined statically without angular displacement, 80 times in total within 2 hours. The single variable is the state of the step motor. In the first phase the rotational unit undergoes several revolutions before the measurements and is

connected to the power in order to replicate a heat state under realistic operating conditions. In phase two, however, the step motor is disconnected from the power supply and hence is passive without any heat emission. In phase 3 the rotational unit undergoes two full revolutions with increments of  $10^\circ$  whereas the determination of the centre points takes place in the breaks in-between, resulting in 72 sphere position datasets. In phase four the incremental rotational displacement is done manually with disconnected power supply and hence in a passive state of the step motor.

#### 4. Results

The results from the static experiments reveal that small changes in ambient temperature of less than 0.15 K produce almost no positional deviations in the radial direction, whereas in the axial direction a divergence of approximately  $0.3 \mu\text{m}$  occurs (see Fig.2). This is slightly higher than the calculated value of  $0.25 \mu\text{m}$  of the total thermal expansion of the measuring setup. As soon as the power supply is connected, a temperature offset of almost 2 K between the two temperature sensors can be observed. The influence of the step motor's heat source seems to have an enhanced impact on the axial position of the BMS. During the experiment a change of the ambient temperature of  $-0.5 \text{ K}$  could be observed resulting in a flatter deviation profile of the positioning accuracy. Even tough disclosing different profiles, both the radial and the axial deviations amount to about  $1.8 \mu\text{m}$  by the end of the experiment. The results from the rotatory table test reveals that the mechanical influence on both axial and radial deviations are quite similar, whereas the axial position reacts more serious on the heat source of the step motor (see Fig.3).

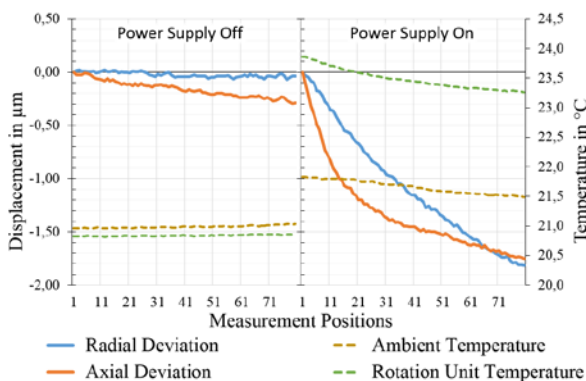


**Fig. 2.** Profiles of BMS sphere centre point position in axial and radial direction; static experiment phases 1 (power supply on) and 2 (power supply off)

Hence, the profile of the axial deviation shows an ascending trend. The temperature increase, resulting from the active step motor, causes a superimposition of errors, which partly cancel each other solution, leading to less distinct differences between local maxima and minima in the deviation profiles. The maxima are higher in the connected power state whereas the minima are significantly lower compared to the passive, manual angular displacement experiments.

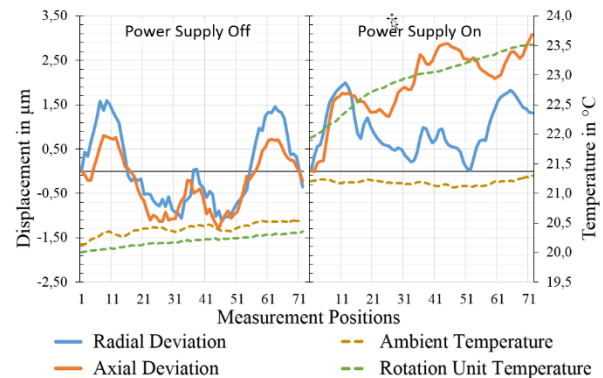


**Fig. 3.** BMS sphere centre point position profiles in axial and radial direction; rotatory experiment phases 3 (power supply on) and 4 (power supply off).

#### 5. Conclusion

Based on the present study a significant temperature influence of the step motor on the positional accuracy of a rotational table unit could be observed under controlled room temperature conditions. As part of further research an investigation of the superimposition of these heat effects and higher ambient temperature changes will be carried out in order to simulate near-production conditions.

#### References

- [1] L. Helfen, T. Baumbach, U. Retzlaff, Patentschrift: "Rotationstisch für räumlich hochauflösende Computer-Laminographie", Veröffentlichungsnr. WO2009121932A2, Veröffentlichungsdatum 8. Okt. 2009.
- [2] VDI/VDE 2627 – Blatt 1, „Meßräume, Klassifizierung und Kenngrößen, Planung und Ausführung“, August 1998.
- [3] H.-J. Neumann, „Genauigkeitsangaben zu Drehtischen und Besonderheiten ihrer Anwendung auf Koordinaten-Meßgeräte“, Koordinatenmeßtechnik, VDI Berichte 529, Tagung Fellbach, 16. und 17. Mai 1984.

## MEASURING PARAMETERS OF PHOENIX-100 GAS-GENERATOR

Nenad Kolarević<sup>1</sup>, Nebojša Kosanović<sup>1</sup>, Marko Miloš<sup>1</sup>, Jovan Isaković<sup>2</sup>

<sup>1</sup> University of Belgrade, Faculty of Mechanical Engineering, Kraljice Marije 16, 11120 Belgrade, Serbia. e-mail: [nkolarevic@mas.bg.ac.rs](mailto:nkolarevic@mas.bg.ac.rs)

<sup>2</sup> Tehnikum Taurunum, College of Applied Engineering Studies, Nade Dimić 4, 11000 Zemun Belgrade, Serbia. E-mail: [jisakovic@tehtnikum.edu.rs](mailto:jisakovic@tehtnikum.edu.rs)

### 1. Introduction

In development of Phoenix family of turbo engines there was a need for a satisfying measuring installation in order to control and monitor engine parameters.

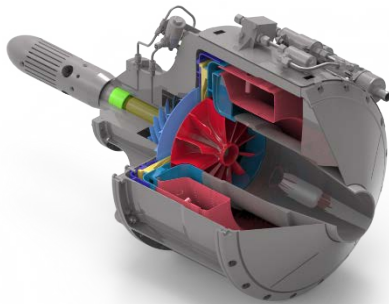


**Fig. 1.** Phoenix-100 gas-generator

As testing installation does not have enough measuring channels, we need to select a few parameters which will satisfy the need for control as well as to provide us with enough information of behavior of engine operation. The problem was the same as in case monitoring the engine parameters on gas-generator on tip-jet helicopter [1]. Because the generator was placed on the top of helicopter, above the blades, it was necessary to reduce a number of sensors for effective operation of tip-jet propulsion system [2].

### 2. Acquisition system

Acquisition system for engine, gas generator [3] Phoenix-100, testing consists of the following sensors: flow meter, accelerometer, two thermocouple probes, two pressure transducers, inductive sensor and load cell (Fig.2).

The flow meter device is installed on the fuel pump and it is used to measure the mass flow rate of fuel for ignition main fuel supply system. It is a part of engine monitoring and control system.

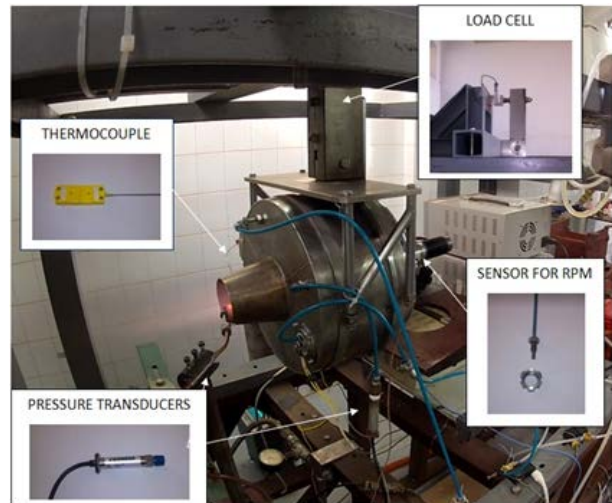


**Fig. 2.** Acquisition system for engine testing and monitoring

The accelerometer, placed near the bearing, is used to monitor the engine behavior during tests, also it can determine resonant areas or some damage appearance.

Two thermocouple probes, OMEGA K-type thermo couple CH+ AL-, are installed. One reads the temperature of more loaded bearing. The other one measures the temperature of operating fluid, mixture of combustion products, placed on the nozzle near its exit section (Fig.2).

Pressure transducer measures maximum static pressure in the gas-generator, in the area behind the diffuser and before the combustion chamber entrance. Therefore, it gives the information of compressor pressure ratio during testing. The sensor that is used is OMEGA PX602-150GV with the following characteristics: span 150 psig, accuracy 1%, input voltage 5-10Vdc, output signal 10mV/V, maximum pressure 300 psig, and etc. (Fig.2). The same sensor is used for measuring the total pressure on the nozzle exit. As the gas temperature is around 700°C there is a pipe system from copper pipes installed between the pitot sonde and the transducer, in order to cool down the

combustion products mixture to an appropriate level so sensor cannot be damaged (Fig.2).

For determining the engine rpm, the inductive sensor DW-AD-405-04-290 is used. Its characteristics are: diameter of stainless housing 4mm, operating distance of 0.8mm, supply voltage 5-30Vdc, output current  $\leq 1/ \geq 2.2$  A, switching frequency  $\leq 10000$ Hz, ambient temperature range -25 - +70°C etc. The measuring is done over the toothed distant bush located between the bearings on the shaft with previously explained probe (Fig.2).

OMEGA S shaped load cell LC111-250 is used to measure engine thrust during testing together with appropriate level system [4] installed on test bench (see Fig.3). It has the following characteristics: range 0-250 lb, output current 3mV/V, supply voltage 10Vdc, with linear errors  $\pm 0.03\%$ , repeatability 0.01%, hysteresis  $\pm 0.02$  of the full range, operating temperature from -40 to 93°C etc.

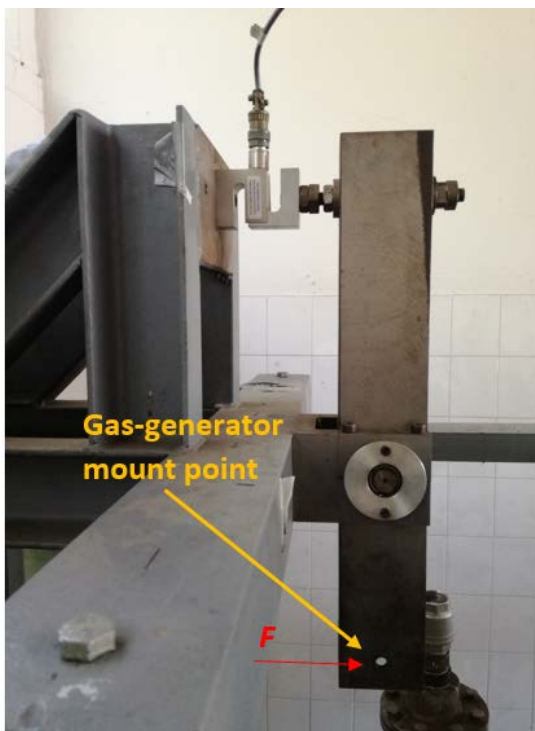


Fig. 3. Level mechanism with S-shaped load cell for measuring the thrust force

The following Figure 4 presents a diagram with measured values of these basic generator parameters at 55,000 rpm during testing. During testing, values of ambient pressure and temperature were measured independently.

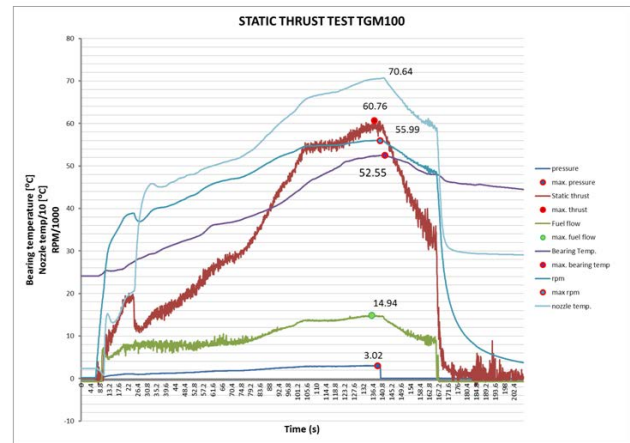


Fig. 4. Static test results for Phoenix-100 gas-generator

### 3. Remarks

The presented acquisition system proved to be useful for determining, monitoring and controlling the gas-generator operation and behavior. With a few presented sensors and their output result, we later managed to simulate the flow in gas-generator with Computation Fluid Dynamic software. The paper also presents a verified idea for the way of force measuring, with appropriate level system and sensor as in the Fig.3, and solution for measuring with simple conventional pressure transducer a total pressure of hot combustion products.

### Acknowledgements

Tests were performed in EDePro d.o.o. facilities in Belgrade as a part of UAV tip jet helicopter development program.

### References

- [1] N. Kosanović, N. Davidović, P. Miloš, B. Jojić, M. Miloš, "Monitoring of engine parameters in tip-jet helicopter tests," Proceedings of the 30th Danubia-Adria Symposium on advances in experimental mechanics, pp. 266-267, 2013.
- [2] N. Kolarević, N. Kosanović, M. Miloš, "Tip-jet helicopter propulsion system testing," KOD 2016- 9th International Symposium Machine And Industrial Design In Mechanical Engineering, pp.221-224, 2016.
- [3] Claire Soares, "Gas Turbines," Elsevier, 2015
- [4] S. Damjanović, P. Miloš, N. Davidović, B. Jojić, M. Miloš, "Measuring of resultant aerodynamic force on vertical tail of the tip-jet helicopter" Proceedings of the 30th Danubia-Adria Symposium on advances in experimental mechanics, 2013.

## NUMERICAL AND ANALYTICAL STUDIES OF A SHAKER TEST SYSTEM FOR FATIGUE TESTING

Philipp Renhart<sup>1</sup>, Igor Milošević<sup>1</sup>, Florian Grün<sup>1</sup>

<sup>1</sup> Montanuniversität Leoben, Chair of Mechanical Engineering, Franz-Josef-Straße 18, 8700 Leoben, Austria. E-mail: [philipp.renhart@unileoben.ac.at](mailto:philipp.renhart@unileoben.ac.at), [igor.milosevic@unileoben.ac.at](mailto:igor.milosevic@unileoben.ac.at)

10	500-1200	1	2,57
----	----------	---	------

### 1. Introduction

Conventional test rigs for fatigue testing (servo hydraulic, resonant test systems) are usually working up to 100 Hz. For the characterization of VHCF (very high cycle fatigue) phenomena up to  $10^9$  load changes should be proved, which leads to an exorbitant standard testing period. The desire for material testing at higher frequencies is obvious. In the design process of high frequency test devices, it is essential to have detailed knowledge of the resonant frequencies for the planned system. Finite-Element calculations are a relatively precise tool for frequency predictions though they are time-consuming. The aim of this work is the development of a solid analytical calculation routine for resonant frequency identification. Resonant frequencies strongly depend on the stiffness of the system; therefore, the focus will be laid on this calculation. For the validation of the simplified calculation an existing testing machine [1] has been used.

### 2. Experimental Setup

Two accelerometers are mounted on the baseplate (control sensor) respectively on the mass (monitor sensor). Fig. 1 shows the experimental device for high frequency VHCF tests. Before the test the specimen is tightened to the base with a M20x1,5 thread. Afterwards the mass (2,42 kg) is loosely screwed onto the specimen and the guides are mounted. Lastly the mass is secured with a secondary bolt (0,148 kg) from the top face.

The performed sweep-test is mainly defined by the constant and absolute value of acceleration ( $a_{Base} = 10 \text{ ms}^{-2}$ ) respectively the frequency range. During a sweep-test the harmonic excitation frequency rises constant (sweep-rate) with time. Detailed test definitions are listed in Tab. 1.

**Tab. 1.** Test definition data of a single sweep- test.

Base-acceleration [m/s <sup>2</sup> ]	Frequency-Range [Hz]	Sweep-Rate [Hz/s]	Applied-Mass [kg]
--	-------------------------	----------------------	----------------------

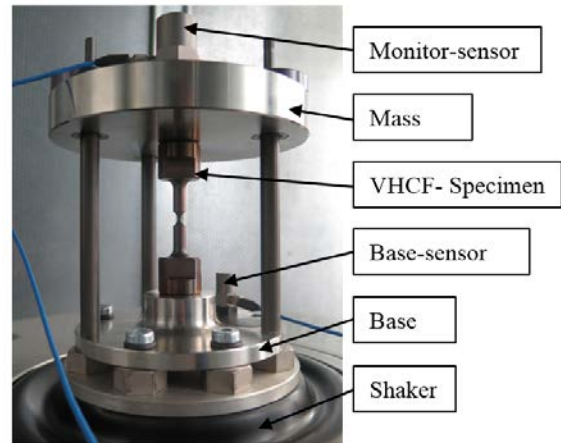


**Fig. 1.** Instrumented experimental setup for VHCF tests.

During the sweep-test the acceleration of the mass is measured to obtain the response of excitation. In the subsequent evaluation resonant frequency and damping ratio behavior can be identified.

### 3. Resonant Frequency Determination

#### 3.1 Analytical approach

The testing system can be simplified to a SDOF (single degree of freedom) oscillator with a point-mass  $m$  and a linear spring (specimen and base) with a constant stiffness  $c$ . The differential equation of a damped SDOF system with viscous damping system is:

$$m\ddot{x} + d\dot{x} + cx = 0. \quad (1)$$

For these SDOF system the un-damped resonant frequency  $f_N$  can be described by Eq. (2)

$$f_N = \frac{1}{2\pi} \sqrt{\frac{c}{m}}. \quad (2)$$

The damped resonant frequency  $f_D$  is given by Eq. (3), whereby the fraction of critical damping equals  $\zeta = d/4m\pi f_N$  [2]

$$f_D = f_N \sqrt{1 - \xi^2} . \quad (3)$$

The value for viscous damping was taken from Yun's [3] work. With  $d = 0.016$  the fraction of critical damping  $\xi$  can be neglected for frequency estimation. With a known mass only the stiffness has to be calculated. The basic approach is to determine the compliance  $\delta$  (reciprocal of  $c$ ) using the differential relation according to Eq. (4)

$$d\delta = \frac{1}{E \cdot A(x)} dx . \quad (4)$$

The specimen Fig. 2 is separated in single springs with cross-sections that can be analytically calculated. The total stiffness of multiple cross-sections is determined by a serial-connection of individual springs.

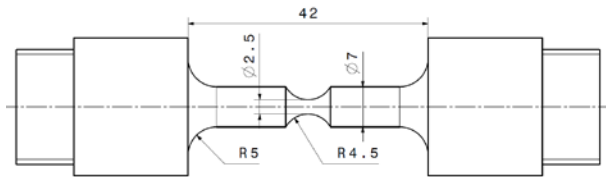


Fig. 2. Dimensions of the specimen.

The base can be seen as a rotationally symmetric plate. By applying Kirchhoff's plate theory [4] in Eq. (5) the central compliance  $w_{max} = \delta$  is calculated analytically

$$\Delta w = \frac{p(r, \varphi)}{K}$$

with  $K = \frac{Eh^3}{12(1-\nu^2)} . \quad (5)$

Lastly the deflection of the screws between the shaker and the base has been considered in the stiffness-calculation (parallel connection). The determined resonant-frequency is 804.9 Hz.

### 3.2 Numerical Approach

Resonant frequency estimations with Finite-Elements were performed in ABAQUS 6.14 using a linear perturbation step (modal analysis). In a further step the sweep-test was virtually performed by using a harmonic excitation at the base with different excitation-frequencies (direct steady-state analysis). First all threaded connections in the 3D model were tightened in which the thread connections were implemented with a clearance contact condition. The numerically determined

resonant-frequency is 796 Hz. For the damping of the system Rayleigh-Damping was used.

### 4. Validation

In the experiment a resonant-frequency of 833 Hz has been detected. The error in the analytic solution is 28,1 Hz (-3,7%). The deviation in the numerical solution is 37 Hz (-4,4%). In Fig. 3 the result of the sweep-test and calculated tests are shown.

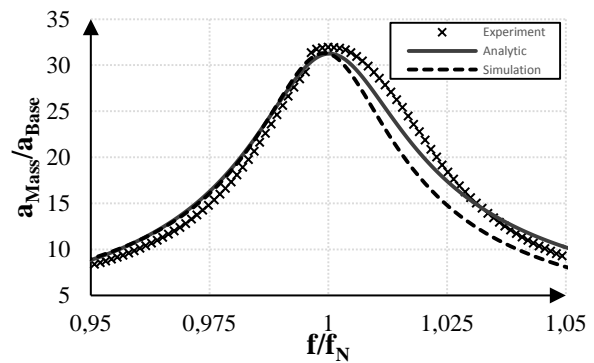


Fig. 3. Comparison of the experimental sweep-test and the analytically respectively numerically calculated response data (a...acceleration).

### 5. Remarks

- Analytic and numerical solutions are tolerably accurate, if comparatively soft connections (e.g. screws, plates) were considered.
- In subcritical ( $f < f_N$ ) acceleration response prediction a good accordance to the experiment has been observed.
- The frictional influence of the guides has not been studied so far. The focus in further studies will be laid on this and other dissipative effects.

### References

- [1] Milošević I., Renhart P., Validating a new high frequency testing method for martensitic high strength steels under tension/compression loading in the VHCF regime., International Journal of fatigue., 2017, **In Press**.
- [2] Harris C.M., Piersol A.G., Shock and Vibration Handbook 5<sup>th</sup> Edition, McGraw-Hill, New York, 2002
- [3] Yun G.J., Development of a Closed-Loop High-Cycle Resonant Fatigue Testing System,



Experimental Mechanics 52, 2012. pp. 275-288.

- [4] Kirchhoff G., Vorlesungen über mathematische Physik, Teubner, Leipzig, 1876.

## DEVELOPMENT OF A NEW SPECIMEN SETUP FOR HIGH PRECISION UNIAXIAL TENSION-COMPRESSION TESTS OF RUBBER

Lars Kanzenbach<sup>1</sup>, Christoph Naumann<sup>2</sup>, Martin Stockmann<sup>1</sup>, Jörn Ihlemann<sup>1</sup>

<sup>1</sup> Chemnitz University of Technology, Professorship of Solid Mechanics, Reichenhainer Str. 70, 09126 Chemnitz, Germany. E-mail: [lars.kanzenbach@mb.tu-chemnitz.de](mailto:lars.kanzenbach@mb.tu-chemnitz.de)

<sup>2</sup> Freudenberg & Co. KG, Höhnerweg 2-4, 69469 Weinheim, Germany

### 1. Introduction

This contribution deals with the development of a new specimen setup, which enables high precision uniaxial tension-compression tests of technical rubber materials. Due to a specific design of the mounting geometry, a nearly homogeneous deformation field can be achieved. Consequently, phenomenological effects of rubbers, like hysteresis, permanent set, softening, Mullins- and Payne-effect, can be investigated up to a compression strain of -50 % [2].

### 2. Functional principle

The mounting geometry of the standard dumbbell [1] leads to an abrupt contact between mounting and test specimen, which results in an inhomogeneous deformation field. To improve the homogeneity of the deformation field and to avoid buckling, the mounting geometry is modified using the algorithm shown in Fig. 1. Using dynamic FE-simulations, the eigenfrequency course can be identified. This course enables the estimation of the buckling risk. The main idea for designing the mounting geometry is to prescribe a special eigenfrequency course and to calculate the corresponding mounting geometry. This approach leads to an gradual contact between the specimen and mounting with a homogeneous deformation field.

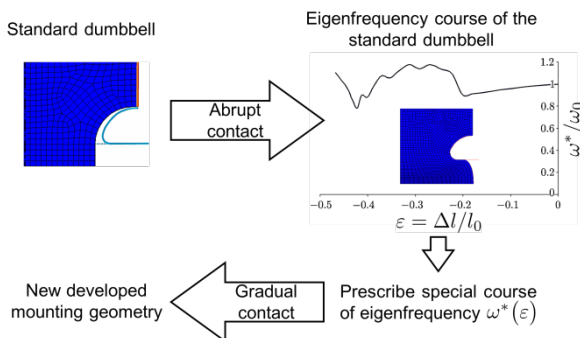


Fig. 1. Algorithm for the identification of the mounting geometry.

### 3. Experimental setup

The identified specimen setup (test specimen and mounting geometry) is manufactured and tested. The experimental setup and the corresponding measuring device are presented in Fig. 2.

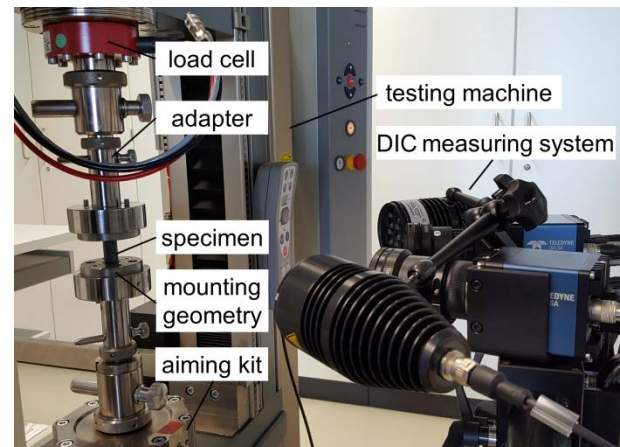


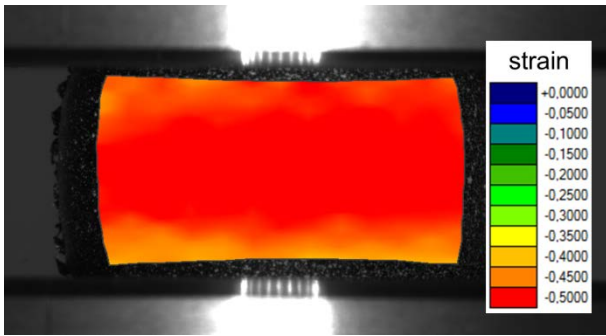
Fig. 2. Experimental setup for the new test specimen with measuring device.

The tests were performed with a ZWICK/Roell testing machine. The force is measured with a load cell and the displacement field was measured and evaluated with a Digital Image Correlation (DIC) measuring system. Note, that arbitrary test sequences can be considered using the external target value control [3].

To avoid axial and angular offset of the specimen from the testing machine, an aiming kit was applied.

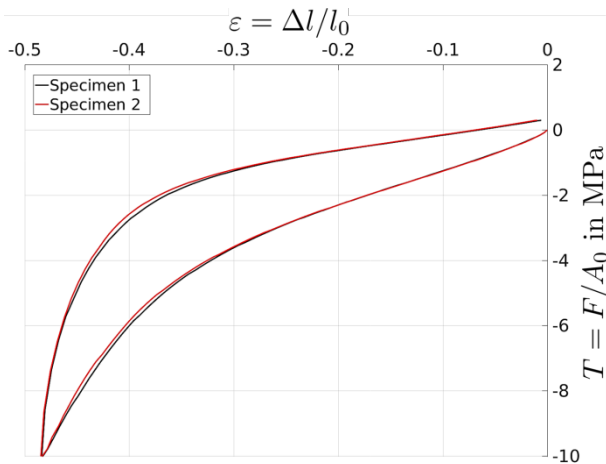
### 4. Experiments and Results

Within this contribution, filled EPDM has been characterized using the developed experimental setup. The deformation field at the highest achievable compression is given in Fig. 3. Note, that even for such high compression no buckling occurs and the strain field is nearly homogeneous.



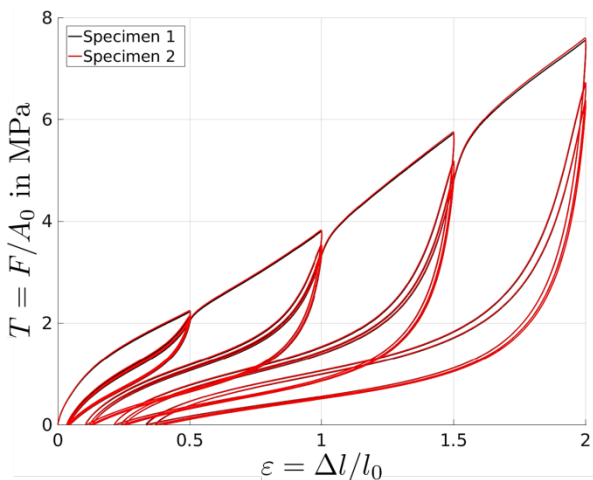
**Fig. 3.** Homogeneous deformation field in compression for the new test specimen.

Fig. 4 shows the corresponding stress-strain curves for two different specimens.



**Fig. 4.** Stress-strain diagram for the compression test.

As shown in Fig. 5 and Fig. 6, the new specimen setup can also be utilized for multi-hysteresis tests as well as cyclic tension-compression tests. The results illustrated in Fig. 6 are required to characterize the Payne-effect.



**Fig. 5.** Multi-hysteresis test.

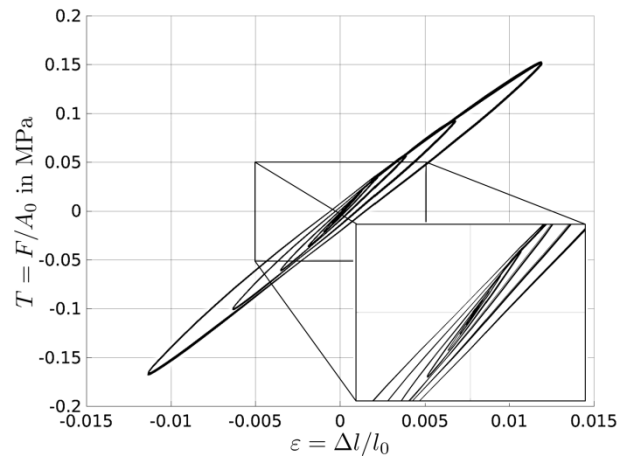


**Fig. 6.** Cyclic tension-compression test.

It should be mentioned, that different types of specimens are no longer required for this experimental investigation. Furthermore, the new specimen setup can be used for the identification of material model parameters.

## 5. Conclusion

The developed specimen setup has a large range of applications and enables new possibilities in the field of material research. For example, the phenomenological effect of technical rubber materials, like Payne- und Mullins-effect, softening, permanent set, relaxation and recovery, can be characterized.

## Acknowledgements

Financial support from Vibracoustic GmbH and Freudenberg & Co. KG is gratefully acknowledged.

## References

- [1] Alshuth, T., Hohl, C., & Ihlemann, J. (2007). Vergleichende Messungen und Simulationen annähernd homogener Belastungsverteilungen. *PAMM*, 7(1), 53-54.
- [2] Kanzenbach, L., Naumann, C., & Ihlemann, J. (2016). Specimen design for high precision tension-compression tests. *PAMM*, 16(1), 207-208.
- [3] Kanzenbach, L., Stockmann, M., & Ihlemann, J. (2016). Extension of the Testing Machine Control for High-precision Uniaxial Tension Measurements. *Materials Today: Proceedings*, 3(4), 993-996.

# DIC DEFORMATION ANALYSES OF MG SPECIMENS AT ELEVATED TEMPERATURES

Thomas Lehmann<sup>1</sup>, Julia Müller<sup>1</sup>, Jörn Ihlemann<sup>1</sup>

<sup>1</sup> Chemnitz University of Technology, Professorship of Solid Mechanics, Reichenhainer Straße 70, 09126 Chemnitz, Germany. E-mail: [thomas.lehmann@mb.tu-chemnitz.de](mailto:thomas.lehmann@mb.tu-chemnitz.de)

## 1. Introduction

Mg alloys have become more and more important for application in lightweight structures. During manufacturing processes by forming of textured AZ31 semi-finished products the difference of the yield strengths in tension and compression has to be considered [1]. This effect is caused by twinning mechanisms (tension twin system, compression twin system) in textures and the activation of additional sliding planes at elevated temperatures [2]. To investigate the influence of the yield strength differences in tension and compression during bending deformation, experimental and numerical investigations were performed. In this contribution the experimental analysis of the material behavior of AZ31 in bending tests at elevated temperatures is demonstrated. The focus is on experimental deformation analyses and testing of different evaluation methods of the displacement fields.

## 2. Experimental setup and procedure

For the bending tests twin roll casted AZ31 (TRC) sheet material of two different thicknesses  $t = 2.5$  and  $1.5$  mm was used. The specimens were separated from the semi-finished products by wire eroding. The geometry, testing temperatures and number of analyzed specimens are given in Tab. 1.

Semi-finished product	Specimen geometry $w \times t \times l$ [mm]	Testing temperature [°C]	Number of specimens
AZ31 (TRC) sheets	5 x 2.5 x 15	250	2
		350	3
	5 x 1.5 x 15	250	3
		350	3

Tab. 1. Subset of testing parameters.

The load was applied by a punch while the specimen was clamped, see Fig. 1. Bending specimen and device were surrounded by a temperature chamber and assembled in a 100 kN

Zwick/Roell testing machine. Because of low loads, forces were measured using a 5 kN GTM load cell.

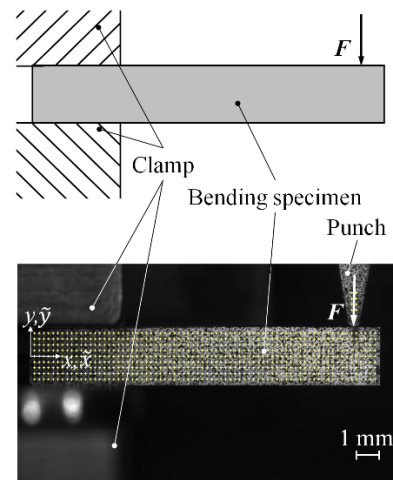


Fig. 1. Bending test, above: load case, below: specimen and device, virtual measuring pattern at the surface.

The specimens were loaded with punch displacements 4 mm (for  $t = 2.5$  mm) and 2.8 mm (for  $t = 1.5$  mm) and a velocity of 2.5 mm/s. The deformation analyses were performed using 2D digital image correlation (DIC) with the software VEDDAC (CWM GmbH, Chemnitz). Hence, a CCD monochrome camera, connected to the measuring laptop, with telecentric lens was applied. A black and white speckle pattern at the specimens surface improved the DIC algorithm. For image sequence acquisition a frame rate of 10 Hz was used. During the DIC analyses subsequent to the bending tests a virtual measuring pattern was defined at the surface of the specimens, see Fig. 1 (below).

## 3. Evaluation method

The DIC displacement data was extended using linear extrapolation to the edges and interpolation between the measuring points. Due to noise of the experimental data the displacement values were smoothed. Additionally, for the calculation of strain tensors differentiability of the determined

displacements was necessary. Therefore, the 2D displacement data at the specimen surface was approximated by two different methods using the software Matlab. By means of the approximation, functions of the displacement vector field  $\mathbf{u}(\tilde{x}, \tilde{y}) = [u_x(\tilde{x}, \tilde{y}) \ u_y(\tilde{x}, \tilde{y})]^T$  in dependency of the Lagrange coordinates were obtained. The first variant was approximation by global polynomial surfaces [3]. Variations of the polynomial degree  $p$  showed that  $p = 8$  for  $u_x$  and  $u_y$  is suitable to represent the specific displacement fields. The second variant used was approximation by cubic B-spline surfaces. The deformation gradient  $\mathbf{F}$  is determined by the identity tensor  $\mathbf{I}$  and the displacement vector  $\mathbf{u}$  using the following equation:

$$\mathbf{F} = \mathbf{I} + (\tilde{\nabla} \otimes \mathbf{u})^T. \quad (1)$$

Based on the deformation gradient the Lagrangian Hencky tensor  $\mathbf{H}$  is given by

$$\mathbf{H} = 0.5 \ln(\mathbf{F}^T \mathbf{F}). \quad (2)$$

#### 4. Results

The evaluation of the displacement data by global polynomial approximation is demonstrated by an example of a deformed specimen with thickness  $t = 2.5$  mm at testing temperature  $350$  °C and a punch displacement of  $4$  mm. In Fig. 2 the  $x$ -coordinate  $H_{xx}$  of the Lagrangian Hencky tensor is plotted versus the Euler coordinates  $x$  and  $y$ . In the deformation zone the method provides a good demonstration of the strain distribution. At the left edge significant strain values appear, which are unrealistic because of nearly deformation free conditions inside the clamp. This effect occurs due to “overshooting” of the polynomial functions in edge sections.

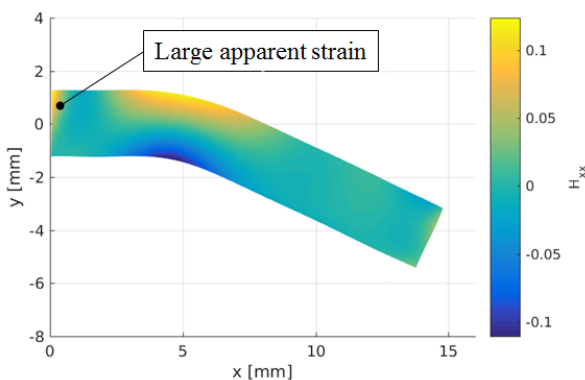


Fig. 2. Hencky strain  $H_{xx}$ , polynomial approximation.

The second evaluation variant shows the same example using B-spline approximation of the displacement data. The distribution of  $H_{xx}$  at the specimen surface is given in Fig. 3. Good results at large and slightly deformed sections at the whole specimen surface are achieved. The reason is the better local adaption of the displacements by means of splines instead of global polynomial surfaces.

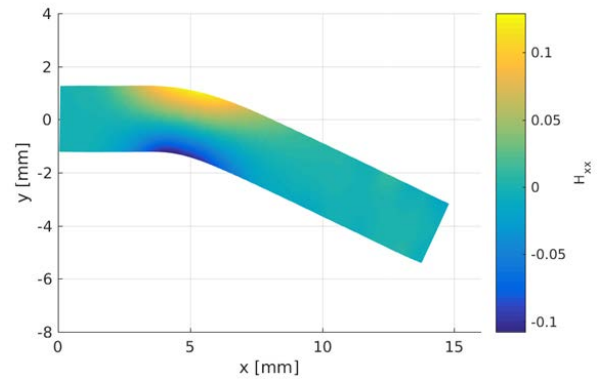


Fig. 3. Hencky strain  $H_{xx}$ , cubic B-spline approximation.

#### 5. Concluding remarks

- Deformation field analyses using DIC with AZ31 specimens were demonstrated.
- Using B-spline approximation of the displacement data leads to better results regarding the determined strain distribution compared to the method using global polynomial surfaces.
- Different levels of deformation in tension and compression sections were determined.

#### References

- [1] Dudamell, N.V., Ulicia, I., Gálvez, F., Yi, S., Bohlen, J., Letzig, D., Hurtado, I., Pérez-Prado, M.T., Influence of texture on the recrystallization mechanisms in an AZ31 Mg sheet alloy at dynamic rates. *Mat. Sci. and Eng. A*, 532, 2012. pp. 528–535.
- [2] Knezevic, M., Levinson, A., Harris, R., Mishra, R.K., Doherty, R.D., Kalidindi, S.R., Deformation twinning in AZ31: Influence on strain hardening and texture evolution. *Acta Materialia*, 58, 2010. pp. 6230–6242.
- [3] Kirbach, C., Lehmann, T, Stockmann, M., Ihlemann, J., Digital Image Correlation Used



34th Danubia-Adria Symposium on Advances in Experimental Mechanics  
University of Trieste, Italy, 2017



for Experimental Investigations of Al/Mg  
Compounds. *Strain*, 51, 2015. pp. 223–234.

# PRELIMINARY STUDIES FOR ALTERNATIVE LATTICE CORE DESIGN FOR FDM 3D PRINTED SANDWICH PANELS

Lam Man Chun <sup>1</sup>, Michał Kowalik <sup>1</sup>

<sup>1</sup> Warsaw University of Technology, Institute of Aeronautics and Applied Mechanics, Nowowiejska 24, 00-665 Warsaw, Poland. e-mail: mkowalik@meil.pw.edu.pl

## 1. Introduction

Lattice structures with different types of open cell topologies are attracting interest as millimetre cell sized lightweight core structures for sandwich panel constructions. Lattices appear to be an alternative improvement to honeycomb structures with flexible and amenable to the creation of singly or compound curved sandwich panels. Currently, lattice structures design is very limited to folding fabrication. Hence, Fused deposition modelling (FDM) 3D printing technologies allows more complex and advanced lattices design.

The purpose of this research is to design and compare capacity of different lattice structures. Z-ULTRAT material was used to simulate the 3D printed materials. All designs will undergo buckling test to simulate the real-world applications of sandwich core panels.

## 2. Design Parameters

### 2.1 Unit Cell Densities

For the design of lattice structure as shown in fig. 1, the unit cell density will be set to 0.3 while the height will be set to 10mm. From there, other dimensions of the lattice structures will be calculated according to Eq. (1). With the added weight of the material not taken account; only the cross sectional area and length determine the relative density of the structures. The unit cell are arranged in an array pattern to contain in 50mm x 50mm area.

$$\tilde{\rho} = \frac{\text{Volume of Truss}}{\text{Volume of Unit Cell}} \quad (1)$$



Fig. 1. Lattices Unit Cell Design of Honeycomb, Pyramidal and Hollow Sphere shape.

## 3. Compression Test

### 3.1 Testing layout

The models are simulated using ANSYS 16.0 and tested via INSTRON Testing system. The sandwich core is placed between two 7cm solid steel cylinder. Load is applied from the bottom while the fixture is set at the top of the sandwich core as shown in fig. 2. The INSTRON Testing system is set to compress 4mm to the core design.

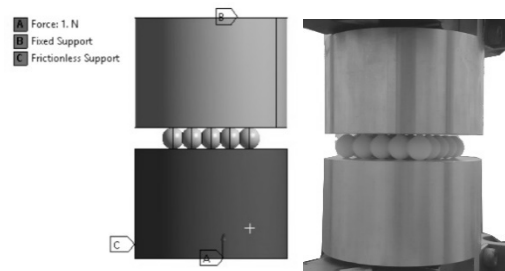


Fig. 2. Compression Test of Sandwich Panel. FE model (left), experimental setup (right).

### 3.2 Testing Material

The material used for the buckling simulation is Z-ULTRAT from Zortrax to simulate the commonly used 3D printing thermoplastics.

Parameters	Z-ULTRAT
Mass Density [g/cm <sup>3</sup> ]	1.04
Young Modulus [MPa]	857
Poisson's Ratio	0.36

Table 1. Properties of the testing materials

## 4. FDM 3D Printing Parameters

The lattice design will be printed by using fused deposition modelling (FDM) 3D printing technology. The models will be slice by Zortrax Z-Suite software with a resolution of 100 microns and print out by Zortrax M200. The Z-ULTRAT materials is melted and printed at a temperature of 270°C.

## 5. Results

Figure 3 shows the result from the Buckling test ANSYS Workbench 16.0 simulated and the Compression test result. Table 2 shows the time and amount of filament required to print out each of the respective core design models.

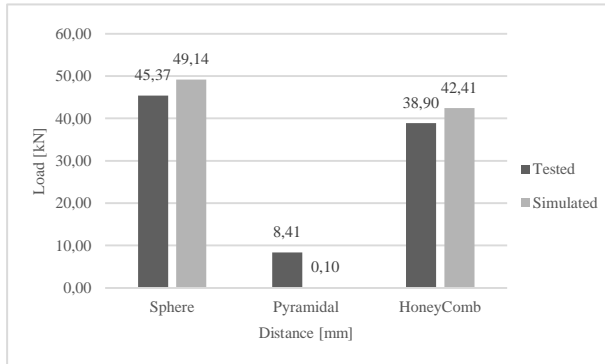


Fig. 3. Buckling Result of Core design

Core Design	Build Time [Hours]	Filament Used [mm]
Honeycomb	2.67	2248.4
Pyramidal	5.38	3231.2
Hollow Sphere	3.75	3387.6

Table 2. Properties of the testing materials

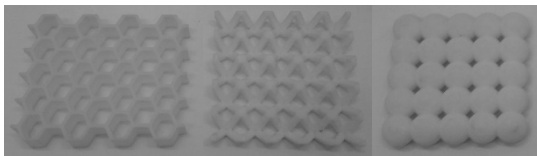


Fig. 4. 3D Printed Model of Honeycomb, Pyramidal and Sphere samples.

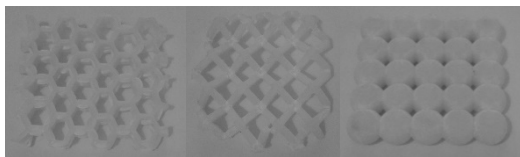


Fig. 5. Result of Compressed Honeycomb, Pyramidal and Sphere samples.

## 6. Conclusions

From initial simulation result, Spherical lattice design has the highest critical buckling load at a given height of 10mm among the 3 lattices designs.

Spherical lattice design also required the second least time but more amount of filament to print. Honeycomb core design has the lower buckling

load but used the least filaments and time to print out the test specimen.

Pyramidal has the longest build time and used the most filament and yet to achieve the lowest critical buckling load. This is because the Pyramidal design is not bonded to a fixed surface at the top and bottom, causing the pyramidal break at the joints of the legs and spilt the legs apart as shown in figure 6.

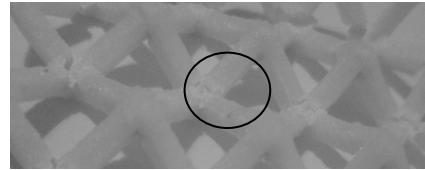


Fig. 6. Fault at Pyramidal Core Design

## 7. Remarks

- Data is created by the simulations has yet to be fully analyzed, therefore only initial findings are reported here.
- The time and amount of filament used to print the core designs varies among different types of 3D printers as they have different calibrations and specifications.

## References

- [1] Douglas T. Queheillalt, Haydn N.G. Wadley, Pyramidal Lattice Truss Structures with hollow Trusses, 2005
- [2] Li Yang, Ola Harrysson, Harvey West, Denis Cormier, A comparison of Bending Properties for Cellular Core Sandwich Panels, 2013.
- [3] Haydn N.G. Wadley, Multifunctional Periodic Cellular Metals, 2005
- [4] Douglas T. Queheillalt, Yellapu Murty, Daydn N.G. Wadley, Mechanical Properties of an extruded pyramidal lattice truss sandwich structure, 2007.
- [5] Brooks W.K, Todd J. and Sutcliffe C.J., The Production of Open Cellular Lattice Structures Using Selective Laser Melting, In: Sixth National Conference on Rapid Prototyping, Design, and Manufacturing, 2005

# RFID SENSOR SYSTEM EMBEDDED IN CONCRETE – VALIDATION OF UHF ANTENNA GEOMETRIES IN DIFFERENT CONCRETE DEPTHS

Sergej Johann, Christoph Strangfeld, Matthias Bartholmai

Federal Institute for Materials Research and Testing (BAM), Unter den Eichen 87, 12205 Berlin, Germany. E-Mail: sergej.johann@bam.de

## 1. Introduction

This paper is a further research on the topic of the complete embedding of radio frequency identification (RFID) sensors in concrete [1]. The focus is on the antenna of the transponder. Earlier investigations of different RFID technologies, embedded in concrete, showed a difference in energy transmission [2]. The transmission through concrete at ultra high frequency (UHF), in spite of the large signal range, does not match the targeted application specific task. Therefore, the antenna characteristics have been examined more closely. The antenna is an important component for the application of RFID. Through the antenna, energy and data transfer takes place, so it is important to design an optimal antenna to accomplish a maximum embedding depths in concrete.

To identify the optimal antenna geometry, different UHF antenna types were selected and investigated. An experimental comparison was performed to gain more information about the damping behavior and antenna characteristics in concrete. Furthermore, Transponders were tested in different construction designs, including rigid and flexible carrier materials, with and without sensor wiring. This paper presents first results.

## 2. Antenna and Transponder



Fig. 1. UHF antennas.

The investigated antenna geometries (Fig. 1) 1 to 9 are planar antennas on flexible plastic carrier material. The application area extends from Library, to Transportation and Healthcare. Antennas 10a/b are planar antennas, too and the first BAM antenna geometry. Antenna 10a (with sensor) and 10b (without sensor), are  $\lambda/2$  antennas, it has been used for the first functional tests of the competed wired sensor

system. The carrier material consists of stare FR4 material.

$$\frac{\lambda}{2} = \frac{c}{f} \quad (1)$$

$\lambda$  = antenna length in meter (for e.g. 868 MHz)

$f$  = frequency in Hz

$c$  = speed of light in m/s

## 3. Experimental Setup and Equipment

The experiments were carried out in laboratory conditions. Fig. 2 shows the test setup with three floating screed test specimen of 5 cm thickness. As a test system the Voyantic Tagformance Pro (Voyantic Ltd. Finland) was used to investigate the antenna characteristics. The experiment was carried out in four steps. In all measurements, the transponder antenna was positioned at a distance of 100 cm from the reader antenna, to avoid being in the near-field area (Long-range antenna). During the first measurement (reference measurement), the transponder with antenna was applied in the middle of the concrete structures surface, while in the case of further measurements, the transponder was positioned step by step behind a further specimen, resulting in ca. 5, 10, and 15 cm of concrete screed between transponder antenna and reader antenna. This setup approximately represents a real-world scenario, with a number of influences and disturbances from environmental conditions.

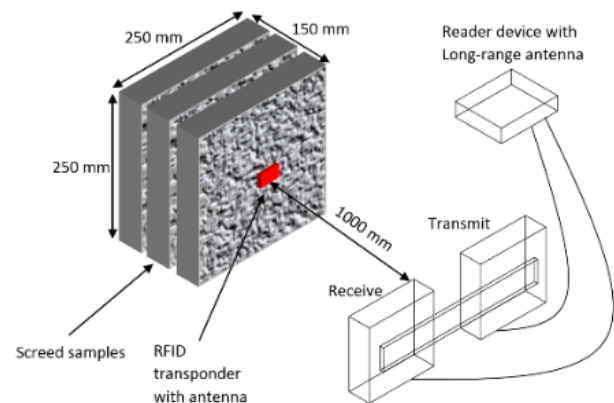


Fig. 2. Experimental concrete setup.

## 4. Results

The main objective of the study was to find an antenna geometry with minimal required power transmission through concrete thicknesses up to 15 cm and stable transmission performance. Because of issues with reflections, the abstract focuses on results up to 10 cm. All results were averaged over a number of 10 measurements.

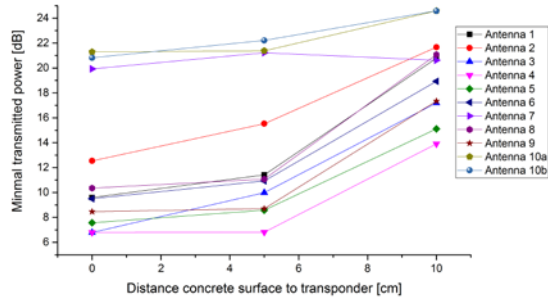


Fig. 3. Minimal required power of all antennas.

Fig. 3 shows the minimal required power to receive a transponder response. Basically, for all antennas the required power increases with additional concrete between transponder and reader. From 10 tested antennas, Antenna 4 enables measurements with the lowest power requirements, qualifying it for further implementation and testing.

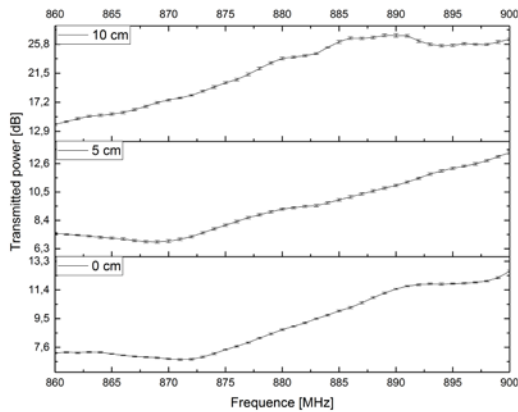


Fig. 4. Frequency response of Antenna 4 and standard deviation behind different concrete thicknesses.

The frequency response of Antenna 4 (Fig. 4) shows best results for frequencies between 860 and 875 MHz, which corresponds well to the European standard operation frequency for UHF RFID systems at around 868 MHz. Error bars indicate the low standard deviation, suggesting a stable transmission performance through different concrete thicknesses and over the whole frequency range.

## 5. Conclusion

The results show that the antenna geometry has a significant impact on the transmission characteristics through concrete and should be further optimized and validated. Of the 10 investigated antennas, Antenna 4 behaved the most stable and has low damping characteristics for transmission through concrete screed up to 10 cm.

## 6. Outlook

Fig. 5 shows the first implementation model which derived from this antenna examination. It was etched on a FR4 carrier material, and consists of copper. This antenna will serve as basis to provide sufficient energy transfer to operate the embedded RFID sensors systems [3]. For further optimization, the antenna impedance must be calculated.



Fig. 5. Implementation model of Antenna 4.

Next steps are the simulation of the antenna geometry in combination with electronics and different concrete depths. Further validation tests in real embedding scenarios should show whether the antenna geometry enables good results (a) with fully wired and embedded systems, (b) regarding installation depths up to 15 cm, and (c) for different concrete materials.

## References

- [1] Johann, S., Strangfeld, C., Müller, M., Bartholmai, M., RFID sensor systems embedded in concrete - requirements for long-term operation, 33rd Danubia - Adria Symposium on Advances in Experimental Mechanics, 2016.
- [2] Bartholmai, M., Strangfeld, C., Johann, S., Kammermeier, M., Müller, M., RFID sensor systems embedded in concrete – systematical investigation of the transmission characteristics, 8th European Workshop On Structural Health Monitoring, 2016.
- [3] Strangfeld, C., Johann, S., Müller, M., Bartholmai, M., Moisture Measurements with RFID based Sensors in Screed and Concrete, 8th European Workshop On Structural Health Monitoring, 2016.

# MECHANICAL PROPERTIES OF TI-6AL-4V SAMPLES PRODUCED WITH ADDITIVE TECHNOLOGY

Zoltan Keresztes<sup>1,a</sup>, David Pammer<sup>1,b,\*</sup>

<sup>1</sup> Budapest University of Technology and Economics, Department of Materials Science and Technology, Bertalan Lajos str. 7, 1111, Budapest, Hungary. <sup>a</sup>E-mail: kzoltan@eik.bme.hu, <sup>b,\*</sup>corresponding author E-mail: pammer@eik.bme.hu

## 1. Introduction

Rapid Prototyping is a term used to describe fabrication processes responsible for creating representations and models during the development of a project. In industrial context, the expression usually refers to technologies that are able to build prototypes from digital data. Nowadays the name of these processes are changed to Additive Manufacturing (AM), due to the most basic features of the technology becomes the fabrication of parts using an additive approach [1]. Synonyms: additive processes, additive fabrication, etc. [2].

The process starts with a computer-aided design software, which sends the information to a professional-grade industrial machine. This machine builds the final 3D objects layer-by-layer from different raw material based on the descriptions sent by the software [3].

Our main aim was to compare the mechanical properties and the microstructures of Grade 5 Ti-6Al-4V samples produced by traditional processes and additive manufacturing. This work represents several tests, such as tensile, bending, hardness and metallography. All samples and tests fulfill the available ASTM and ISO standards.

## 2. Materials and methods

During the tests Ti-6Al-4V samples were used, with the following chemical composition (Tab.1.).

Component	Percentage (%)
Titanium (Ti)	88.1 – 91
Aluminum (Al)	5.5 – 6.5
Vanadium (V)	3.5 – 4.5
Iron (Fe)	< 0.25
Oxygen (O)	< 0.13
Carbon (C)	< 0.08
Nitrogen (N)	< 0.03
Hydrogen (H)	< 0.125

**Tab.1.** Chemical composition of Ti-6Al-4V produced by traditional process

AM has many types, such the main processes as: VAT photopolymerisation; Material Jetting; Binder Jetting; Material Extrusion; Powder Bed Fusion; Sheet Lamination; Direct Energy Deposition.

The samples were produced by a 3D printing technology of Powder Bed Fusion called Direct Metal Laser Sintering (DMLS). During the production with EOS M 280 machine the model is built by very thin layers and fused raw powder. The schematic illustration of the 3D printing technology is showed below (Fig.1.) [4].

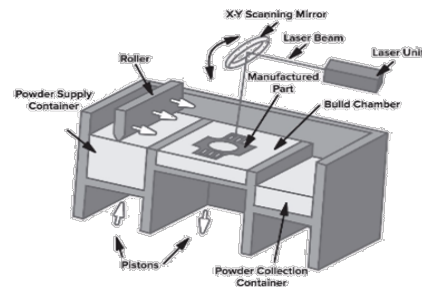


**Fig.1.** Schematic illustration of DMLS technology

## 3. Mechanical properties and tests

The tensile specimens were built following ASTM E8M:11. The specimens total length was 50 mm. The bending specimens were built with a total length of 50 mm also and a cross section of 4 mm x 4 mm, where the geometry do not influence the manufacturing direction, because there symmetry. The manufacturing direction of the tensile specimens are shown on Fig.2.

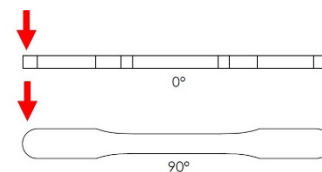


**Fig.2.** Tensile specimens with the manufacturing direction

Tensile and bending (TPB) test was performed with Instron 5965 tensile test machine, with 6-6 specimens (Fig.3. and Fig.4.). 3 with 0 deg and 3 with 90 deg manufacturing direction.

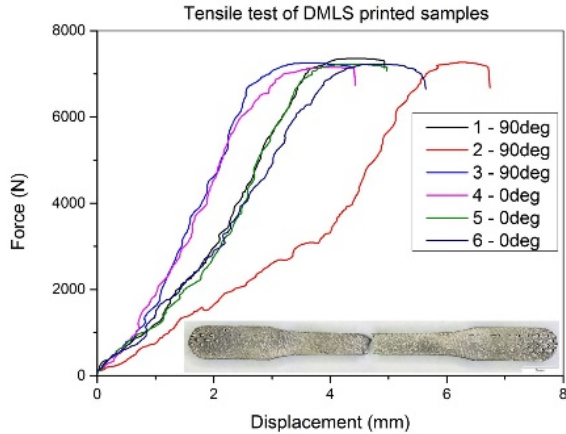


**Fig.3.** Tensile test of DMLS produced Ti-6Al-4V parts

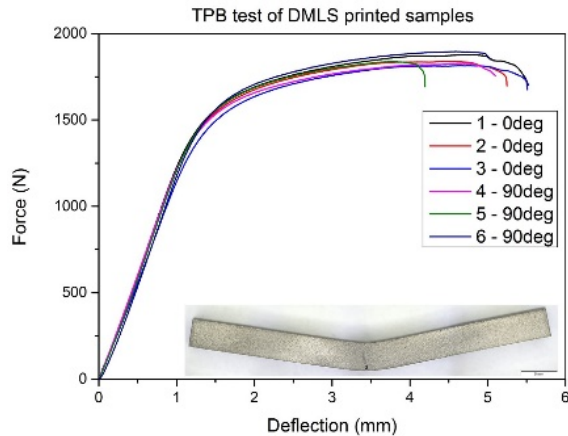


**Fig.4.** Bending test of DMLS produced Ti-6Al-4V parts

The stress-strain values were calculated after the measurement. Tensile strength:  $1134 \pm 10.67$  MPa, and flexural resistance:  $1957.5 \pm 31.05$  MPa.

#### 4. Metallography

For a metallography study first of all the samples must be fixed in resin to make the grinding, polishing and etching effective. For etching, we used Keller's reagent (190 ml H<sub>2</sub>O, 5 ml HNO<sub>3</sub>, 3 ml HCl, 2 ml HF), which is optimal for titan alloys. Fig. 5. shows the microstructure of Ti-6Al-4V produced traditionally and Fig.3. represents the microstructure of additive manufactured Ti-6Al-4V sample etched with Keller's reagent.

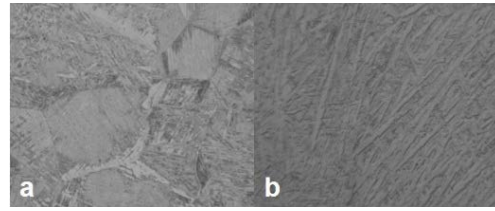


**Fig.5.** a) Microstructure of traditionally produced Ti-6Al-4V parts; b) Microstructure of DMLS produced Ti-6Al-4V parts

For more precise information the microstructures were investigated by Inspect S50 30 kV SEM. Two different areas were examined. Firstly, the outer part of the sample was tested and secondly the inner area was investigated (Fig.6.). We inspected the chemical composition, were Ti=86.86%, Al=10.58% and V=2.56%.

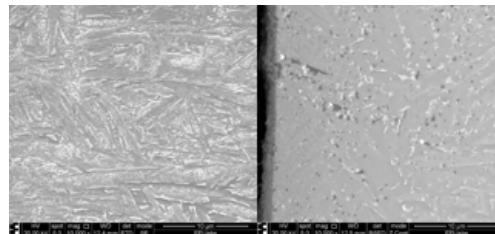


**Fig.6.** SEM pictures of the DMLS produced sample, outer part (left), inside part (right)

#### 5. Remarks

Considering the average tension results for Ti-6Al-4V, which varies between 900 MPa and 1200 MPa, the DMLS samples have values over 1100 MPa, independent of the manufacturing direction (0 or 90 deg), and the near similar microstructure and chemical composition causes that the DMLS produced parts can be used in the same application fields as the traditional manufacturing method.

#### Acknowledgements

The present work was funded by the National Research, Development and Innovation Fund, connecting to the NVKP\_16-1-2016-0022 project.

#### References

- [1] Ian Gibson, David Rosen, Brent Stucker, Additive Manufacturing Technologies. 2. ed. New York, Springer, 2009.
- [2] William E. Frazier, Metal Additive Manufacturing: Journal Of Materials Engineering And Performance, 2014
- [3] Sharon L.N. Ford, Metal Additive Manufacturing Technology: Potential



Implications for U.S. Manufacturing Competitiveness, Journal Of International Commerce And Economics, 2014

- [4] Loughborough University, The 7 Categories of Additive Manufacturing, <http://www.lboro.ac.uk/research/amrg/about/the7categoriesofadditivemanufacturing>, 2016

# AN INNOVATIVE MECHANICAL TESTING METHOD FOR MEASURING YOUNG'S MODULUS OF A THIN FLEXIBLE MATERIAL (OWN-WEIGHT CANTILEVER METHOD)

Atsumi OHTSUKI<sup>1</sup>

<sup>1</sup> Meijo University, Faculty of Science and Technology, Department of Mechanical Engineering, 1-501 Shiogamaguchi, Tenpaku-ku, Nagoya, 468-8502 Japan. E-mail: [ohtsuki@meijo-u.ac.jp](mailto:ohtsuki@meijo-u.ac.jp)

## 1. Introduction

This paper describes a new Young's modulus measuring method (*Own-Weight Cantilever Method*). By applying a nonlinear large deformation theory, analytical solutions are derived by using Bessel functions. Using this method, Young's modulus of a thin and long flexible material can be easily obtained by just measuring the horizontal displacement or the vertical displacement at the free end of the cantilever.

Besides the Own-Weight Cantilever Method studied here, the *Axial Compression Method* [1], [2], the *Cantilever Method* [3], the *Circular Ring Method* [4], [5] for a thin flexible material.

## 2. Theory

Although conventional testing methods (e.g. three- or four-point bending test and so) are based on the small deformation theory are very simple, they have several disadvantages (e.g., a stress concentration, a gripping problem of specimen). From this point of view, a new testing method (*Own-Weight Cantilever Method*) is derived

considering large deformation behaviors of a test specimen.

### 2.1 Basic equations

A typical illustration of deformations is given in Fig.1 for a thin flexible cantilever (length  $L$ ) subjected to the own-weight  $w$  (distributed load per unit length) with a supporting angle  $\theta_0$ . The horizontal displacement is denoted by  $y$ , the vertical displacement by  $x$ , and  $\theta$  is the deflection angle. Furthermore, the arc length is denoted by  $s$ , the radius of curvature by  $R$  and the bending moment by  $M$ . The relationships between  $R$ ,  $M$ ,  $s$ ,  $x$ ,  $y$  and  $\theta$  are given by:

$$1/R = -d\theta/ds = M/(EI), dy = ds \cdot \sin\theta, dx = ds \cdot \cos\theta. \quad (1)$$

where  $E$ ,  $I$  are Young's modulus, the second moment of area, respectively.

Finally, the nonlinear equation is derived from Eqs.(1) in the form of :

$$EI(d^2\theta/ds^2) + w(L-s)\sin\theta = 0. \quad (2)$$

Introducing the following nondimensional variables

$$\xi = \frac{x}{L}, \eta = \frac{y}{L}, \zeta = \frac{s}{L}, \gamma = \frac{wL^3}{EI}, \beta = \frac{ML}{EI}. \quad (3)$$

and transforming the variables ( $s \rightarrow \zeta$ ), equation (2) reduces to Eq.(7).

$$d^2\theta/d\zeta^2 + \gamma(1-\zeta)\sin\theta. \quad (4)$$

Assuming the following relationships [Eq.(5)] in Eq.(4), equation (6) is obtained.

$$\psi = \theta - (\theta_A + \theta_0)/2. \quad (5)$$

$$[-\{(\theta_A - \theta_0)/2\} \leq \psi \leq \{(\theta_A - \theta_0)/2\}]$$

$$d^2\psi/d\zeta^2 + \gamma(1-\zeta) \left[ \begin{array}{l} \cos\{(\theta_A + \theta_0)/2\} \cdot \sin\psi \\ + \sin\{(\theta_A + \theta_0)/2\} \cdot \cos\psi \end{array} \right] = 0. \quad (6)$$

where

$$\sin\psi = \sum_{n=0}^{\infty} 2 \cdot \sin\left(\frac{n \cdot \pi}{2}\right) \cdot J_n\left(\frac{\theta_A - \theta_0}{2}\right) \cdot T_n\left(\frac{2\psi}{\theta_A - \theta_0}\right). \quad (7)$$

$$\cos\psi = J_0\left(\frac{\theta_A - \theta_0}{2}\right) + \sum_{n=1}^{\infty} 2 \cdot \cos\left(\frac{n \cdot \pi}{2}\right) \cdot J_n\left(\frac{\theta_A - \theta_0}{2}\right) \cdot T_n\left(\frac{2\psi}{\theta_A - \theta_0}\right) \quad (8)$$

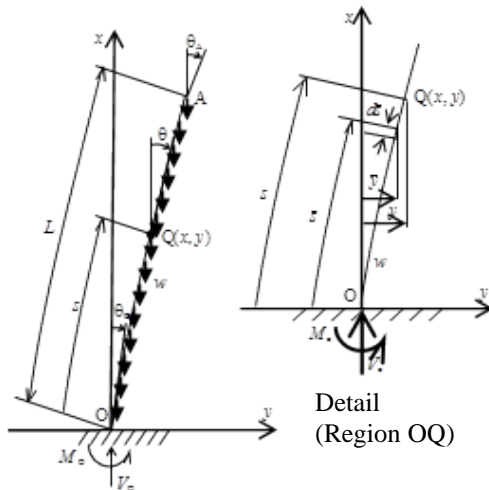


Fig.1 Large deformations of vertical cantilever subjected to own-weight.

The functions  $T_n(x)$ ,  $J_n(x)$  in Eqs.(7), (8) are Chebyshev polynomial and Bessel function, respectively.

The non-dimensional horizontal and vertical displacements  $\xi$  ( $=x/L$ ),  $\eta$  ( $=y/L$ ) at an arbitrary position  $Q(x,y)$  are obtained as follows.

$$\xi = \int_0^\zeta \cos \left[ \left\{ \frac{\theta_A - \theta_o}{2} - q \right\} \cdot \left\{ 1 + \frac{m^2 \cdot \delta^3}{2 \cdot (4/3)} + \frac{m^4 \cdot \delta^6}{2 \cdot 4 \cdot (8/3) \cdot (10/3)} + \dots \right\} + q + \frac{\theta_A + \theta_o}{2} \right] d\zeta \quad (9)$$

$$\eta = \int_0^\zeta \sin \left[ \left\{ \frac{\theta_A - \theta_o}{2} - q \right\} \cdot \left\{ 1 + \frac{m^2 \cdot \delta^3}{2 \cdot (4/3)} + \frac{m^4 \cdot \delta^6}{2 \cdot 4 \cdot (8/3) \cdot (10/3)} + \dots \right\} + q + \frac{\theta_A + \theta_o}{2} \right] d\zeta \quad (10)$$

where,

$$\delta = \gamma \cdot (1 - \zeta) \quad [0 \leq \delta \leq \gamma] \quad (11)$$

$$q = - \frac{(\theta_A - \theta_o) \cdot J_0 \left( \frac{\theta_A - \theta_o}{2} \right) \cdot \sin \left( \frac{\theta_A + \theta_o}{2} \right)}{4J_1 \left( \frac{\theta_A - \theta_o}{2} \right) \cdot \cos \left( \frac{\theta_A + \theta_o}{2} \right)} \quad (12)$$

$$m^2 = - \frac{16J_1 \left( \frac{\theta_A - \theta_o}{2} \right) \cdot \cos \left( \frac{\theta_A + \theta_o}{2} \right)}{9\gamma^2 \cdot (\theta_A - \theta_o)} \quad (13)$$

### 3. Experimental investigation

In order to assess the applicability of the new method, several experiments were carried out using a thin piano wire (SWP-A, length:  $L=500.0-1400.0$  mm, diameter:  $d=0.9$  mm, distributed load per unit length:  $w=49.245 \times 10^{-3}$  N/m) Horizontal and vertical displacements  $y_A$ ,  $x_A$  at the free end are measured by using a grid paper(1 mm spacing).

Young's modulus obtained by applying Method 1 and Method 2 are shown in Figs. 2 and 3, respectively. The measured values of each method remain nearly constant for various lengths  $L$  in the range of  $500.0 - 1400.0$  mm and the standard deviation (S.D.) is small although every method has a little scattered values. As a reference, Young's modulus measured by using conventional three-point bending test based on the small deformation theory is  $E_0=205.8$  GPa.

In this manner, Young's modulus can be obtained by applying an easy method without a large scale testing machine.

### 4. Conclusions

The principal conclusions are drawn as follows

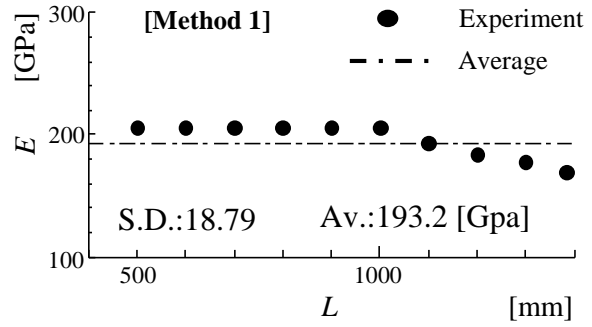


Fig.2 Comparison of Young's moduli for  $\phi=0.9$  piano wires(SWPA)(: Data  $x_A$ ).

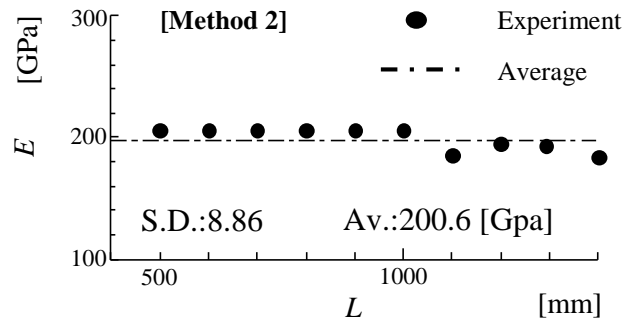


Fig.3 Comparison of Young's moduli for  $\phi=0.9$  piano wires(SWPA)(: Data  $y_A$ ).

from the results of theoretical and experimental analyses.

- (1) The new method is based on the nonlinear large deformation theory.
- (2) A thin material (a piano wire, SWP-A) was tested.
- (3) Experimental results clarify that the new method is suitable for measuring Young's modulus of a thin flexible material.
- (4) Based on the assessments, the proposed method is applied to thin sheets and thin fiber materials (e.g., steel belts, glass fibers, carbon fibers, optical fibers, etc.).

### References

- [1] A.Ohtsuki Proc. 4th Inter. Conf. Exp. Mech., Southampton, Vol.3-4, pp 53-58, 2005.
- [2] A.Ohtsuki 4<sup>th</sup> Inter.Conf.Thin-Walled Struct. Loughborough, Vol.1, pp 233-240, 2004.
- [3] A.Ohtsuki Proc. 2006 SEM Ann. Conf. Exp. Appl. Mech, St.Louis, 78, pp.78(1)-78(8).
- [4] A.Ohtsuki and H. Takada Trans.JSSR No.47, pp 27-31, 2002
- [5] A.Ohtsuki Proc.2005 SEM Ann. Conf. Exp. Appl.Mech., Portland, 72, pp 113(1)-113(8).

# DEPENDENCE OF MECHANICAL PROPERTIES ON VOLUME OF Si AND Cu IN SECONDARY Al-Si-Cu CAST ALLOY

Lenka Kuchariková<sup>1</sup>, Eva Tillová<sup>1</sup>, Denisa Závodská<sup>1</sup>

<sup>1</sup> University of Žilina, Department of Materials Engineering, Univerzitná 8215/1, 01026, Žilina, Slovakia. E-mail: lenka.kucharikova@fstroj.uniza.sk

## 1. Introduction

Mechanical properties testing plays an important role in evaluating fundamental behaviour of engineering materials as well as in developing new materials and in controlling the quality of materials for use in design and construction. Materials used for engineering construction are subjected to a load, and it is important to know that the material is strong enough and rigid enough to withstand the loads that it will experience in service [1].

Aluminum alloys have growing applications in the automotive industry, with respect to reducing the fuel utilization and shielding the environment, where they can successfully reinstate steel and cast iron parts [1, 2]. The group Al-Si alloys are highly versatile materials, comprising 85% to 90% of the total of all aluminium cast parts produced for the automotive industry. Depending on the Si concentration in weight percent, Al-Si alloys fall into three major categories: hypoeutectic (<12% Si), eutectic (12%-13%Si), and hypereutectic (14%-25% Si) [3]. The addition of Si to aluminium reduces melting temperature and improves fluidity. Si alone in aluminium produces a nonheat-treatable alloy; however, in combination with Mg or Cu it produces a precipitation hardening heat-treatable alloy. Si additions to aluminium are commonly used for the manufacturing of castings. The Cu provides substantial increases in strength and facilitates precipitation hardening (increases tensile strength, fatigue strength and hardness of the alloys due to the effect of solid solution hardening). The introduction of Cu to aluminium can also reduce ductility and corrosion resistance [4].

The present study is part of large research project, which was conducted to investigate and to provide a better understanding of mechanical properties dependence on microstructure in secondary (recycled) AlSiCu cast alloys.

## 2. Experimental material and procedure

Experiments were performed on two types of Al-Si-Cu cast alloys (AlSi9Cu3, AlSi6Cu4). Chemical composition both of experimental material is given in Tab. 1. Experimental materials have a lower corrosion resistance, but are suitable for high-temperature (up to max. 250°C) applications (dynamically exposed casts): pistons, cylinder heat, water-jacket, gearbox and so on [5-6].

AlSi9Cu3					
Si	Cu	Fe	Mn	Mg	Cr
9.4	2.4	0.9	0.24	0.28	0.04
Ni	Zn	Ti	Al		
0.05	1.0	0.04	balance		
AlSi6Cu4					
Si	Cu	Fe	Mn	Mg	Cr
6.52	3.88	0.43	0.45	0.29	0.01
Ni	Zn	Ti	Al		
0.01	0.46	0.15	balance		

Tab. 1 The chemical compositions, wt. %

The mechanical properties of cast component are mostly determined by the shape and distribution of Si particles and intermetallic phases in  $\alpha$ -matrix [7]. The experimental tensile and hardness specimens for experimental procedure were made from the casting with turning and milling operation. Mechanical properties were measured according to the standards: STN EN ISO 6892-1 and STN EN ISO 6506-1. Hardness measurement for secondary aluminium alloy was performed by a Brinell hardness tester with a load of 62.5 kp, 2.5 mm diameter ball and a dwell time of 15s. Tensile strength (UTS) was measured on testing machine ZDM 30. The evaluated UTS and Brinell hardness reflect average values of at least six separately bars. The optical microscope Neophot 32 and image analyser software were used for evaluation of experimental material microstructure. The samples for metallography study were prepared by standard metallographic

procedures. The image analyser software was used for quantitative analysis of surface fraction [in %] and surface area size [in  $\mu\text{m}^2$ ] of Si and Cu particles in experimental materials.

### 3. Results of experiment

The results of mechanical properties are documented in Tab. 2. The results of mechanical properties of secondary AlSi9Cu3 cast alloy shows that this material has lower values of mechanical properties in comparison with secondary AlSi6Cu4 cast alloy. However, mechanical properties depend upon microstructure of material and therefore the evaluation of microstructure was carried out [7].

Mechanical behaviour Material	UTS [MPa]	HBW
AlSi9Cu3	211	98
AlSi6Cu4	218	103

Tab. 2. The mechanical properties

The quantitative analysis of surface fraction and surface area size of Si particles in experimental materials shows (Fig. 1) that material AlSi9Cu3 has surface fraction 10.17 % and surface area size  $83.4 \mu\text{m}^2$  and the second AlSi6Cu4 has surface fraction 8.3 % and surface area size  $60.6 \mu\text{m}^2$ . Analysis shows that AlSi9Cu3 material can have a lower UTS because contain more and larger Si particles as the second materials and therefore have a larger amount of initiator of crack.

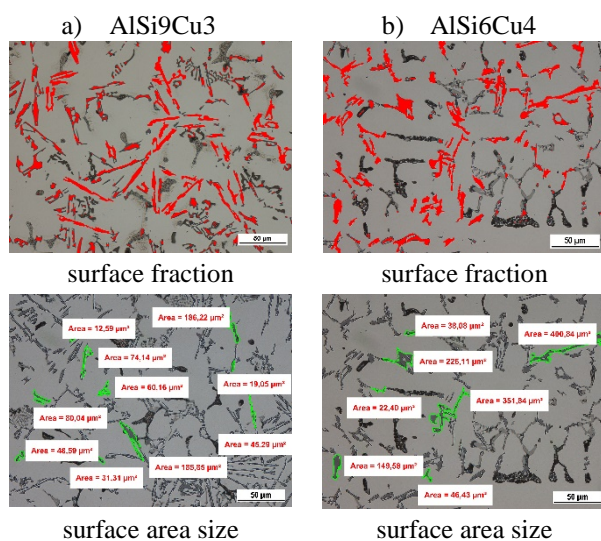


Fig. 1. Quantitative assessment of Si particles

The quantitative analysis of Cu-rich phases shows that material AlSi9Cu3 has surface fraction

2.69 % and surface area size  $31.3 \mu\text{m}^2$  and the second AlSi6Cu4 has surface fraction 3.1 % and surface area size  $82.2 \mu\text{m}^2$ . This analysis shows that material AlSi6Cu4 can have better HBW because have a larger amount of Cu phases in microstructure.

### 4. Conclusions

The experiment shows that material AlSi6Cu4 have higher mechanical properties comparison to the AlSi9Cu3 cast alloy, but the differences are not as great as was expected. The great differences are expected at the other experiment on samples after heat treatment, because Cu is the major elements which strengthening the matrix of aluminium alloy.

### Acknowledgements

This research has been supported by the Scientific Grant Agency of the Ministry of Education of the Slovak Republic VEGA 01/0533/15 and European Union project ITMS 26220220154.

### References

- [1] Kalhapure, G.M., Dighe, P.M., Impact of Silicon Content on Mechanical Properties of Aluminum Alloys. International Journal of Science and Research, 4/6, 2015, pp. 38-40.
- [2] Matvija, M., et al., The effect of ECAP and subsequent Post-ECAP annealing on the microstructure and mechanical properties of AlSi7Mg0.3 alloy. Acta Metallurgica Slovaca. Volume 18, Issue 1, 2012, Pages 4-12
- [3] Jian, X., Han, Q., Formation of hypereutectic silicon particles in hypoeutectic Al-Si alloys under the influence of high-intensity ultrasonic vibration. Overseas Foundry, 10/2, 2016, pp. 118-123
- [4] Kopeliovich, D., Effects of alloying elements on properties of aluminum alloys, on-line: [http://www.substech.com/dokuwiki/doku.php?id=effects\\_of\\_alloying\\_elements\\_on\\_properties\\_of\\_aluminum\\_alloys](http://www.substech.com/dokuwiki/doku.php?id=effects_of_alloying_elements_on_properties_of_aluminum_alloys).
- [5] Náprstková N., Influence of inoculation AlSi7Mg0.3 alloy on roughness of machining surface. Engineering for Rural Development 2013 Jelgava-Latvia, 2013, pp. 278-282.
- [6] Hansen, S. C., Loper, Jr. C. R., Effect of antimony on the phase equilibrium of binary Al-Si alloys. Calphad, 24/3, 2000, pp. 339-352.
- [7] Michna, S., et al., Aluminium materials and technologies from A to Z. Adin, s.r.o. Prešov, 2007.



34<sup>th</sup> Danubia-Adria Symposium on Advances in Experimental Mechanics  
University of Trieste, Italy, 2017



# MECHANICAL CHARACTERIZATION OF 3D-PRINTED SAMPLES

Alberto Dal Maso<sup>1</sup>, Francesca Cosmi<sup>1</sup>

<sup>1</sup> University of Trieste, Department of Engineering and Architecture, Via A. Valerio 10, 34127, Trieste, Italy. E-mail: [cosmi@units.it](mailto:cosmi@units.it), [albertodalmaso92@gmail.com](mailto:albertodalmaso92@gmail.com)

## 1. Introduction

Additive manufacturing is gaining greater and greater popularity in the last few years [1], with fused deposition modelling (FDM) becoming an accessible tool for rapid prototyping with plastic-based materials. Due to its building process, the mechanical properties of 3D-printed objects are substantially different from those of the same object of the same material, but obtained by a different manufacturing process, i.e. injection molding [2]. In this paper, we investigate the results of tensile tests on 3D-printed specimens made of various plastic and composite materials.

## 2. Methods

ASTM D1822 standard specimens were used in tensile tests, Fig.1. The specimens were built in two different orientations: flat on the buildplate, and standing on one side, as shown in Fig. 2.

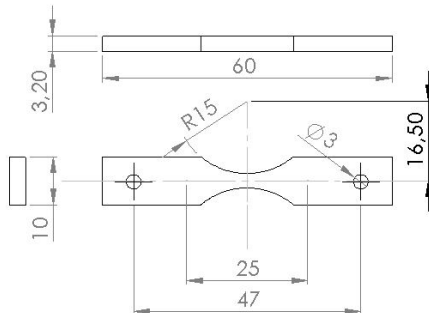


Fig. 1. Geometry of the ASTM D1822 specimen

The specimens were printed by a 3D Builder Premium™ machine in three different materials: a PLA (Poly Lactic Acid) plastic filament by Builder™, a composite material, Bronzefill by ColorFabb™, made of a bronze powder in a PLA matrix, and the thermoplastic elastomer Innoflex 45 by Innofil™. The main printing parameters are given in Tab. 1.

All specimens were tested in tension using a test-rig originally designed to apply small loads during micro-CT acquisitions [3], equipped with a load cell and an encoder coupled with a computer

interface, which read and saved these values at regular time intervals.

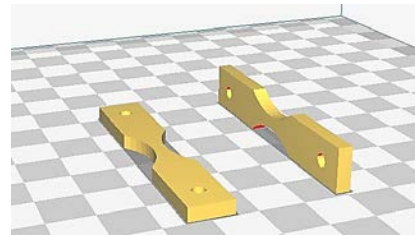


Fig. 2. Flat-built (left) and side-built (right) specimen.

The stress-strain curve of each specimen was obtained. Young's modulus, maximum stress and

	PLA	Bronze fill	Innoflex 45
# flat-built samples	20	6	3
# side-built samples	3	1	2
Print temperature, °C	210	210	220
Print speed, mm/s	60	50	40
Layer height, mm	0.2	0.2	0.2
Wall thickness, mm	0.8	0.8	0.8
Infill density	100%	100%	100%
Infill pattern	Grid	Grid	Grid

strain at maximum stress were computed as well.

Tab. 1. Samples and print parameters.

## 3. Results

The specimens exhibit different behaviors depending not only on the material but also on the building orientation, as shown in Figg. 3-6.

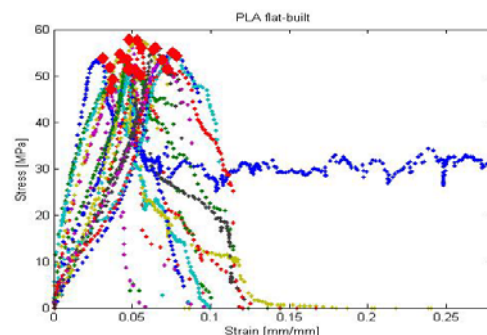


Fig. 3. Stress–Strain curves of PLA flat-built samples.

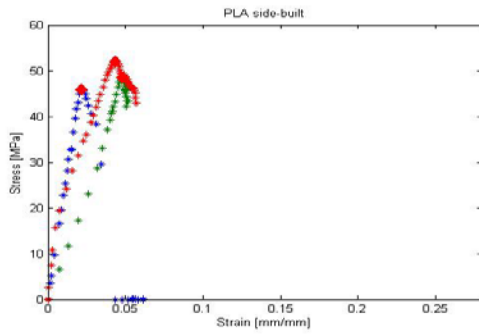


Fig. 4. Stress–Strain curves for PLA side-built samples.

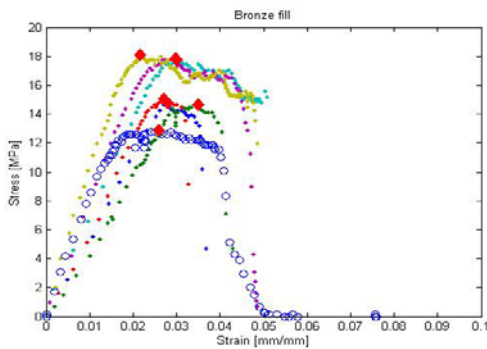


Fig. 5. Stress–Strain curves for flat-built (◆) and side-built (○) PLA bronze fill samples.

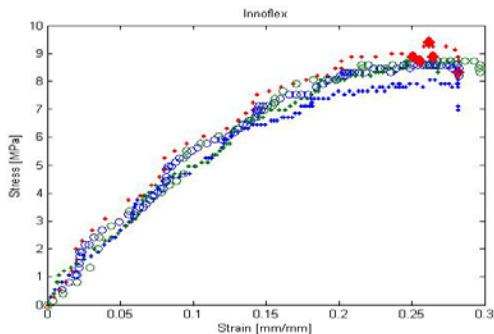


Fig. 6. Stress–Strain curves flat-built (◆) and side-built (○) Innoflex 45 specimens.

Tab. 2 summarizes the results (average and standard deviation) of the measured parameters.

The stress-strain curves are often far from linear, which is an issue when defining Young’s modulus [4]. In this work, Young’s modulus was obtained as the linear regression in the elastic part of the curve that gave the minimum RMS error.

It should be noted that, on average, pure PLA exhibits a greater Young’s modulus than the other materials and pure PLA also shows the greatest maximum stress, notwithstanding the relatively high dispersion of these results, which is typical of polymeric materials [5].

	PLA flat-built	PLA side-built	Bronze fill (all)	Innoflex 45 (all)
<b>Maximum stress, MPa</b>	<b>53.20</b> (2.70)	<b>48.8</b> (2.59)	<b>15.86</b> (1.88)	<b>8.84</b> (0.34)
<b>Strain at max. stress, mm/mm</b>	<b>0.053</b> (0.013)	<b>0.038</b> (0.012)	<b>0.028</b> (0.004)	<b>0.263</b> (0.011)
<b>Young’s modulus, MPa</b>	<b>1610</b> (1132)	<b>2091</b> (916)	<b>705</b> (207)	<b>73</b> (27)

Tab. 2. Average and standard deviation of the measured parameters.

#### 4. Remarks

- It should be noted that the speed at which a specimen is loaded affects the curve but cannot be exactly controlled since the test-rig is hand-driven. Upgrade to a motor-driven device has already been planned.
- The PLA Bronzefill composite material has definitely poorer mechanical properties than pure PLA. Since the metal particles are not fibers, they do not improve the material’s resistance. We expect the opposite behavior on 3D-printed carbon-reinforced composites, which we plan to test.
- The Innoflex 45 elastomer specimens underwent large deformations with no specimen reaching the breaking point within the range of operation of the test-rig.

#### References

- [1] Dr. Ian Gibson et al. Additive Manufacturing Technologies - Rapid Prototyping to Direct Digital Manufacturing. Springer, 2010.
- [2] Constance Ziemian, Mala Sharma, Sophia Ziemian, Anisotropic Mechanical Properties of ABS Parts Fabricated by Fused Deposition Modelling. Bucknell University, Duke University, 2014.
- [3] F. Cosmi, A. Bernasconi. Micro-CT investigation on fatigue damage evolution in short fibre reinforced polymers, Composites Science and Technology 79 (2013) 70–76.
- [5] Helmut Fahrenholz, Plastics: Determination of tensile properties. Zwick/Roell, October 2014.



34th Danubia-Adria Symposium on Advances in Experimental Mechanics  
University of Trieste, Italy, 2017



- [4] Roger Brown, Handbook of Polymer Testing,  
UK, 2002.

## DO MODERN CONCRETES EXHIBIT SIMILAR EARLY-AGE STIFFNESS AND STRENGTH DEVELOPMENTS AS THEIR PREDECESSORS?

Eva Binder<sup>1</sup>, Gerald Maier<sup>2</sup>, Olaf Lahayne<sup>1</sup>, Roland Reihnsner<sup>1</sup>, Mario Auswegger<sup>1</sup>,  
Martin Peyer<sup>1</sup>, Bernhard Pichler<sup>1</sup>

<sup>1</sup> TU Wien – Vienna University of Technology, Institute for Mechanics of Materials and Structures, Karlsplatz 13/202, 1040 Vienna, Austria. E-mails: [Eva.Binder@tuwien.ac.at](mailto:Eva.Binder@tuwien.ac.at), [Olaf.Lahayne@tuwien.ac.at](mailto:Olaf.Lahayne@tuwien.ac.at), [Roland.Reihnsner@tuwien.ac.at](mailto:Roland.Reihnsner@tuwien.ac.at), [Mario.Auswegger@gmail.com](mailto:Mario.Auswegger@gmail.com), [Bernhard.Pichler@tuwien.ac.at](mailto:Bernhard.Pichler@tuwien.ac.at)

<sup>2</sup> Smart Minerals GmbH, Franz-Grill-Straße 9, 1030 Vienna, Austria. E-mails: [maier@smartminerals.at](mailto:maier@smartminerals.at), [peyerl@smartminerals.at](mailto:peyerl@smartminerals.at)

### 1. Introduction

Some 5 % of global anthropogenic CO<sub>2</sub> emissions result from the production of cement-based materials [1]. Therefore, the cement and concrete industry is challenged to produce less CO<sub>2</sub>-intensive binders. The currently implemented strategy is to replace traditional Portland cement clinker partly by Supplementary Cementitious Materials, resulting in so-called *blended cements*.

Supplementary Cementitious Materials (SCMs) are typically waste products of other industrial sectors, e.g., fly ashes from combustion power plants or blast furnace slags from steel production. SCMs exhibit a hydraulic reaction when mixed with water, but the reaction kinetics are slower compared to the hardening reaction between traditional Portland cement clinker and water.

Concretes produced with blended cements are known to exhibit a reliable and durable field performance at mature ages (> 28 days), but a comparably slow development of mechanical properties such as stiffness and strength, particularly during the first week after production. Suitably well-developed early-age mechanical properties, in turn, are required, such that (i) formworks may be removed, or (ii) prestress may be applied without damaging the concrete.

This antagonism is setting the scene for the present contribution that aims at characterizing the early-age evolutions of stiffness and strength of twelve different concrete mixes, typically used for bridge construction.

### 2. Standard formulas for early-age strength and stiffness development of concrete

The most important material property of concrete is its uniaxial compressive strength at an

age of 28 days. It can be quantified by means of a simple-to-perform destructive cube compression test. The pre-standard, “Model Code 2010”, see [2], provides many formulas that relate other material properties of interest to the uniaxial compressive strength at 28 days,  $f_{cm}$ . In more detail the Model Code provides (i) a mathematical function for quantifying the early-age increase of strength with increasing material age, up to the strength value at 28 days, with coefficient  $s$  accounting for the strength class of cement [2],

$$f_{cm}(t) = f_{cm} \cdot \exp \left\{ s \cdot \left[ 1 - \sqrt{\frac{28 \text{ days}}{t}} \right] \right\}, \quad (1)$$

(ii) a function for estimation of the Young’s modulus of concrete at 28 days, with coefficient  $\alpha_E$  accounting for different types of aggregates [2],

$$E_{ci} = 21.5 \text{ GPa} \cdot \alpha_E \cdot \sqrt[3]{\frac{f_{cm}}{10 \text{ MPa}}}, \quad (2)$$

and (iii) a function for quantifying the early-age increase of Young’s modulus with increasing material age, up to the stiffness value at 28 days

$$E_{ci}(t) = E_{ci} \cdot \sqrt{\exp \left\{ s \cdot \left[ 1 - \sqrt{\frac{28 \text{ days}}{t}} \right] \right\}}. \quad (3)$$

These mathematical relations were historically developed based on many experimental data obtained from early-age testing of concretes made with traditional Portland cements. The applicability of Eqs. (1) – (3) is, thus, questionable when it comes to modern concretes produced with blended cements.

### 3. Testing campaigns

A comprehensive experimental campaign is carried out in order to check the reliability of

Model Code functions (1) – (3) for the early-age development of uniaxial compressive strength and Young’s modulus. It involves 12 different concrete mixes. They are referring to three different compressive strength classes, they are made of three different types of cement and two types of aggregates, and they are targeting at two different air contents.

Standard experiments refer to the determination of the uniaxial compressive strength and the unloading modulus at material ages amounting to 1, 3, 7, 14, and 28 days after production. Non-standard experiments follow the experimental protocol developed in [3]. This test protocol includes hourly repeated loading-unloading cycles under uniaxial compression. The first test is carried out 24 hours after production. Hourly testing is repeated until the tested concrete specimen reaches an age of 8 days. Therefore, each specimen undergoes some 170 loading-unloading cycles during the first week after production. In order to ensure that the specimens remain undamaged, the maximum forces are selected such that the loading does not exceed 20 % of the strength of the specimen at the time of testing. In addition, a few loading-unloading cycles are carried out 28 days after production. From these tests, the unloading modulus is determined.

The standard strength values, determined at the material age amounting to 28 days, are used as input for Eqs. (1) – (3). Corresponding outputs are compared with the experimental data. This is shown exemplarily for one of the tested concretes in Figs. 1 and 2.

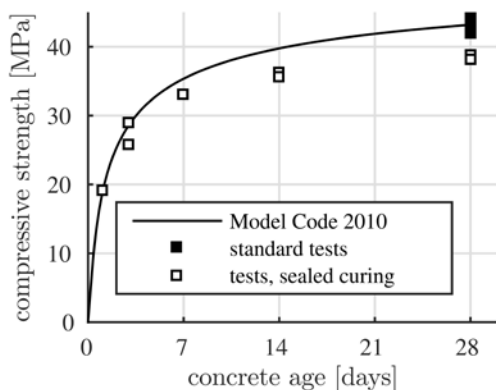


**Fig. 1.** Uniaxial compressive strength as a function of material age of one of the tested concretes: test data from testing, see squares, and expectations of Model Code 2010 [2], see the solid line and Eq. (1)

Figs. 1 and 2 underline exemplarily (i) that Eqs. (1) to (3) are qualitatively quite satisfactory, (ii) that

quantitative aspects deserve improvement, (iii) that the early-age strength development of concrete strongly depends on the curing condition, and (iv) that Eqs. (2) and (3) significantly underestimate the early-age stiffness evolution.

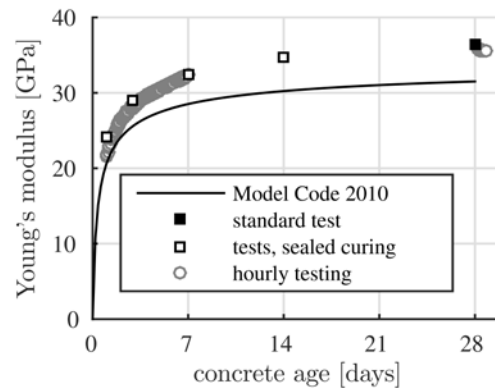


**Fig. 2.** Young’s modulus as a function of material age of one of the tested concretes: test data from standard tests, see squares, test data from hourly testing, see circles, and expectations of Model Code 2010 [2], see the solid line as well as Eqs. (2) and (3)

## Acknowledgements

Financial support of the experiments by the Austrian Ministry for Transport and Technology (bmvit), the Austrian Research Promotion Agency (FFG), ÖBB Infrastruktur AG, ASFINAG Bau Management GmbH, provided within VIF-project 850554 „Österreichischer Beton Benchmark” as well as help of the laboratory staff both at the TU Wien – Vienna University of Technology and Smart Minerals GmbH are gratefully acknowledged.

## References

- [1] Worrell, E., Price, L., Martin, N., Hendriks, C., & Meida, L. O., Carbon dioxide emissions from the global cement industry, Annual Review of Energy and the Environment, 26(1), 2001. pp. 303-329.
- [2] The International Federation for Structural Concrete (fib), The fib Model Code for Concrete Structures 2010, Ernst & Sohn, 2010.
- [3] Irfan-ul-Hassan, M., Pichler, B., Reihnsner, R., & Hellmich, C. Elastic and creep properties of young cement paste, as determined from hourly repeated minute-long quasi-static tests. Cement and Concrete Research, 82, 2016. pp. 36-49.

# CORROSION RESISTANCE OF S355J2 STEEL WELDED BY SAW BEFORE AND AFTER SURFACE TREATMENT BY PHOSPHATING

Kamil Borko<sup>1</sup>, Filip Pastorek<sup>2</sup>, Branislav Hadzima<sup>1,2</sup>

<sup>1</sup> University of Žilina, Faculty of Mechanical Engineering, Department of Materials Engineering, Univerzitná 8515/1, 010 26 Žilina. E-mail: [kamil.borko@fstroj.uniza.sk](mailto:kamil.borko@fstroj.uniza.sk)

<sup>2</sup> University of Žilina, Research Centre, Univerzitná 8515/1, 010 26 Žilina. E-mail: [branislav.hadzima@rc.uniza.sk](mailto:branislav.hadzima@rc.uniza.sk), [filip.pastorek@rc.uniza.sk](mailto:filip.pastorek@rc.uniza.sk)

## 1. Introduction

Corrosion resistance is of great importance for the materials usage, particularly for steel. The corrosion resistance depends on an environment where the material is present, on the chemical composition and structure of the material. Resistance to atmospheric corrosion of steel can be increased by addition of a small addition of copper. Addition of Ni is also effective. Increase of atmospheric corrosion resistance can be also reached by sufficient amounts of Cr in a combination with Cu. In general, maximal resistance to atmospheric corrosion can be achieved by a higher content of alloying elements [1, 2].

Submerged arc welding (SAW) is an arc welding process and the arc is shielded by a layer of flux which protects the molten weld metal from atmospheric contamination. The base metal (BM), the heat affected zone (HAZ) and the weld metal (WM) are parts of the welded joint and define the properties of the welded joints and welded constructions [3, 4].

SAW is the most widespread method for welding large diameter pipes because of its elevated productivity. Its main drawback, however, is that very high residual stresses develop around the welded area [5]. This may also influence the corrosion resistance of the weld metal.

## 2. Experiment

S355J2 steel was used as an experimental material with a known chemical composition listed in table 1. The microstructure of the S355J2 steel (Fig. 1) is formed by ferrite-pearlite matrix with a low pearlite content (local pearlite occurrence) and with the grain size of about 10 microns. Fillet welds were made on plates of 250 mm × 500 mm × 30 mm using SAW.

elem.	C	Mn	P	S	Si	Cu	Fe
wt. %	0.2	1.600	0.025	0.025	0.550	0.550	bal.

Tab. 1 Chemical composition of S355J2 steel

Electrochemical characteristics of the material ( $E_{\text{Corr}}$ ,  $i_{\text{Corr}}$ ,  $v_{\text{Corr}}$ ) were investigated on the ground material (P1000 emery paper) with and without further surface treatment. Electrochemical characteristics were measured in a 0.1M  $\text{Na}_2\text{SO}_4$  solution by potentiodynamic tests using a potentiostat SP300.



Fig. 1 Microstructure of S355J2 steel

Phosphating process was carried out in phosphating bath composed of: 1000 ml demineralized water, 15 g  $\text{H}_3\text{PO}_4$ , 15 g  $\text{MnO}_2$  and 5 g very fine steel wires. The temperature of phosphating process was set to 92 - 95 °C.

## 3. Results

As can be seen from the measured potentiodynamic curves (Fig. 2) and electrochemical characteristics (Table 2) in 0.1M  $\text{Na}_2\text{SO}_4$  evaluated by the Tafel analysis, the base material (BM) has higher thermodynamic stability than weld metal (WM), because the value of corrosion potential ( $E_{\text{Corr}}$ ) is more positive about 41 mV. However, higher kinetic stability

is reached by WM than by BM, representing by lower corrosion current density ( $i_{Corr}$ ) value and corresponding corrosion rate ( $v_{Corr}$ ) value.

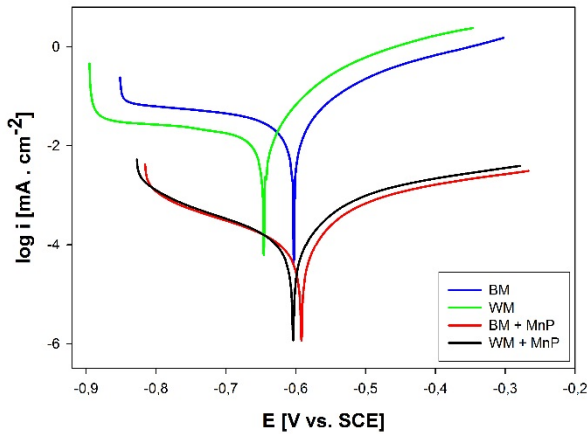


**Fig. 2** Potentiodynamic curves of S355J2 steel

Created phosphate layer has porous nature and homogenous crystallic structure with negligible visual differences on both tested surfaces (BM and WM). By forming a stable mechanical barrier against corrosion mechanisms this layer increased the corrosion resistance of the tested surfaces in 0.1M Na<sub>2</sub>SO<sub>4</sub> environment. Electrochemical corrosion characteristics of the phosphate layer created on BM and WM are very similar as seen in table 1.

	$E_{Corr}$ [mV]	$i_{Corr}$ [ $\mu A.cm^{-2}$ ]	$v_{Corr}$ [ $\mu m.y^{-1}$ ]
<b>BM</b>	-604 ± 10	20.3 ± 1.5	472 ± 21
<b>WM</b>	-645 ± 13	14.1 ± 1.9	325 ± 18
<b>BM + MnP</b>	-592 ± 12	0.086 ± 0.003	1.95 ± 0.1
<b>WM + MnP</b>	-603 ± 10	0.099 ± 0.005	2.29 ± 0.2

**Tab. 2** Electrochemical characteristics of S355J2 steel

The difference between corrosion properties of the surface with and without phosphate layer is mainly in  $i_{Corr}$  and  $v_{Corr}$  values as the corrosion potential (-592 mV resp. -603 mV) of the phosphate layer is similar to values of BM (-604 mV) This means, that forming a phosphate layer results in increase of corrosion resistance through a reduction of the corrosion current density from 20.3  $\mu A.cm^{-2}$  resp. 14.1  $\mu A.cm^{-2}$  to 0.086  $\mu A.cm^{-2}$  resp. 0.099  $\mu A.cm^{-2}$  and corrosion rate from 472  $\mu m.y^{-1}$  resp. 325  $\mu m.y^{-1}$  to 1.95  $\mu m.y^{-1}$  resp. 2.29  $\mu m.y^{-1}$ .

## 4. Conclusions

The present work describes the influence of surface treatment by phosphating on corrosion properties of S355J2 steel and welded SAW joint in 0.1M Na<sub>2</sub>SO<sub>4</sub> solution. It may be concluded:

- ✓ Tested base material (S355J2 steel) has higher thermodynamic stability than weld metal, which shows higher kinetic stability in 0.1M Na<sub>2</sub>SO<sub>4</sub>.
- ✓ Corrosion resistance of BM and WM after phosphating is very similar.
- ✓ Increased corrosion resistance of phosphate surfaces is reached kinetically by reducing values of  $i_{Corr}$  and  $v_{Corr}$ .

## Acknowledgements

The research was supported by the Slovak Research and Development Agency, project No. APVV-14-0096 and by ERDF projects: ITMS 26220220183, ITMS 26220220048 and ITMS 2014+313011D011.

## References

- [1] Fundamentals of electrochemical corrosion of metals. Hadzima, B. - Liptáková, T.: 1st edition. Žilina: EDIS Publishing. ŽU 2008. 112p. ISBN 978-80-8070-876-4.
- [2] Thompson, D.H., General Tests and Principles. Handbook on Corrosion Testing and Evaluation. John Wiley & Sons, 1975.
- [3] Sirin, K., Sirin, Y.S., Kaluc, E., (2016). Influence of the interpass temperature on  $t_{8/5}$  and the mechanical properties of submerged arc welded pipe, Journal of Materials Processing Technology, 238, 2016. pp. 152-159.
- [4] Pu, J., Yu, S., Li, Y., (2017). Role of inclusion in flux aided backing submerged arc welding, Journal of Materials Processing Technology, 240, 2017. pp. 145-153.
- [5] Forouzan, R.M., Nasiri, M.M.S., Mokhtari, A., Heidari, A., Golestaneh, J.S., (2012). Residual stress prediction in submerged arc welded spiral pipes, Materials & Design, 33, 2012. pp. 384-394.

# THE EFFECT OF ULTRASONIC IMPACT TREATMENT (UIT) ON ELECTROCHEMICAL CHARACTERISTICS OF AZ31 MAGNESIUM ALLOY

Daniel Kajánek<sup>1,2</sup>, Branislav Hadzima<sup>2</sup>, Ján Lago<sup>3</sup>, Martina Neslušán Jacková<sup>2</sup>

- <sup>1</sup> University of Žilina, Department of Materials Engineering, Univerzitná 1, 010 26, Žilina, Slovakia. E-mail: daniel.kajaneck@fstroj.uniza.sk
- <sup>2</sup> University of Žilina, Research Centre, Univerzitná 8215/1, 010 26, Žilina, Slovakia. E-mails: branislav.hadzima@rc.uniza.sk, martina.jackova@rc.uniza.sk
- <sup>3</sup> LAGO Nástrojárň spol. s r. o, Veľké Rovné 1571, 013 62, Veľké Rovné, Slovakia, E-mail: lago@lago.sk

## 1. Introduction

Magnesium based alloys are the lightweight materials with high specific strength, good machinability and recyclability. However, they have low corrosion resistance and this problem limits their wider usage [1,2]. Various types of surface treatments have been investigated to solve this problem [3,4]. Ultrasonic impact treatment (UIT) is relatively new method for improving surface characteristics of materials by usage of ultrasonic peening. According to recent studies, UIT improves fatigue properties and corrosion resistance [5,6]. Influence of this technology on corrosion behavior of magnesium alloys has not been investigated yet hence the aim of this study is to evaluate the effect of UIT on electrochemical characteristics of AZ31 magnesium alloy.

## 2. Experimental material and methods

The continually cast heat treated (homogenous aging: 420 °C/16 h) AZ31 magnesium alloy has been used as the experimental material and its chemical composition is listed in Tab. 1.

Tab. 1. Chemical composition of AZ31 Mg alloy

Elem.	Al	Zn	Mn	Si	Cu	Fe	Mg
wt. %	2.96	0.82	0.43	0.004	0.004	0.002	bal.

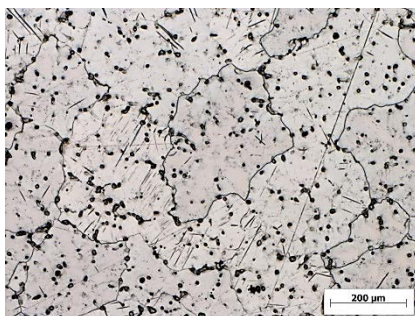


Fig. 1. Microstructure of AZ31 magnesium alloy

The microstructure (Fig. 1) consists of polyedric grains of solid solution of aluminium, zinc and other alloying elements in magnesium. There are also areas created by intermetallic phase  $Al_{12}Mg_{17}$ .

The samples have been ground by an emery paper p1000 before the UIT process has been realized. The UIT has been carried out on CNC mill using the ultrasonic impact head (Fig. 2). The parameters of UIT have been set as follows: pressure force of 85 N and ultrasonic frequency of 20 kHz.



Fig. 2. Ultrasonic impact head

The corrosion electrochemical characteristics ( $E_{corr}$ ,  $i_{corr}$  and  $r_{corr}$ ) of ground samples and UIT samples have been obtained by potentiodynamic polarization (PD) tests after 5 minutes of potential stabilization in aggressive aqueous solution of 0.1M NaCl. The measurements have been performed using VSP Biologic potentiostat in three electrode cell system. The applied potential has ranged from -200 mV to +500 mV with step rate of  $1 \text{ mV}\cdot\text{s}^{-1}$ . The measured PD curves have been analyzed using Tafel extrapolation method.

### 3. Results and discussion

The Fig. 3 shows the PD curves of non-treated and UIT treated samples measured in 0.1M NaCl and the values of electrochemical characteristics are listed in Table 2. The results of PD tests show that AZ31 samples treated by UIT exhibit more positive corrosion potential  $E_{\text{corr}}$  (-1387 mV) compared to the value reached by non-treated samples (-1496 mV). More positive value of  $E_{\text{corr}}$  means that the UIT has positive effect on the corrosion thermodynamics of AZ31 Mg alloy. On the contrary, the UIT has negative effect on corrosion kinetics of AZ31 as the treated samples have reached higher value of corrosion current density ( $71.3 \mu\text{A}\cdot\text{cm}^{-2}$ ) compared to the  $i_{\text{corr}}$  of non-treated AZ31 ( $19.7 \mu\text{A}\cdot\text{cm}^{-2}$ ). Forasmuch as the corrosion rate ( $r_{\text{corr}}$ ) is in direct proportionality with corrosion current density ( $i_{\text{corr}}$ ), it means that corrosion will be faster in case of the UIT treated AZ31 samples.

The higher  $i_{\text{corr}}$  values of the UIT treated AZ31 samples could be the result of accumulated energy on the Mg surface caused by the ultrasonic impacts which lead to the higher reactivity of the surface. The highly soluble magnesium oxide film is rapidly formed on the sample's surface during UIT process. This type of film is unstable and does not provide a good protection which means that the corrosion rate of AZ31 is higher after the application of UIT.

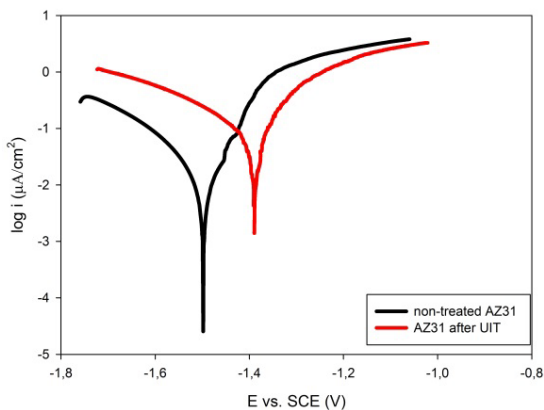


**Fig. 3.** PD curves of non-treated AZ31 and AZ31 after UIT treatment in 0.1M NaCl

**Tab. 2.** Electrochemical characteristics of non-treated AZ31 and AZ31 after UIT in 0.1M NaCl

State of the AZ31 surface	$E_{\text{corr}}$ [mV]	$i_{\text{corr}}$ [ $\mu\text{A}\cdot\text{cm}^{-2}$ ]	$r_{\text{corr}}$ [ $\text{mm}\cdot\text{yr}^{-1}$ ]
Non-treated	-1496	19.7	0.9
UIT	-1387	71.3	3.2

### 4. Conclusions

The ultrasonic impact treatment (UIT) has been performed on the AZ31 Mg alloy followed by the evaluation of its effect on corrosion resistance of this alloy. According to the results of PD tests UIT improved the thermodynamic stability of the samples. This is proved by the more positive  $E_{\text{corr}}$  values after UIT. In terms of corrosion kinetics, UIT has negative effect on corrosion rate as the UIT treated samples exhibit higher values of  $i_{\text{corr}}$ . The negative effect of UIT could be overcome by the immersion in proper pickle to remove the oxide film from the AZ31 surface.

### Acknowledgements

Authors acknowledge the financial support for ERDF and Slovak state budget by the projects ITMS 313011D011, ITMS 26220220048 and for Slovak Scientific Grant Agency by the project no. 1/0045/17.

### References

- [1] Song, G.L., Corrosion of magnesium alloys. Woodhead Publishing Ltd, 2011.
- [2] Liu, L. Welding and joining of magnesium alloys. Woodhead Publishing Ltd, 2010.
- [3] Czerwinski, F. Magnesium alloy – Corrosion and Surface Treatments. InTech, 2011.
- [4] Drábiková, J., Pastorek, F., Fintová, S., Doležal, P., Wasserbauer, J.: Improvement of bio-compatible AZ61 magnesium alloy corrosion resistance by fluoride conversion coating. In *Koroze a ochrana materiálu*, 60(5), 2016, pp. 132-138.
- [5] Mordyuk, B.N. et al., Enhanced fatigue durability of Al-6 Mg alloy by applying ultrasonic impact peening: Effects of surface hardening and reinforcement with AlCuFe quasicrystalline particles. In *Materials Science and Engineering A*, 563, 2013, pp. 138-146.
- [6] Vasylyev, M.A., Chenakin, S.P., Yatsenko, L.F., Ultrasonic impact treatment induced oxidation of Ti6Al4V alloy. In *Acta Materialia*, 103, 2016, pp. 761-774.

## FATIGUE PROPERTIES OF AW 6082 ALUMINIUM ALLOY AFTER SHOT PEENING AND ANODIZING

**Branislav Hadzima<sup>1</sup>, Libor Trško<sup>1</sup>, Otakar Bokůvka<sup>2</sup>, František Nový<sup>2</sup>, Filip Pastorek<sup>1</sup>, Michal Jambor<sup>2</sup>**

<sup>1</sup> Research Centre of the University of Zilina, Univerzitna 8215/1, 01026, Zilina, Slovak Republic. E-mails: [branislav.hadzima@rc.uniza.sk](mailto:branislav.hadzima@rc.uniza.sk), [libor.trsko@rc.uniza.sk](mailto:libor.trsko@rc.uniza.sk), [filip.pastorek@rc.uniza.sk](mailto:filip.pastorek@rc.uniza.sk)

<sup>2</sup> University of Zilina, Department of Materials Engineering, Univerzitna 8215/1, 01026, Zilina, Slovak Republic E-mails: [otakar.bokuvka@fstroj.uniza.sk](mailto:otakar.bokuvka@fstroj.uniza.sk), [frantisek.novy@fstroj.uniza.sk](mailto:frantisek.novy@fstroj.uniza.sk), [michal.jambor@fstroj.uniza.sk](mailto:michal.jambor@fstroj.uniza.sk)

### 1. Introduction

Even when it seems that anodized coatings are solving the major corrosion issue of aluminium alloys, they have negative effects on other, mainly mechanical properties. The amorphous coating is not completely uniform and contains many micro-cracks and micro-pores. Cracking also occurs during loading of the component due to extremely different moduli of elasticity of the coating and the substrate. These cracks serve as a strong stress concentration points (notches) in the process of cyclic (fatigue) loading, thus accelerate the process of fatigue crack initiation [1-3].

The shot peening as a surface treatment has proven that it is possible to significantly improve the fatigue resistance of various structural materials by introduction of compressive residual stresses and grain refinement of the surface layer. This application includes all commonly used structural materials as steels [4], aluminium alloys [5], nickel and titanium alloys [6] and even magnesium alloys [6]. Using the shot peening as a pre-treatment to anodize coating provides a chance to restore the fatigue properties of an anodized component.

### 2. Experimental material and surface treatment

The wrought AW 6082-T651 aluminium alloy was used as experimental material, which is widely used in automotive and aeronautical applications. For more information about used experimental material reader can refer to [7].

Surface strengthening was performed by the air blast shot peening with Almen intensity 6N and coverage of 100 %. To avoid the surface contamination by steel residues from ordinary cast

steel peening media, fine glass beads with diameter of 0.4 mm and the impact angle 90° with respect to the specimen's axis were used. The surface topography after shot peening (Fig. 1) well documents the negative side effect of shot peening, which is the increase of the surface roughness.

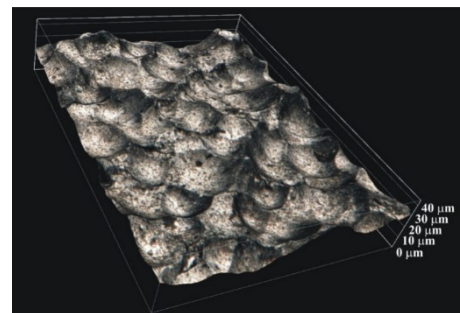


**Fig. 1.** Topography of surface after shot peening.

After the surface strengthening by shot peening, the sulfuric acid anodizing process at a constant current density of 40 mA·cm<sup>-2</sup> in a bath containing 250 g·dm<sup>-3</sup> H<sub>2</sub>SO<sub>4</sub> at 20 ± 0.5 °C for 20 min, was carried out. Sealing was done in deionised water at 97 °C for a period of 4 min. The thickness of coating layer was measured by optical microscopy and was later confirmed by the SEM studies, as well. The average thickness of coating layer reached approximately 30 μm (Fig. 2).

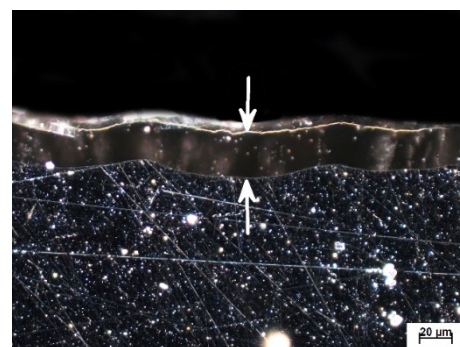


**Fig. 2.** Thickness of the anodized coating.

### 3. Results and discussion

According to the fatigue test results (Fig. 3), the shot peening significantly improved the fatigue strength of the AW 6082 aluminium alloy and the improvement is more or less constant over the whole measured interval of loading cycles ( $N \approx 10^5 \div 10^{10}$ ). As expected, creation of the brittle anodized coating on the shot peened surface decreased the fatigue strength of the specimens. However, the total fatigue strength of the shot peened specimens with anodized coating is still higher than of the specimens without any surface treatment. An interesting fact is that the fatigue life curve of the shot peened surface and anodized tends to converge at approximately  $N \approx 4 \times 10^8$  cycles with the fatigue life curve of shot peened specimens. Beyond this point, the fatigue strengths of specimens with shot peened and shot peened + anodized surfaces are very similar.

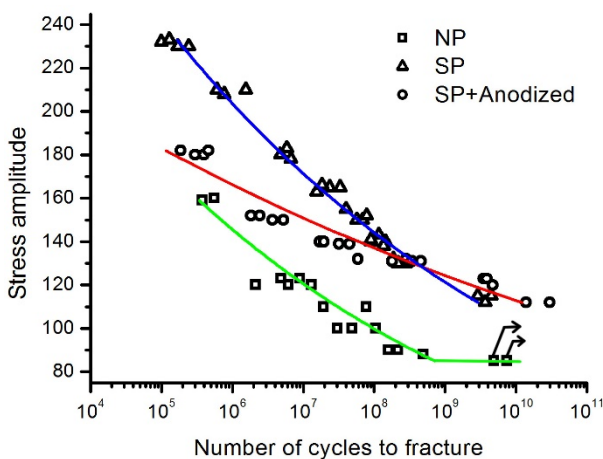


**Fig. 3.** S – N curves of not peened, shot peened and shot peened + anodized specimens.

When the high loading stress amplitude is applied (corresponding to the lower number of loading cycles to fracture), the brittle anodized layer starts to crack and the cracks serve as sharp notches and accelerate the fatigue crack initiation in the substrate. However, when the crack from the anodized surface layer hits the strengthened shot peened layer of the substrate, the compressive residual stresses cause necessity of re-initialization of the fatigue crack and slow down the fatigue crack growth in early stages. At low stress amplitudes, corresponding with the region above  $N = 5 \times 10^8$  cycles, the anodized layer is able to stay compact longer and together with the strengthened surface layer by shot peening further improves the fatigue life.

### 4. Conclusions

The shot peening with glass beads was used as a pre-treatment to anodizing on AW6082 aluminium alloy with aim to reduce the negative effect of anodizing on fatigue properties of the substrate. According to results of experimental works and their discussion, the following can be concluded:

- The shot peening performed with Almen intensity 6N and coverage of 100 %, was able to improve the fatigue properties of the AW 6082 aluminium alloy in the whole measured region.
- Despite the negative effect of anodizing on fatigue life, application of the shot peening as the pre-treatment caused that even with anodized surface layer, the fatigue strength was higher than that of the not treated material in the whole investigated region of fatigue loading.

### Acknowledgements

The research was supported by projects ITMS: 313011D011 and 26220220048 and VEGA project No. 1/0123/15.

### References

- [1] Fares, L., et. al., Coupled effects of substrate microstructure and sulphuric acid anodizing on fatigue life of a 2017A aluminum alloy, *Mater. Des.*, 86, 2015. pp. 723-734.
- [2] Gröber, D., et. al., The effect of anodising on the fatigue performance of self-tapping aluminium screws, *Int. J. Fatigue*, 75, 2015. pp. 108-114.
- [3] Baohua, N., et. al., Effect of anodizing treatment on the very high cycle fatigue behavior of 2A12-T4 aluminum alloy, *Mater. Des.*, 50, 2013. pp. 1005-1010.
- [4] Trško, L., et. al., Effect of severe shot peening on ultra-high-cycle fatigue of a low-alloy steel, *Mater. Des.*, 57, 2014. pp. 103-113.
- [5] Trško, L. The effect of different shot peening intensities on fatigue life of AW 7075 aluminium alloy, *Mater. Eng. - Mater. Inz.*, 20, 2013. pp. 167-173.
- [6] Baiker, S. (editor). Shot peening: a dynamic application and its future. Wetzikon: Metal Finishing News, 2009.
- [7] ASM Handbook: Properties and selection: nonferrous alloys and special-purpose materials, ASM International, Novelty, 1992.

# DEPENDENCE OF INTERNAL DAMPING ON TEMPERATURE IN AUSTENITIC STAINLESS STEELS

Tatiana Oršulová<sup>1</sup>, Monika Oravcová<sup>1</sup>, Peter Palček<sup>1</sup>, Milan Uhrčík<sup>1</sup>

<sup>1</sup> University of Žilina, Faculty of Mechanical Engineering, Department of Material Engineering, Univerzitná 8215/1, 010 26, Žilina, Slovakia. E-mail: tatiana.orsulova@fstroj.uniza.sk

## 1. Introduction

Austenitic stainless steels are ternary alloys of Fe-Cr-Ni. Their microstructure is austenitic at room temperature. These steels exhibit a unique combination of strength and ductility. Austenitic stainless steels are used in applications, where are needed high strength, good formability and good corrosion resistance [1].

Impact of gradual storage of mechanical energy in the material produces a change of mechanical and physical characteristics. It can cause degradation of material properties. These properties are e.g. reduction of the machine tools accuracy, initiation of fatigue cracks, generation of noise and vibration in the working environment, changes of material properties, reduction of corrosion resistance, degradation of regulatory devices and sensors, eventually damage of entire device. Measurement of the internal damping allows monitoring of the ongoing structural changes and various mechanisms [2,3].

## 2. Experimental material

There were used three types of austenitic stainless steels- AISI 304, Cr-Ni-Mo low-carbon steel AISI 316L and Cr-Ni-Mo steel stabilized with Ti AISI 316Ti. Dimensions of each sample are visible in Fig. 1.

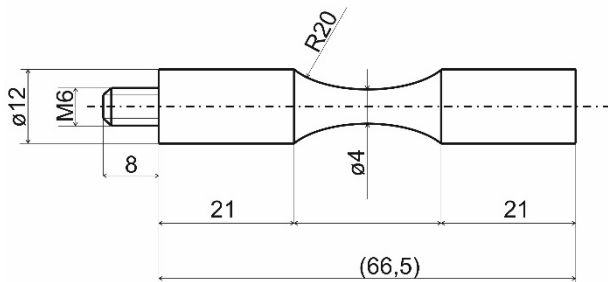


Fig. 1. Experimental sample

## 3. Experimental procedure

The internal damping was measured three times at each sample on the experimental equipment used at Department of Materials Engineering, University of Žilina, that consists of mechanical and electronic parts (Fig. 2.). First measurement was carried out on the samples in initial state, second measurement on the samples after recrystallization- the samples were heat treated at temperature 800 °C for 15 minutes before measurement. Before third measurement the samples were cooled to -70 °C for 20 minutes and then they were deformed by impact deformation. Temperature dependence of internal damping of materials was observed in interval of temperatures from 25 °C to 400 °C, and back. Heating rate was 1°C/ 1 min.

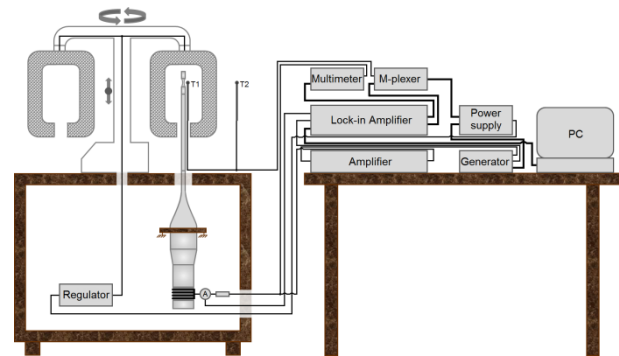
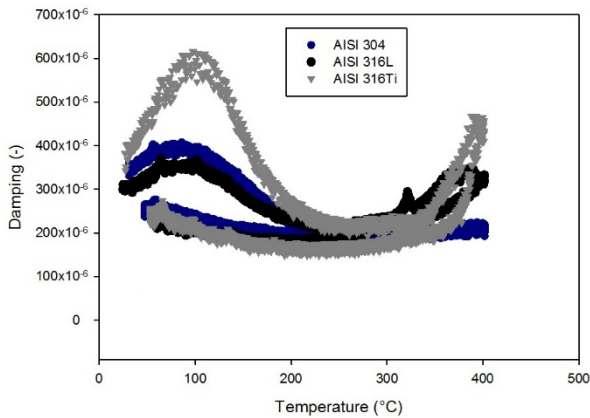


Fig. 2. Device for measurement of internal damping

## 4. Experimental results

The results for samples in initial state showed one-way memory effect of austenitic stainless steels. The peaks created at temperature about 100 °C have not been created during the way back to lower temperatures (Fig. 3.). Decrease of internal damping with increasing temperature is caused by phase transformation. Material with higher content of deformation twins has got higher peak of internal damping.



**Fig. 3.** Internal damping of samples in initial state

Recrystallization annealing (800 °C/15 min) was used for removing of hardening after cold forming. Results in Fig. 4. show substantial change in comparison with graphs for initial state. Highest change of values was observed in AISI 316Ti, curve of AISI 304 was lower and covered by curve of AISI 316L. Decrease of internal damping in all of the samples was caused by structural changes in experimental samples during recrystallization.

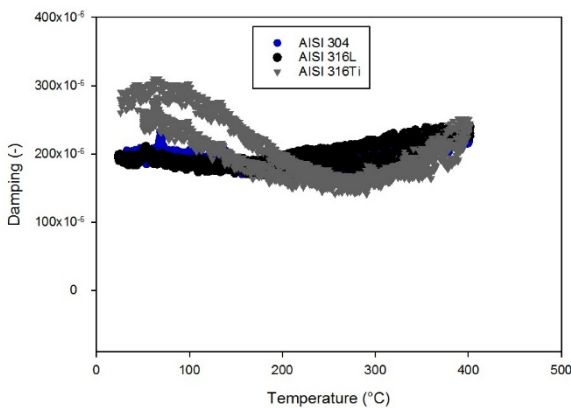


**Fig. 4.** Measurement after recrystallization

Before third measurement, it was necessary to create new deformation twins in experimental samples. For deformation twinning are needed low temperatures and high speeds of deformation, so the samples were cooled to -70 °C for 20 minutes and then they were deformed by impact deformation. Results in Fig. 5. show, that the curves of internal damping returned to similar values as they were before recrystallization. There was proved memory effect of austenitic stainless steels.

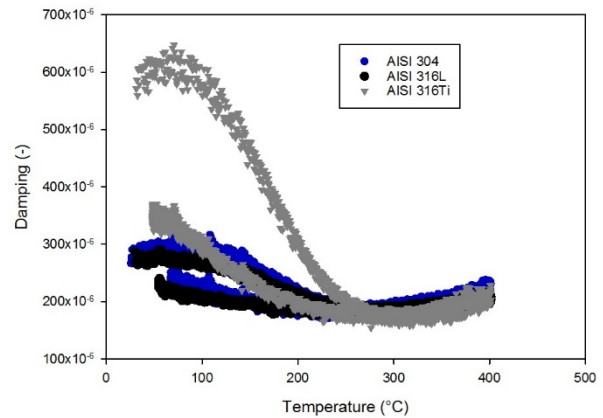


**Fig. 5.** Measurement after cooling and impact deformation

## 5. Conclusion

- The internal damping increased with increasing temperature in interval of temperatures higher than 300 °C.
- Austenitic stainless steels showed one-way memory effect.
- Memory effect was verified by experiment with heat treatment and following impact deformation, where new deformation twins were created.

## Acknowledgements

The project presented in this article is supported by Scientific Grant Agency of Ministry of Education of Slovak republic VEGA 1/0683/15.

## References

- [1] Talonen, J., Hänninen, H., Damping properties of austenitic stainless steels containing strain-induced martensite. Metallurgical and materials transactions A, Volume 35A, 2004, pp.2401-2406.
- [2] Schaller, R., Fantozzi, G., Gremaud, G., Mechanical spectroscopy Q-1 2001 with applications to materials science. Switzerland Trans Tech Publications, 2001, 683p. ISBN 0-87849-876-1.
- [3] Blanter, M., Internal Friction in Metallic Materials. Springer-Verlag: Berlin Heidelberg, 2007, 539 p. ISBN 3-540-68757-2.

# DELAMINATION GROWTH ANALYSIS IN MODE I BY MEANS OF LAMB WAVES

Lenka Michalcová<sup>1</sup>

<sup>1</sup> Aerospace Research and Test establishment, Strength of Structures Department, Beranových 130, 19905, Prague – Letňany, Czech Republic. E-mail: [michalцова@vzlu.cz](mailto:michalцова@vzlu.cz)

## 1. Introduction

Guided wave based monitoring of composite structures plays an important role in the area of structural health monitoring (SHM) of aerospace structures [1, 2]. Delamination growth of double cantilever beam specimens (DCB) using Lamb waves is investigated from the point of frequency tuning, actuation waveform, sensor placement and selection of parameter sensitive to delamination growth [3].

## 2. Materials and methods

Specimens were made of carbon fiber plain weave fabric reinforced epoxy resin with a sequence of lamination [45/0]<sub>4S</sub>. DCB tests were performed according to the ASTM D5528 standard. A polymer foil with the length of approximately 25 mm was inserted into the midplane of the laminated panels as an artificial initial delamination (Fig. 1).

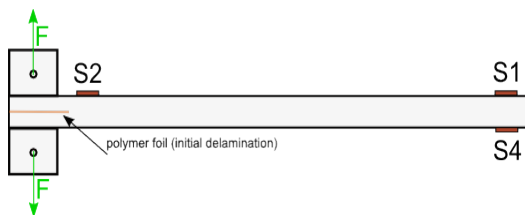


Fig. 1 Scheme of DCB specimen

Mechanical tests were performed on INOVA ZUZ-50 and a load cell with capacity of 1kN was used. Acellent Scan-genie II system with 3 smart layers sensors was utilized for periodical guided wave monitoring.

The objective of this work is to compare visually based and Lamb wave based method of crack growth curve determination.

### 2.1 Selection of actuating parameters for Lamb wave measurements

Lamb waves propagate only in plate-like structures and propagating modes – symmetric and asymmetric (Fig. 2) – are dependent on actuating frequency and structure thickness. Pitch-catch configuration with transducer S2 as the actuator and S1 and S4 as sensors was utilized. Parameters suitable for signal actuation were selected experimentally before the test. Fundamental A0 mode propagated without any interference with other modes in the frequency range of 30-50 kHz. Burst 5 (a sine wave of 5 cycles) actuation pulse with the frequency of 40 kHz and applied voltage of 50V and 20 dB amplification was set as optimal.

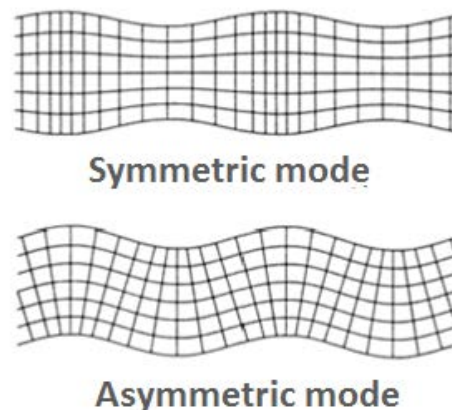


Fig. 2 Lamb wave modes

### 2.2 Parameter sensitive to delamination growth

Group velocity of Lamb waves is dependent on the product of frequency and thickness. These relations in general describe dispersion curves. With delamination growth the part of the specimen with half thickness extends which results in time delays of signal arrivals compared to the baseline measurement.

### 3. Results

Example of signal delay and resulting signals plot from all measurements (10 measurements as the delamination propagated) are shown in Fig. 3. The first arrival time shift curve was highlighted on order to show the trend of time delays and delamination length.

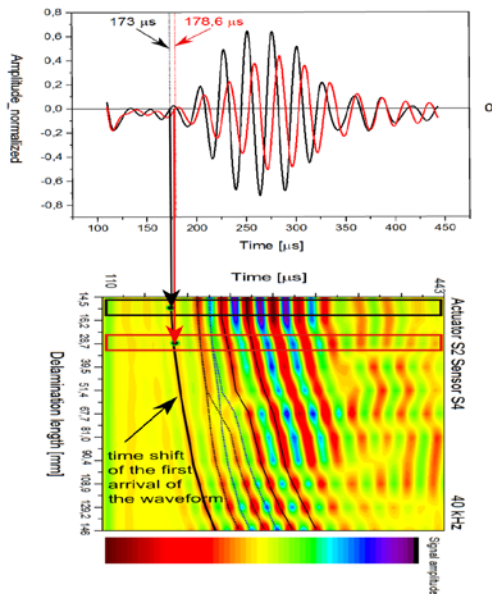


**Fig. 3** Time shift of the first arrival of the waveform

Time shifts of the first signal arrival compared to the baseline measurement was utilized for the exact crack tip localization according to the following equation:

$$a_n = \frac{v_1 v_2 dt_n}{v_2 - v_1}, \quad (1)$$

where  $a_n$  represents the crack length,  $v_1$  and  $v_2$  represent group velocity of 40 kHz Lamb wave in the specimen with half of thickness and full thickness respectively and  $dt_n$  denotes the time difference of the  $n$ th measurement compared to the baseline state.

The knowledge of both velocities is conditional. Velocity  $v_1$  was determined using the Eq. (1) with one example of visually identified crack length and corresponding  $dt_n$ .

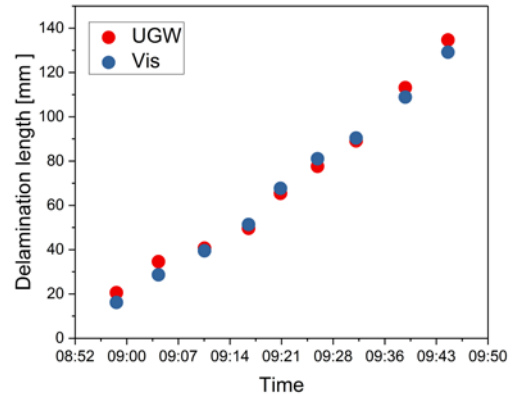


**Fig. 4** Comparison of visually based and Lamb wave based delamination length

### 4. Conclusion

To conclude, Lamb wave monitoring of delamination growth showed great agreement with visually based data. However, from the point of view of SHM approach the velocity of lamb waves in the delaminated specimen should not be determined using visually identified delamination length since this supposed to be the output. The velocity should be determined before the test e.g. by dispersion curves calculation.

### Acknowledgements

This work was funded by the Ministry of Industry and Trade of the Czech Republic in the framework of Institutional support of Research organizations.

### References

- [1] Rose, J.L., Ultrasonic Guided Waves in Solid Media. Elsevier, 2014.
- [2] Giurgiutiu, V., Structural Health Monitoring with Piezoelectric Wafer Active Sensors. Cambridge University Press, 2008.
- [3] Ramadas, C., Hood, A., Balasubramaniam, K., Joshi, K., Ultrasonic Lamb Wave Based Crack Growth Prediction for Estimation of Strain Energy Release Rate, editors B.S.S. Daniel, and G.P. Chaudhari, Advanced Materials Research, 2012. pp. 24-28.

# COMPARISON OF THE METALLURGICAL PROPERTIES AND SURFACE CHARACTERISTICS OF DIFFERENT ORTHODONTIC ARCHWIRES ALLOYS

Anna Zięty<sup>1\*</sup>, Victoria Hoppe<sup>2</sup>, Dominika Grygier<sup>3</sup>, Jerzy Detyna<sup>1</sup>

- <sup>1</sup> Wrocław University of Science and Technology, Department of Mechanics, Material Science and Engineering, Smoluchowskiego str 25, Wrocław 50-360, Poland. \*e-mail: anna.ziety@pwr.edu.pl
- <sup>2</sup> Wrocław University of Science and Technology, Student Scientific Circle of Material Science named doc. Rudolf Haimann
- <sup>3</sup> Wrocław University of Science and Technology, Department of Materials Science, Strength and Welding, Smoluchowskiego str 25, Wrocław 50-360, Poland

## 1. Introduction

There are lots of properties which describe an ideal orthodontic archwire. Unfortunately, this kind of alloy does not exist. This is because of different requirements of each stage of orthodontic treatment. In the first stage, where the initial teeth rotation and alignment are needed, archwire should provide a large range of forces with low, constant values. At this stage, use of Ni-Ti alloys is crucial. [1], [2], [3] These shape memory wires are characterized by a high resilience and high elastic limit. Nowadays, there are lots of types of NiTi orthodontic archwires from conventional, I generation (55% of nickel and 45% of titanium) to newer one, e.g. CuNiTi alloy which are superelastic and thermoelastic. [4], [5], [6] At the last stadium, a small, but still constant movement of teeth is required. A stainless steel, the 18:8 austenitic type (18% chromium and 8% nickel), due to its high stiffness (about 200 MPa) and a low springiness, is ideal for it. What is more, it is characterized by high resistant to corrosion (thanks to coherent oxide layer and passivation process) and a very high strength ( $R_m=2,1$  GPa). [3], [7].

According to this, for the correct use of orthodontic appliance one must have a thorough knowledge of these materials. [2] The aim of the present paper is to compare and evaluate metallurgical properties and surface characteristics of three widely used archwires materials, which are applied to various stage of orthodontic treatment.

## 2. Material and methods

To investigate metallurgical and surface properties of selected materials, structural analysis by light microscopy (MA200 model / Nikon company) and scanning electron microscopy (*Phenom ProX Desktop SEM*) were performed.

Furthermore, SEM was also applied to do roughness tests. The sample hardness measurement was carried out on a Vickers 1A VH-1000B microhardness tester.

Mentioned experiments were carried out on each of three different materials: Ni-Ti (I generation), Ni-Ti Copper and stainless steel (SS 18:8). All of them are in conventional use. Their manufacture characteristics, sizes and brand names are presented in a table 1.

Sample Material	Brand	Cross-section	Size
Ni-Ti	<i>Swiss Dental Specialties</i>	rectangle	0.16x0.22"
Ni-Ti Copper	<i>Ormco Corporation</i>	rectangle	0.16x0.22"
Stainless Steel	<i>G&amp;H Orthodontics</i>	rectangle	0.16x0.22"

**Tab. 1.** Types of materials used in the investigation

Brand new archwires were randomly chosen from the one batch and divided on three sections (two sides of archwires – left, right and the centre of it). It is shown on figure 1. Next, they were rinsed with acetone in ultrasonic washer.

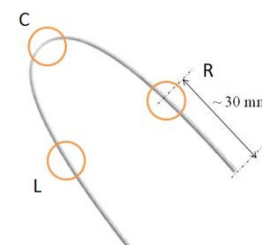


**Fig. 1.** Three measuring points which were chosen to do research: L, R – a straight wire, C – a bent section of a wire

## 3. Results

The surface topography of each archwires, as observed by SEM, had its own characteristic

surface structure. The differences were noted among studied materials, but also inside one material between a straight wire (L, R) and a bent section of a wire (C). NiTi family wires showed more grooves, especially in the centre measuring place, which were parallel to the long axis of the archwire. Conventional NiTi alloy exhibited some irregularities, but not such depth as NiTi with a copper. Both of them have lots of peaks, while stainless steel mostly has a smooth surface with a few areas of valleys.

The roughness tests confirmed the microscopic observations. As it is seen on figure 2, values of roughness average of a surfaces (Ra) are similar for NiTi family and higher than steel SS.

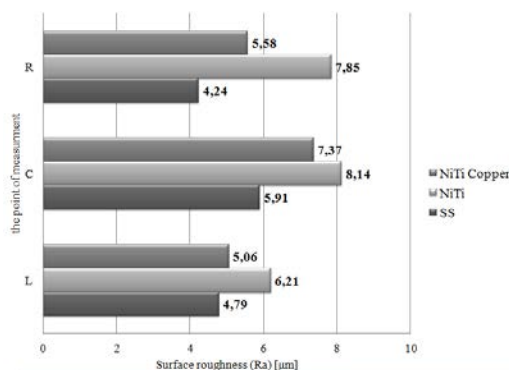


Fig. 2. The mean surface roughness of the wires studied

Obtained results of surface roughness also showed irregularities inside one material, especially between the straight elements and curved parts of archwire. The value of Ra coefficient for C places is higher for each studied material. Microhardness tests demonstrated similar trend as roughness research.

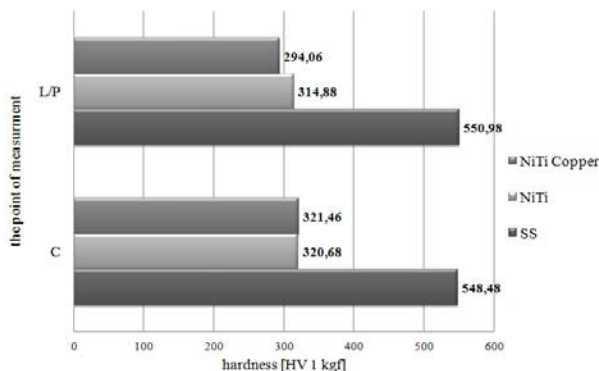


Fig. 3. The mean surface microhardness of the wires studied, where L/R – straight section of wire, C – bent section

Figure 3 presented results of hardness [HV 1] for all three biomaterials and points of measuring too. There are higher values for bent parts of

archwires than R and L points. Furthermore, these experiments proved that stainless steel has the highest hardness than both Ni-Ti alloys along the entire length of the wire.

#### 4. Conclusions

Summarizing, it is clearly seen that the NiTi archwires have more defects than the SS archwires. It is related to the chemical composition of each material, but also to the various material structure and existence of a large number of non-metallic inclusions.

It is observed that NiTi alloys (I generation and alloy with copper) have similar values of both tests (roughness and hardness). What is more, these biomaterials showed the same tendency during surface observation: lots of peaks and depth grooves. The SS has higher hardness, so that its surface is smoother (the smallest value of Ra)

Archwires are first pulled and straighten during drawing process. After that, they are bent. These activities generate strengthening mechanism near C places. This is a confirmation of obtained differences in values for C and R/L points of measuring.

#### References

- [1] Kusy Robert P. , *A review of contemporary archwires: Their properties and characteristics*, The Angle Orthodontist, 1997, 67 (3): 197-207
- [2] Shuhanek C., *Material Characteristics of the orthodontic archwires*, DAAAM International Scientific Book 2011, 24: 301-308
- [3] Kotha R. S., Alla R. K., Shammas M., Ravi R. K., *An overview of orthodontic wires*, Trend in Biomaterials and Artificial Organs, 2014, 28(1): 32-36
- [4] Fercec J., Kos M., Bruncko M., Anzel I., Glisic B., Markovic E., Rudolf R., *Comparison of NiTi orthodontic archwires and a determination of the characteristic properties*, Materials and technology, 2014, 48: 99-104
- [5] Redyy K.V., *Nickel titanium wires in orthodontics: a review*, Journal of Dentistry and Oral Biosciences, 2012, 3 (2): 40-42
- [6] Fernandes D.J., Elias C.N., Vidal R., Mendes Alvaro de Moraes, *Mechanical Performance of Nickel-titanium Archwires*, Materials Research, 2015, 6 (18): 1264-1277, 201
- [7] Szust A. Łukasiewicz M., Rutkowska-Gorczyca M. J., *Studies on structure of selected dental alloys after TMT*, Hellenic Society for Theoretical and Applied Mechanics, s. 1-5

# EXPERIMENTAL MODELING APPROACH FOR DETERMINING THE MOISTURE DAMPING EXPONENT OF A BLUETOOTH LOW ENERGY SIGNAL IN MOIST BUILDING MATERIAL

Laura Moldenhauer<sup>1</sup>, Rosemarie Helmerich<sup>2</sup>, Enrico Köppe<sup>3</sup>, Jochen Wittmann<sup>4</sup>

<sup>1</sup> Federal Institute for Materials Research and Testing (BAM), Unter den Eichen 87, 12205 Berlin, Germany. E-Mail: [laura.moldenhauer@bam.de](mailto:laura.moldenhauer@bam.de); [rosemarie.helmerich@bam.de](mailto:rosemarie.helmerich@bam.de);

<sup>2</sup> University of Applied Sciences, HTW, Wilhelminenhoffstr., 12587 Berlin, Germany.

## 1. Introduction

The presented development of a damping model is a research component of an experimental feasibility study about moisture in building materials measured with Bluetooth® Low Energy (BLE) signals [1]. This study may be part of a structural health monitoring [2] aiming on early damage detection in the built infrastructure and is increasingly focusing on wireless sensor network technology [3]. It is investigated, how the Received Signal Strength Indicator (RSSI) of a BLE signal, transmitted from the BLE-module embedded in building materials with changing moisture content is damped. The BLE-module communicates with a mobile Smart Device as tablet or mobile phone via 2.45 GHz-ISM-frequency band where water dipoles start to oscillate. If the BLE-signal transfers through a moist material, the moisture content influences the RSS-Indicator.

The damping model demonstrates this damping effect on RSSI by the abstraction of the reality observed in a real system. Through the reproduction of the active relationships, the system behavior is decomposed in such a way that a separate consideration of the required system parameters is possible. The aim of the modelling is the derivation of a damping equation for the formal model to determine the moisture damping exponent to find a correlation.

## 2. Model development

The assumption is that the signal damping corresponds to the power transmission balance. This balance is the sum of the three damping components; Environmental damping, material damping (environment + material) and moisture damping (environment + material + moisture). Therefore, a model for these damping variables is

required. The development of the formal model refers to the Log-Distance Path Loss Model (FSPL) Eq. (1) [3].

$$FSPL = 10 * \log_{10} \left( \frac{4\pi r * f}{c} \right)^2 \quad (1)$$

$4\pi r$  = Area of a circle from a antenna

$f$  = is the signal frequency (in Hertz),

$c$  = is the velocity of light in a vacuum

This model, known from electrical engineering, is not applicable. It applies only in a vacuum and does not consider the influence of the distance. Provided the distance high -n (negative path loss exponent) is proportional to the received power, the equation can be extended to the Log-Distance Path Loss Modell Eq. (2).

$$RSSI_d = - (10 * n) \log_{10} \left( \frac{d}{d_0} \right) - RSSI_{d_0} \quad (2)$$

$n$  = Path loss exponent (The exponent  $n$  increases with increasing damping)

$d$  = Distance between transmitter and receiver

$d_0$  = Distance between transmitter and receiver (rm)

$RSSI_d$  = Received signal strength indicator in dBm

$RSSI_{d_0}$  = Received signal strength indicator in dBm (rm)

The Log-Distance Path Loss Model is applied by switching on  $n$  for determining the damping components Eq. (3).

$RSSI_{Environment}$

$$= -(10 * n_{Environment}) * \log_{10} \left( \frac{d}{d_0} \right) - RSSI_{d_0} \quad (3)$$

At first, the environmental damping was considered. After insertion and conversion, the equation (4) is obtained.

$$\begin{aligned} n_{\text{Environment}} \\ = \frac{\text{RSSI}_{\text{Environment } d} + \text{RSSI}_{d_0}}{-10 * \log_{10} \left( \frac{d}{d_0} \right)} \end{aligned} \quad (4)$$

If the material damping is considered, the signal damping is the sum of environment and material damping, as shown in equation (5).

$$\begin{aligned} n_{\text{Material}} \\ = \frac{\text{RSSI}_{\text{Material } d} + \text{RSSI}_{\text{Material } d_0}}{-10 * \log_{10} \left( \frac{d}{d_0} \right)} \\ - n_{\text{Environment}} \end{aligned} \quad (5)$$

The same damping is considered as the result for moisture. Eq. (6).

$$\begin{aligned} n_{\text{Moisture}} \\ = \frac{\text{RSSI}_{\text{Moisture } d} + \text{RSSI}_{\text{Moisture } d_0}}{-10 * \log_{10} \left( \frac{d}{d_0} \right)} \\ - n_{\text{Environment}} - n_{\text{Material}} \end{aligned} \quad (6)$$

### 3. Data validation and results

The hypotheses for the damping models were validated with the analyzed system data. In the evaluation of the experimental system data we can establish a proportional relationship between the moisture content and the logarithm of the received strength. To do this, the model experiment was carried out without moisture. By transferring the experimental data to the formal model, the following values are obtained for the environment and the material. See Fig. 1.

<b>ENVIRONMENTAL DAMPING EXPONENT</b>	
$n_{\text{Environment}}$	→ average = 3,99
<b>MATERIAL DAMPING EXPONENT</b>	
$n_{\text{Material}}$	→ sensor depth 10 cm = 4,55
+ $n_{\text{Environment}}$	→ sensor depth 20 cm = 5,15
	→ sensor depth 30cm = 5,57

Fig 1: Results of the damping exponents

The evaluation of the system data and its application to the formal model has resulted in the environment damping exponent of 3.99. This damping exponent for the environment correlates with the expectations for shaded buildings. The material and moisture damping are determinable

with the model and grow in exponential relation to the signal path in the material, see Fig 2.

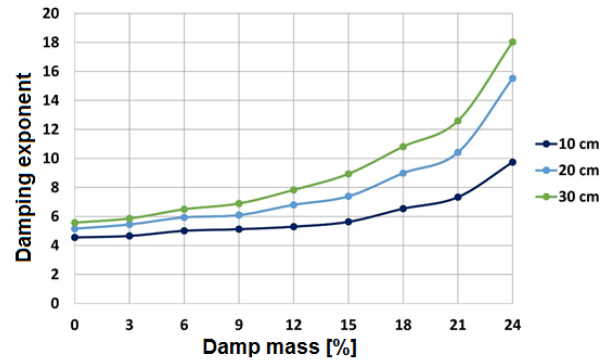


Fig 2: Damping exponents in moist building material in three different sensor depths

The calculated damping exponents from the model of the investigated moisture content (in %) show the dependence of the RSSI on the damp mass inside the building material. It can be observed, that the exponents of the damping grow continuously exponentially with the moisture content. said it can be concluded that water massively attenuates the BLE signal during data transmission. Based on the RSSI, it is possible to derive statements about the moisture content in the material. In accordance with the results of the model, the information value of moisture content decreases with the embedding depth of the sensor.

### Acknowledgements

The experimental work was carried out during my Bachelor thesis. The contribution to the project for BLE sensor development and application to construction monitoring funded during a German ZIM project, by the German Minister of Economy and Energy is kindly acknowledged.

### References

- [1] Moldenhauer, L., Investigation and visualization of the damping of Bluetooth Low Energy signals under the influence of damp mass in building materials, Bachelor thesis HTW, Berlin, 2016
- [2] Köppe, E., Bartholmai, M., Long term monitoring and early damage detection in structures applying an energy wireless efficient sensor network Presentation TC Structural Health Monitoring, Airbus, Hamburg, 2008
- [3] Helmerich, R., Nondestructive Evaluation and Structural Health Monitoring, Civil Structural



34th Danubia-Adria Symposium on Advances in Experimental Mechanics  
University of Trieste, Italy, 2017



Health Monitoring Workshop, CSHM-5, Ube,  
Japan, 2008

# IMPACT OF THE ECAP PROCESS ON THE MACHINABILITY OF ALUMINUM (EN AW-6082)

**GERHARD WIESINGER<sup>1</sup>, CHRISTIAN BAUMANN<sup>1</sup>, MACIEJ KRYSZTIAN<sup>2</sup>**

<sup>1</sup> Vienna University of Technology, Institute of Production Engineering and Laser Technology, Landstraßer Hauptstraße 152, 1030 Vienna, Austria. E-mail: [wiesinger@ift.at](mailto:wiesinger@ift.at)

<sup>2</sup> AIT Austrian Institute of Technology GmbH, Center for Health & Bioresources, Biomedical Systems, Viktor-Kaplan-Straße 2, 2700 Wr. Neustadt, Austria. E-mail: [maciej.krystian@ait.ac.at](mailto:maciej.krystian@ait.ac.at)

## 1. Introduction

Transforming the conventional coarse-grained microstructure of metallic materials to the ultra-fine grained (UFG) state can significantly enhance the mechanical properties. Nowadays, different technologies exist to produce metals with UFG microstructure. Severe Plastic Deformation (SPD) has proven to be the only technically viable, direct method for production of bulk, fully dense and massive UFG metallic materials by means of very large plastic deformation [1]. SPD is defined as a metal forming process, in which an ultra-large plastic strain is applied on a metal in order to generate bulk UFG metals with both high strength and ductility. The dominating SPD technology is Equal Channel Angular Pressing (ECAP). During the ECAP process the raw material is pressed through a die consisting of two equal channels intersecting at a set angle. It undergoes a very high plastic deformation by simple shear under enhanced hydrostatic pressure without change in the cross-sectional dimensions. Thus, the ingot can be pressed repetitively through the same die as well as rotated between consecutive passes (routes) to activate different slip systems and to attain extremely large, multidimensional strain. These facts lead to a microstructural refinement down to ultrafine grained (UFG) microstructure and consequently to altered (mechanical) properties i.e. high strength at still decent ductility as well as enhanced fatigue limits.

However, little is known about the influence of the UFG microstructure on the machinability. So the effects of the ECAP procedure on the machinability of aluminum (EN AW-6082) were examined by turning.

## 2. Machining Experiments

In order to analyze the effects of the ECAP process on the machinability, the cutting forces, the chip formation and the surface quality of the machined parts were examined.

Tab. 1 shows mechanical properties of the ECAP material compared to the as-received material.

	AR	ECAP
Ultimate tensile strength [MPa]	494	655
Yield strength [MPa]	413	427
Elongation at break [%]	38	21

**Tab. 1.** Mechanical properties of EN AW-6082 as-received (AR) and after ECAP.

To evaluate the influence of the ECAP process on the machinability 100 longitudinal turning tests with ECAP aluminum, as well as untreated aluminum were performed. The cutting parameters were set according to recommendations of the tool manufacturer for Sandvik© Coromant DCGX 11 T3 08-AL H10 cutting tool. Thus, the cutting speeds was varied between 80 and 170 m/min, feeds between 0.05 and 0.5 mm/rev and depths of cut from 0.5 to 2 mm. In Fig. 1, the setup for the turning tests is shown.

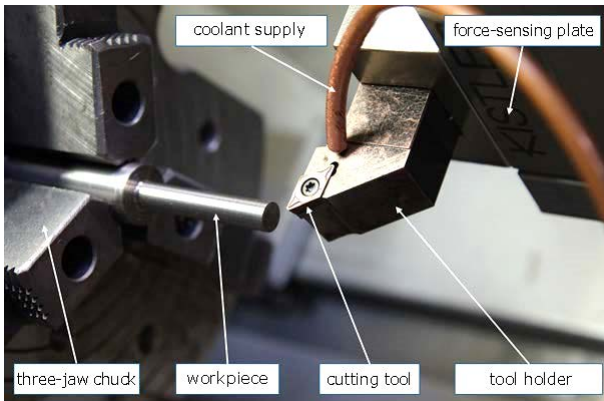


**Fig. 1.** Experimental setup.

In Fig. 2 the cutting force at a 2 mm depth of cut is plotted as a function of the feed. The ECAP aluminum has at all investigated feeds a lower cutting force than the untreated reference material.

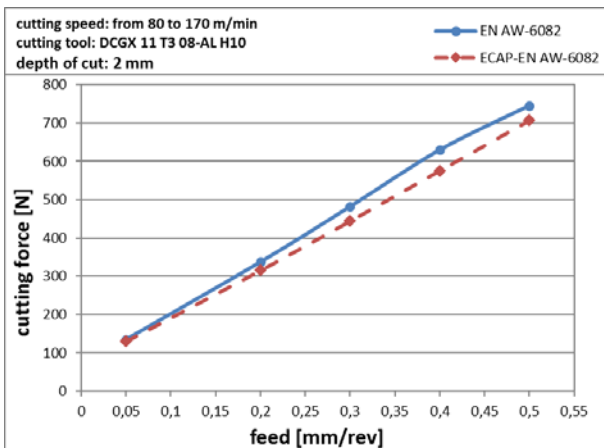


**Fig. 2.** Machining force for 2 mm depth of cut and averaged cutting speed from 80 to 170 m/min.

In [2] a classification for the different chip shapes at the mechanical processing of metals is defined. Category 1 to 4 is inconvenient because the chips are continuous and have a high volume. So the risk for damages at the machine tool and the danger of injury for the machine operator is very high. The chips in category 5 to 8 are convenient because of the periodic chip break.

Fig. 3 shows, that at a cutting speed of 170 m/min, a depth of cut of 1.5 mm and a feed of 0.4 mm/rev the chips from the ECAP aluminum (category 5 to 8) are better than them from the untreated material (category 1 to 4).

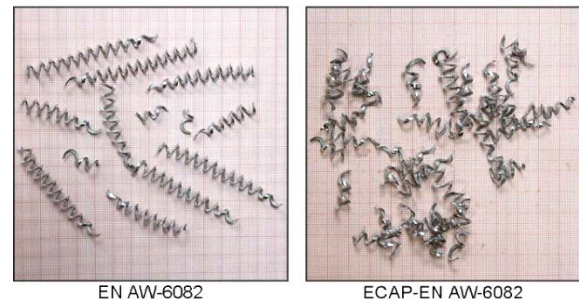


**Fig. 3.** Chips of untreated (left) and ECAP processed (right) EN AW-6082 for cutting speed 170 m/min, depth of cut 1.5 mm and feed 0.4 mm/rev.

The average surface roughness  $R_z$  of the machined surfaces for the ECAP aluminum is between 0.8 to 4.6% depending on the chosen machining parameters, lower than the  $R_z$  value of the untreated aluminum.

### 3. Discussion & Summary

With the ECAP process treated aluminum has not only advantages in the material strength but also the machinability improves. The cutting force of ECAP processed aluminum is lower compared to untreated material despite of the higher strength. The fact that the cutting process happens at high temperatures and not at room temperature, like the measurement of the material properties, can be used as an explanation for the results. In [3] the same effect was observed for ECAP copper and untreated copper. In [4] it is shown, that a reduction of 12% of the friction coefficient leads to a reduction of 15% in cutting forces.

### Acknowledgements

The authors appreciate the financial support of the Austrian Research Promotion Agency (FFG) in the frame of the 7<sup>th</sup> funding programme “COIN Cooperation & Innovation”, project “inForm” (845933).

### References

- [1] Valiev R Z and Langdon T G 2006 Progress Mater. Sci. 51 881–981
- [2] Verband Deutscher Ingenieure, VDI: Stahl-Eisen-Prüfblatt 1178-90 für die Klassifizierung von metallischen Spänen aus der mechanischen Bearbeitung, Verlag Stahleisen GmbH.
- [3] R. Zemann, M. Zillner: Impact of the ECAP Process on the machinability of copper; 33rd



Danubia-Adria Symposium (DAS) on Advances in Experimental Mechanics, Portoroz, Slovenia, 2016, ISBN 978-961-94081-0-0, pp. 46-47.

- [4] M. Morehead, Y. Huang and K. Hartwig, Machinability of ultrafine-grained copper using tungsten carbide and polycrystalline diamond tools, USA: Department of Mechanical Engineering, Texas A&M University, 2006.

## INFLUENCE OF MHP-TECHNOLOGY ON THE SURFACE NEAR MATERIAL STRUCTURE OF STAINLESS STEEL 1.4301

Stephan Krall<sup>1</sup>, Manuel Reiter<sup>1</sup>, Friedrich Bleicher<sup>1</sup>

<sup>1</sup> Technische Universität Wien, IFT – Institute for Production Engineering and Laser Technology, Getreidemarkt 9/311, 1060 Wien, Austria. E-mail: [krall@ift.at](mailto:krall@ift.at)

### 1. Introduction

By the application of machine hammer peening (MHP), the treated surfaces may show increased hardness and near-surface compressive residual stresses, next to optimized surface topographies. Due to plastic deformation of the crystalline steel material in the upper layers of the workpiece, phase transformations may be enforced. The aim of this work is the detection of the deformation-induced phase transition to martensitic structures as well as the effects on the hardness in the near-surface areas by multiple machining of the processed material.

### 2. Machine hammer peening

For the desired application of the machine hammer peening (MHP)-process, an electromagnetic hammer peening device was used. The processed material, a stainless steel of the type X5CrNi18-10 (1.4301), has high resistance to corrosion and consists of a metastable  $\gamma$ -phase. The experiments were performed on a MoriSeiki NHX 6300 machining center. The applied process parameters have been as follows: Each sample was multiple machined ( $n = 4$ ) with a constant frequency  $f$  of 200 Hz. A feed rate  $v$  of 1.200 mm/min, a stroke  $h$  of 0,8 mm and a distance of indentation  $a$  of 0,1 mm, that is equal to the stepover distance  $s$ , have been used. Sample No. 1 was peened with a ball-shaped  $\varnothing 6$  mm tool tip and, apart from that, sample No. 2 was treated with a  $\varnothing 3$  mm tool tip.

### 3. Fundamentals of phase transformation

Due to plastic deformation on a material, a transformation of a metastable austenitic material to an  $\varepsilon$ -phase with hexagonal closed packed crystal structure and an  $\alpha'$ -phase structure with body-centered cubic crystal (bcc) structure can be formed. Previous investigations, like e.g. [1], show that the creation of an  $\alpha'$ -phase is boosted and a phase transformation from  $\gamma - \varepsilon - \alpha'$  or even

directly from  $\gamma - \alpha'$  could take place. In contrast to an  $\varepsilon$ -martensitic microstructure,  $\alpha'$ -martensitic structure shows ferromagnetic properties. In general, the martensitic transformation can happen thermally-, stress- or strain/deformation-induced; cf. [2]. For this work, the deformation-induced martensitic transformation is the major effect. Since the transformation from an austenitic phase to a martensitic one is not done by a temperature drop for this work, an additional energy must be provided to start the transformation at room temperature. This can be achieved by a mechanical treatment process.

### 4. Microstructural investigations

For the investigation of the metallographic condition of the material, the color etching method according to Lichtenegger and Bloech (LBV) was employed. The outcomes of the color etching are shown in Figure 1. Sample No. 0 represents the initial surface condition before MHP-treatment (homogenous microstructure, single undeformed grains). The resulting microstructure of the etched sample No. 2 clearly shows high deformed areas (measured at a depth of 200  $\mu\text{m}$ ) with a high dislocation density. The images were created using an Axioplan microscope of the company Zeiss.

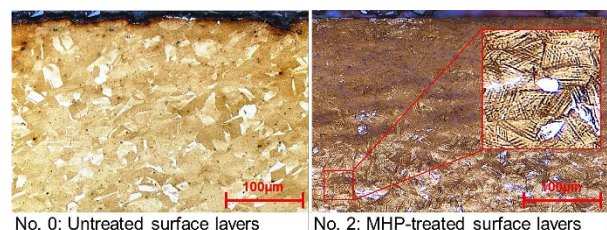


**Fig. 1.** (a) Untreated and etched surface layers; (b) MHP-treated and etched surface layers.

### 5. Hardness measurements

In order to determine the depth of impact of the MHP-process, Vickers hardness measurements were carried out to create a depth profile of the subsurface material conditions. The measurements

were performed using a HV05 Vickers probe at a standardized exposure time of 15 sec. on an EMCO Test MIC 010. The results of the performed measurements of the investigated samples are shown in Figure 2. The initial hardness of the material (as delivered) is  $263 \pm 5$  HV05 and is represented as a red dotted line. Sample No. 2, which was processed with smaller ball diameter of the tool tip, shows a higher increase in hardness with an achieved value of  $490 \pm 4$  HV05 and higher reachable penetration depth than sample No. 1. This value decreases to the initial hardness of the untreated material until a depth of approximately  $800 \mu\text{m}$ .

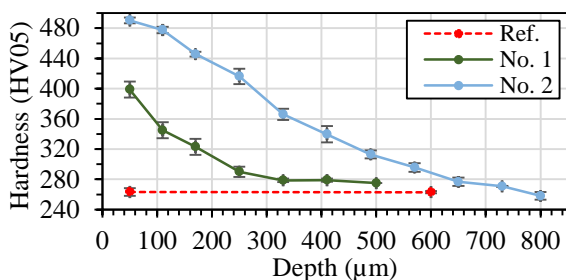


Fig. 2. Vickers HV05/15 hardness depth profile for X5CrNi18-10 (1.4301) after MHP-machining.

## 6. Microstructural-crystallographic investigations

To characterize the microstructural-crystallographic structure of a material and to understand the crystal orientation and its phases, a scanning electron microscope equipped with a field emission gun of the type FEI Quanta 200 FEG was used to analyze the material behavior. An electron backscatter diffraction (EBSD) analysis was faced to get a deeper knowledge of the MHP-treated areas. An accelerating voltage of 15 kV was used to influence the electron wavelengths and therefore improve the diffraction patterns. To investigate a possible phase transformation from an austenitic to a martensitic structure, the specimen was tilted to approximately  $70^\circ$  inside the measuring instrument. The EBSD analysis was carried out for both samples as follows: Sample No. 2 was evaluated according to a depth of  $160 \mu\text{m}$  and a measurement area of  $3 \mu\text{m}^2$ , whereas the measurement properties of sample No. 1 are a depth of  $200 \mu\text{m}$  and an area of  $15 \mu\text{m}^2$ . The preparation of the surfaces was performed by an electrochemical polishing process. However, Figure 3 shows the resulting IPF (inverse pole figure) of both samples No. 1 and 2, and the

CCPM (color coded phase map) for sample No. 2. In the IPF of sample No. 1, the individual grains in the slightly deformed state of the material can be seen. This area shows solely austenitic parts regarding its phase mapping. However, sample No. 2 shows significant deformed structures and deformation patterns. Because of its high dislocation density, a smaller measurement area compared to sample No. 1 was chosen. The phase mapping for the detection of the martensitic proportion was carried out by the bcc crystal structure of a ferrite. Both,  $\alpha'$ -martensite and  $\alpha$ -ferrite have a bcc crystal structure [3].

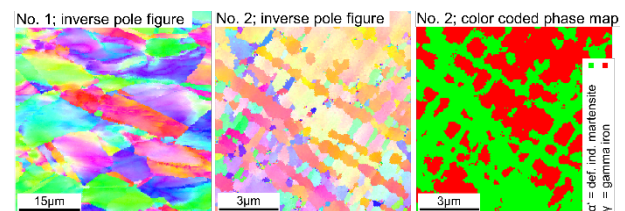


Fig. 3. IPF of samples No. 1 and No. 2, and CCPM of sample No. 2.

## 7. Conclusion

In order to summarize the results of experimental investigation the following main topics can be emphasized:

- cold forming by MHP achieves martensitic crystallographic structures while machining X5CrNi18-9, but with same chemical composition as base material.
- EBSD analysis is appropriate for  $\alpha'$ -martensite detection (phase mapping by using the bcc crystal structure of a ferrite).
- multiple machining leads to a higher deformation and thus more martensite is created; smaller tool tips lead to a higher induced energy level.

## Acknowledgements

The authors want to thank the Machine Tool Technologies Research Foundation (MTTRF) for supporting the research work.

## References

- [1] Hans-J. Christ et al., "Metastable Austenitic Stainless Steels and the Effect of Deformation-Induced Phase Transformation on the Fatigue Properties," Universität Siegen, 2015.



- [2] Jan Scheil, “Entwicklung von Austenitisch-Ferritischem Gusseisen (ADI) aus EN-JS2070,“ TU Darmstadt, 2016.
- [3] George Krauss, “Steels: Processing, Structure, and Performance,“ ASM International, Ohio, 2015.

## EXPERIMENTAL AND NUMERICAL ANALYSES OF THE IMPACT RESPONSE OF LIGHTWEIGHT SANDWICH PANELS

Oana Mocian, Dan M. Constantinescu, Stefan Sorohan, Marin Sandu

University POLITEHNICA of Bucharest, 060042 Bucharest, Romania. E-mails: [mocianoana@gmail.com](mailto:mocianoana@gmail.com), [dan.constantinescu@upb.ro](mailto:dan.constantinescu@upb.ro), [stefan.sorohan@upb.ro](mailto:stefan.sorohan@upb.ro), [marin.sandu@upb.ro](mailto:marin.sandu@upb.ro)

### 1. Introduction

Sandwich panels with lightweight different cores are nowadays essential structural components which offer integrity and reliability to ground vehicles and aircrafts. Low speed impacts may result from the collision with roadside safety elements, e.g., guard and bridge rails, median barriers or sign supports, hail or debris thrown up from runaways and even from tools dropped during maintenance. Experimental determination of the impact behavior of sandwich panels is neither resourceful nor cost effective [1-2], and in many cases finite element modeling (FEM) and analysis are used for these types of studies to predict the behavior and failure of these panels, [3-5]. However, the calibration of the FEM impact model should be carefully done and only experimental results can provide a good understanding of the impact phenomena and response of the sandwich panel in conjunction to the localized damage produced after the low-velocity impact.

### 2. Experimental impact testing

An instrumented Instron Ceast 9340 Drop Tower Impact System used a striker of 20 mm diameter and the impact force was measured during the impact. The initial impact velocity of the striker was measured with an optical cell. The sandwich plates of 140x140 mm were placed on an adjustable in height test specimen support with a circular hole of 100 mm diameter (Fig. 1), which eventually allowed the striker to fall if the plate was perforated. A clamping ring was pressed over the sandwich plate by a pneumatic system with a maximum force of 3 kN. A special attention was given to the positioning and the alignment of the specimen as to obtain the impact in the middle of the plate. Fig. 1 shows the sandwich panel fixed in between the specimen support and the clamping ring. The energy carrier of gravitationally accelerated type had a mass of 3.15 kg and two

additional masses of 5 kg each were added. Therefore the total mass of the energy carrier was 13.15 kg. The European Standard ISO 6603-2: 2000, "Plastics - Determination of puncture impact behavior of rigid plastics - Part 2: Instrumented impact testing" was used. This standard was last reviewed and confirmed in 2015. Data acquisition was done with a frequency of 200 kHz.



Fig. 1. Impact of sandwich plate during testing.

### 3. Description of sandwich panels

The sandwich panels had skins made of aluminum Al 6082-T6 of 1.5 mm thickness glued with Araldite AW106 (Huntsman) to two types of core: polyurethane Necuron 100 of density 100 kg/m<sup>3</sup> and commercial extruded polystyrene of density 30 kg/m<sup>3</sup> having thicknesses of 12 mm, respectively 19 mm. The polyurethane core sandwich was abbreviated as PS\_PUR and the polystyrene core sandwich as PS\_PE. Although the thickness of the polystyrene core of the PS\_PE sandwich is greater than the polyurethane core of the PS\_PUR sandwich the average mass of the PS\_PE panel is about 186 grams compared to about 199 grams for the PS\_PUR panel. So, from the point of view of a lightweight panel, the polystyrene sandwich core stands in fact better. The initial velocity of impact was increased from 0.77 m/s up to 3.5 m/s (height of impact from 30 mm up to 625 mm), in some cases reaching 4.5 m/s for both panels as being the maximum speed considered in these tests.

#### 4. Finite element simulations

The core material was modeled using three different core material models supplied by the LSDyna software: honeycomb, low density and crushable foam material model [5]. Both skins and the core were meshed with one single integration point, eight node solid elements. The mesh was refined in the region of impact in order to better describe the behavior of the plate (Fig. 2). A total number of 16000 elements were used for the skins and 24000 for the core. The impactor, the support and the clamping ring were all modeled as rigid bodies, with the same type of solid elements.

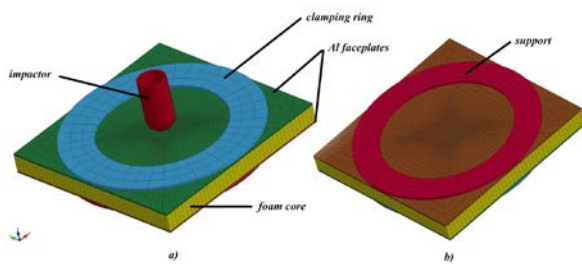


Fig. 1. Finite element model of sandwich plate:  
a) top view; b) back view.

#### 5. Comparison of experimental and numerical results

In the case of a linear elastic impact event the impact force curve variation in time should be symmetric for loading and unloading. This does not happen even for the lower initial speed of impact of 1.5 m/s showing that unloading is accompanied by additional damage phenomena. For a polyurethane panel sandwich (PS\_PUR) the first impact events take about 9 ms at 1.5 m/s to 13 ms at 3.5 m/s. At 3.5 m/s, as seen in Fig. 3, the force drops suddenly from 11790 N to 4450 N due to the severe damage of the aluminum top face of the sandwich which is penetrated by the striker.

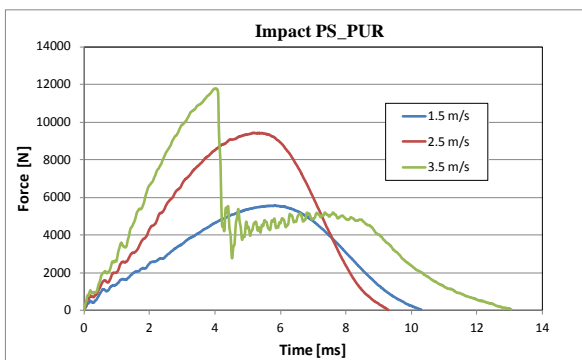


Fig. 3. Impact response of the PS\_PUR at three speeds of impact.

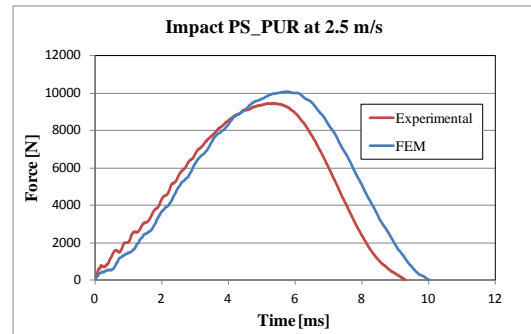


Fig. 4. Comparison of experimental and FEM force-time response of PS\_PUR.

At 2.5 m/s the response of the polyurethane sandwich panel is compared in Fig. 4 as resulting from the experiment and FEM simulation, considering a honeycomb material model for the core. The agreement is good.

#### Acknowledgements

Miss Oana Mocian acknowledges the PhD student scholarship given by the Ministry of National Education from Romania through the contract no. 06.40/2014 which made possible the present researches.

#### References

- [1] Wang, J., Waas, A.M., Wang, H., Experimental and numerical study on the low velocity impact behavior of foam-core sandwich panels, *Compos. Struct.*, 96, 2013, pp. 298-311.
- [2] Caliskan, U., Apalak, M.K., Low velocity impact behavior of foam core sandwich beams: Experimental, *Compos. Part B-Eng.*, 112, 2017, pp. 158-175.
- [3] Hazizan, M.A., Cantwell, W.J., The low velocity impact response of foam-based sandwich structures, *Compos. Part B-Eng.*, 33, 2002, pp. 193-204.
- [4] Chang, F.S., Hallquist, J.O., Lu, D.X., Shahidi, B.K., Kudelko, C.M., Tekelly, J.P., Finite Element Analysis of Low-Density High-Hysteresis Foam Materials and the Application in the Automotive Industry, SAE Paper 940908, SAE International Congress and Exposition, Detroit, February 1994, pp. 71-78.
- [5] Croop, B., Lobo, H., Selecting Material Models for the Simulation of Foams in LS-DYNA, 7th European LS-DYNA Conference, Salzburg, Austria, May, 2009.

# MODEL BASED RESEARCH OF CLIMBING CARABINERS

Agnieszka Szust<sup>1</sup>, Szymon Wierzowiecki<sup>2</sup>

<sup>1</sup> Wrocław University of Technology, Faculty of Mechanical Engineering, Wybrzeże Wyspiańskiego St. 27, 50-370 Wrocław, Poland. E-mail: [agnieszka.szust@pwr.edu.pl](mailto:agnieszka.szust@pwr.edu.pl)

## 1. Introduction

The goal of this work was to conduct model based, comparative, experimental research on screw-gate climbing carabiners (HMS type) made from aluminum alloy and steel connectors used in altitude work (OVO type).

Climbing carabiner is a type of openable binding element which is used by a climber to form a direct or indirect connection to an anchor point. It constitutes a part of personal protection system [4]. Another name used for carabiner is climbing connector.

The conducted experimental research had a goal of measuring displacements of two different types of carabiners: oval shaped basic connectors of type B (OVO) and pear shaped carabiners of type H (HMS). The tests were in all cases done on new carabiners, along long axis, with fully closed and locked gate.

## 2. Methods and material

Even though norms differ on criteria constituting carabiner's endurance conditions of all tests are the same. All endurance tests were done according to norm [1, 2]. In each experiment 3 carabiners were tested.

Displacement measurements were done using optical system Digital Image Correlation System Q-400 (DIC) in a contactless manner [3].

Before the experiments all specimens were covered in stochastically placed markers. Carabiners prepared for test are shown on Fig. 1. Samples were loaded using endurance testing machine Instron 5982. Testing stand together with list of components is shown on Fig 2.



Fig 1. Carabiners prepared for test.

A – type B (OVO), B – type H (HMS).

On the left side – new, before test.

On the right side – prepared for test with Digital Image Correlation System Q-400.

### 2.1 Experimental research procedure

For HMS (type H) carabiner norm PN-EN 12275:2013 is binding and tests were conducted according to it. Carabiner was initially loaded with a force of 250 N and then loaded to a point of failure with a speed of 20 mm/min.

In case of OVO (type B) carabiner the tests were done according to norm PN-EN 362:2006.

The specimen was initially loaded with a force of 250 N. Next it was loaded with a speed of 20 mm/min until a loading force of 20 kN was reached. This load was maintained for 3 minutes.

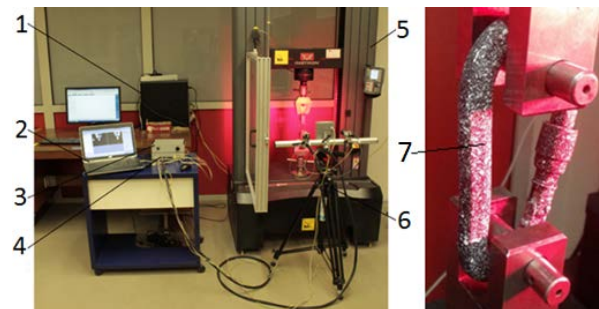


Fig 2. Testing stand:

- 1–load controlling computer, 2–camera video capture computer, 3–light controls, 4–A/C converter,
- 5–endurance machine, 6–set of two cameras,
- 7–specimen prepared for testing.

At the same time, during each test, displacements in 3 directions on surface of carabiner were measured in a contactless manner using DIC.

### 3. Experiment results

Results of strength tests for HMS (type H) carabiners are shown in Tab. 1.

Test piece	Declared strength [kN]	Tested strength [kN]
HMS 1	24	27
HMS 2	24	29
HMS 3	24	27

Tab. 1 Strength results for type H carabiners.

All OVO (type B) carabiners withstood test load of 20 kN for 3 minutes.

Orientation of displacement	OVO1 [mm]	OVO2 [mm]	OVO3 [mm]
X	0,897	1,027	0,599
Y	2,724	3,663	3,048
Z	2,276	1,744	1,417
total	3,547	3,760	3,346

Tab. 2 Maximum displacements values for type B carabiners under 20 kN load.

Fig. 3 shows maximum displacement values for OVO carabiners, for each axis after loading with speed of 20 mm/min and a constant load of 20 kN maintained for 3 minutes.

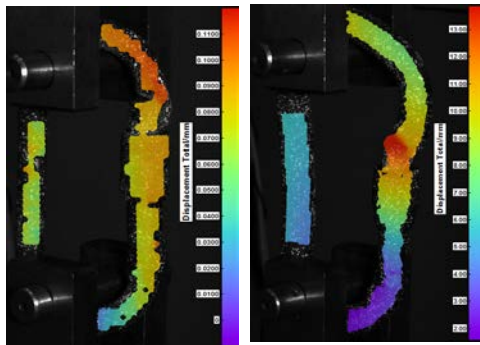


Fig. 3 Total displacement distribution for test sample OVO1, F=20kN and HMS1, F=27kN, obtained with DIC

### 4. Discussion

All tested carabiners withstood the projected loads. Evaluation of displacement distribution have shown which parts of the tested elements are most prone to damage because of biggest displacements and exactly those fragments failed during test. For OVO type carabiner, after constant load test a

breaking load test was done to verify DIC results and establish real breakage point.

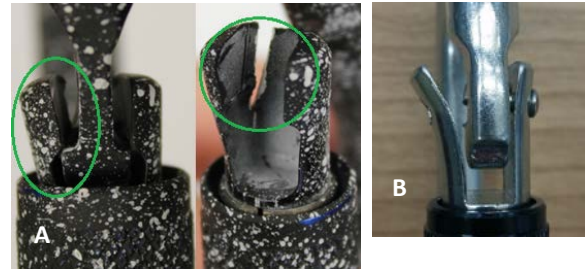


Fig. 4 Damaged gate arm of A – HMS, B – OVO

In each tested connector a gate was damaged, even though the tested elements differed in both construction material and geometric properties. Because of the construction differences the gate damages look different for both carabiner types.

In this study two drastically different - both geometrically and in their construction material - carabiner types were compared. Nevertheless because of their similar application it seems valid to compare their strength properties.

### References

- [1] PN-EN 362:2006 – „Środki ochrony indywidualnej chroniące przez upadkiem z wysokości – Łączniki”
- [2] PN-EN 12275:2013 – „Sprzęt alpinistyczny, karabinki, wymagania bezpieczeństwa i metody badań.”
- [3] Dantec Dynamics: Q – 400 System - Operation Manual
- [4] Alex Strait: „Rock Climbing Clip Analysis Report. A Comparison of Tensile Testing and FEA Modeling for the Black Diamond Neutrino Carabiner.”, 2015
- [5] Steven McGuinness: „What Determines the Strength of Climbing Karabiners?”, Final Year BEng Honours Technical Paper, University of Strathclyde, Glasgow, 2004.

# IMPROVING THE FATIGUE STRENGTH OF IMPAIRED WELDS BY OVERLOADING

Eubomír Gajdoš<sup>1</sup>, Martin Šperl<sup>2</sup>, Andrés Burgos Braga<sup>3</sup>

- <sup>1</sup> Institute of Theoretical and Applied Mechanics, Academy of Sciences of the Czech Republic, Prosecká 76, Prague 9, Czech Republic, E-mail: gajdos@itam.cas.cz
- <sup>2</sup> Institute of Theoretical and Applied Mechanics, Academy of Sciences of the Czech Republic, Prosecká 76, Prague 9, Czech Republic, E-mail: sperl@itam.cas.cz
- <sup>3</sup> On leave from the Institute of Theoretical and Applied Mechanics, Academy of Sciences of the Czech Republic, Prosecká 76, Prague 9, Czech Republic

## 1. Introduction

The defects in the weld can be defined as irregularities in the weld metal produced due to incorrect welding parameters or wrong welding procedures or wrong combination of filler metal and parent metal. Various welding defects can be classified into groups such as cracks, porosity, solid inclusions, lack of fusion and inadequate penetration, imperfect shape and miscellaneous defects. A lack of root fusion (LRF) is one of the weld defects which may develop to a crack and cause failure of the gas pipeline [1]. They also reduce the fatigue limit [2]. In order to investigate the positive effect of overloading of welded joints with LRF on their fatigue properties fatigue tests were carried out on strip-type specimens taken from a helically welded pipe  $\varnothing$  630/7 mm made from low-C steel ČSN 411373.

## 2. Procedure

The specimens were taken perpendicularly to the weld seam. The weld with LRF was left in the natural state and it was located in the middle of the specimen. The specimens were fatigued in zero-to-tension loading with the maximum stress in a cycle 132 MPa. Most of the defects of the LRF type were about 0.5 mm deep; however, by the post-test analysis of the fracture surface there were also some deeper defects found. The results obtained on such specimens were disregarded. The testing program was composed by four groups of specimens, namely groups I to IV - see Tab.1. Group I corresponded to specimens with welds without presence of defects. Group II represented specimens with LRF but without applied overloading. Groups III and IV considered specimens with the existence of LRF and with

applied overloading of  $0.8R_{t0.5}$  and  $R_{t0.5}$ , respectively. In the table, G stands for group and O stands for overloading.

G	No.S	LRF	O [MPa]	Stress cycles	
				$\sigma_{min}$ [MPa]	$\sigma_{max}$ [MPa]
I	1-5	No	---	0	132
II	6-10	Yes	---	0	132
III	11-16	Yes	220	0	132
IV	17-22	Yes	276	0	132

**Tab.1.** Specimen groups and loading data

After fixing the specimens to the loading machine, they were subjected to their respective overloading and, subsequently, they were excited until the maximum cyclic stress was achieved. A photo of a specimen fixed in the grips of the machine is given on Fig.1.



**Fig. 1.** Specimen fixed in the grips

### 3. Evaluation of the results

Test results were evaluated assuming the same initial depth of LRF and assuming a Gaussian distributions of logarithms of lives of specimens. A value of life  $N_f = 10^7$  was assigned to specimens that did not develop cracking after  $10^7$  cycles. The outcome of the statistical evaluation is shown in Tab. 2 with the equivalent life at the far-right column. Symbol  $\mu$  stands her for the mean and the symbol  $s$  stands for the standard deviation of logarithms  $N_f$ . The probability density function of  $\log N_f$  for all four groups of specimens is presented on Fig. 2.

G	$\mu$	$s$	$10^\mu$ [cycles]
I	5.845	0.243	699,800
II	5.504	0.245	319,200
III	5.843	0.104	696,600
IV	6.732	0.341	5,395,100

**Tab.2.** Statistical results. Gaussian distribution of logarithms  $N_f$

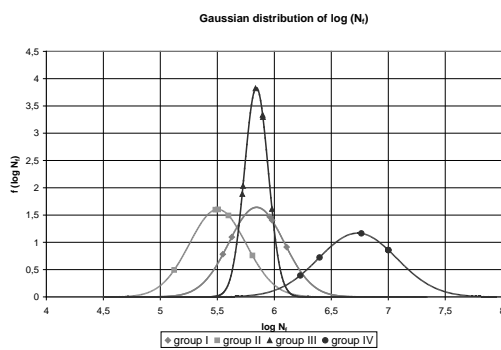


**Fig. 2.**  $f(\log N_f)$  vs.  $\log N_f$  for tested groups

It is seen from these results that the LRF in welds caused a reduction of the fatigue life by more than a half. The overloading of specimens with LRF to the level of  $0.8R_{10.5}$  eliminated the influence of the defects, so the achieved fatigue life after tests reached the life expectancy of specimens without LRF. Likewise, the overloading level of  $R_{10.5}$  had an even greater positive impact on the improvement of the fatigue life of the specimens.

Based on a qualitative assessment, the morphological characteristics of the fatigue fracture surfaces of all tested specimens can be considered alike. In areas near the crack initiation site the fracture surface is substantially broken. It consists of a series of micro-facets, separated by micro-steps, without discernible fatigue grooves – striations. As the length of a crack increases the fatigue micro-facets widen and fatigue striations start to be discernible (Fig. 3).

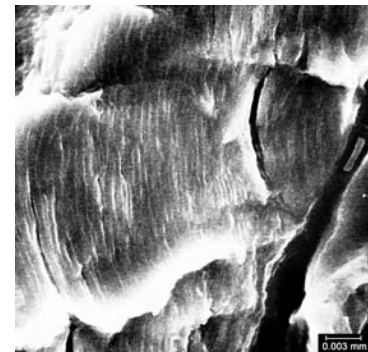


**Fig.3.** Fatigue microfacets covered by striations

### 4. Conclusions

Because the beneficial effects of overloading as determined in this study can be expected when the level of tensile stress, acting in perpendicular direction to the weld seam, is  $(0.8 - 1.0) R_{10.5}$ , helically welded pipes are disqualified to some extent because even for the hoop stress equal to the yield stress the stress perpendicular to the weld is only a part of the hoop stress. So that full beneficial effects of overloading can be experienced for longitudinally welded pipes only.

### Acknowledgements

This work was supported by the grant project No. TE020000162 of the Technological Grant Agency of the Czech Republic

### References

- [1] Gajdoš, L., Šperl, M., Strength of Defective Welds, 18th D-A Symposium, Sept.2001, Steyr, Austria, pp. 79-80
- [2] Jaske, C.E., Fatigue Strength Reduction Factors for Welds in Pressure Vessels and Piping. J. Press. Vesel Technol. 122(3), 2000, pp.297-304

# ANALYSIS OF THE PROPERTIES OF AW6082 ALUMINIUM ALLOY WELD JOINTS PRODUCED WITH DISK LASER

Miroslav Sahul<sup>1</sup>, Martin Sahul<sup>2</sup>, Ján Lokaj<sup>3</sup>

- <sup>1</sup> Slovak University of Technology in Bratislava, Faculty of Materials Science and Technology in Trnava, Department of Welding and Foundry, J. Bottu 25, 917 24 Trnava, Slovakia. E-mail: [miroslav.sahul@stuba.sk](mailto:miroslav.sahul@stuba.sk)
- <sup>2</sup> Slovak University of Technology in Bratislava, Faculty of Materials Science and Technology in Trnava, Institute of Materials Science, J. Bottu 25, 917 24 Trnava, Slovakia. E-mail: [martin.sahul@stuba.sk](mailto:martin.sahul@stuba.sk)
- <sup>3</sup> Slovak University of Technology in Bratislava, Faculty of Materials Science and Technology in Trnava, Institute of Materials Science, J. Bottu 25, 917 24 Trnava, Slovakia. E-mail: [jan.lokaj@stuba.sk](mailto:jan.lokaj@stuba.sk)

## 1. Introduction

Aluminium and its alloys have been extensively used for their unique properties such as high specific strength and corrosion resistance. Application of laser beam welding (LBW) for joining aluminium alloys offers great potential due to the advantages of this welding method. The LBW is characteristic mainly by low heat input, low deformations and high welding speeds. Fusion welding of heat treatable aluminium alloys is associated with the decrease in mechanical properties. Another weld defects which could be encountered in fusion welding of aluminium alloys are porosity and hot cracking. Hot cracking is one of the major challenges in welding of the 2XXX, 6XXX and 7XXX series of aluminium alloys. Furthermore, aluminium alloys possess high reflectivity of laser radiation by their surface [1-5].

This study is focused on the analysis of the effect of welding parameters on the properties of AW6082 heat treatable aluminium alloy weld joints, which were produced with TruDisk 4002 disk laser.

## 2. Experimental

AW6082 heat treatable aluminium alloy with the thickness of 1 mm was proposed as the base material.

Butt weld joints were produced by TruDisk 4002 disk laser. The maximum laser power is 2 kW. BEO D70 focusing optics was used for welding. Focal length was 200 mm. Laser light cable with the core diameter of 400 µm was used for transporting laser radiation from the source to

the focusing optics. Laser beam was focused on the surface of materials to be welded. The spot size was 400 µm. Welding without the use of filler metal was carried out. Argon with the flow rate of 18 l/min was used as shielding gas in order to protect the weld pool against ambient atmosphere.

Light microscopy, electron microscopy including EDS analysis, microhardness measurements and tensile testing were used for assessment of the properties of produced weld joints.

## 3. Results

The cross section of selected weld joint is given in Fig. 1. The weld bead is smooth, no porosity and hot cracking was observed in this case.



Fig. 1. Cross section of selected weld joint

Weld metal – AW6082 aluminium alloy interface is documented in Fig. 2. Columnar dendrite structure was observed at the fusion boundary. Heat affected zone was very narrow, due to the low heat input characteristic for LBW and high thermal conductivity of aluminium alloys.

The higher the laser power the larger the weld metal. Only partial penetration of base metals was observed at the welding speed of 90 mm/s. It was necessary to reduce the welding speed and thus increase the heat input.



**Fig. 2.** Weld metal – AW6082 interface

The microstructure of weld metal is given in Fig. 3. The matrix is formed by  $\alpha$ -Al solid solution. Based on EDS analysis results, it could be stated that aluminium content up to 96.9 wt. % was detected in this location. Contrary, higher amounts of alloying elements such as Si, Mn and Fe were detected in interdendritic areas due to segregation.

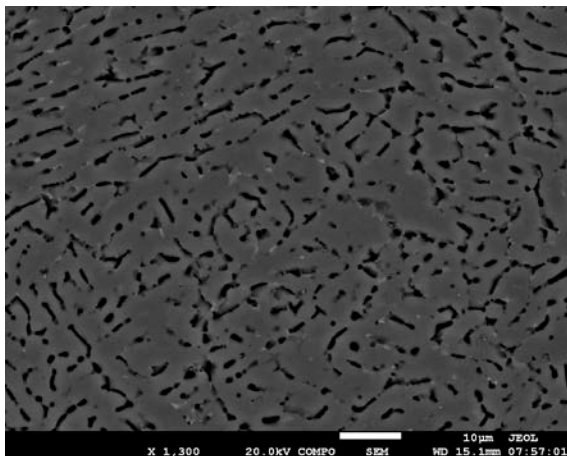


**Fig. 3.** Microstructure of weld metal

#### 4. Conclusion

- butt weld joints on AW6082 heat treatable aluminium alloy without the presence of hot cracking and porosity were successfully produced by disk laser,
- weld metal was formed by aluminium matrix ( $\alpha$ -Al solid solution), interdendritic areas were enriched by alloying elements due to segregation,

- decrease in microhardness from base material towards weld metal was observed due to the dissolution of strengthening precipitates in weld metal during welding,
- tensile strength of weld joints was lower in comparison to the strength of base metal, i.e. the fracture occurred in weld metal.

#### Acknowledgements

The paper was prepared under the support of the VEGA grant agency of the Ministry of Education, Science, Research and Sport of the Slovak Republic, projects No. 1/1010/16 and 1/0503/15.

#### References

- [1] Sanchez-Amaya, J.M., Delgado, T., Gonzalez-Rovira, L., Botana, F.J.: Laser Welding of Aluminium Alloys 5083 and 6082 under Conduction Regime. In *Applied Surface Science* 255, 2009, pp. 9512–9521
- [2] Von Witzendorff, Ph., Kaieler, S., Suttman, O., Overmeyer, L.: Using Pulse Shaping to Control Temporal Strain Development and Solidification Cracking in Pulsed Laser Welding of 6082 Aluminum Alloys. In *Journal of Materials Processing Technology* 225, 2015, pp. 162–169
- [3] Zhang, Ch., Gao, M., Wang, D., Yin, J., Zeng, X.: Relationship between Pool Characteristic and Weld Porosity in Laser Arc Hybrid Welding of AA6082 Aluminum Alloy. In *Journal of Materials Processing Technology* 240, 2017, pp. 217–222
- [4] Kolařík, L., Kovanda, K., Vondrouš, P., Dunovský, J.: Houldcroft Weldability Test of Aluminium Alloy 6082 T6. In *Scientiae Agriculturae Bohemica*, 1, 2012, pp. 14–21
- [5] Costa, M.I., Verdera, D., Leitão, C., Rodrigues, D.M.: Dissimilar Friction Stir Lap Welding of AA 5754-H22/AA 6082-T6 Aluminium Alloys: Influence of Material Properties and Tool Geometry on Weld Strength. In *Materials & Design*, 87, 2015, pp. 721-731

## SECONDARY CAST AL-ALLOYS WITH HIGHER CONTENT OF IRON

Denisa Závodská<sup>1</sup>, Eva Tillová<sup>1</sup>, Ivana Švecová<sup>1</sup>, Lenka Kuchariková<sup>1</sup>, Mária Chalupová<sup>1</sup>

<sup>1</sup> University of Žilina, Faculty of Mechanical Engineering, Univerzitná 8215/1, 010 26 Žilina, Slovakia.  
e-mail: [denisa.zavodska@fstroj.uniza.sk](mailto:denisa.zavodska@fstroj.uniza.sk)

### 1. Introduction

Recycling aluminum alloys provides major economic benefits. Recycling aluminum scrap results in the production of only 5 % of the carbon dioxide produced in making new primary metal. Thus, the energy savings of recycling aluminum also translates into reduced environmental emissions [1].

Recycled aluminium is produced from both new and old scrap. New scrap is surplus material that arises during the production, fabrication and manufacture of Al-products up to the point where they are sold to the final consumer. The production route of new scrap from collection to recycled metal is thus controlled by the Al-industry. Old scrap is Al-material that is treated and melted down after an existing Al-product has been used, discarded and collected. Based on statistics and existing knowledge of the European Al-scrap flow (excluding internal scrap), approximately 40 % of recycled Al-originate from old scrap, and the rest is new scrap [2].

With increasing recycled scraps, mixing and thickening impurity elements in the recycling of aluminum alloy components lead to a serious problem, because the cast components are expected to exhibit their higher performance. That is a reason why virgin ingots containing low iron as an impurity element are supplied to some of highly secured automotive components, instead of manufacturing with recycled ingots. Typical products made from recycled aluminium include castings like cylinder heads, engine blocks, gearboxes and many other automotive and engineering components on the one hand, and extrusion billets or rolling ingots for the production of profiles, sheets, strips and foil on the other [3].

The present study is part of a larger research project which was conducted to study of secondary Al-Si cast alloys. The article describes the evaluation of porosity in secondary AlSi7Mg0.3 cast alloys with major amount of iron.

### 2. Experimental part

Experimental material was secondary unmodified AlSi7Mg0.3 cast alloy with chemical composition (in weight %): **alloy A** - 0.036 Zn; 7.028 % Si; 0.013 % Cu; **0.123 % Fe**; 0.009 % Mn; 0.354 % Mg; 0.123 % Ti; 0.002 % Ni; 0.002 % Cr; 0.0003 % Bi; 0.0007% Sb; rest - Al; **alloy B** - 0.020 Zn; 7.340 % Si; 0.021 % Cu; **0.454 % Fe**; 0.009 % Mn; 0.302 % Mg; 0.118 % Ti; 0.002 % Ni; 0.002 % Cr; 0.0003 % Bi; 0.0007% Sb; rest - Al; **alloy C** - 0.028 Zn; 7.315 % Si; 0.030 % Cu; **0.655 % Fe**; 0.0010 % Mn; 0.292 % Mg; 0.118 % Ti; 0.002 % Ni; 0.002 % Cr; 0.0003 % Bi; 0.0007% Sb; rest - Al; with good casting properties, very good machining, wear resistance and with low thermal expansion. This experimental alloy have the widest application in mechanical, electrical vehicles and aviation engineering, wheels, parts requiring good electrical conductivity and high strength, etc.

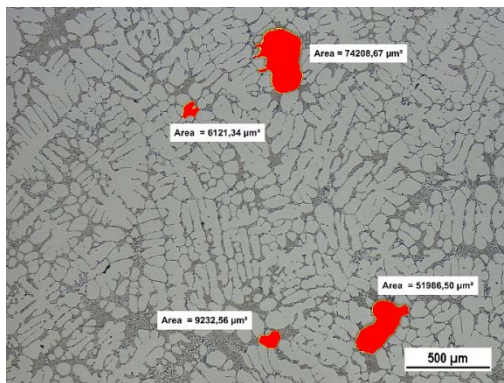
Test bars were produced by process such as sand casting in UNEKO, Zátor, Ltd. Czech Republic with diameters  $\varnothing$  20 mm, length 300 mm. Sand casting is the easiest and the most common used casting method. The melt was not modified or refined. We used casted bars without any heat treatment. Metallographic samples were sectioned from these casted bars and they were standard prepared for metallographic observation (wet ground on SiC paper, DP polished with 3  $\mu$ m diamond past followed by Struers Op-S and etched by H<sub>2</sub>SO<sub>4</sub>). Quantitative metallography was carried out on an Image Analyzer NIS - Elements 4.2 to quantify amount and size of pores as determination of average values [4].

wt. % of Fe	0.123	0.454	0.655
Pore size; $\mu$ m <sup>2</sup>	20 878	16 031	18 781

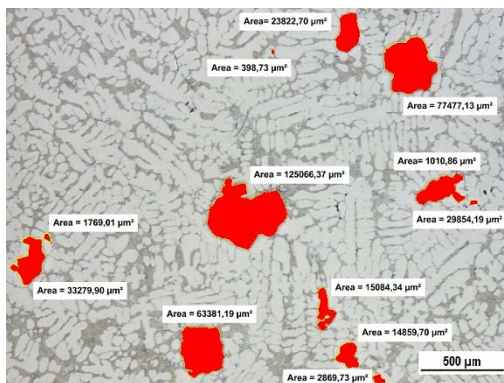
**Tab. 1.** Influence of iron on porosity

The total results in average of the pores sizes with different % of iron are evaluated in Tab. 1 and documented in Fig. 1.

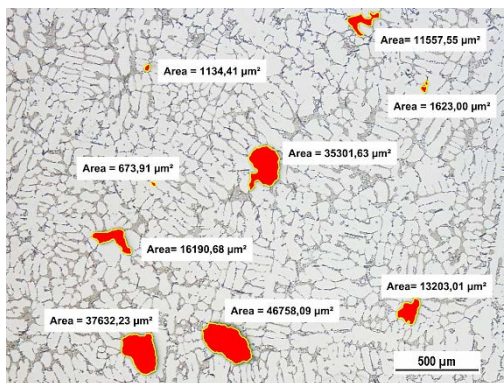
Porosity is directly proportional with % Fe. First, as the iron content increases, the total porosity values of extended-defect formation at high iron levels during stage initially decrease (from cca 20 878  $\mu\text{m}^2$  to 16 031  $\mu\text{m}^2$ ), until a minimum value is reached at 0.454 %, it was not known if the minimum total porosity would % Fe, after which further increases in iron result in increased occur at 0.4 %. These results are in accord with works [5] and [6]. As further iron of additions are made, the overall porosity level increases.



a) 0.123 % Fe.



b) 0.454 % Fe.



c) 0.655 % Fe.

**Fig. 1.** Effect of iron on surface porosity

A change in pore morphology from discrete isolated pores to spongy interdendritic pores occurs even at small, additions of iron (Fig. 1).

### 3. Conclusion

Addition of higher amount of Fe to the secondary AlSi7Mg0.3 alloy showed the results:

- the surface porosity level decreases with iron content until a minimum value occurs at 0.454 % Fe. As further iron additions are made, the overall porosity level increases;
- the pores have been found near to Fe-phases;
- a change in pore morphology from discrete isolated pores to spongy interdendritic pores occurs even at small, additions of iron (0.123 %);
- we can predict, that with the increasing amount of pores are decreasing the mechanical properties.

### Acknowledgements

This research has been supported by the Slovak Research of the project VEGA 1/0533/15 and KEGA 049ŽU-4/2017.

### References

- [1] Das, Subodh K., Yin, W., The Worldwide Aluminum Economy: The Current State of the Industry, JOM, 11, 2007. pp. 57-63.
- [2] Aluminium Recycling in Europe - The Road to High Quality Products. European Aluminium Association (EAA) and the Organisation of European Aluminium Refiners and Remelters (OEA).
- [3] Kuchariková, L. et al., Recycling and properties of recycled aluminium alloys used in the transportation industry, Transport problems, 11, 2, 2016. pp. 117-122.
- [4] Tillová, E., Chalupová, M., Hurtalová, L., Belan, J., Manufacturing Technology, 15 (4), 2015. pp. 720-727.
- [5] Taylor, J. A., Iron-containing intermetallic phases in Al-Si based casting alloys, Procedia Materials Science 1, 2012. pp. 19-33.
- [6] Taylor, J.A. et al., The Role of Iron in the Formation of Porosity in Al-Si-Cu-Based Casting Alloys: Part I. Initial Experimental Observations, Metallurgical and Materials Transactions A, 30A, 6, 1999. pp. 1643-1650.

# EXPERIMENTAL STUDIES ON EFFECT OF HYDROLYTIC DEGRADATION ON ADDITIVE MANUFACTURED POLYMERIC PARTS

Angela Andrzejewska<sup>1</sup>, Tomasz Topoliński<sup>1</sup>

<sup>1</sup> UTP University of Science and Technology in Bydgoszcz, Faculty of Mechanical Engineering, Dept. of Biomedical Engineering, Al. Prof. S. Kaliskiego 7, 85-796 Bydgoszcz, POLAND. E-mails: [angela.andrzejewska@utp.edu.pl](mailto:angela.andrzejewska@utp.edu.pl), [tomasz.topolinski@utp.edu.pl](mailto:tomasz.topolinski@utp.edu.pl)

## 1. Introduction

Damage of the polymer chains can be a result of one of three processes: depolymerization, destruction or degradation. For aliphatic biopolymers used in medical applications the main area of research interest is investigation of hydrolytic degradation. Hydrolytic degradation leads to erosion of biomaterials matrix. This process starts, when aliphatic polymers are immersed in water. The effect of immersion in aqueous medium is absorption of degrading agents. Absorbed water penetrate the polymer matrix and changes the water gradient between the surface and the inner part of the material. This process was described in paper [4].

Currently additive manufacturing (AM) is strongly developing method of Rapid Prototyping (RP) and Rapid Tooling (RT). One of widely used Rapid Prototyping method is Fused Deposition Modeling (FDM). FDM is also called 3D printing technology. In this method 3D objects are constructed directly from 3D CAD data and then prepared with thermoplastic materials. These thermoplastic materials are melted in extruder. Then thin fibers are deposited on flat surface to become all layers of the model.

Literature analysis has been shown to increase interest in mechanical properties of 3D printed parts, like porous scaffolds [3] and standardized specimens [1]. However, these results are not sufficient to determine the mechanical behavior of 3D printed biodegradable materials.

The purpose of this paper is to preliminary investigate the use of polylactic acid (PLA) in fused deposition modeling (FDM) to fabricate specimens for determination effects of hydrolytic degradation in new material model. It also aim to examine the effects of different printing raster patterns on mechanical properties of PLA specimens.

## 2. Methods

### 2.1 Materials

In these investigation specimens according to the ISO 527-1:2012 standard geometry 1A/1B were used. FDM specimens were prepared in three raster patterns (DaVinci 1.0A). The raster patterns were dependent on percentage infill and print direction. Specimens type are presented in tab. 1.

No.	Infill [%]	Print direction [°]	Pattern
I.	90	0	
II.	90	45	
III.	30	0	

**Tab. 1.** FDM specimens.

As a reference material model the injection molded specimens were used (Engel e-victory 310/110 injection molding machine). To the injection molding Ingeo™ Biopolymer 3100 HP, Nature Works LLC was used.

### 2.2 Hydrolytic degradation

All groups of specimens were immersed in Phosphate Buffered Saline. The type of degrading medium and other conditions, like temperature, was chosen based on prior investigations of injection molded specimens [2]. Degradation time for FDM specimens was 12 weeks.

### 2.3 Medium absorption

The percentage amount of medium absorption was calculated from the relationship Eq. (1), corresponding to the difference between specimen mass before degradation ( $m_0$ ) and specimen mass measured after a specified period of degradation ( $m_t$ ). Sample mass after degradation was determined for specimens,

## EXPERIMENTAL DETERMINATION OF MATERIAL MODEL OF MACHINE PARTS PRODUCED BY SLS TECHNOLOGY

Peter Ficzer<sup>1</sup>, Lajos Borbas<sup>2</sup>, Gyorgy Falk<sup>3</sup>, Gabor Szebenyi<sup>4</sup>

- <sup>1</sup> Budapest University of Technology and Economics, Department of Vehicle Parts and Structures Analysis, H-1111 Budapest, Sztoczek u. 2.; [ficzere@kge.bme.hu](mailto:ficzere@kge.bme.hu)
- <sup>2</sup> Budapest University of Technology and Economics, Department of Vehicle Parts and Structures Analysis; and EDUTUS College, Technical Institution, H-2800 Tatabánya, Stúdió tér. [borbas.lajos@editus.hu](mailto:borbas.lajos@editus.hu)
- <sup>3</sup> VARINEX Zrt., President of management, honorary associate professor, [falk@varinex.hu](mailto:falk@varinex.hu)
- <sup>4</sup> Budapest University of Technology and Economics, Department of Polymer Engineering, H-1111 Budapest, Bertalan L. str, MT. bldg., [szebenyi@pt.bme.hu](mailto:szebenyi@pt.bme.hu)

### 1. Introduction

The role and importance of additive production technologies became increasingly important in several fields of our life. Due to the development of materials and technologies the applicability of the procedure is expansive. We can state, that in case of additive production technologies used earlier the material properties of the parts show orientation features [1]. The fact mentioned above in case of the design procedure of different elements, medical implants have great importance. The production technology with its parameters play important role in the material properties on the basis of our earlier experiences [2], [3]. In our paper the SLS technology – as the most reliable one - was investigated in order to compare the results with other parameters of different additive technologies.

### 2. Methodology

In case of SLS technology the previously developed method has been followed. [4]. Despite some references [5] it has been assumed, - similarly to Polyjet [4] and FDM [2] technologies – that the material properties could be described by orthotropic theory. The behavior of the material – in this case – depends on the load direction. The material behavior could be described by the orthotropic Hook's Law. Concerning the behavior to determine the orthotropic material law nine independent material parameters must be determined. In that case, when the properties are independent of the direction we can speak about isotropic material. This is the case of reduced Hook's Law for isotropic materials.

In case of an isotropic material the behavior can be described by two independent parameters.

The comparison of the material parameters in different production directions seems to be important. The specimens printed in different directions (x, y, z) can be seen in Fig.1.

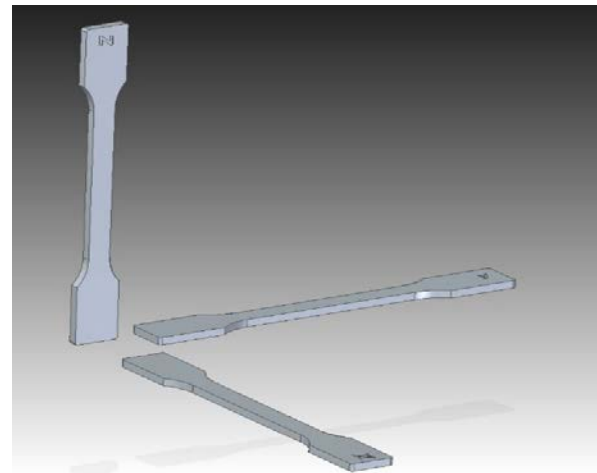


Fig. 1. Tensile specimen printed in different position.

When the tensile test has been realized we can draw conclusions what type of material law can describe the investigated specimen.

### 3. Experimental Results

The test results of the investigation can be seen in Fig. 2. and Fig. 3. In the linear section of the diagrams the homogeneity of the material can be realized. In this part of the tensile test diagrams the behavior of the specimens from practical point of view is the same.

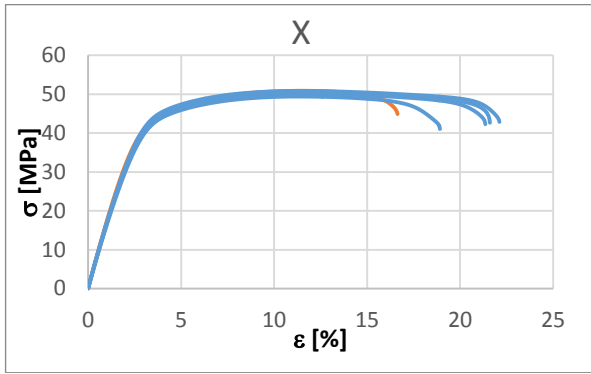


Fig. 2. Tensile test diagram in x-direction.

The test results in y direction correspond with the results measured in x direction in characteristic and in extent values as well. Based on our results and our estimation the material can be considered as an isotropic one in a given plane.

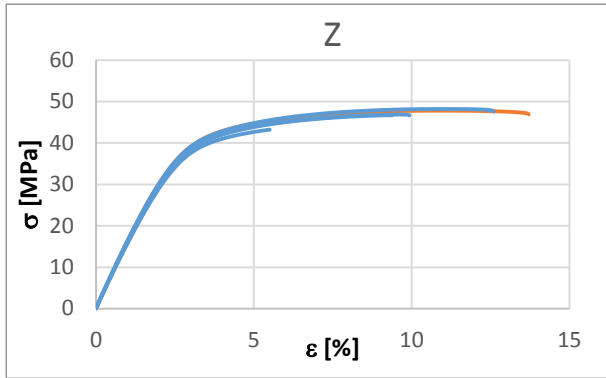


Fig. 3. Tensile test diagram in z-direction.

As in Fig. 4 the test results can be seen in z direction similarly as determined in direction x and y. The difference can be seen in the feature of the ultimate elongation in characteristic and extent values as well.

The evaluated results are summarized in Table. 1.

	Ultimate strength $R_m$ [MPa]	Young modulus $E$ [MPa]
Laying (x-y)	$49.93615 \pm 0.9$	$1713.48 \pm 40$
Standing (z)	$47.4045 \pm 0.8$	$1661.039 \pm 30$

Table. 1. Tensile test results of SLS material

#### 4. Analysis

Investigating our results we can state the following things: in case of SLS production technology there is no essential difference in the material parameters in a function of the production direction (printing in laying and in standing direction). Remember: the direction dependence is

strong in case of Polyjet and FDM technologies. Another conclusion is that the characteristics of the plastic zone in case of printing direction z show different behavior. Some difference is observable in the ultimate elongation (elongation at rupture).

#### 5. Summary

Based on our investigation of SLS production technology it could be stated that the material properties of the technology are independent of the printing direction. One important final conclusion is that the behavior of the material produced by SLS technology can be described by isotropic material law.

#### Acknowledgements

This project results have been realized with a subsidy of the National Research Development and Innovation Office from the fund of NKIH. The title of the project is “Development of the New Generation of Production Technology for Individual Medical-Biological Implantation and Tools”. Project identification No.: NVKP\_16-1-2016-0022. The elaborators express their thanks for the support. Gábor Szebényi acknowledges the financial support received through János Bolyai Scholarship of the Hungarian Academy of Sciences.

#### References

- [1] Ficzer, P., Borbas, L., Torok, A., Validation of Numerically Simulated Rapid-prototype Model by Photoelastic Coating, ACTA MECHANICA SLOVACA 18:(1) pp. 14-24. (2014)
- [2] Ficzer, P., & Borbás, L. (2016). New Application of 3D Printing Method for Photostress Investigation. Materials Today: Proceedings, 3(4), 969-972.
- [3] Péter, F., & Lajos, B. (2010, September). Material law for numerical analysis of rapid prototype products. In Youth Symposium on Experimental Solid Mechanics.
- [4] Ficzer, P., & Borbás, L. (2009). Gyorsprototípus készítő eljárással gyártott termékek anyagtulajdonságainak meghatározása vége-selemes analízis számára. GÉP, 60, 10-11. (in Hungarian)
- [5] Hatos I, Fémek 3D nyomtatásának technológiája és alkalmazása



34th Danubia-Adria Symposium on Advances in Experimental Mechanics  
University of Trieste, Italy, 2017



GÉPGYÁRTÁSTECHNOLÓGIA 2015:(2)  
pp. 6-10. (2016) (In Hungarian)

which were dried with paper towels in order to remove medium from the specimen surface.

$$\Delta m = \frac{m_t - m_0}{m_0} \cdot 100\% \quad (1)$$

### 2.4 Static mechanical properties

Static mechanical properties and their changes as a function of degradation time were determined based on uniaxial tensile test. The testing machine was electromagnetic actuator Instron E3000 ( $\pm 3$  kN). Test speed was 1 mm/min.

### 3. Results and discussion

Results of amount of medium absorption are presented in Tab. 2.

Specimen type	Degradation week		$\Delta m$	SD ( $\sigma$ )
	W0	W12		
	$m_0, g$	$m_t, g$		
IM	12,4548	12,5820	0,0102	0,0005
90	11,1900	11,6140	0,0379	0,0037
90.45	10,9784	11,3327	0,0323	0,0037
30	7,3917	7,6826	0,0393	0,0157

Tab. 2. Average amount of degrading medium absorption.

The percentage test results were calculated from the Eq. (1). Results after 12 weeks of degradation were similar for each FDM specimens. Amorphous injection molded specimens (IM) was less medium than FDM specimens absorbed, also they were characterized by lower dispersion of results.

Tab. 3. shows results of static mechanical properties.

Specimen type	Degradation week		SD ( $\sigma$ )	
	W0	W12	W0	W12
	$\sigma_M, MPa$		-	-
IM	57,5643	55,4794	0,8238	0,3311
90	38,6772	20,2685	1,7813	0,5083
90.45	35,3055	27,3844	0,3790	0,9633
30	25,1771	14,5511	1,0752	0,6534

Tab. 2. Average tensile strength.

It was noted that injection molded specimens have the highest tensile strength, and they were measured only as a reference material model. In the comparison of the test results for FDM materials differences for raster patterns can be

observed. Thus, modification of the structure, affects on varied behaviors of specimens with the same percentage infill. Specimens with infill along load axis (90.45) have lower strength, than specimens with angular oriented infill (90). Also, it was noted that specimens with axially oriented infill can degrade more slowly than specimen with angular oriented infill.

### 4. Remarks

Based on the investigation, it can be observed that the proposed research methodology can be applied in the study of FDM materials. For all samples received lower dispersion of the test results.

In the further research plans other raster patterns would be included. Likewise increasing the number of short-term degradation measurements (to 12 weeks) is provided. In long-term degradation of injection molded specimens it has been shown that up to 12 weeks in the mechanical strength changes are statistically insignificant. Therefore, in the preliminary studies of FDM specimens, only the strength and medium absorption changes for week 0 and 12 were compiled.

### References

- [1] Afrose, M.F. Masood, S.H. Iovenitti, P. et al., Effects of part build orientations on fatigue behavior of FDM-processed PLA material, Progress in Additive Manufacturing, 1 (1), 2016, pp. 21-28
- [2] Andrzejewska, A., Andryszczyk, M., Topoliński, T., Effect of water absorption on the mechanical properties of biodegradable materials for medical applications. In: Engineering Mechanics 2016, editors I. Zolotarev and V. Radolf, V., Inst. Thermomechanics, Prague, 2016, pp. 30-33
- [3] Jariwala, S.H., Lewis, G.S., Bushman, Z.J., Adair, J.H., Donahue, H.J., 3D Printing of Personalized Artificial Bone Scaffolds, 3D Printing and Additive Manufacturing, 2(2), 2015. pp. 56-64
- [4] Vieira, A.C., Vieira, J.C., Guedes, R.M. and Marques, A.T., Degradation and Viscoelastic properties of PLA-PCL, PGA-PCL, PDO and PGA fibers, Materials science forum, 636-37, 1, 2010. pp. 825-832.

# PULSE PHASE THERMOGRAPHY: IMPACT DAMAGE RETRIEVAL

Petra Bagavac<sup>1</sup>, Lovre Krstulović-Opara<sup>1</sup>, Željko Domazet<sup>1</sup>

<sup>1</sup> University of Split, Faculty of Electrical engineering, Mechanical Engineering and Naval Architecture, R. Boškovića 32, 21000 Split, Croatia. E-mail: [petra.bagavac@fesb.hr](mailto:petra.bagavac@fesb.hr), [lovre.krstulovic-opara@fesb.hr](mailto:lovre.krstulovic-opara@fesb.hr), [zeljko.domazet@fesb.hr](mailto:zeljko.domazet@fesb.hr).

## 1. Introduction

Impact damage in composite materials is hard to reveal with methods of IR thermography as flaw has no sharp edges.

Generally authors [1-4] are inspecting composite materials which have been deliberately damaged with flat bottom holes or with inserts of foreign material (e. g. Teflon) causing sharp images. Authors in [5, 6] analyzed impacted specimens with methods of passive thermography during the impact, where IR camera recorded increase in temperature caused by the release of heat energy liberated by the plastic deformation.

## 2. The Pulse-Phase Thermography

A typical configuration to perform a PPT is shown on Fig. 1. Specimen is heated with high power photographic flash and temperature decay on the surface of the specimen is recorded with IR camera. After acquisition, N thermograms form the sequence written as 3D array, where  $x$  and  $y$  are pixel position and  $z$  is time axis [7, 8].

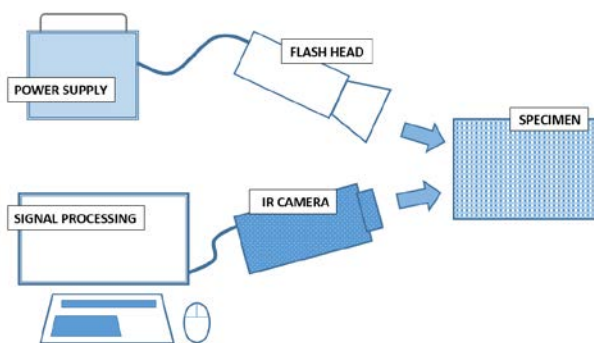


Fig. 1. PPT experimental setup.

Follows, temperature decay of observed pixel ( $i, j$ ) is a vector containing temperature values during observed time axis. Temperature decay curve of each pixel is reconstructed by applying the Fourier Transform. By using the FT is possible to reconstruct any 1D function as a sum of sinusoidal terms of increasing frequency.

$$F_n = \Delta t \sum_{k=0}^{N-1} T(k\Delta t) e^{-j2\pi\omega k/N} = Re_n + Im_n \quad (1)$$

where  $j^2 = -1$ ;  $n$  designates the frequency increment ( $n = 0, 1, \dots, N$ );  $\Delta t$  is the sampling interval;  $Re$  and  $Im$  are the real and the imaginary parts of the transform, respectively [8]. Real and imaginary parts of Eq. (1) can be used to calculate the amplitude and the phase of the transform in order to reconstruct 3D matrices as illustrated in Fig. 2.

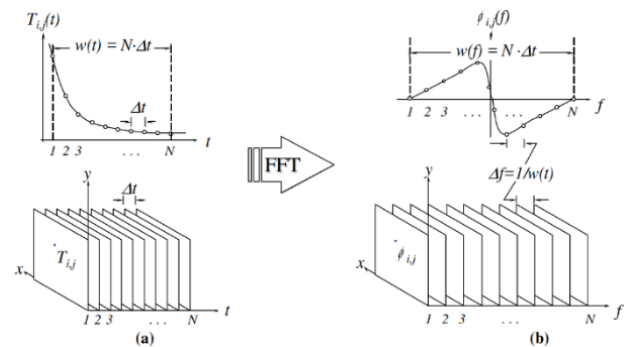


Fig. 2. (a) Thermogram sequence and temperature profile for a pixel, and (b) phasegram sequence after application of the FFT.

## 3. Experimental procedure and results

Test specimens are made from the GFRP (specimen A) and the CFRP (specimen B). Specimens are deliberately damaged with the controlled metal rod impactor. The metal rod was released from the height of 2 m, releasing 19.62 J of impact energy.

The surface of the specimen is heated by the Hensel<sup>®</sup> flash head and power supply, able to emit 6 kJ in 1/400 s. Measurements of exposed specimens are taken with cooled MW FLIR<sup>®</sup> SC 5000 Infrared camera. Resulting thermogram sequence for each specimen is shown in Fig. 3.

The resulting thermographic sequence is processed by the MATLAB<sup>®</sup> program package, and resulting PPT phasegrams are shown in Fig. 4.

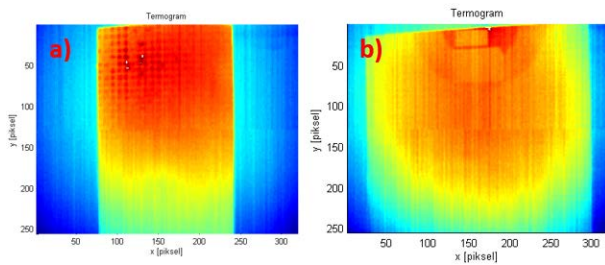


**Fig. 3.** Raw data thermogram: a) GFRP, b) CFRP.

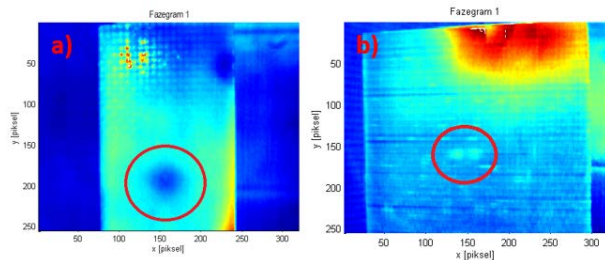


**Fig. 4.** Phasegram: a) GFRP, b) CFRP.

#### 4. Preprocessing of the row data

Thermal decays are characterized by the high level of noise resulting from differences in the responsivity of detectors to the incoming irradiance. It is a common problem of focal plane arrays (FPA) detectors. In this work in order to reduce the noise level, the preprocessing technique based on fitting the decay curves with smooth polynomial curve, is proposed. The thermal decay for each pixel of specimen A is fitted by the polynomial curve  $T(t) = at^2 + bt + c$  (Fig. 5a). The thermal decay for each pixel of specimen B is fitted with the exponential curve  $T(t) = ae^{bt} + ce^{dt}$ , (Fig. 5b).

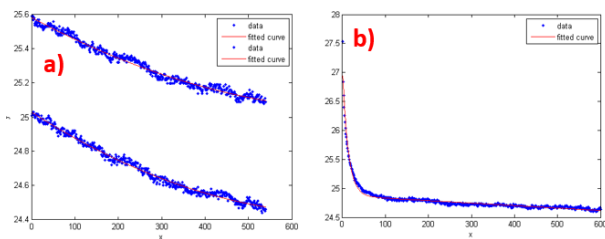


**Fig. 5.** Raw data and fitted curve: a) GFRP, b) CFRP.

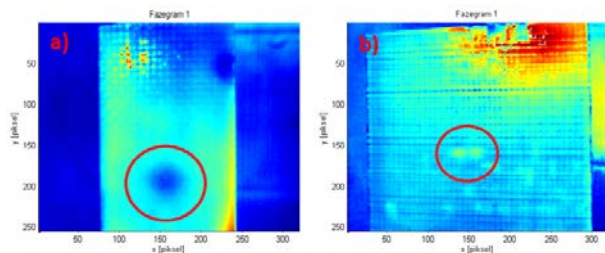


**Fig. 6.** Fitted data phasegram: a) GFRP, b) CFRP.

After fitting the row data, fitted data are reconstructed by the Fourier Transform and phase images are shown in Fig. 6. The increased detail of impact damage for CFRP specimen is shown in Figure 7.

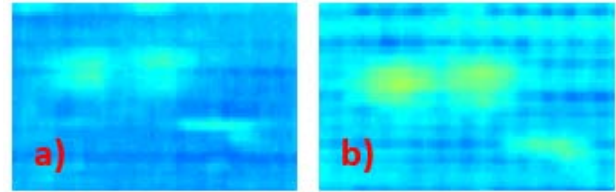


**Fig. 7.** Impact damage phasegram for CFRP sample: a) before preprocessing, b) after preprocessing.

#### 5. Concluding remarks

The progressive and continuous increase in computer power together with the availability of transformation tools in used software packages encourages further developments in the field.

#### References

- [1] Ibarra-Castaneda, C.: „Quantitative subsurface defect evaluation by pulsed phase thermography: depth retrieval with phase“, Ph. D. Thesis, Laval University, 2005
- [2] C. Meola, G. M. Carlomagno, L. Giorleo: „Geometrical Limitations to Detection of Defects in Composites by Means of Infrared Thermography“, Journal of Nondestructive evaluation, 2004
- [3] Mohammed A. Omar, Yi Zhou: “A quantitative review of three thermography processing routines”, Infrared Physics & Technology, p. 300-306, 2008
- [4] Takahide Sakagami, Shiro Kubo: “Applications of pulse thermography and lock in thermography to quantitative nondestructive evaluations”, Infrared Physics & Technology, p. 211-218, 2002
- [5] Meola, C.; Carlomagno, G. M.; Ricci, F.; Lopresto, V.; Caprino, G.: “Investigation of Impact Damage in Composites with Infrared Thermography”, 6<sup>th</sup> NDT in Progress, Prague, 2011
- [6] C. Ibarra Castaneda, A. Bendada, X. Maldague: “Thermographic Image for NDT”, IV Conferencia Panamericana de END, 2007
- [7] C. Ibarra-Castaneda, X. Maldague: “Defect Depth Retrieval from Pulsed Phase Thermographic Data on Plexiglas and Aluminium Samples”, Proceedings of SPIE, 2004
- [8] Maldague X. P. and Marinetti S.: “Pulse phase infrared thermography”, J. Appl. Phys., p. 2694-2698, 1996

# RATE DEPENDENCY OF INTERFACE FRAGMENTATION IN AL-MG-COMPOUNDS

Carola Kirbach<sup>1</sup>, Martin Stockmann<sup>1</sup>, Jörn Ihlemann<sup>1</sup>

<sup>1</sup> Technische Universität Chemnitz, Faculty of Mechanical Engineering, Department of Solid Mechanics, Reichenhainer Straße 70, 09126 Chemnitz, GERMANY. E-mail: carola.kirbach@mb.tu-chemnitz.de

## 1. Introduction

Due to their high strength and low density magnesium and aluminum offer a high potential in light-weight constructions. To minimize the impact of magnesium's high corrosion sensitivity the hydrostatic extrusion process [1] is used to coat magnesium with aluminum. Thereby a bolt is pressed through a die creating a bimetal rod, Fig. 1, made up of magnesium as core material and aluminum as sleeve material, with a brittle intermetallic boundary layer between the two materials.

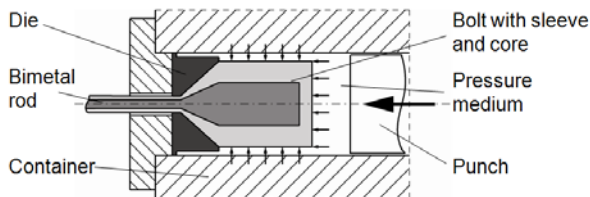


Fig. 1. Hydrostatic extrusion process [2].

Previous investigations regarding the boundary layer behaviour during the subsequent hot forging process spreading by Feuerhack [3] revealed an enormous grow of the boundary layer during the thermal treatment from 2-3 $\mu\text{m}$  up to 25 $\mu\text{m}$  and a fragmentation during the test execution. After splitting, the fragments drift apart, the basic materials refill the gaps and a new secondary boundary layer is built after contact. To investigate the fragmentation dependency regarding the rate of deformation a channel upsetting process is used with different stamp velocities.

## 2. Channel upsetting

The forging process spreading of the entire compound [3] is substituted by channel upsetting with a miniature specimen, Fig. 2, which is necessary to integrate the deformation process into a testing machine with a wide range of stamp velocities. All specimens are extracted by wire eroding.

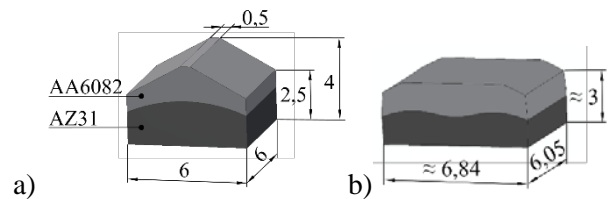


Fig. 2. Dimension of the specimen a) initial state b) deformed state.

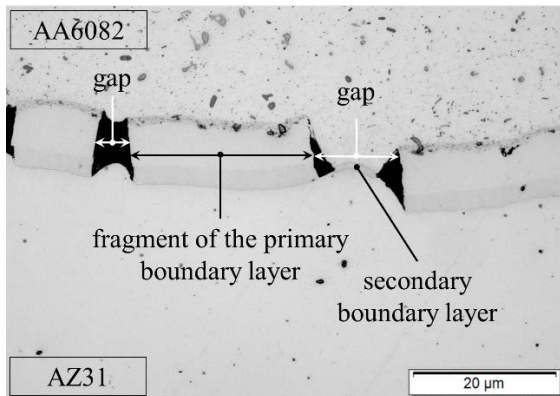
The channel upsetting device, Fig. 3, is installed in a 50 kN INSTRON hydraulic testing machine with a gas heater using air as the transfer medium to achieve a device and specimen temperature of 300°C. Thermal isolation is attained by ceramic punches. The stamp is shift-driven up to a height reduction of 1 mm with velocities of 200, 20, 2 and 0.2 mm/s.



Fig. 3. Experimental setup.

## 3. Metallography

After test execution all specimens are metallographically evaluated. The boundary layer thickness is about 22 $\mu\text{m}$  due to the heat treatment during testing. For every specimen the length of each fragment and gap is measured, Fig. 4, to get an information about the deformation behaviour of the boundary layer.



**Fig. 4.** Exemplary image of the boundary layer and gaps after channel upsetting.

#### 4. Results

At first, the lengths of the fragments are summed up to a total length of the boundary layer which is shown in Fig. 5. Additionally, the total length has to be considered in relation to the initial state. To this end, the analytical length of the initial interface is used.

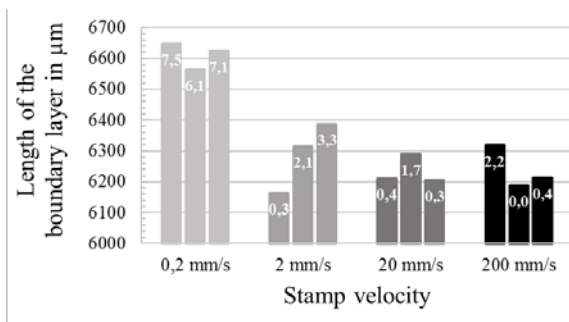


**Fig. 5.** Total interface length after channel upsetting of three specimens for every stamp velocity with the percentage extension of the interface in the bars.

Especially at a stamp velocity of 0.2 mm/s the interface shows a ductile behaviour with an extension of about 7%. At higher deformation rates the elongation at break is negligible.

In contrast, the length and amount of the gaps increase with the stamp velocity up to 20mm/s, Fig. 6. Then at higher deformation rates the percentage of the gaps on the total interface length stays equal. Only the number of gaps increases and accordingly the length of each gap decreases.

The evolution of the boundary layer fragments and the gaps at increasing stamp velocity shows a transition from ductile to brittle material behaviour. The boundary layer is then fully stiff and breaks into a large amount of small fragments.

A limit of fracture toughness could not be reached in this study.

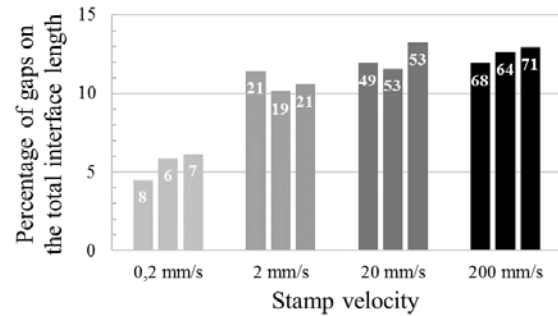


**Fig. 6.** Percentage of gaps on the total interface length after channel upsetting of three specimens for every stamp velocity with the amount of gaps in the bars.

However, the results indicate the possibility to deform the compound without fragmentation at low deformation rates.

#### 5. Remarks

- Despite the fact that the boundary layer of the compound shows a brittle behavior the compounds can be formed without a destruction of the metallurgically bonded connection.
- The boundary layer fragmentation increases dramatically with the rate of deformation during the channel upsetting process.
- Further investigations including the dependency of the boundary layer thickness caused by different thermal treatments are planned.

#### Acknowledgements

The authors thank the German Research Foundation (DFG) for financial support of this work, which is a part of SFB692, subproject B3.

#### References

- [1] Gers, H., Strangpressen. Wiley-VCH, 2007.
- [2] Kirbach, C, Lehmann, T, Stockmann, M, and Ihlemann, J, Digital Image Correlation Used for Experimental Investigations of Al/Mg Compounds. *Strain*, 51, 2015, 223–234. doi: 10.1111/str.12135
- [3] Binotsch, C., Nickel, D., Feuerhack, A., Awiszus, B., Forging of Al-Mg Compounds and Characterization of Interface. *Procedia Engineering*, Volume 81, 2014. pp. 540-545.

# FATIGUE PERFORMANCE OF REINFORCED SINGLE LAP JOINTS IN A CARBON FIBRE COMPOSITE

Martin Kadlec<sup>1</sup>, Robin Hron<sup>1</sup>, Petr Bělský<sup>1</sup>, Patrick Bara<sup>2</sup>

- <sup>1</sup> VZLU – Aerospace Research and Test Establishment, Beranových 130, Prague, Czech Republic. E-mails: [kadlec@vzlu.cz](mailto:kadlec@vzlu.cz), [hron@vzlu.cz](mailto:hron@vzlu.cz), [belsky@vzlu.cz](mailto:belsky@vzlu.cz)
- <sup>2</sup> SABCA - Société Anonyme Belge de Constructions Aéronautiques, 1130, Brussels, Belgium. E-mail: [patrick.bara@sabca.be](mailto:patrick.bara@sabca.be).

## 1. Introduction

Carbon fibre-reinforced polymer (CFRP) laminates are used in aerospace due to their effective strength to weight ratio. Until today thin walled composite structures are joined by using a large number of fasteners. Secondary adhesive bonding of primary parts would considerably contribute to the weight and cost reduction but they cannot fulfil the airworthiness requirements up to now [1]. Using fasteners as crack stopping features is one way to achieve the certification [2]. This work investigates possible innovations for the bolted connection using inserted washers to reinforce the bolted area [3].

## 2. Materials and Methods

The reference sample and two types of innovative technologies for joining of CFRP laminates were evaluated. Two types of washers inserted into the carbon fibre fabric laminate during manufacturing were used for the innovative specimens - smooth washer and spiked 3D print washer. The specimens were single lap joints with one fastener. Two slabs of 20 and 13 plies were joint for each specimen. The joints were bonded by adhesive (REDUX FM300) and fastened by a fastener (ABS1707 B C2 V1 A).

The fatigue tests were performed on INOVA ZUZ 100 kN and Hydropuls Schenck 250 kN with maximum load of 8 600 N and coefficient of asymmetry  $R = 0.1$ . In selected intervals C-scan using a phased array probe was performed.

## 3. Results

The results of fatigue crack growth of a single lap joint with adhesive bonding and a fastener are shown in Fig. 1 and Fig. 2. Fatigue crack fronts during loading were marked based on single transducer ultrasonic probe. Typically the crack

propagated first from the bottom edge and then from the upper. The C-scan revealed also crack initiation from the washer border. Fatigue crack growth curves were determined based on the ultrasonic detection. The reinforced series showed less final crack acceleration, and thus improved fatigue behaviour in comparison with the reference specimen and with the smooth washer.

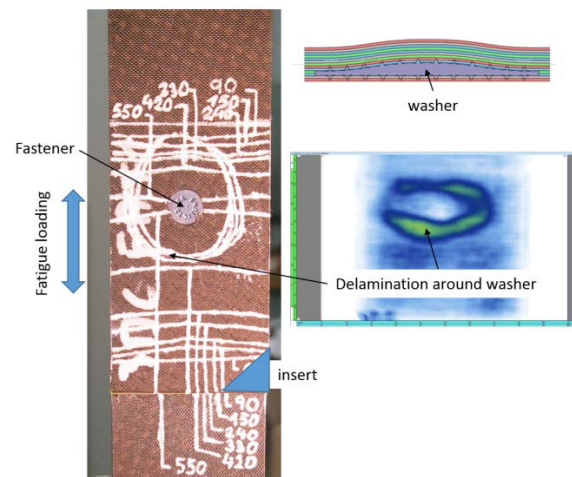


Fig. 1. Fatigue crack fronts during loading and a delamination initiation from the washers

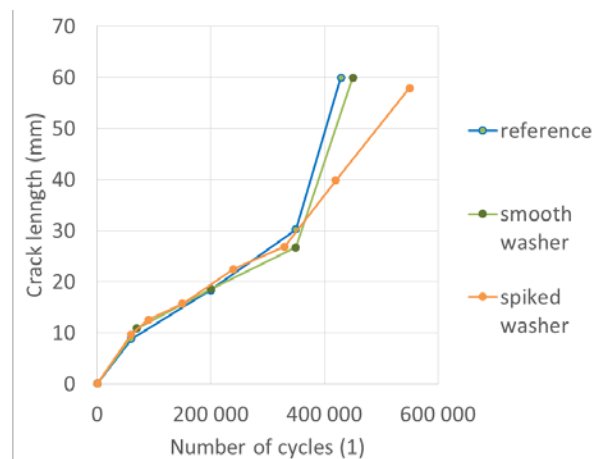
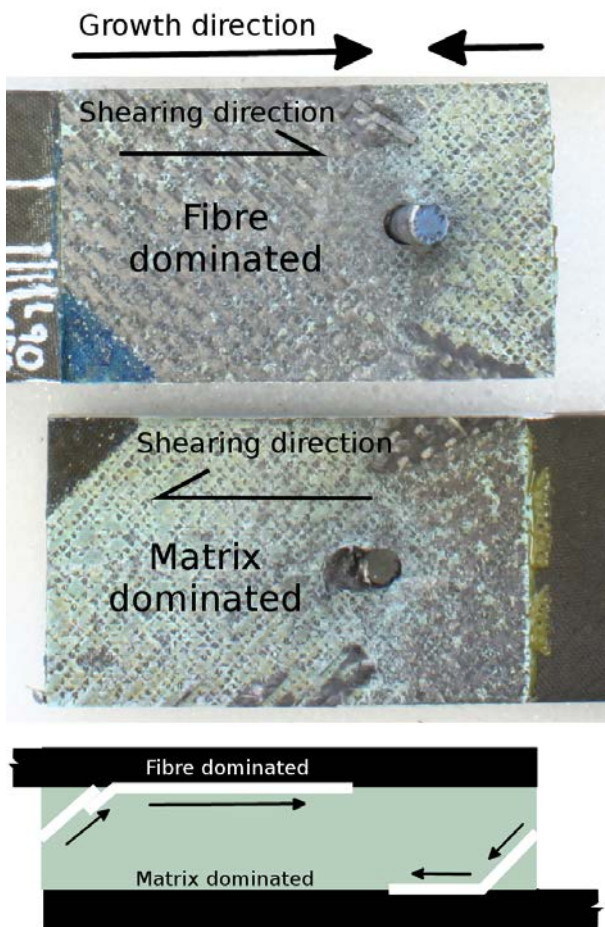


Fig. 2. Fatigue crack growth curves.

A macro photograph of fracture surfaces revealed fibre and matrix dominated fracture which corresponded with crack growth and shearing direction. The mechanism of angled cracks is explained in Fig. 3. The cracks initiated at both free edges and then they were driven diagonally toward one of the bonded surface due to the shear forces that caused 45° major stress direction. The cracks propagated along the interfaces until they reached the bolt.



**Fig. 3.** Fatigue crack fracture surface with explained angled crack mechanism leading to fibre and matrix dominated fracture.

#### 4. Conclusion

To conclude, the results of fatigue loading of single lap shear joints showed that the reinforcement influenced only the final stage of crack growth where it hindered the crack and increased the joint lifetime by 30%. The fatigue crack growth mechanism was explained. The crack stopping features have great potential to enable certification of adhesive joints for primary aerospace structures.

#### Acknowledgements

This work was funded by the European Union Seventh Framework Programme under grant agreement n° 314180 – Project BOPACS: Boltless Assembling of Primary Aerospace Composite Structures and by Ministry of Industry and Trade of the Czech Republic in the framework of Institutional support of Research organizations.

#### References

- [1] Jones, R., Kinloch, A.J., Hu, W., Cyclic-fatigue crack growth in composite and adhesively-bonded structures: The FAA slow crack growth approach to certification and the problem of similitude, *International Journal of Fatigue*, 88, 2016. pp. 10-18.
- [2] Tserpes, K.I., Peikert, G., Floros, I.S., Crack stopping in composite adhesively bonded joints through corrugation, *Theoretical and Applied Fracture Mechanics*, 83, 2016. pp. 152-157.
- [3] Kolks, G., Tserpes, K.I., Efficient progressive damage modeling of hybrid composite/titanium bolted joints, *Composites Part A*, 56, 2014. pp. 51-63.

# A LOW-COST CABLE-SUSPENDED PARALLEL MANIPULATOR FOR TESTING 3D OLFACTION ALGORITHMS

Patrick P. Neumann<sup>1</sup>, Malte Detlefsen<sup>1</sup>, Dino Hüllmann<sup>1</sup>, and Harald Kohlhoff<sup>1</sup>

<sup>1</sup> Bundesanstalt für Materialforschung und -prüfung (BAM), Department 8 Non-destructive testing, Unter den Eichen 87, 12205 Berlin, Germany. E-mail: [patrick.neumann@bam.de](mailto:patrick.neumann@bam.de)

## 1. Introduction

Cable-suspended parallel manipulators have been a topic of research for multiple decades and called special attention in the fields of simulations [1]. However, they are also well-suited for the simple evaluation of aerial-based mobile robot olfaction (MRO) algorithms, such as gas source localization and gas distribution mapping. Based on an open source framework for 3D printers, we designed a low-cost underconstrained, cable-suspended parallel manipulator. Computations are carried out purely on an Atmel ATmega2560 microcontroller.

## 2. Testbed Setup

The testbed built at BAM (see Fig. 1) consists of four stepper motors connected to an aluminum metal frame with four cables leading to the end-effector. The robot is operated by an 8-bit Atmel ATmega2560 microcontroller running at 16 MHz and connected to the Rumba<sup>1</sup> electronics board, from which the motors are being controlled. An LCD-display is attached to the board to display further information during operation such as the end-effector's position. Furthermore, commands can be sent to the device via serial connection.

The robot is designed to work as an underconstrained parallel manipulator allowing for spatial movements using gravity (see Fig. 1). Since the end-effector tends to lean towards the side with the shortest cables due to the distribution of mass, we found a pointwise connection of the cables at the end-effector to be of best use to keep the end-effector most stable. Alternatively, a gimbal can be equipped to level out the end-effector. Microstepping greatly enhances smoothness of operation and offers precise positioning within the range of millimeters. Using TMC2100 (TRINAMIC Motion Control GmbH & Co. KG) stepper drivers in stealth-chop mode, the robot runs extremely silent.



**Fig. 1.** Construction of an underconstrained, cable-suspended parallel manipulator with four cables for spatial positioning of an end-effector using gravity.

The robot can be operated through on-board memory or SD card to manoeuvre the end-effector along predefined trajectories. Via serial connection, a host system such as a PC can communicate with the robot to control the end-effector's position and in turn react on information received from it.

A 2.4 GHz XBee module connected to a microcontroller board (Arduino Leonardo) serves as basis for the end-effector's payload. The bidirectional wireless data link enables sending measurement data to and controlling the payload from the PC. Furthermore, a 2 DoF robot arm with gripper and servos have been attached to the end-effector for test purposes.

### 2.1 Limitations

The Atmel ATmega2560 microcontroller is a well-known processor among communities such as Arduino. But despite its relatively low pricing, it lacks useful features such as DMA (Direct Memory Access), which help to reduce processor load significantly. Especially in situations, in which an interrupt might overpower the serial interface, information loss can occur, thus bringing communication to a halt. Therefore, switching to more powerful processors might be necessary de-

<sup>1</sup> See <https://reprap.org/wiki/RUMBA>

pending on the application. Furthermore, the proposed parallel manipulator acts as an open-loop-controller, meaning, that no information about the state of the parallel manipulator in the real world, i.e., cable lengths and end-effector's position, are propagated back to the system. Thus, the software must rely on the accountability of the hardware in terms of precision, since it cannot filter its own state using feedback from outside. This also means, the system is not able to self-calibrate its end-effector's position or cable lengths. Each deviation from the model is irrecoverably lost. Though, during tests this has not been an issue, since the motors have proven to work with reliable precision.

To overcome the limitations, additional sensors, such as an IMU or a camera, could be attached to the end-effector's payload, providing necessary information for position filtering, which could be carried out on the host system and then fed back to the robot. Force sensors installed at the cables of the robot could additionally support self-calibration of cable lengths.

### 3. Plume Characterization

Evaluating algorithms in the field of MRO can quickly become cumbersome due to the challenges of creating a controlled test environment, both indoors and outdoors. Simulations have therefore become a common tool to evaluate algorithms regarding chemical plume tracking [2]. However, to evaluate performance quality, real-world tests are inevitable. For this reason, the testbed has been equipped with an artificial gas source located within the workspace of the robot to form a basis for evaluating algorithms under controlled conditions.

#### 3.1 Plume Generation

A carbon dioxide (CO<sub>2</sub>) gas cylinder connected via a small tube to a fan is installed at a fixed location within the workspace. The 12V fan is operated by an adjustable power supply to allow for variable air flow during experiments. The payload of the cable-suspended parallel manipulator is equipped with a SprintIR infrared CO<sub>2</sub> sensor (GSS Ltd.<sup>2</sup>) with a sampling rate of 20 Hz. The sensor has a measurement range of 0 to 100 %<sub>vol</sub> with an accuracy of ±5% per reading.

#### 3.2 Experimental Results

The plume depicted in Fig. 2 has been obtained via measurements by the robot's payload following a cubic grid with a total of 405 points. The gas source emitted CO<sub>2</sub> with 8 liters per minute, while the fan was operated at 12V, creating a relative smooth dispersion in all three dimensions. By adjusting the emission rate and power voltage, the plume can be controlled to represent different scenarios, which may reveal different aspects of an algorithm, when compared to another.

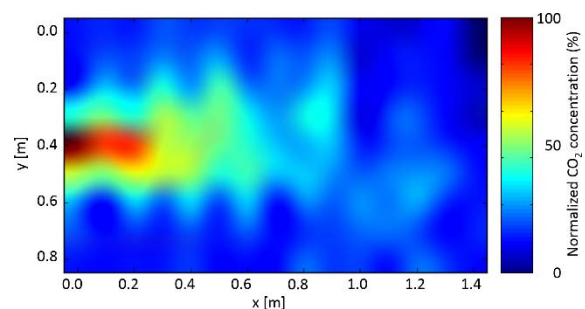


**Fig. 2.** Bilinear interpolation of the gas distribution measured by the robot's payload during experiments. Air flow from left to right with source located at the left mid-section.

### 4. Summary and Conclusions

We present a low-cost cable-suspended parallel manipulator based on a single Atmel ATmega2560 microcontroller. Through serial and wireless connection, a host system can communicate with both the robot and the processing unit installed at the end-effector, making the system suitable for robotic applications.

In a first test, we successfully characterized the plume showing the applicability of the system for testing and evaluating algorithms in the field of 3D mobile robot olfaction.

### References

- [1] Bruckmann, T., Auslegung und Betrieb redundanter paralleler Seilroboter, Dissertation, Universität Duisburg-Essen, 2010.
- [2] G. Kowadlo, G., Russell, R. A., Robot Odor Localization: A Taxonomy and Survey, Int. J. Rob. Res., 2008, vol. 27, no. 8, pp. 869–894.

<sup>2</sup> [www.gassensing.co.uk](http://www.gassensing.co.uk)

# THE FMECA ANALYSIS AND THE MECHANICAL FAILURES IN RADIOLOGY

**Manuela Stroili<sup>1</sup>, Francesco Taddeo<sup>2</sup>, Federico Meini<sup>3</sup>**

<sup>1</sup> Master SMMCE, Department of Engineering and Architecture, University of Trieste, Via A. Valerio 10, 34127 Trieste and ASUI of Trieste, Department of Technology Assessment, Ospedale Maggiore, piazza dell'Ospitale n.1, 34125 Trieste, Italy. E-mail: [manuela.stroili@tin.it](mailto:manuela.stroili@tin.it);

<sup>2</sup> Master MIC, Department of Engineering and Architecture, University of Trieste, Via A. Valerio 10, 34127 Trieste, Italy. E-mail: [francesco.taddeo1991@gmail.com](mailto:francesco.taddeo1991@gmail.com)

<sup>3</sup> Hospital Consulting, SIC USL 6 Livorno, Italy. E-mail: [federico.meini@hospital-consulting.it](mailto:federico.meini@hospital-consulting.it)

## 1. Introduction

This study consisted in a risk analysis of the possible failures involving all the technical elements of the medical devices used in the Radiology unit in hospital. It has been used the FMEA technique [1,2,3] in order to analyze failures.

## 2. Materials

An interdisciplinary working group, coordinated by the Technology Assessment of Trieste, was formed to analyze failures of two ultrasound and two X-ray devices that occurred in 7 years. A software with a medical device inventory and their relevant failures was installed at the hospital in Livorno [4].

## 3. Methods

The data collected were elaborated using the FMEA methodology [2]. The FMEA uses RPN index (Risk Priority Number) which is calculated with three rating stairs and assigns a risk score to each type of failure. The highest value is a relevant risk to the patient and/or operator in the use of Medical Devices.

$$RPN = S * O * D$$

*S Severity*: is an assessment of the significance of the failure mode's effect on item operation, causing possible damage to patients. It is assigned by the working group.

*O Occurrence*: denotes the frequency or probability of occurrence of each failure mode is determined in data base of medical devices

*D Detectability*: means detection, i.e. an estimate of the chance to identify and eliminate the failure before the system or customer is affected.

RPN may then be used for prioritization in addressing the mitigation of failure modes.

## 4. Results

The group chose 4 devices (2 ultrasound and 2 fixed X-ray devices) and collected the following data which refer to a period of time of 7 years: 155,391 X-ray (Fig.1) and 62,405 ultrasound devices (Fig.2).



**Fig. 1.** Fixed X-ray device.



**Fig. 2.** Ultrasound device.

182 electrical, electronic, mechanical, software and staff training failures were detected. The mechanical failures are described in Table 1.

Types	Mechanical failures
I.	fragility of materials
II.	worn-out belt
III.	a low engine power
IV.	blocked keyboard and trackball
V.	deposit box/cassette poorly flowing
VI.	poor/non-existent lubrication
VII.	insufficient cleaning of sensors and filters
VIII.	radiation button short circuit

**Tab. 1.** Description of mechanical failures.

Then an improvement plan has been drawn up for all failures and then a 2<sup>nd</sup> RPN Index has been calculated [5]. Comparing 1<sup>st</sup> and 2<sup>nd</sup> RPN, the working group estimated a reduction of the risk of failures in a range between 20% and 85.7% (1).

$$\Delta RPN \% = \frac{1^{\circ} RPN - 2^{\circ} RPN}{1^{\circ} RPN} * 100 \quad (1)$$

### 5. Remarks and Conclusion

- In order to perform these studies is important to have a well-populated computerized Data Base and well-designed for the collection of all the important data of medical devices.
- With regard to mechanical failures, the group formulated performance improving solutions which are described in table n.2.
- The corrective actions identified are being implemented with a resulting improvement in devices performances for the patients and the health professionals safety.
- This FMEA risk analysis has been shared with the A.S.U.I.'s radiology department in Trieste for training purpose.

Types	Possible failure improvements
I.	substitution wit high-fatigue strength materials
II.	movement chain (crown-pinion system)
III.	design change, use of optical sensors in place of the mechanical limit switch
IV.	Touchscreen
V.	barcode identifier format cassette/optical limit switches/digital radiography (DR) systems
VI.	self-lubricating on principal movements
VII.	localized aeration system
VIII.	remote manual action: assess transmission problems, battery life and interference

**Tab. 2.** Description of solution for mechanical failures.

It is known that developments in technology are key to the improvement of medical diagnosis and safety at work.

### Acknowledgements

The Authors thank the hospital's radiology unit of Livorno and the specialist Marcello Galiberti for the kind assistance provided during data analysis.

### References

- [1] International Standard CEI IEC 60812:2006-1, second edition "Analysis techniques for system reliability (FMEA)".
- [2] M.Stroili, M.Ianche, A.Cressi, F.Cosmi "FMEA risk analysis in a dialysis unit", 30h DAS 2013, Primoster Croatia.
- [3] Petaros E."Applicazione della tecnica FMEA per l'analisi degli effetti di guasto dei broncoscopi." Master thesis, University of Trieste 2015.
- [4] Stroili M. "Disinvestimenti di strutture ospedaliere ed innovazioni clinico-gestionali in Italia con accreditamento istituzionale e all'eccellenza" 5th SIHTA 2012, Roma, Italy.
- [5] Taddeo F. "La prima applicazione dello standard internazionale IEC 60812–tecnica FMEA per l'analisi dei rischi di apparecchi radiologici ed ecografi nel servizio di radiologia dell'ospedale di Livorno." Master thesis, University of Trieste 2016.

# LASER WELDED INCONEL ROTOR BLADES FOR TIP-JET HELICOPTER

Nebojša Kosanović<sup>1</sup>, Nenad Kolarević<sup>1</sup>, Marko Miloš<sup>1</sup>

<sup>1</sup> University of Belgrade, Faculty of Mechanical Engineering, Kraljice Marije 16, 11120 Belgrade, Serbia. e-mail: [nebkos@gmail.com](mailto:nebkos@gmail.com)

## 1. Introduction

On a tip-jet helicopter [1], hot cycle system transmits power pneumatically by lightweight ducting and a nozzle that directs high-energy gas from a turbine engine to the rotor blade tips to drive the rotor for helicopter flight.

This requires a unique solution for the rotor blade of the tip-jet helicopter that will permit distribution and acceleration of hot gasses from jet engine through its construction.

Blades are developed to withstand additional internal overpressure loads at very high temperatures, up to 700°C, with strict aerodynamic demands. The idea was to use Inconel sheets, laser welded as basic material, and outside flow of cold air for cooling and reducing pressure loads.

Numerical simulations are used to calculate stress-strain state of rotor blade structure. After that, blades are produced and experimentally verified in helicopter hovering tests.

## 2. Blade design

Design of rotor blades for tip-jet helicopter is unlike any other conventional helicopter blade design. A conventional blade would, in the most cases, use composite materials and some sort of cross-section optimization [2]. In our case, the blade cross-section is very different because it needs to ensure efficient flow of hot gasses inside the blade.

To accommodate this difference in design, instead of using one spar at 25% of airfoil chord, we used two beams located as far as possible from each other (Fig. 1.). This allowed for a large hole in the middle of the blade needed for ducting of hot gasses. Additional stiffeners at the thickest part of the blade cross-section provide required structural strength. Also, during rotation a centrifugal force forces cold air in the small area between the stiffener and the blade skin and reduces thermal load of the blade.

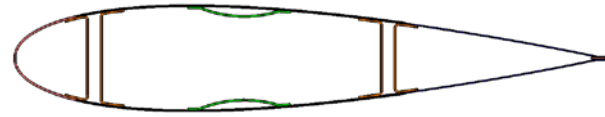


Fig. 1. Blade cross-section

Aside from the difference in the cross-section, the blade also must have a different tip and root (Fig. 2.). At the tip, there is a nozzle assembly (fig. 3), and at the root there is a blade mount with ducting and inlet for hot gasses.

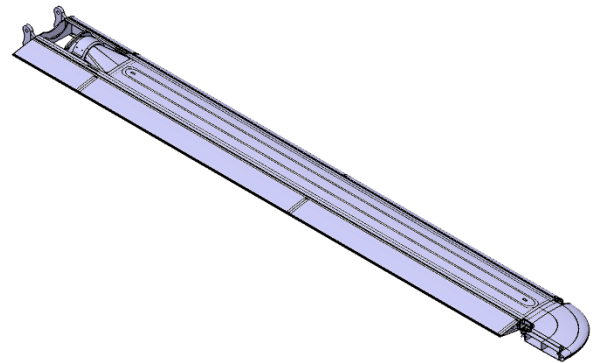


Fig. 2. Blade 3D model

### 2.1 Nozzle design

The nozzle at the end of the blade could be considered as an engine nozzle since its area directly influences the performance of the engine. The area of nozzle exit is too small for easy engine start, when a bigger nozzle is needed, so we used a variable spring loaded nozzle mechanism actuated by centrifugal force. When the engine starts, helicopter's rotor is stationary and the nozzle area is kept maximal. As the power increases, the rotor starts to move and rpm rise and centrifugal force increases, which reduces the nozzle area and increases power. Equilibrium is obtained at operational rotor speed when the nozzle area is minimal and the thrust is maximal. This design allows for easier and more reliable engine starts and smoother operation of propulsion system.



Fig. 3. Blade tip with nozzle

### 3. Manufacturing processes

The blade is completely made from thin Inconel sheets that were laser welded. The welding was done using special tools to hold the sheet metal in place and to ensure adequate quality and repeatability, especially because there need to be two same blades for one rotor. Fig. 4. shows the middle section of the blade at the initial stage of manufacturing process.

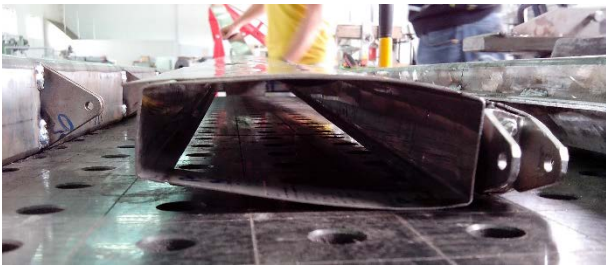


Fig. 4. Laser welding of blade in special tool

### 4. Design validation

After series of tower tests (Fig. 5.) [3], all data relevant for analysis of rotor lift characteristic was extracted and compared with theoretical calculations. Some parameters were recalculated by using experimental data [4].



Fig. 5. Tower test

The tests show that the drag on  $0^{\circ}$  angle of attack is smaller than theoretical value of NACA0018 airfoil [5] which means that our airfoil is thinner than the theoretical (Fig. 6.).

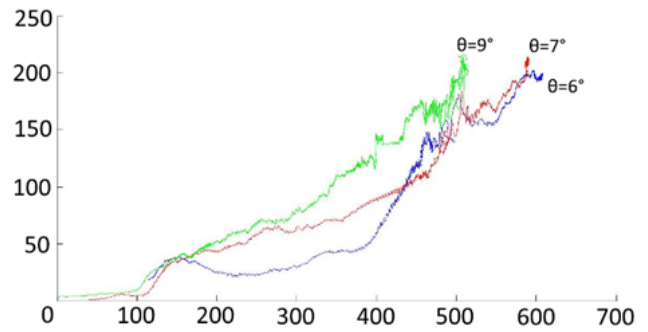


Fig. 6. Tower test results

### 5. Remarks

All Blades proved good for test purposes, because of their toughness and reliability, and aerodynamic characteristics are better than we expected. However, the production process is very long and complicated with a possibility of repeatability difficulties, which could be solved only by using different production methods and using Inconel sheet duct only as an insert.

### Acknowledgements

Design and tests were performed at EDePro d.o.o. in Belgrade as a part of UAV tip jet helicopter development program.

### References

- [1] J. Watkinson, the Art of the Helicopter, Elsevier Butterworth-Heinemann, 2004.
- [2] Jae Hoon Lim, Sang Joon Shin, Young Jung Kee, Optimization of Rotor Structural Design in Compound Rotorcraft with Lift Offset, Journal Of The American Helicopter Society 61, 012005 (2016).
- [3] N. Kosanović, M. Miloš, B. Jojić, Testing of tip-jet helicopter rotor lift force, Proceedings of the 33th Danubia-Adria Symposium on advances in experimental mechanics, Portorož, Slovenia, 2016
- [4] N. Kolarević, N. Davidović, P. Miloš, B. Jojić, M. Miloš, Experimental determination of light helicopter rotor lift characteristics with tip-jet propulsion system, Proceedings of the 30th Danubia-Adria Symposium on advances in experimental mechanics, Primošten, Croatia, 2013, pp. 268-269
- [5] I. Abbott, A. Doenhoff, L. Stevens, Summary of Airfoil Data, NACA REPORT No. 824, 1945.

## STRAIN GAUGE MEASUREMENT OF PROPELLER BLADE VIBRATION DURING OPERATION ON AIRCRAFT DIESEL ENGINE

Jindřich Rosa<sup>1</sup>, Jan Cagán<sup>2</sup>

<sup>1</sup> Aerospace Research and Test Establishment, Beranových 130, 199 05, Prague, Czech Republic.  
E-mail: [rosa@vzlu.cz](mailto:rosa@vzlu.cz)

<sup>2</sup> Aerospace Research and Test Establishment, Beranových 130, 199 05, Prague, Czech Republic.  
E-mail: [cagan@vzlu.cz](mailto:cagan@vzlu.cz)

### 1. Introduction

The propeller propulsion unit is still the most effective way to drive light sport and tourist aircraft for which high initial thrust, steep climbing, minimum fuel consumption and low operational costs are requested. The limit is no very high flight velocities, in comparison with jet business planes. Such airplanes equipped with a reciprocating spark ignition engine have been developed to perfection practically during all century of history of flying. But another pressure on reducing of consumption and emissions has been still exerted. The innovative using of a reciprocating engine based on diesel cycle is one of possible way. The fuel for this kind of engines is kerosene oil – in comparison with common aviation gasoline (AvGas) the low consumption means longer range of flight and other substantial advantage is its availability on each airports practically because the same fuel is used for jet airplanes. For these reasons various attempts with diesel engines has been performed for all history of aviation, but on the field of so called general aviation they have not been very successful. Of course, there are some disadvantages and problematical aspects. It is well-known that these types of engines generate higher levels of torque oscillation on the shaft during their operation in comparison with the AVGAS engines and this fact has to be respected during design of the propulsion unit. Especially for maintenance of contemporary levels of reliability and safety it is necessary to regard the mentioned factors during choice of an appropriate propeller, let us say the propeller should be designed specially.

The Aerospace research and test establishment (VZLU) has took part in an innovative project focused on design of such specific aircraft propeller. Next to the demand on a structure capable to withstand the increased levels of

vibratory excitation, the aerodynamics of the propeller will be optimized for the diesel conditions of operation, i.e. lower rotational speed. The other advantage of such solution will lead to lower noise of the propulsion unit, because the contribution of aerodynamic noise of the propeller is often more than half of the total output of aircraft noise.

The French engine SMA SR305 is an air and oil cooled flat four-cylinder aircraft engine, operating on the four-stroke diesel cycle with direct fuel injection into the cylinder. It is supplied with air by a turbocharger via an intercooler. The operation is controlled by an electronic system of the Engine Control Unit nowadays, of course. A propeller is direct driven and its maximal rotational speed is limited up to 2200 RPM. The 230E engine version was certified by EASA and FAA in 2010.

The Horizon 2020 / Clean Sky 2 project is aimed to verification of behavior of the engine – propeller dynamic system with the main target to design a propeller together with appropriate solutions. The leader of the consortium of participants for this project is the company Woodcomp Propellers. As the first step the vibration survey of a common propeller type mounted on the SR305 engine was assumed.

### 2. Methods of measurement

Strain gauges are the only one method of realization of measurement on the rotating propeller in practice. Recently, some attempts of use of optical means of measurement have been done, but these experiments are still under development, usually on the ground operation only because of extent devices. The main advantage is a complex vibration scan of all propeller blades. While the strain gauges provide loading data only from small areas of their grids and so their number

depending on purpose of measurement can be considerable.

The key part of the measuring chain is a device for transmission of measured signals from rotating part to a stationary base. In the past, contact slip-rings were used. Nowadays, wireless telemetry systems are preferred because of their high noise immunity. Another reason is the measurement on the single-engined aircraft equipped with a tractor propeller can be realized, as there was an invincible problem in former time. Digital data acquisition devices must provide an appropriate rate of sampling, because various components of the propeller oscillation can be in the range up to 1000 Hz. VZLU uses a Kraus MT-32 system.

### 3. Tests and evaluation

The Woodcomp KW-15 type is three-bladed propeller with hydro-mechanical control of blade angle settings for constant-speed operation. It is intended for typical engine applications in general aviation: The AVGAS engines of Lycoming or Continental with power up to 300 HP and rotational speeds up to 2700 RPM. The prototype has been retained as the firm testing propeller equipped with strain gauges for ever and so it was used as an initial propeller for the first testing of the SR305 diesel engine. The vibration survey measured on the propeller blades was performed on the Woodcomp ground testing station – a special bench embedded in a wind tunnel.



**Fig. 1.** KW-15 propeller equipped with strain gauges and mounted on SR305 diesel engine during tests.

The evaluation of the measured signals contains both over-all values of strain oscillation (Fig. 2) and spectral decomposition of the signals to verify levels of vibration frequency components caused by various exciting effects with their typical

frequencies. So called Campbell diagram serves to detect possibility of resonances.

### 4. Conclusion

The measurements and their evaluations described shortly above are routine operations for the VZLU Aircraft Propeller Testing Laboratory in principle, but working on the new kind of engine characterized by different behavior is an appealing challenge.

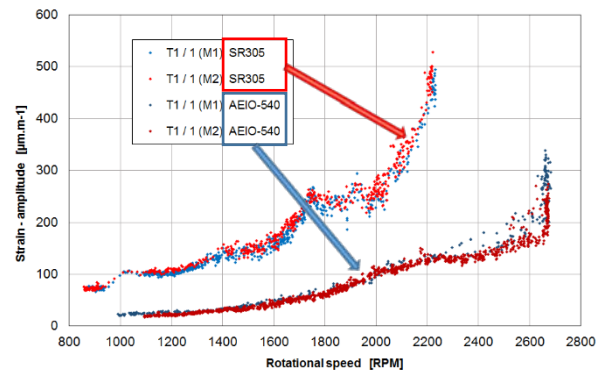


**Fig. 2.** Comparison of dynamic loading measured in T1 strain gauge position on the blade root for operation on diesel SR305 and Lycoming AEIO-540 engines.

The results of the measurement of propeller blade vibration on diesel SR305 engine was compared with the operation of the same propeller on a six-cylinder spark-ignition engine of Lycoming AEIO-540 type. The comparison with a four-cylinder AVGAS engine with similarly close power (as the tested SR305 engine) would be more interesting, but unfortunately, there are no relevant data in our database.

### Acknowledgements

This project has received funding from the Clean Sky 2 Joint Undertaking under the European Union's Horizon 2020 research and innovation programme under grant agreement No 714030.

### References

- [1] Miller, M.F., Wind-tunnel vibration tests of dual-rotating propellers, NACA report ARR No. 3111, National Advisory Committee for Aeronautics, 1943.
- [2] Dorshimer, R.C., Aircraft propeller vibration measurement system, FAA report No. NA-69-23, Federal Aviation Administration, 1969.

# A CONCEPT FOR AN AERIAL BASED LANDFILL MONITORING SYSTEM

Niels Paul, Dino Hüllmann, Harald Kohlhoff, Patrick P. Neumann

<sup>1</sup> Bundesanstalt für Materialforschung und -prüfung (BAM), Unter den Eichen 87, 12205 Berlin, Germany. E-mails: [niels.paul@bam.de](mailto:niels.paul@bam.de), [patrick.neumann@bam.de](mailto:patrick.neumann@bam.de)

## 1. Introduction

The paper at hand introduces a functional UAV for mobile robot olfaction tasks, namely gas source localization and gas distribution mapping. The remote gas sensing unit is a newly developed lightweight Tunable Diode Laser Absorption Spectroscopy (TDLAS) sensor, attached to a gimbal with three degrees of freedom (DOF), which enables the UAV to perform plume reconstruction and localization of gas sources. The systems software is based on the Robot Operating System (ROS).

## 2. Background

Methane ( $\text{CH}_4$ ) is a colorless and odorless gas, which is extremely flammable and forms an explosive mixture with air at concentration levels from 5%<sub>vol</sub> to 15%<sub>vol</sub>. For instance, it is generated at landfill sites by decomposition of organic waste.

To measure  $\text{CH}_4$  in industrial areas or on landfills ground-based as well as aerial solutions are researched. Also the deployed sensing units vary from in-situ sensors like metal oxide (MOX) sensors to TDLAS sensors [1]. The latter measure the integral concentration along a laser beam. Based on the absorption along the path, the concentration of a certain gas can be calculated. The laser has to be restricted to a small range of wavelengths, to make them less susceptible to other molecules, changing temperatures or humidity [2].

The gas sensor will be attached to a proprietary developed gimbal, using sensor fusion to control its orientation. Experiments with proprietary gimbal solutions already showed satisfactory results but also show potential for further improvement [3].

## 3. Gas Sensing Unit

The gas sensing TDLAS being in development will be able to measure as few as 1 ppm · m at a rate of 10 Hz. The measurement light is emitted

with a wavelength near of 1653 nm. In order to calculate the integral concentration along the path of the beam the sensor uses the Beer-Lambert-Law. Its computed data is transmitted via I<sup>2</sup>C bus.

## 4. System Setup and Kinematics

The whole system in general consists of a UAV platform, an attached gimbal carrying inter alia the TDLAS sensor, and at least one computing unit. The whole system weighs less than 3.6 kg.

As the central computing unit an Intel<sup>®</sup> Joule is deployed, providing sufficient computing power, GPIOs, UART, and I<sup>2</sup>C.

The currently used aerial platform is manufactured by DJI. The onboard computing unit is able to communicate with a SDK provided by DJI in order to control the UAV, i.e. pilot waypoints or receive flight data. The latter includes the UAVs position, measured via GPS, as well as its orientation, measured by an inertial measurement unit (IMU). Both, the UAV's flight controller and the Intel compute module, are connected via UART.

The gimbal is independent of the aerial platform. To allow for compensating all three DOF of the UAV, the gimbal also has three DOF. It carries the TDLAS Sensor, a Lidar Sensor for distance measurements, an IMU, and a lightweight USB 3.0 camera, which is able to capture UXGA Videos with up to 40 fps. The camera is used for visual servoing. The control algorithms take the gimbal's absolute position into account, which is measured by merging IMU and visual odometry data. By combining these information with the flight data and the distance measurements of the lidar sensor, a precise description of the measurement is possible.

To avoid a gimbal lock, the orientation of both the UAV and the gimbal are defined as unit quaternions  $\|\mathbf{q}\| = 1$ . The control algorithms are consequently based on quaternion rates. The gimbals speed control is programmed using the spherical linear interpolation (SLERP) algorithm

[4]. The autonomous navigation or gimbal control is thus computed through forward kinematics, starting from a point of interest in the ground coordinate frame (see figure 1).

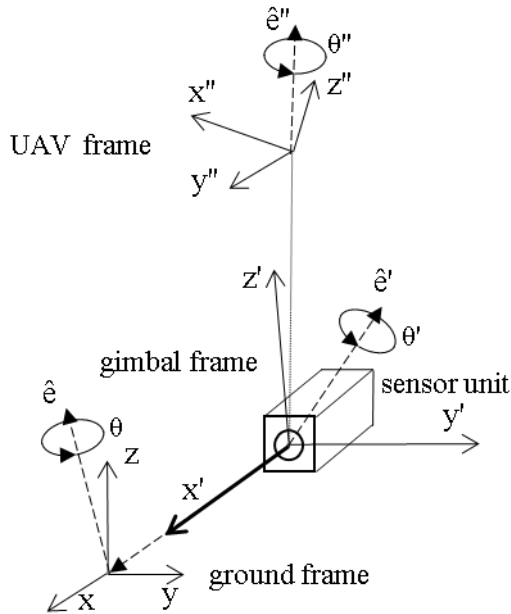


**Fig. 1.** The sensor orientation characterized by the UAV's orientation and its initial coordinate system

The lidar sensor mentioned before is furthermore used to perform simultaneous localization and mapping (SLAM). The odometry data is composed by estimating the UAV's position and orientation as well as the gimbal's orientation.

The UAV is controlled via a groundstation, where the missions are planned and all collected data is evaluated. Missions consist of waypoints as well as sensing procedures, including i.a. the gimbal's orientation. Since algorithms for tomographic plume reconstruction are computationally intense, these calculations are executed by the groundstation. Based on these results, missions can be planned autonomously and online.

## 5. Experiments

The experiments will take place at the BAM Test Site (BAM-TTS). Several different scenarios are to be carried out, including fan based gas discharging and visual ground truth motion.

The aim by using the latter is to measure the error in the UAV's pose and consequently the deviation in the ground frame. Therefore, the UAV

measures predefined points of interest from different given waypoints while being recorded. In the post processing, the pose error can be computed by merging the UAV's position, orientation, and camera data.

Furthermore, the TDLAS sensor is validated by measuring concentrations of gas from different angles, positions, and against different ground surfaces.

## 6. Evaluation

First experiments prove the ability to fly the drone autonomously and incorporate different sensor data. The sensor can be pointed at arbitrary spots with satisfyingly precision by manipulating the UAV's and the gimbal's orientation and position.

Detailed results of all experiments will be part of the conference presentation.

## 7. Conclusions

The lightweight aerial platform constitutes an enhancement in safely measuring  $\text{CH}_4$  concentrations. The implemented autonomous routines of the UAV are assisting the pilot while performing the measurement flights.

## References

- [1] Bonow, G., Kroll, A., Gas leak localization in industrial environments using a TDLAS-based remote gas sensor and autonomous mobile robot with the Tri-Max method. In: Robotics and Automation (ICRA), 2013 IEEE International Conference on. IEEE, 2013. pp. 987-992
- [2] Bergamaschi, P.; Harris, Geoffrey W. Measurements of stable isotope ratios ( $^{13}\text{CH}_4/^{12}\text{CH}_4$ ) in landfill methane using a tunable diode laser absorption spectrometer (TDLAS). *Global Biogeochemical Cycles*, 1995, 9. Jg., nr. 4, pp. 439-447. 1995.
- [3] Neumann, P. P., et al., Bringing Mobile Robot Olfaction to the Next Dimension – UAV-based Remote Sensing of Gas Clouds and Source Localization. In 2017 IEEE International Conference on Robotics and Automation (ICRA), Singapore, 2017.



- [4] Diebel, J., Representing attitude: Euler angles, unit quaternions, and rotation vectors, Matrix, 2006, nr. 15-16, p.1-35.

# A METHOD PRESENTED BY MEASUREMENTS TO PREVENT HARMFUL EFFECTS OF ICING FORMING ON GROUND WIRES OF HIGH-VOLTAGE TRANSMISSION LINES

Tamas Bagi<sup>1</sup>

<sup>1</sup> University of Óbuda, Department of Safety Sciences, 96/b. Bécsi Street, H-1034 Budapest, Hungary.  
E-mail: [bagi.tamas@elinor.hu](mailto:bagi.tamas@elinor.hu)

## 1. Introduction

Due to global warming-up impacts of climate changes could be observed in the National Hungarian Electricity Network. [3]

Extreme weather conditions (glaciations, extreme squall) are more common and their impacts are more significant that is why they need to be taken into consideration as well.

It is also confirmed by interruptions in the transmission and distribution network in 2013 and 2014. Consequently The Hungarian Transmission System Operator Company Ltd. (hereunder MAVIR Ltd.) requires an emergency plan to find solutions to avoid and prevent similar equipment failures in future. (havaria) [2]

In order to elaborate the incurred ideas more accurately it was necessary to perform measurements under authentic circumstances.

After coordinating with MAVIR Ltd. transmission line THE-Sajószöged 400kV has been administered by choice as it has been out of service and Tiszai Thermal Power Plant was put of service.

## 2. Measurement tasks

### 2.1 Measurement of induced current in ground wire of THE-Sajószöged 400 kV transmission line in case of zero-rated supply

In the course of preparing measurement staff of MAVIR Ltd. grounded the phase conductors of tower Nr. 2 to the body of the tower, as well as they prepared the 0,4 kV power supply from substation Nr.2 which is required for measurements in field 3B of Sajószöged substation 400/200/120 kV. Moreover we were informed about the conditions of field, transmission line and isolators.

In order to perform measurements in a successful and safe way we established two measuring teams. The first team stayed at the substation to ensure proper contacts, release of power, as well as it informed the second team measuring at the transmission line – about the induced current intensity.

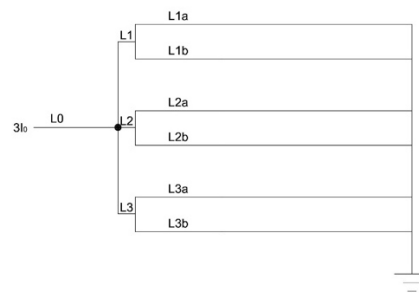


Fig. 1. 3F 0,4 kV power supply.

The transmission line team, according to previous agreement, established 3 measuring spots. One at the beginning of transmission line (between 2<sup>nd</sup> and 3<sup>rd</sup> tower); one in the middle of transmission line (between 11<sup>th</sup> and 12<sup>th</sup> tower); as well as at the end of transmission line (between 21<sup>st</sup> and 22<sup>nd</sup> tower)

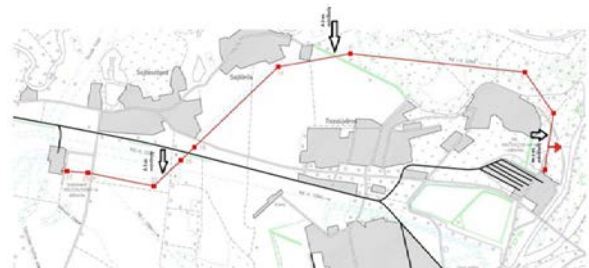


Fig. 2. Measuring spots [1]

The purpose of the measurement is to prove our assumption which is the following: in case the transmission line is supplied with zero sequence current, approximately 50-60% of the value of  $I_0$

supply power will be induced in the ground wire of the transmission line.

	$I_{VV1}$ [A]	$I_{VV2}$ [A]
Measured value	46,8 A	6,2 A
Measured value ( $I_0$ [%])	159,7 %	21,1 %
Issued value ( $3I_0$ [A])	88 A	

Tab. 1. Measurement results: bw. 2<sup>nd</sup> and 3<sup>rd</sup> tower [4]

	$I_{VV1}$ [A]	$I_{VV2}$ [A]
Measured value	19,9 A	16,6 A
Measured value ( $I_0$ [%])	67,9 %	56,6 %
Issued value ( $3I_0$ [A])	88 A	

Tab. 2. Measurement results: bw. 11<sup>th</sup> and 12<sup>th</sup> tower

	$I_{VV1}$ [A]	$I_{VV2}$ [A]
Measured value	15,1 A	13,9 A
Measured value ( $I_0$ [%])	51,5 %	47,4 %
Issued value ( $3I_0$ [A])	88 A	

Tab. 3. Measurement results: bw. 21<sup>st</sup> and 22<sup>nd</sup> tower

Measurements were performed with a clamp type MW 3500 with a measuring range of 2000 A using a platform provided by MAVIR Ltd.



Fig. 3. MW 3500



Fig. 4. Measuring spot



Fig. 5. Measuring spot

### 3. Summary

Based on the measurements it can be stated that according to previous assumptions – in case of 3I<sub>0</sub> supply (zero sequence) the amount of current induced in the protective conductor is about 50-60% of the I<sub>0</sub> supply power. Discrepancies could be measured only near the 2nd grounded tower. Furthermore, based on the measurements it can also be stated that in case of more ground wire the previously assumed current is induced in each ground wire of which values are approximately the same, symmetrical.

### Acknowledgements

I would like to thank Óbuda University and MAVIR Ltd. for allowing of measurements and preparations.

### References

- [1] MAHALIA database: THE – Sajószöged 400 kV
- [2] MAVIR: Az átviteli hálózat jegesedése 2015, Ember Gyula – Ivády Árpád, Dr. Morva György
- [3] Elektrotechnika, Volume 109. 2016/3, 5-7pp. ISSN:0367-0708



34th Danubia-Adria Symposium on Advances in Experimental Mechanics  
University of Trieste, Italy, 2017



[4] Measurement Report–2016.01.28. Óbuda  
University, Bagi Tamás – Bálint András – Horváth  
István

# HIGH PERFORMANCE FLYWHEEL TECHNOLOGY FOR ELECTRIC ENERGY STORAGE USING MAGNETIC BEARINGS

Stefan Gössinger<sup>1</sup>, Philipp Unterberger<sup>1</sup>, Friedrich Bleicher<sup>2</sup>

<sup>1</sup> researchTub GmbH, Seestadtstraße 27/3, 1220, Vienna, Austria.  
E-mails: [stefan.goessinger@researchtub.at](mailto:stefan.goessinger@researchtub.at), [philipp.unterberger@researchtub.at](mailto:philipp.unterberger@researchtub.at)

<sup>2</sup> Technische Universität Wien, IFT – Institute for Production Engineering and Laser Technology, Getreidemarkt 9/311, 1060 Wien, Austria. E-mail: [bleicher@ift.at](mailto:bleicher@ift.at)

## 1. Introduction

Flywheel energy storage systems (FESS) provide the typical energy storage application approaches, as exemplary presented in [1-2]: grid services, industrial applications and renewable integration. In the presented work, the development and implementation of a FESS is summarized. The design process as well as the manufacturing and assembly of the system were carried out by researchTub GmbH in collaboration with the Institute for Production Engineering and Laser Technology from the Technical University Vienna. Furthermore, a test rig was established, which provides the possibility to investigate and optimize the flywheel prototype under laboratory conditions.

## 2. Flywheel setup

When building a FESS, one of the main task is reducing losses, mainly caused by mechanical and aerodynamic friction. Therefore, it is common to apply a vacuum environment in combination with contact-free electromagnetic bearings, to overcome these major drawbacks. A general overview of the FESS highlights Fig. 1a. The rotor (blue) is supported by a bearing system (orange), consisting of one axial- and two radial supports. The axial bearing holds the rotor in levitated position, whereby an electro magnet in combination with permanent magnets generates the bearing force. However, the two radial bearings consist of contact free electromagnetic bearings and mechanical touchdown safety bearings, which support the rotor in case of an emergency shutdown, caused by a magnetic bearing failure. The rotor is spinning in a vacuum chamber (grey) under high vacuum conditions. The pressure level of  $10^{-6}$  mbar is generated by combining a rotary vane pump and a turbomolecular pump. The rotor material is high-strength forged steel, normally applied in the field

of power generation machinery. A customized synchronous motor generator (green) with embedded magnets drives the system. Tab. 1. resumes a selection of the technical main data of the actual FESS configuration.

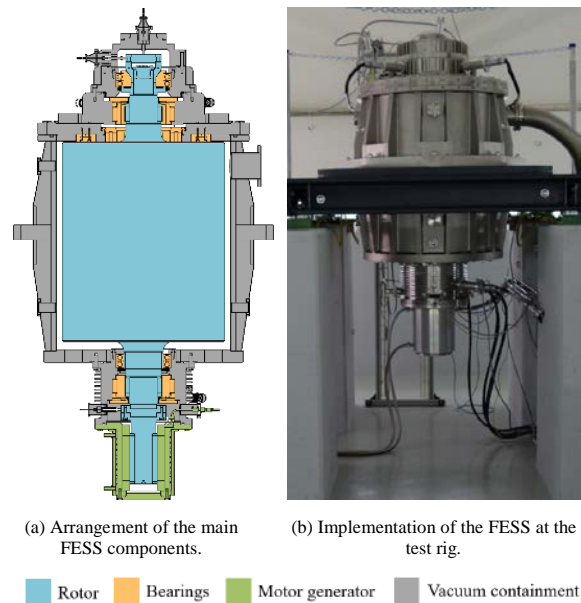


Fig. 1. Flywheel Energy Storage System (FESS).

Rated power	20	kW
Capacity	20	kWh
Power/ Capacity ratio	1	-
Rotor mass	2.200	kg
Length/ Diameter ratio	1,23	-
Maximum speed	> 10.000	rpm
Minimal bearing air gap	0,15	mm

Tab. 1. Selection of the technical main data.

## 3. Flywheel design process

The design process of a FESS represents a multidimensional and multidisciplinary optimization problem. Describing the complex design process with regard to an optimized mechanical solution in conjunction with cost optimization and grid integration, would go

beyond the scope of this paper. However, the basic design task is shortly described following. The main principle of a FESS is to store energy by a rotating mass, characterized by its moment of inertia  $I$  and its angular speed  $\omega$ :

$$E_{kin} = \frac{1}{2} I \omega^2 = \dots = \frac{1}{4} \rho \pi \omega^2 l R^4 \quad (1)$$

The right side of Eq. (1) represents the solution for the specific case of a thin disk with  $l \ll R$ . Further, the maximum mechanical stress is of interest [3]:

$$\sigma_{max} = C_1 \rho \omega^2 R^2 \quad (2)$$

As can be concluded from the stated equations, the geometry, the stored energy and the occurring stress state of the gyrating mass can be described by four basic parameters: density  $\rho$ , speed  $\omega$ , disk thickness  $l$  and radius  $R$ . Thereby, the radius has a stronger influence on the kinetic energy, with the power of 4, as the rotating speed (power of 2), and both have the same strong influence on the stress state (power of 2). By exemplarily assuming a constant amount of energy, doubling the radius, reduces the rotating speed to  $\frac{1}{4}$ . Hence, the design process of the FESS considers a broad range of disciplines, e.g. rotor dynamics, vibration analysis, temperature field calculation, fracture mechanic analyses and also manufacturing boundary conditions, to name only a few. To meet these requirements, various analytical and numerical calculations were carried out to finalize the presented solution. For the numerical investigations, ANSYS Mechanical V16 was applied to perform the mentioned multidimensional and multidisciplinary calculations.

#### 4. Flywheel test rig

For prototype testing purpose, a customized test rig has been established in a former material testing bunker. This bunker provides a safe testing environment, for maximum speed tests, emergency shut down investigations, rotor drop tests, etc. Apart from the flywheel setup discussed above, multiple auxiliary systems had to be developed, e.g. the vacuum equipment, the motor generator cooling system, a condition monitoring system, as well as the control unit and control cabinet with electrical grid integration elements. Fig. 2a. shows the ground floor of the test rig with its control station (left), control cabinets (right) and the

bunker with its moveable ceiling elements (in the front). These elements provide an appropriate accessibility for the overhead crane during the assembly of the system when opened and as well as the mentioned safe testing environment when closed. In Fig. 2b. the test rig basement (bunker) is depicted, with the actual FESS configuration and its machine frame and machine foundation.



(a) Test rig ground floor.



(b) Test rig basement (bunker).

Fig. 2. Impressions of the FESS test rig.

#### 5. Conclusion and Outlook

This paper presents the structural approach, basic considerations and a test rig description for a FESS developed and established. The presented FESS has already been commissioned and actually, endurance tests are being performed. Based on the test findings, it is intended to elaborate optimization potentials and to pave the way for further improvements with the final target of establishing a system ready for market entry.

#### References

- [1] Bai J.G., Zhang X.Z., Wang, L.M, A Flywheel Energy Storage System with Active Magnetic Bearings, Energy Procedia, 16, 2012. pp. 1124- 1128.
- [2] Genta, G., Kinetic Energy Storage. Butterworths & Co, 1985.
- [3] Dubbel, H., Taschenbuch für den Maschinenbau. Springer Berlin Heidelberg, 2007.

# CHATTER DETECTION AND AVOIDANCE USING A SENSORY TOOL HOLDER

Paul Schörghofer<sup>1</sup>, Friedrich Bleicher<sup>1</sup>, Thomas Weiler<sup>1</sup>, Christoph Habersohn<sup>1</sup>

<sup>1</sup> Technische Universität Wien, IFT – Institute for Production Engineering and Laser Technology, Getreidemarkt 9/311, 1060, Vienna, Austria. E-mail: [schoerghofer@ift.at](mailto:schoerghofer@ift.at), [bleicher@ift.at](mailto:bleicher@ift.at), [weiler@ift.at](mailto:weiler@ift.at), [habersohn@ift.at](mailto:habersohn@ift.at)

## 1. Introduction

In a modern, networked production, the possibility of optimizing the machining process can be achieved by the use of work piece- and tool-side sensors and actuators. Thereby, the application possibilities of sensors and actuators move closer to the process due to a progressive reduction of their size. The use of intelligent tool systems allows recording data of the machining process near the cutting zone and applying them for in-process control of process parameters.

## 2. Sensor implementation

Machining processes with long and slender tools or with minor wall thickness of the work piece can lead to instabilities, which can result in chatter marks on the work piece surface as illustrated in figure 1.

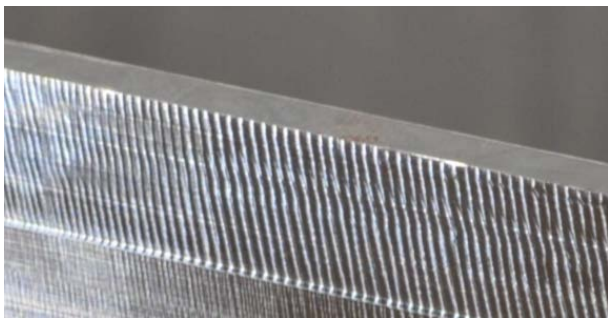


Fig. 1. Chatter marks on a thin-walled work piece.

The most vivid form of chatter is the so-called regenerative chatter effect. Self-excited vibration can occur by cutting of wavy surfaces, which are generated by the previous tool rotation. This has direct impact on the cutting depth. The crossing of small defects in the work piece surface can then lead to the destabilization of the milling process [1]. In order to avoid dynamic instabilities or process failures a sensor integration for a tool holder SK 45 was developed. The approach for this sensor system integration attached on the tool

holder is to gain more detailed process information compared to e.g. the sensing of the spindle engine power and therefore, be able to detect chatter vibrations in an early stage. Figure 2 depicts the sensor system and the sensor signal receiving unit. Small capacitive sensors with single sensing axis have been chosen for this solution, which can be implemented in in three different slots for vibration measurement in radial, axial or tangential direction. An analogue radio transmitter proceeds the vibration data out of the rotational system to the receiver unit. The antenna of the transmitter is positioned alongside the outer surface of the housing in the shape of a cylindrical ring. The system is sealed and can therefore be applied with cooling lubricant.

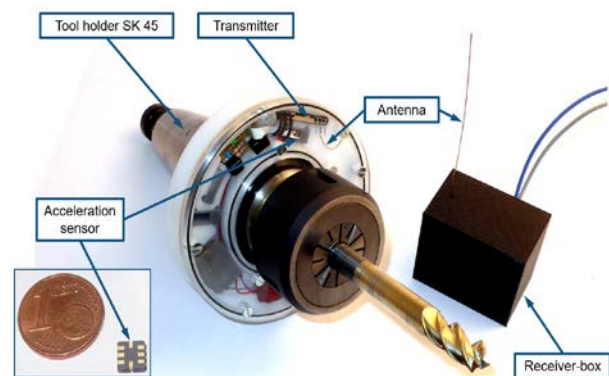
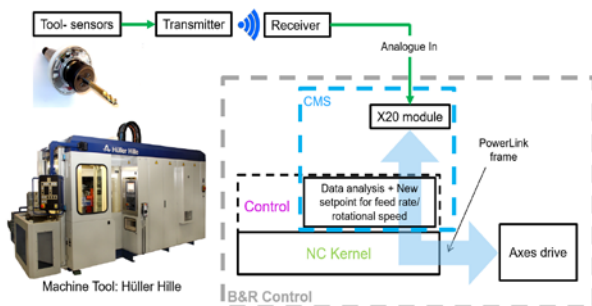


Fig. 2. Measurement Ring and receiving unit.

## 3. Adaptive control of cutting parameters

A condition monitoring system (CMS) was implemented in a B&R control system of a Hüller Hille machine tool. Figure 3 illustrates this application with the data flow from the sensory system to the machine tool control system. The output of the received vibration data is forwarded to the CMS in which algorithms are used to analyze the data with respect to process instabilities or process failures. The analogue signal output of the receiver conforms the interface to the machine tool control system in this

application. This test rig represents a specific case of implementing a condition monitoring system in a machine tool control system. Due to a development project within a collaboration between the IFT and the control system provider, it was possible to integrate a CMS directly into the control system. This solution can act as a faster opportunity to initiate countermeasures in the machining process compared to an external CMS. Other control systems do not open the possibility of a direct integration of a CMS. In such cases, the data analysis has to be conducted in an external evaluation unit. Therefore, the time to initiate countermeasures increases and a reaction of the axis drives on detected chatter vibration occurs more slowly.



**Fig. 3.** Coupling of CMS to control system.

In order to react correctly on chatter vibrations, Figure 4 has to be considered, which shows a stability lobe diagram. A stability lobe diagram depicts that specific combinations of spindle speed and cutting depth lead to instable machining processes, which can result in chatter vibrations [2]. By reducing the feed rate or shifting of the spindle speed, it is possible to move the process out of instable into stable machining zones.

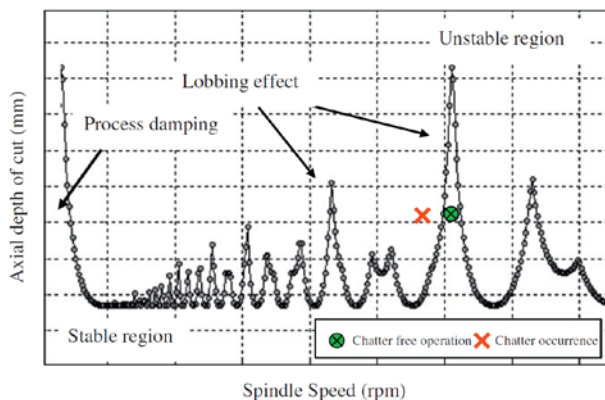


**Fig. 4.** Stability lobe diagram [2].

With the realized test set up shown in Figure 3 it was possible to achieve an automated adaption of

the feed rate if an exceedance of a predefined vibration limit can be detected by the measuring system. Therefore, this experiment reflects the approach of an automated reaction of the machine tool based on vibration data of a sensory system. Due to the implementation close to the cutting zone even vibrations of small tools can be controlled and monitored.

#### 4. Remarks

As a result of the experimental evaluation the following remarks and findings can be summarized:

- The approach of the presented sensory system integration attached on a tool holder enables to acquire process vibration data near the cutting zone.
- A condition monitoring system (CMS) analyzes the received data of the integrated sensor system in order to detect process instabilities or process failures. However, this opens the opportunity for process documentation and monitoring.
- By coupling the CMS with the machine tool control system, countermeasures can be initiated to stable the machining process and thus an in-process-control will be introduced.

#### 5. Outlook

A miniaturization of the measurement system could lead further towards an industrial application. Aside from the detection of instable milling processes, the prevention of drill breakage for drills with  $D < 3$  mm could be an area of application. Strategies of how to initiate the right countermeasures to stable an instable processes needs further research work.

#### Acknowledgements

The authors want to express the appreciation and thanks to the Machine Tool Technologies Research Foundation (MTTRF) for supporting the research work in the field of production engineering.

#### References

- [1] Denkena B., Litwinski, K.M., Ratterschwingungen an Werkzeugmaschinen. Institut für Fertigungstechnik und Werkzeugmaschinen, 2010.



- [2] Quintana, G., Ciurana, J., Chatter in machining processes: A review, International Journal of Machine Tools & Manufacture, 2011. pp. 365-366.

## POSSIBILITY OF APPLICATION OF THE SIMULATION BASED ASSESSMENT METHOD IN MODELLING OF STRUCTURES

Petr Kesl<sup>1</sup>, František Plánička<sup>2</sup>

<sup>1</sup> University of West Bohemia in Pilsen, Faculty of Applied Sciences, Department of Mechanics, Univerzitní 8, 306 14 Plzeň, Czech Republic. E-mail: [pkesl@kme.zcu.cz](mailto:pkesl@kme.zcu.cz)

<sup>2</sup> University of West Bohemia in Pilsen, Faculty of Applied Sciences, Department of Mechanics, Univerzitní 8, 306 14 Plzeň, Czech Republic. E-mail: [planicka@kme.zcu.cz](mailto:planicka@kme.zcu.cz)

### 1. Introduction

The article deals with an ability to assess the reliability of structural element on its model by means of the simulation based reliability assessment SBRA Method. The aim is to present a possibility of judgement of probability of failure of real component on its model. A simply supported steel beam of rectangular cross section area loaded by a simple concentrated force  $F$  (Fig. 2) was taken into account as a model of real steel beam. That model was available. That's why that opposite approach was chosen when for the existing model actual corresponding beam was searched using rules of modelling. Using modelling rules the bending stresses were determined in the real beam using experimentally determined strains and stresses in the model. Stresses of steel beam and its model were determined using SBRA Method too and that method was used for judgement of their probability of relatively simple failure. Obtained results were compared.

The simulation Based Reliability Assessment Method is a probabilistic method using the Monte Carlo simulation [1, 3]. Substance of that method consist in repeated calculations of relatively simple equations, where variables as dimensions of the body, mechanical properties, loads, etc. can be insert. That variables can be constant or defined by histograms, respectively. Probability of failures of model and real beam were determined using Anthill software [3].

Modeling of engineering problems can be very often a way to solve them. It is generally based on the conditions

$$(\pi_i)_S = (\pi_i)_M, \quad i = 1, 2, \dots, m \quad (1)$$

where  $\pi_i$  are so called dimensionless parameters for structure (subscript  $S$ ) and model (subscript  $M$ ).

$$\pi = x_1^{e_1} x_2^{e_2} \dots x_n^{e_n} \quad (2)$$

If the solved problem depends on  $n$  variables  $x_i$  (expressing physical, geometrical etc. quantities). Exponents  $e_i, i = 1, 2, \dots, n$  has to fulfil the condition of dimensionless of  $\pi$  terms, see [2].

$m = n - r$  represents number of independent  $\pi$  terms,  $r$  is rank of so called dimensional matrix, see [2]. There is assumed that solved problem is described by  $n$  physical quantities  $x_i, i = 1, 2, \dots, n$  containing  $k$  so called primary quantities with primary units  $[L_j], j = 1, 2, \dots, k$ . The necessary procedure is described in [2].

Probability of failure is guided by so called safety function, see Fig. 1.

$$P_{f(i)} = R_{(i)} - S_{(i)} \quad (3)$$

Where  $S$  is the load effect And  $R$  is the structural resistance. The probability of failure  $P_f$  of a body can be then expressed as a ratio between the number  $N_f$  of results that do not fulfil the defined before safety function and the total number of results that do not fulfil the defined before safety function  $N_f$  and  $N_t$ , is total number of results [1].

$$P_f = N_f / N_t \quad (4)$$

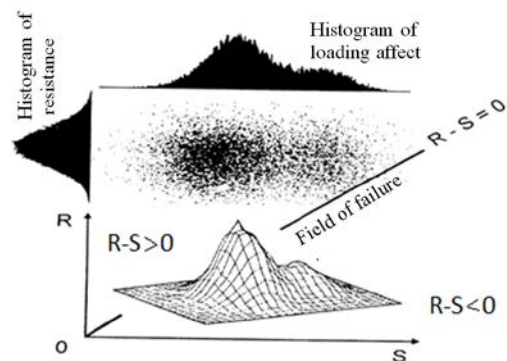


Fig. 1. Probability of failure.

## 2. Experimental results

The used steel model is stated in Fig. 2. Loading forces were  $F=100, 200, 300, 400, 450$  N. Strains were measured using electrical-resistance gages. Their positions are obvious in Fig. 2. Recorded values of strains and corresponding stresses are, in the Tab. 1.

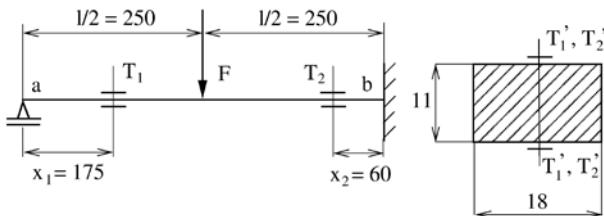


Fig. 2. Model of the beam.

To determine corresponding state in real steel beam length of the beam  $l=2500$ mm and rules of modelling were used and loading forces  $F_B$  and section modulus  $W_B$  were determined. Material of model and of real beam was the same therefore stresses in the model and in the real beam are the same, steel S235 with Young's modulus of elasticity  $E = 2,1 \cdot 10^5$  MPa, see the Tab. 1.

Model experiment	$F_m$ [N]	300	450
	$2\varepsilon_{1m} \cdot 10^{-3}$	0,225	0,33
	$\sigma_{1m}$ [Mpa]	47,25	69,30
	$2\varepsilon_{2m} \cdot 10^{-3}$	-0,165	-0,26
Beam	$\sigma_{2m}$ [Mpa]	-34,65	-54,6
	$F_B$ [kN]	7,5	11,25

Tab. 1. Results of the Modell and of the beam

$F_m$ [N]	300		
$F_B$ [kN]	7,5		
	MODEL exp.	SBRA-m	SBRA-B
$2\varepsilon_{1m} \cdot 10^{-3}$	0,225	-	-
$2\varepsilon_{2m} \cdot 10^{-3}$	-0,165	-	-
$\sigma_1$ [MPa]	47,25	45,190	45,202
$\sigma_2$ [MPa]	-34,65	34,289	34,195
$\sigma_{1Det.}$ [MPa]	45,2		
$\sigma_{2Det.}$ [MPa]	-35,82		

m - Model, B - Beam, Det. - beam determined

Tab. 2. Results of Modell and of SBRA simulation.

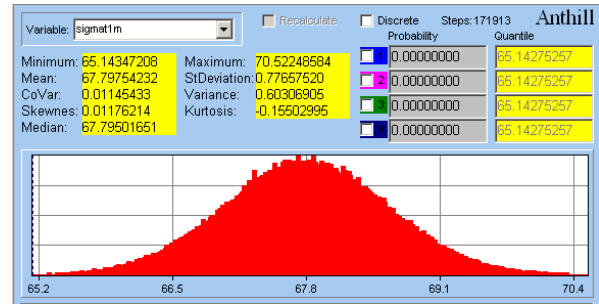


Fig. 3. The resulting stress  $\sigma_{1m}$  [MPa].

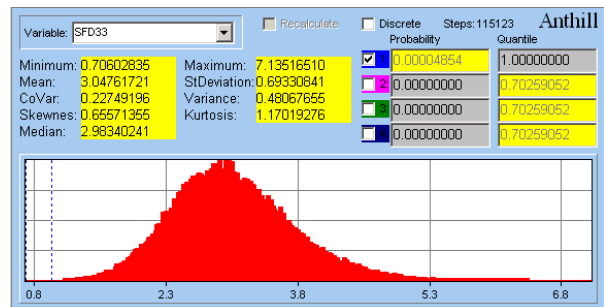


Fig. 4. Probability of failure  $P_f(i)$ ,  $SF(i)$ .

In Fig.3 there is for illustration presented histogram of the resultant stress of the model and in Fig. 4. histogram of probability of failure. Probability of failures of the beam determined using SBRA method were  $P_{f(i)B} = 4,8 \cdot 10^{-5}$  and for the model  $P_{f(i)m} = 4,103 \cdot 10^{-5}$ .

Obtained results show very good correspondence. It gives a sure possibility for determination of failure probability of structure to determine it using corresponding model.

### Acknowledgements

The research work was supported by the Project SGS-2016-038.

### References

- [1] Plánička, F., Šolc, M., Marek, P.: From Partial Factors Design to the SBRA Probabilistic Method, Acta Mechanica Slovaca Vol.15, No 2, 2011, ISSN 1335-2393, pp. 22-27.
- [2] Plánička, F., Krystek, J.: Dimensional Analysis and Modelling in Mechanics of Materials, Proceedings of 28<sup>th</sup> Danubia-Adria Symposium on Advances in Experimental Mechanics 2011, Siófok, Hungary, ISBN 978-963-9058-32-3, pp. 229-230.
- [3] [www.sbra-anthill.com/lit/publications](http://www.sbra-anthill.com/lit/publications).

## DEVELOPMENT OF THE ADAPTABLE ENERGY ABSORBERS FOR CAR CRASHES

Milan Růžička<sup>1</sup>, Nikola Schmidová<sup>1</sup>, Tereza Zavřelová<sup>1</sup>, Michal Vašíček<sup>2</sup>, Filip Zavadil<sup>2</sup>

<sup>1</sup> Department of Mechanics, Biomechanics and Mechatronics, Faculty of Mechanical Engineering, Czech Technical University in Prague. Technická 4, Praha 6, Czech Republic. Tel +420 22 435 56 05. Email: [Milan.Ruzicka@fs.cvut.cz](mailto:Milan.Ruzicka@fs.cvut.cz), [Nikola.Schmidova@fs.cvut.cz](mailto:Nikola.Schmidova@fs.cvut.cz), [Tereza.Zavrelova@fs.cvut.cz](mailto:Tereza.Zavrelova@fs.cvut.cz).

<sup>2</sup> Centre of Vehicles for Sustainable Mobility, Faculty of Mechanical Engineering, Czech Technical University in Prague. Technická 4, Praha 6, Czech Republic. Tel +420 22 435 24 98. Email: [Michal.Vasicek@fs.cvut.cz](mailto:Michal.Vasicek@fs.cvut.cz), [Filip.Zavadil@fs.cvut.cz](mailto:Filip.Zavadil@fs.cvut.cz)

### 1. Introduction

Passive safety of vehicle is one of the basic parameter defining the overall safety of the vehicle. It is determined primarily by the ability to protect the passengers in case of an unavoidable accident. It is given by ability of the structure (body) to absorb the kinetic energy of the impact by the conversion to potential energy in their deformation and/or damage. This ability is fixed at the present designs by the structure design (shape and choice of material). It is clear that such a construction meets safety requirements in different collision scenarios but in none optimally. It potentially means that cars are safe only in the cases of configured collisions that were considered during the design. There are unlimited amounts of real crash scenarios which show the need to adapt the design according to real crashes. Because of all these facts our intention is to develop composite beam that can adapt its force response as required by the actual situation. Fiber composite materials compared with conventional structural materials excel in their ability to absorb the damage energy and subsequent fragmentation.

Price of these materials is still quite high, which has prevented its wider application so far. Increased demand for electromobility and related requirement for better mass to absorbed energy ratio will nevertheless require their use. For further development, it is necessary to find reliable mechanism of damage initiation and completely understand the mechanism of fragmentation.

### 2. Searches

At the beginning of this project the searches were done. There are many possibilities how to influence the energy absorbers in the passenger

cars during the impact. We focused on methods, which has potential to affect the material response very quickly. There is the possibility of modification the properties of composite material using temperature. Thermoset and thermoplastic matrix could be used. Both can be affected by heat as is written in [1]. Another option is an infraction of the beam by controlled impacts circumferentially before the front impact during the vehicle crash. The suggestion is based on the results from the literature [2]. Here was confirmed that initiation of fragmentation is possible to achieve by a localized weakening before impact. Controlled impacts could cause both interruption of fibers and delamination of the composite material. Both can influence the stiffness of the absorber during impact. The suggested absorber might be impacted before compression in several (2-3) levels circumferentially.

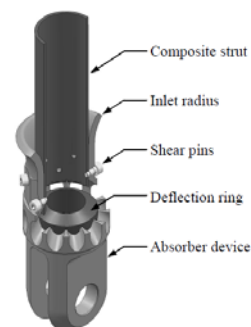


Fig. 1. Energy absorber device and components [3]

Next possibility is the construction of the absorber device that will be placed at the end of the composite beam and facilitate the initiation of fragmentation the composite beam in case of the crash. Device should have a form of a head with

holes from that the rupture materials goes through. This option is still used in the aerospace industry as is written in [3], see Fig. 1.

### 3. Experimental investigation and numerical simulation

The experiments to test these methods written above were designed. The all specimens have a shape of the composite tube and its length corresponds to size of the space in the real cars. The specimens are made from the eight layers of fabric prepreg (carbon fibers and epoxy resin). The dimensions of the beam and material is written in Tab. 1 below.

Length [mm]	170
Inner diameter [mm]	70
Thickness of the wall [mm]	3
Number of layers [-]	8
Material SIGRAPREG C W305 - TW2/2 - E323/42%	

Tab.1. The characteristics of the specimen

One simulation example of the absorber idea: Different configurations of the initiation damage (circular holes of varying size) along the circumference at the end of tested tube was chosen as the first realization.

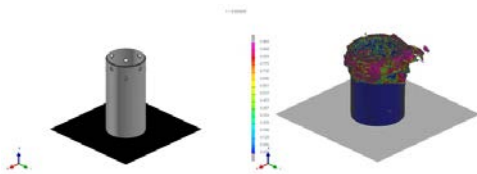


Fig. 2. FEM model of the configuration before and after the impact

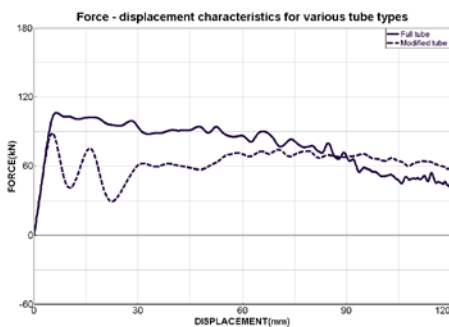


Fig. 3. Crash characteristics non-damaged and pre-damaged specimens

The position of the holes was numerically optimized and the test results were compared with the simulations performed by the Pam-Crash

software using multi-layer shell global fabric material model (MAT 131, PLY 7) and TIED interface with Pickett-Payen delamination model (MAT 303). The FEM model and results of simulations are depicted on Fig. 2 and Fig. 3. It can be seen that initiation damage can effectively modified the impact force (blue curve) comparing to non-damaged absorber (red curve).

### 4. Conclusions

The searches in the issue of vehicle safety were done. It was selected several different approaches to energy absorbers in car crashes. There are possibilities of the modification the properties of composite material using temperature, , infraction the beam by the controlled impact, or fixing the beam in the head with holes to initiate fragmentation of the composite material. All these methods will be tested in the further research. The first research was done on the composite tube, which was pre-damaged by circular holes along the circumference on the end of tube. Numerical calculations have shown a significant effect of location and diameter of the initiation damage (circular holes) on the absorbed energy. It is shown that various initiation damage configurations can be used for the solution of adaptive energy absorbers.

### Acknowledgements

Development of the adaptive composite materials and structures for crash applications SGS16/214/OHK2/3T/12

### References

- [1] Kwang-Hee Im, et al., Effects of temperature on impact damages in CFRP composite laminates. Composites. Part B, 2001, vol. 32, pages 669-682.
- [2] Troiani, Enrico, et al., Influence of Plying Strategies and Trigger Type on Crashworthiness Properties of Carbon Fiber Laminates Cured through Autoclave Processing., Journal of Mechanical Engineering. 2014, vol. 60, pages 375-381. [Online] [Citation: 30.11.2015]: [http://ojs.sv-jme.eu/index.php/sv-jme/article/view/sv-jme.2013.1506/pdf\\_20](http://ojs.sv-jme.eu/index.php/sv-jme/article/view/sv-jme.2013.1506/pdf_20).
- [3] Heimbs, S., et al., Composite crash absorber for aircraft fuselage. [Online] [Citation:

Commento [NS1]: Nevypustit?



34th Danubia-Adria Symposium on Advances in Experimental Mechanics

University of Trieste, Italy, 2017



30.11.2015] [http://www.heimbs-online.de/Heimbs\\_2010\\_CrashAbsorber.pdf](http://www.heimbs-online.de/Heimbs_2010_CrashAbsorber.pdf).

# PEG-IN-HOLE OPERATION USING A COBOT WITHOUT USING EXTERNAL SENSORS

Luca Debortoli<sup>1</sup>, Simona D’Attanasio<sup>2</sup>, Paolo Gallina<sup>1</sup>, Stefano Seriani<sup>1</sup>

- <sup>1</sup> University of Trieste, Department of Engineering and Architecture, Via A. Valerio 10, 34127, Trieste, Italy. E-mails: [luca.debortoli2@studenti.units.it](mailto:luca.debortoli2@studenti.units.it), [p.gallina@units.it](mailto:p.gallina@units.it) and [sseriani@units.it](mailto:sseriani@units.it)
- <sup>2</sup> Icam, Department of Electronics and Computer Science, 75 Avenue de Grande Bretagne, 31330, Toulouse, France. E-mail: [simona.dattanasio@icam.fr](mailto:simona.dattanasio@icam.fr)

## 1. Introduction

Collaborative robots, or cobots, represents nowadays the technological challenge of industrial robotics. Unlike traditional industrial robots, that perform fully automated task and have to be confined in a protected environment, cobots are designed to share the environment and the task with the human operator. This results in a reduction of physical constraints to the production. Moreover, cobots are also designed to be easy to program and use, drastically reducing the need of extra costs for equipment integrators and experts. It is for these reasons that the use of cobots can be attractive for medium and small companies, with a limited capacity of investment. On the other end, peg-in-hole insertion is one of the most common automated task to be performed by an industrial robot. This kind of operation usually requires the use of a force and/or torque sensor to control robot trajectory [1], [2], thus raising again the costs and the complexity of development. In this paper, we present the automation of an industrial peg-in-hole operation, without the use of external force or torque sensors. The cobot used for the study is an UR5 from Universal Robots, equipped with a standard RG2 gripper and a simple pvc adaptor manufactured with 3D printing. This robot is one of the less expensive cobot actually on the market; therefore, it does not integrate joint force sensors. Nevertheless, it is possible to recover the value of the force vector at the tool center point (tcp) and the torque value at each of the 6 joints. These values are calculated based on the motor internal current consumption. The following paragraph describes the method used to perform an operation, that is at present performed by a human operator.

## 2. Methods

The part that has been used is a mechanical part from Brovedani Group, that has to be inserted in

the corresponding sawtoothed hole, as illustrated in the left side of Figure 1.

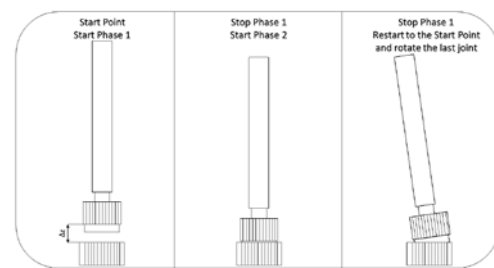


**Fig. 1.** Part configurations: initial (on the left), end of first phase (in the middle), stop dead (on the right).

The sawtoothed part has 48 tooth and the main risk during insertion is the stop dead of the part, causing the part blocking. Moreover, the part has a flat cylindrical first portion (at its bottom), that needs to be correctly centered in the sawtoothed hole before starting the real insertion. Therefore, the operation can be divided into 2 phases:

- a first phase, during which the part is centered and the robot performs a vertical descent till the very first contact among tooth (see middle part of Figure 1);
- a second phase, during which the robot continues the vertical descent and performs the part insertion.

During both phases, the UR5 performs a helicoidal descent: at each step the vertical z value is decreased of 1mm and the tcp frame is rotated of 2°. Several hundreds of insertion operations have been performed with the cobot and the following conclusions have been drawn:

- during the first phase, the value of the force vector applied at the tcp can be used to reliably monitor if the part is successfully centered;
- during the second phase, the variation of the shoulder torque of a step with respect to

the previous one can be used to monitor if the part has been successfully inserted.

The implemented algorithm is illustrated in Figure 2.

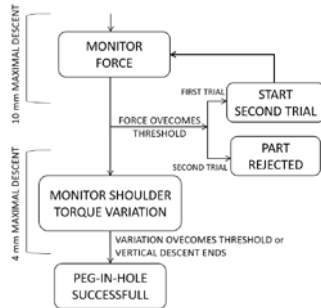


Fig. 2. Peg-in-hole algorithm.

During the first phase, the real-time force is compared to a threshold of 60N. This value, experimentally determined, is far enough to the UR5 maximal force limit of 150N and allows the detection of “bad” centered trials, as illustrated in the right side of Figure 1 and in the curves of Figure 3.

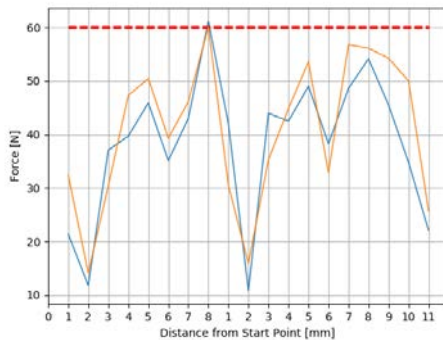


Fig. 3. The part is not correctly centered, the vertical force overcomes the limit threshold (horizontal line).

If it is the case, a second trial is performed (rise and again descent), at the end of which, either the part starts the second phase, or it is rejected. If the force threshold is not overcome, the first phase ends after a helicoidal descent of 10mm and the second phase begins. During this phase, the variation of the shoulder torque is calculated at each step and compared to a threshold, in percentage equal to 50%. This value has also been experimentally calculated: if the threshold is overcome, it means that the part has been successfully inserted and can be released and gripper opened (see curves of Figure 4). It is possible that the part is already correctly inserted from the beginning of the second phase: in this case, no important variation of the torque can be

observed and the descent continues because of the sliding of the grasping. It is for this reason that in any case, the descent is stopped at most after 4 mm, and the part is released.

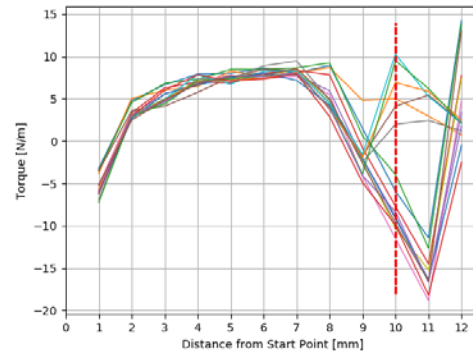


Fig. 4. The part is inserted after 12 mm of descent: 10mm for the first phase (vertical dotted line) and 2 more mm for the second phase.

### 3. Results

Over 1000 peg-in-hole operations, 967 have been successfully inserted, i.e. 96,7% of successful rate. Among these parts, 870 have been inserted at the first trial (90%). A second trial was needed for the remaining 10%. The overall mean time for an operation is 5,5 seconds. This value does not include part picking. The 3,3% of failure is certainly due to the lack of precision during part grasping, performed with a standard gripper and without any part positioning tool. The use of a customized tool will contribute to a vertically centered part grasping and will most likely improve the results.

### Acknowledgements

This research is the result of an international collaboration started thanks to the Erasmus program, between the Department of Engineering and Architecture of Trieste in Italy and the engineering school of Toulouse, Icam, in France.

### References

- [1] Y. Kim, B. Kim, J. Song, "Hole detection algorithm for square peg-in-hole using force-based shape recognition", *8th IEEE Int. Conf. on Automation Science and Engineering*, pp. 1074-1079, August 2012.
- [2] Kramberger *et al.*, "Transfer of contact skills to new environmental conditions," *2016 IEEE-RAS 16th International Conference on*



34th Danubia-Adria Symposium on Advances in Experimental Mechanics  
University of Trieste, Italy, 2017



*Humanoid Robots (Humanoids)*, Cancun,  
2016, pp. 668-675.

# ANALYSIS OF A SEGMENTED LOCKING RING FOR SHELL-BOTTOM CONNECTION IN PRESSURE VESSELS

A. Strozzi<sup>1</sup>, E. Bertocchi<sup>1</sup>, S. Mantovani<sup>1</sup>

<sup>1</sup> University of Modena and Reggio-Emilia, Department of Engineering Enzo Ferrari, Via Vivarelli 10, 41125, Italy. E-mail: [antonio.strozzi@unimore.it](mailto:antonio.strozzi@unimore.it), [enrico.bertocchi@unimore.it](mailto:enrico.bertocchi@unimore.it), [sara.mantovani@unimore.it](mailto:sara.mantovani@unimore.it)

## 1. Introduction

An approximate structural analysis is presented of a shell-bottom connection in which a locking ring, partially protruding from an annular slot machined in the vessel wall, supports the bottom loaded by the internal pressure. The ring is segmented into four parts, to permit assembling. The contact pressure between the ring and the slot lower face may be conveniently approximated. Simplified expressions of the internal forces within the ring are obtained.

## 2. The modelling of the split ring

This paper presents a structural analysis of a shell-bottom connection in which a locking ring, partially protruding from an annular slot machined in the vessel wall, supports the bottom loaded by the internal pressure. The ring is segmented into four parts, to permit assembling, Fig. 1. In comparison to a flanged bottom, this shell-bottom connection may be more quickly disassembled and, therefore, it is preferred when frequent maintenance is needed.

Previous analytical, numerical, and photoelastic studies [1-4] have evidenced the presence of highly concentrated reaction force peaks between the ring and slot lower face and at the ring sector extremities. Another peculiar aspect is the possibility of a contact between the ring and slot upper surfaces, as a consequence of the rotation of the ring cross section; previous studies have shown that in a ring with a square cross section the above contact does not occur, [4], whereas it may take place in a rectangular, radially elongated cross section, [5].

Based on the available studies, a simplified model of the contact force between the ring and the slot is developed, and the ring maximum internal forces are evaluated.

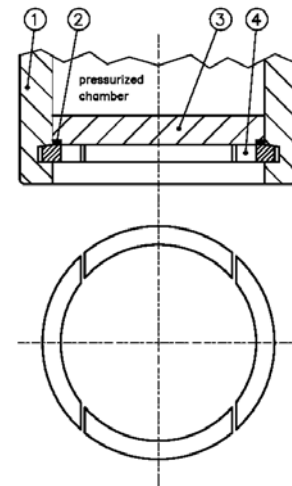


Fig. 1. The segmented locking ring.

## 3. Approximate analytical modelling

The segmented ring is loaded by a distributed pressure  $p_b$  (the index  $b$  stands for bottom) uniformly applied to the circular crown at the ring upper face, described by the radii  $R_i$  and  $R_p$ . The approximate contact reaction is assumed to be constituted by a) a distributed, constant, linear force  $F_c$  acting along the radius  $r_c$  defining the transition between the lower face of the slot and its filleted edge defined by  $R$ , and b) by two concentrated forces  $P_c$  applied to the contact extremities and at the radius  $r_c$ . Figures 2 and 3 clarify the meaning of the main symbols.

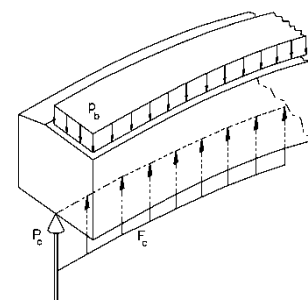


Fig. 2. The segmented locking ring.

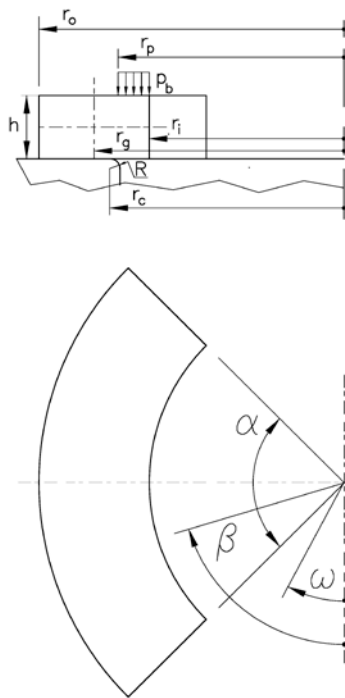


Fig. 3. The segmented locking ring.

The values of  $F_c$  and of  $P_c$ , Fig. 2, may be expressed in terms of the geometry of the locking arrangement, of the angular extent  $\alpha$  of the ring sectors, and of the contact pressure  $p_b$ , by imposing the vertical and rotational equilibrium conditions for the ring sector.

The expressions for  $P_c$  and  $F_c$  are:

$$P_c = \frac{p_b \alpha \sin \frac{\alpha}{2} (r_p - r_i) [3 r_c (r_i + r_p) - 2(r_i^2 + r_i r_p + r_p^2)]}{6 r_c \left( 2 \sin \frac{\alpha}{2} - \alpha \cos \frac{\alpha}{2} \right)} \quad (1)$$

$$F_c = \frac{p_b (r_p - r_i) \left[ 4 \sin \frac{\alpha}{2} (r_i^2 + r_i r_p + r_p^2) - 3 r_c \alpha \cos \frac{\alpha}{2} (r_i + r_p) \right]}{6 r_c^2 \left( 2 \sin \frac{\alpha}{2} - \alpha \cos \frac{\alpha}{2} \right)} \quad (2)$$

Having computed  $P_c$  and  $F_c$ , it is possible to formulate the analytical expressions of the maximum bending moment and of the maximum torque in the ring. The maximum bending moment occurs at the sector centre, whereas the maximum torque occurs at an intermediate section, whose angular position may be determined analytically.

For instance, the expression for the maximum bending moment  $M_{\max}$  is:

$$M_{\max} = \frac{p_b \alpha \left( 1 - \cos \frac{\alpha}{2} \right) (r_p - r_i) [3 r_c (r_i + r_p) - 2(r_i^2 + r_i r_p + r_p^2)]}{6 \left( 2 \sin \frac{\alpha}{2} - \alpha \cos \frac{\alpha}{2} \right)} \quad (3)$$

## 4. Conclusions

An approximate structural analysis has been carried out of a shell-bottom connection in which a locking ring, partially protruding from an annular slot machined in the vessel wall, supports the bottom loaded by the internal pressure. The ring is segmented into four parts, to permit assembling. The contact pressure between the ring and the slot lower face has been approximated in terms of a uniform contact pressure and of two concentrated forces acting at the ring-slot contact extremities. Approximate expressions of the internal forces within the ring have been obtained. The whole of the results indicates that, while the stresses in the segmented ring appreciably deviate from axisymmetry, the stresses in the vessel may be estimated with an axisymmetric model.

## References

- [1] Sciortino, L., Strozzi, A., Studio di un Particolare Dispositivo di Arresto del Fondo di un Recipiente in Pressione, In V Convegno Nazionale AIAS, Bari, 1977, pp.37/1-37/12.
- [2] Strozzi, A., Studio Fotoelastico di un Particolare Dispositivo di Arresto del Fondo di un Recipiente in Pressione, In VI Convegno Nazionale AIMETA, Genova, 1982, pp. 37-47.
- [3] Strozzi, A., Analisi Strutturale di un Dispositivo di Arresto del Fondo di un Recipiente in Pressione in Presenza di Contatto Recessivo, In XII Convegno Nazionale AIAS, 1984, pp. 325- 336.
- [4] Strozzi, A., Theoretical analysis of a segmented locking ring for shell-bottom connection in pressure vessels, J. Strain Anal. Eng. Des., 19(3), 1984, pp.153-160.
- [5] Chong-de, L., & Huston, R. L., Contact stresses in locking rings of pipeline closures—An iterative finite-element approach, Computers & Struc, 19(3), 1984, pp. 467-473.
- [6] Ryś, J., Computation of a plate-key closure of natural gas filter, J. Theor. Applied Mechs., 38, 2000, pp. 377-385.

# SURFACE PROPERTIES OF PLASMA NITRIDED TEMPERED STEEL

Dorina Kovács<sup>1</sup>, János Dobránszky<sup>2</sup>

- <sup>1</sup> Budapest University of Technology and Economics, Faculty of Mechanical Engineering, Department of Material Science and Technology, Műegyetem rkp. 3, 1111, Budapest, Hungary. E-mail: dorina@eik.bme.hu
- <sup>2</sup> MTA–BME Research Group for Composite Science and Technology, Műegyetem rkp. 3, 1111, Budapest, Hungary. E-mails: Dobranszky.Janos@eik.bme.hu

## 1. Introduction

Plasma nitriding, known also as ion nitriding is a kind of thermochemical surface treatment. Plasma nitriding provides an industrially important technique for modifying the surface layers of steels to improve their surface hardness and wear-resistance. [1-3]. The process enriches the steel surface with nitrogen to enhance its mechanical and tribological properties. The nitrided layer resulting from this thermochemical process comprises two sublayers: an outer compound layer and an underlying diffusion zone (layer). The compound layer is often composed of  $\epsilon$ -Fe- $_{2,3}$ N and  $\gamma'$ -Fe $_4$ N nitrides [1, 2].

## 2. Experimental procedure

Laboratory plasma nitriding equipment was built by own plan in the Department (Fig 1). The chamber of the equipment is a glass bell, which is perfectly suited to observe the plasma.

Plasma nitriding treatments were performed in DC plasma (Table 1). After completing the process, samples were slowly cooled in the chamber to temperatures below 100°C to minimize surface oxidation.

Parameters	
p (mbar)	3
T (°C)	490
t (hour)	4
gas [H $_2$ -N $_2$ ] (%)	50-50

Tab.1. Parameters of plasma nitriding

The material used in this study was C45 type steel. The samples ( $\varnothing 20 \times 8$  mm) were cut from a round steel which made by different type of plasma nitriding: DCPN (direct current plasma nitriding), ASPN (active screen plasma nitriding), ASPN+bias (active screen plasma nitriding with bias) [2]. The bias is a second voltage on the samples, which is 11% of the screen's voltage.



Fig. 1. Plasma nitriding equipment

After the nitriding, all surfaces of the samples were examined by using binocular stereo-microscope. The cross sections of each sample was polished in a clamping and chemically etched in 2% Nital.

## 3. Results and discussion

Edge effect shows different color from the center of the specimens which treated by DCPN process or using bias, in contrast, ASPN process (Fig. 2). At the ASPN process the glow discharge didn't occur on the surface, samples was heated by the radiation from the screen which causes higher homogeneity of the temperature [5].

Comparison the compound layer of the samples revealed that the different type of nitriding cause different thickness layer (Table 2) on the surface (Fig. 3).

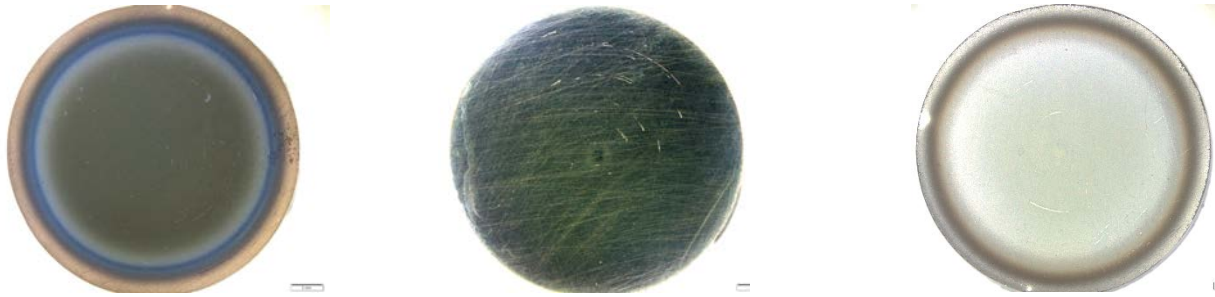


Fig.2. Samples surfaces after plasma nitriding: 1. DCPN, 2. ASPN, 3. ASPN+bias

Thickness ( $\mu\text{m}$ )		
DCPN	ASPN	ASPN+bias
9,2	4	8,7

Tabl. 2. Thickness of the nitrided layer

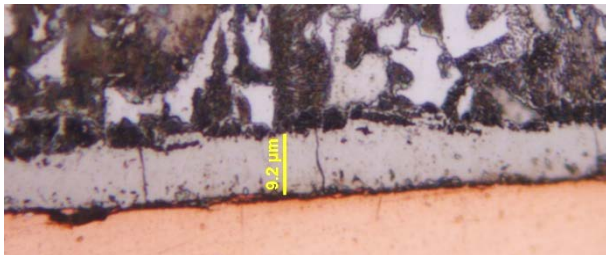


Fig. 3. Nitrided layer that etched in 2% Nital

As the hardness values (Fig. 4.) and the thickness values show, the ASPN process has lower quality, but the surface is more homogeneous compared to the other two.

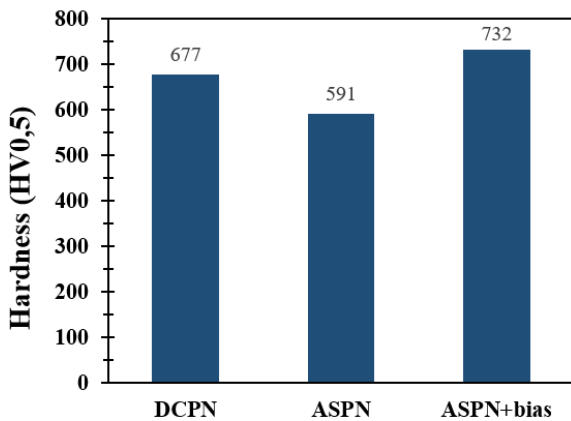


Fig. 4. Hardness of the nitrided samples

#### 4. Remarks

- The edge effect was observed on the surface of the different type of plasma nitriding samples.

- ASPN process has more homogenous surface, but the layer thickness and the hardness is lower than the other processes.

#### Acknowledgements

This work was supported by the scholarship of Hungarian Ministry of National Resources (National Talent Programme; NTP-NFTÖ-17-0086)



#### References

- [1] Pye D: Practical nitriding and ferritic nitrocarburizing. ASM International, 2003. 71–107.
- [2] Kocsisné Baán M., Marosné Berkes M., Szilágyiné Bíró A.: Nitridálás – korszerű eljárások és vizsgálati módszerek. Miskolci Egyetem, 2015. pp. 126-154.
- [3] Kuzsella L., Frigyik G., Kocsisné Baán M., Varga Zs., Sávolyi S.: Plazmanitridálási kísérletek szerszámacélokon. HTSART Nyomda és Kiadó, 2014. pp. 246-256.
- [4] Zhao C., Li C.X., Dong H., Bell T.: Study on the active screen plasma nitriding and its nitriding mechanism. Surface & Coatings Technology 201, (2006) 2320–2325.
- [5] Szilágyiné Bíró A.: Aktív ernyős plazmanitridálás gyakorlati tapasztalatai gyengén és erősen ötvözött nemesíthető acélokon. Gépipari Tudományos Egyesület, Hőkezelő Szakosztály, 2016. pp. 185-189.

# TENSION IDENTIFICATION OF PIPELINE COMPENSATORS

Tadeusz SMOLNICKI<sup>1</sup>, Paweł MAŚLAK<sup>2</sup>, Piotr ODYJAS<sup>3</sup>, Jacek KARLIŃSKI<sup>4</sup>

- <sup>1</sup> Wrocław University of Science and Technology, Faculty of Mechanical Engineering, Wybrzeże Wyspiańskiego 27, 50-370, Wrocław, Poland. E-mail: [tadeusz.smolnicki@pwr.edu.pl](mailto:tadeusz.smolnicki@pwr.edu.pl)
- <sup>2</sup> Wrocław University of Science and Technology, Faculty of Mechanical Engineering, Wybrzeże Wyspiańskiego 27, 50-370, Wrocław, Poland. E-mail: [pawel.maslak@pwr.edu.pl](mailto:pawel.maslak@pwr.edu.pl)
- <sup>3</sup> Wrocław University of Science and Technology, Faculty of Mechanical Engineering, Wybrzeże Wyspiańskiego 27, 50-370, Wrocław, Poland. E-mail: [piotr.odyjas@pwr.edu.pl](mailto:piotr.odyjas@pwr.edu.pl)
- <sup>4</sup> Wrocław University of Science and Technology, Faculty of Mechanical Engineering, Wybrzeże Wyspiańskiego 27, 50-370, Wrocław, Poland. E-mail: [jacek.karlinski@pwr.edu.pl](mailto:jacek.karlinski@pwr.edu.pl)

## 1. Introduction

Process installations in the chemical industry often undergo very high thermal stresses, which cause significant changes in linear dimensions. Flexible slings and supports and compensators are used to limit the stresses caused by thermal phenomena. The basic problem in selecting a compensation circuit is the complex spatial state of the load occurring in the installation. The required rigidity of system components is determined solely on the basis of a simple linear model that does not take into account the complex form of the deformation of the compensators. This particularly applies to lens compensators (Figure 1.), which, in addition to the low axial stiffness, also have low stiffness and significant transverse and torsional stiffness. Stiffness characteristics are nonlinear and temperature dependent.



**Fig. 1.** 3-lens compensator

## 2. Methodology of research

Determining the state of the expansion of the compensators due to interactions between the individual pipelines requires the construction of computational models of the whole system (Figure 2). With such large models it is impossible to faithfully donate the geometry of the compensators [1].

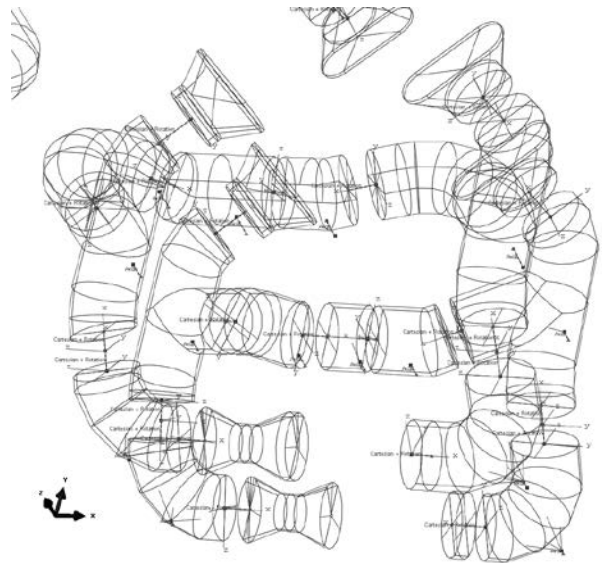


**Fig. 2.** Part of of the analyzed process installation

Therefore, it is necessary to conduct the analysis at different levels of detail (fig.3) [2,3].

The first step is to determine the stiffness matrix of the substitute element of compensators.

In the second step, substitute elements are applied to the global model of the whole system. After thermal-displacement analysis, the displacement of the connector points of the

connectors to the local models and the further strength and fatigue analysis are extrapolated.

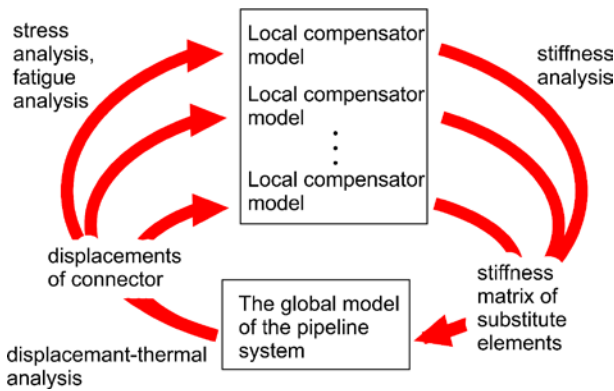


Fig. 3. Methodology.

### 3. Determination of boundary conditions

Boundary conditions for global model analysis are measured long-term during system operation. These are the temperature of the flowing medium and the pressure. Data acquisition time was 2 months. Because of the aggressiveness of the environment and the thermal insulation, it was impossible to measure displacements. Additional load is gravity. Figure 4 shows an example of the temperature waveform recorded for 48h.

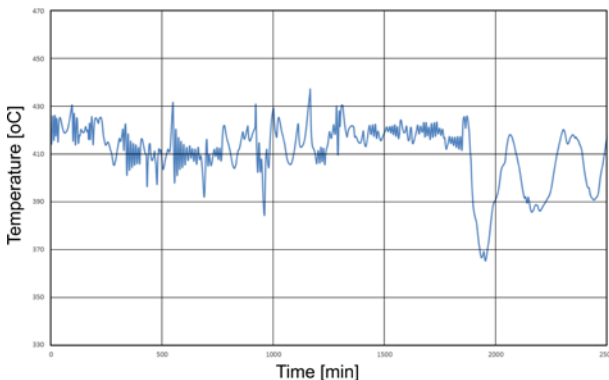


Fig. 4. Temperature waveform.

### 4. Summary

The purpose of the calculations was to check the correct choice of compensators. The methodology used was based on analysis at two different levels of model detailing. The average stresses and the amplitude of the stresses in the compensators were determined. It has been shown that some of the expansion joints mainly work on bending, ie, they mainly compensate the angular displacement, although their selection is based on

the assumption of linear compensation. Further analysis will be based on the analysis of the variability rainflow stress in a long time operation on the basis of the waveforms recorded actual operating parameters to estimate fatigue life.

### References

- [1] Rusiński E., Czmochowski J., Smolnicki T.: Zaawansowana metoda elementów skończonych w konstrukcjach nośnych. Oficyna Wydaw. PWroc., 2000
- [2] Smolnicki T., Karliński Jacek, Derlukiewicz D.: Identification of internal stresses in bolted flanged joints. Solid State Phenomena. 2010, vol. 165, s. 353-358
- [3] Smolnicki T., Rusiński E., Karliński J.: FEM modelling of fatigue loaded bolted flange joints. Journal of Achievements in Materials and Manufacturing Engineering. 2007, vol. 22, iss. 1, s. 69-72

# NUMERICAL AND EXPERIMENTAL IDENTIFICATION OF CRACK IN THE STACKER CONSTRUCTION

Jerzy CZMOCHOWSKI<sup>1</sup>, Paweł MAŚLAK<sup>1</sup>, Grzegorz PRZYBYLEK<sup>1</sup>,

Mariusz STAŃCO<sup>1</sup>, Damian PIETRUSIAK<sup>1</sup>

<sup>1</sup> Wrocław University of Science and Technology, Faculty of Mechanical Engineering, Department of Machine Design and Research, Łukasiewicza 7/9, 50-371 Wrocław, Poland. e-mail: [jerzy.czmochowski@pwr.edu.pl](mailto:jerzy.czmochowski@pwr.edu.pl), [grzegorz.przybylek@pwr.edu.pl](mailto:grzegorz.przybylek@pwr.edu.pl), [pawel.maslak@pwr.edu.pl](mailto:pawel.maslak@pwr.edu.pl), [mariusz.stanco@pwr.edu.pl](mailto:mariusz.stanco@pwr.edu.pl), [damian.pietrusiak@pwr.edu.pl](mailto:damian.pietrusiak@pwr.edu.pl)

## 1. Introduction

In lignite mines, mining and quarrying machines are used for the extraction of coal and overburden. The set of machines is used to remove the overburden: excavator - belt conveyor - stacker [1]. Due to the long life of these machines (often above 30 years) there is a problem to assess their continued safe use. Excavators and stackers are especially heavy loads. In today's mines the overburden is characterized by hard rock layers, resulting in faster degradation of the load-bearing structures of these machines. The publications describe the failures of these machines, the main caused by fatigue cracks [2]. Also in the bearer carrier systems due to their large size, large extensibility, there are significant inertia forces especially in transient states, such as start-up of ride or start-up of rotate of the bodywork.



Fig. 1. Stacker A2RsB 15400

Using the method presented in the paper [3], one of the largest stacker shown on Fig. 1 was carried out in Poland in the lignite mine Bełchatów. FEM numerical method was used to identify the places with the highest stress due to fatigue strength and non-destructive experimental methods.

## 2. Numerical analysis

One of the basic tasks in determining the condition of machines after long-term use is to determine the places of high stress [3, 4]. For this purpose, the finite element method was used. The numerical model of the stacker carrier structure is shown in Fig. 2.



Fig. 2. The numerical model of the stacker

The numerical model uses discretization using beam and shell finite elements. The bar structures of the discharge boom, the counterweight boom and the masts were modeled using beam finite elements, the support structure, the tower were modeled with shell elements. Numeric calculations were performed for load cases defined in DIN 22261 [5]. Particularly important in these calculations are the cases to determine the fatigue strength used in the proof of service life. The results from these calculations show the places susceptible to fatigue cracks. Figure 3 shows stress of the structure with a high level of stress difference, in which serious fracture has been identified. This is a particularly important place, as all machine assemblies are connected to this carrier system. The failure of one of the beams of this carrying system could have resulted in a catastrophe of the whole machine.

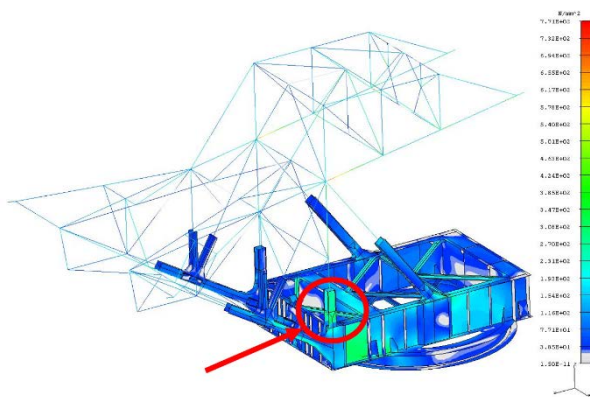


**Fig. 3.** Stress for load case H1b [5] with marked place of crack

### 3. Experimental investigations

Detailed inspection, vibration measurement at work [6, 7], deformation measurements, corrosion defects measurements and non-destructive defectoscopy (NDT) tests at welded joints are carried out in the assessment of the condition of machines after many years of operation. Weld joints due to the notch effect and changes in the material structure are susceptible to fatigue cracks. In the investigated stacker, special attention was paid to the examination of welds in places of high fatigue stress. A fatigue crack was detected at the location of one of the joint in its central section (Figure 4.). Magnetic-powder method [8] was used to detect cracking.



**Fig. 4.** Cracking at the weld in the tower supporting structure

A crack of about 20 cm in length was found at the weld at the change of box cross section to I-beam. Upon detection of this cracks, the machine has been stopped to repair the damage.

### 4. Remarks

- The finite element method was used to determine the places of high fatigue life in the structure of the stacker
- For the identification of cracks, a non-destructive (NDT) method was used in welded joints.

### References

- [1] Kasztelewicz Z., Koparki wielonaczyniowe i zwalowarki taśmowe. Technologia pracy. Fundacja Nauka i Tradycje Górnicze Wydział Górnictwa i Geoinżynierii AGH, Kraków 2012
- [2] Rusiński E., Czmochoowski J., Iluk A., Kowalczyk M., An analysis of the causes of a BWE counterweight boom support fracture. Engineering Failure Analysis 2010, 17, 179–91
- [3] Rusiński E., Czmochoowski J., Moczko P., Pietrusiak D., Surface Mining Machines. Problems of Maintenance and Modernization. Springer, 2017
- [4] Czmochoowski J., Przybyłek G., Działak P., Maślak P., Stańco M., Method of Technical Check of Superstructure of Bucket-Chain Excavator. Materials Today: Proceedings, 2017
- [5] DIN 22261-2:2006 – Bagger Absetzer und Zusatzgeräte in Braunkohlentagebauen
- [6] Czmochoowski J.: Identyfikacja modeli modalnych maszyn urabiających w górnictwie węgla brunatnego, Oficyna Wydawnicza Politechniki Wrocławskiej, Wrocław 2008
- [7] Lalanne C. Mechanical Vibration and Shock Analysis, Fatigue Damage, Wiley, 2009
- [8] Lewińska-Romicka A.: Badania nieniszczące. Podstawy defektoskopii. Wydawnictwo Naukowo-Techniczne. Warszawa 2001

## EXPERIMENTAL INVESTIGATION OF FRICTION REDUCTION BY SUPERIMPOSED VIBRATIONS

Martin Meindlumer<sup>1</sup>, Helmut J. Holl<sup>1</sup>, Viktoria Simader<sup>1</sup>, Dominik Schnürer<sup>1</sup>, Andreas Brandl<sup>1</sup>

<sup>1</sup> Johannes Kepler University Linz, Department of Technical Mechanics, Altenberger Straße 69, A-4040, Linz, Austria. E-mail: [martin.meindlumer@jku.at](mailto:martin.meindlumer@jku.at)

### 1. Introduction

The presence of friction in machines and devices causes energy dissipation and frequently stick slip vibrations and acoustic emission are excited. It is important to understand the macroscopic behavior of friction in contact areas, which is present and relevant in a lot of technical applications. Energy dissipation and wear results from this friction model. A reduction of the effects of friction is possible with suitable superimposed vibrations. An experimental setup was designed and constructed to evaluate the possible reduction of friction by superimposing vibrations to a defined motion in a certain frequency range. Various frequencies and vibration amplitude parameters can be adjusted in the experimental setup where cutting and friction forces are studied.

### 2. Mechanical model for a contact with friction

For a friction model considering the direction of the relative velocity between the particle under consideration and the moving base, see the sketch of the contact pair in Fig. 1, the direction and amplitude of the friction force can be calculated for a given contact force  $F_N$ . It is assumed that the friction coefficient  $\mu$  of the Coulomb friction is constant and independent of the absolute value of the relative velocity.

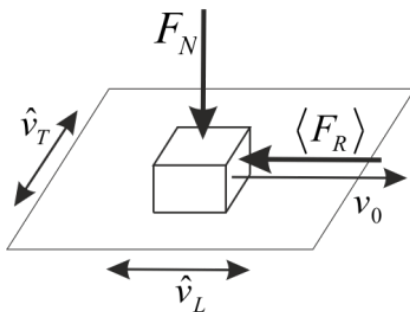


Fig. 1. Sketch of the contact pair

In [1] a similar friction model is demonstrated for two orientations of the relative motion and a constant as well as a harmonic velocity profile excited by a piezoelectric actor was used. The equations for the reduction of friction force depend on the ratio between average transport speed and the amplitudes of longitudinal and transversal vibrations considering the relative speed direction and the resulting direction of the friction force.

For longitudinal vibrations of the particle the average friction force  $\langle F_R \rangle$  can be computed based on one vibration period and is given by

$$\langle F_R \rangle = \begin{cases} \frac{2\mu F_N}{\pi} \arcsin\left(\frac{\hat{v}_L}{v_0}\right) & \text{for } v_0 < \hat{v} \\ \mu F_N & \text{for } v_0 > \hat{v} \end{cases}, \quad (1)$$

where  $F_N$  is the normal force between the contact pair,  $\mu$  is the friction coefficient (Coulomb friction),  $v_0$  is the average velocity between the contact pair and  $\hat{v}_L$  is the velocity amplitude of a longitudinal harmonic vibration superimposed to the average movement between the contact pairs.

For harmonic transversal motion of the specimen the average friction force over one oscillation period is given by

$$\langle F_R \rangle = \frac{\mu F_N}{2\pi} \int_0^{2\pi} \frac{d\xi}{\sqrt{1 + \left(\frac{\hat{v}_T}{v_0} \cos \xi\right)^2}}. \quad (2)$$

in the form of a Jacobian elliptic integral. In the equations the relation of absolute values of the amplitudes of the harmonic speed  $\hat{v}_L$  and  $\hat{v}_R$  and the base motion  $v_0$  is present. For high frequencies small vibration amplitudes and for low frequencies higher amplitudes are necessary. For the above friction model the average power consumption is computed and it can be shown that there is no reduction.

### 3. Experimental setup

In order to verify the computed results an experimental setup was constructed. A special cutting tool was specially mounted on a crank shaft mechanism, which is driven by an induction motor, in order to introduce vibrations excited with various parameters. As a reference material for the specimen several layers of bast fiber were used and mounted on a linear guide unit, which provides (adjustable) constant velocity of the specimen during the experiments. In a first step cutting and friction forces are measured together. In a second step the cutting tool is driven once more through the die clearance so that only the friction force is measured separately. The velocity of the linear guiding unit and the speed of the induction motor are fixed during one run of the experiment. In the results of the low pass filtered measurement data shown in Fig. 2 five different speed ratios were used.

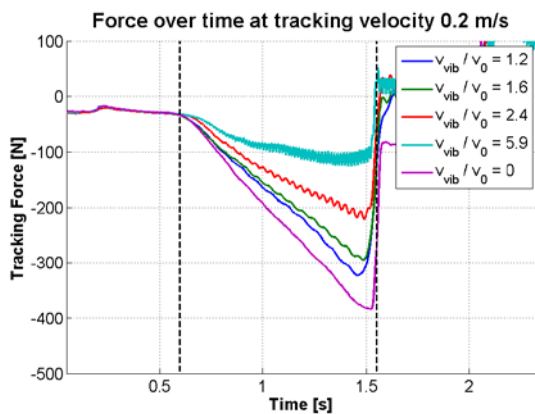


Fig. 2. Representative tracking force functions.

In Fig. 2 representative time functions of tracking forces for a tracking velocity of 200 mm/s and for different ratios of transport to oscillation velocity are shown. Power consumption and tracking force are averaged in time for the range between the dashed lines in Fig. 2 for the performed experiments. The driving force of the linear guiding unit, accelerations of one point of the cutting tool and the power consumption of the induction motor were measured. Idle power consumption of the whole setting measured and is subtracted in the results.

### 4. Results

The tracking force and the power consumption are averaged over one period related to the corresponding values without a vibrating tool for the tracking velocity and are shown in Fig. 3 and

Fig. 4. The dots mark the average reduction and the colored area marks the 90% confidential area. In the results a reduction of the traction force similar to the values predicted by the theory can be seen.

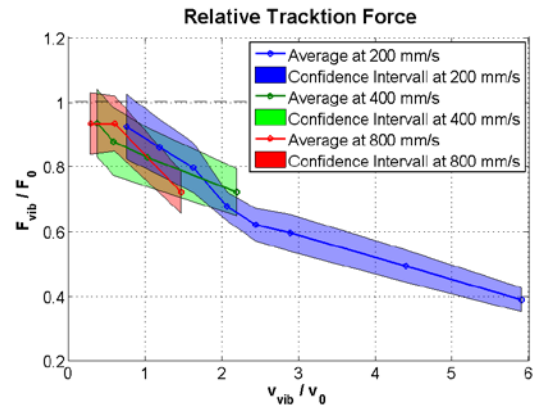


Fig. 3. Relative traction forces over velocity ratio

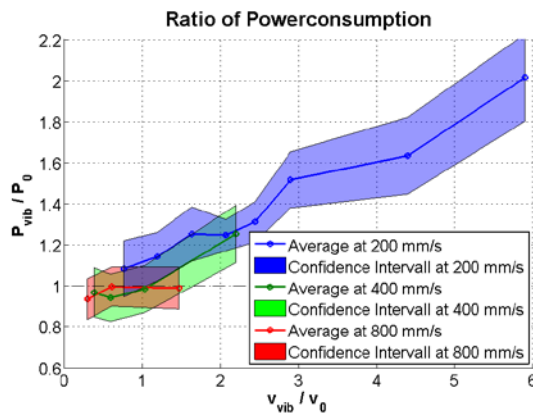


Fig. 4. Relative power consumption over velocity ratio

### 5. Conclusion

A model for friction and cutting evaluated was derived and the measurements have been carried out for a lot of selected parameters. The traction force was reduced to 50 % of its value without vibrating tool and the power consumption of the setup increases.

### Acknowledgements

The support of this work in the framework of the Comet-K2 Austrian Center of Competence in Mechatronics (ACCM), Area 2, Mechanics and Model Based Control, is gratefully acknowledged.

### References

- [1] Popov, V.L., Contact Mechanics and Friction. Springer Heidelberg Dordrecht London New York, 2010.